Alkaline water electrolysis enhanced by radio frequency alternating magnetic field

Vivien Gatard

THÈSE

Pour obtenir le grade de

DOCTEUR DE L'UNIVERSITÉ GRENOBLE ALPES

Spécialité : 2MGE : Matériaux, Mécanique, Génie civil, Electrochimie

Arrêté ministériel : 25 mai 2016

Présentée par

Vivien GATARD

Thèse dirigée par **Marian CHATENET**, Professeur INP, Université Grenoble Alpes
et codirigée par **Julian CARREY**, Professeur INSA, Institut National des Sciences Appliquées de Toulouse
et encadrée par **Jonathan DESEURE**, Maitre de Conférences, UGA
et co-encadrée par **Stéphane Faure,** Docteur
et co-encadrée par **Bruno Chaudret**, Directeur de recherche, LPCNO

préparée au sein du **Laboratoire d'Electrochimie et de Physico-Chimie des Matériaux et des Interfaces** et du **Laboratoire de Physique et Chimie des Nano-Objets**
dans **l'École Doctorale I-MEP2 - Ingénierie - Matériaux, Mécanique, Environnement, Energétique, Procédés, Production**

Electrolyse de l'eau en milieu alcalin assistée par champ magnétique alternatif radio fréquence

Alkaline water electrolysis enhanced by radio frequency alternating magnetic field

Thèse soutenue publiquement le **17 décembre 2021**,
devant le jury composé de :

Monsieur Marian CHATENET
PROFESSEUR DES UNIVERSITES, Grenoble INP, Directeur de thèse
Madame Marie-Cécile PERA
PROFESSEUR DES UNIVERSITES, Université de Besançon-Franche Comté, Rapporteure
Madame Sylvie BEGIN-COLIN
PROFESSEUR DES UNIVERSITES, Université de Strasbourg, Rapporteure
Monsieur Olivier LOTTIN
PROFESSEUR DES UNIVERSITES, Université de Lorraine, Examinateur
Monsieur Laurent DAVOUST
PROFESSEUR DES UNIVERSITES, Grenoble INP, Examinateur, Président
Monsieur Julian CARREY
PROFESSEUR DES UNIVERSITES, Université de Toulouse 3 - Paul Sabatier, Co-directeur de thèse
Monsieur Stéphane FAURE
DOCTEUR, invité
Monsieur Bruno CHAUDRET
DIRECTEUR DE RECHERCHE, LPCNO, Université de Toulouse, invité

« Vous ne jugerez pas de leurs aptitudes sur leur seule apparente facilité dans telle ou telle direction. Car celui-là va le plus loin et réussit le mieux qui a travaillé le plus contre soi-même. Vous tiendrez donc compte d'abord de l'amour. »

Citadelle, A. de Saint-Exupéry

Remerciements

Je tiens à remercier ici les personnes qui, sciemment ou inconsciemment, ont rendu ces trois années et demi de stage-thèse un moment si riche de rencontres, de partage, de rires et d'apprentissage. Toutes m'ont apporté, et je souhaite remercier chacune d'entre elle. Je vais d'ailleurs essayer de me limiter pour ne pas écrire 10 pages… mais, au vu de la longueur de la thèse, ce n'est pas gagné !

D'abord, mes encadrants.

A commencer par Marian, qui a permis cette aventure en me faisant confiance, dès le début du stage, pour changer de domaine et m'en apprendre un autre, celui de l'électrochimie. Tu as été patient quand il a fallu l'être, et, bien qu'il soit parfois difficile de comprendre ce que tu penses, je me suis rendu compte de la chance que j'avais d'avoir un directeur de thèse qui fait tout son possible pour être disponible, en étant d'une efficacité incroyable, toujours de bon conseil, et étant un chercheur modèle. J'ai beaucoup appris grâce à toi, et j'apprendrai sans doute encore en repensant à ton encadrement. Ainsi, pour tout cela, je te remercie grandement.

Ensuite, j'ai rencontré Jonathan, alias Jojo. J'ai particulièrement apprécié toutes nos discussions, aussi longues que variées, et le temps que tu as pris pour celles-ci. Tu as été une grande aide pour toute la partie physique et génie des procédés de la thèse. Sans toi, bien moins d'axes de recherche et d'analyses seraient apparus dans le manuscrit. Ta curiosité et ton partage y sont pour beaucoup. Petit clin d'œil à ton humour également, qui a aidé à décompresser et à prendre du recul. Je te remercie chaleureusement pour tout cela.

Allons à présent du côté Toulousain, rencontrer Julian. Julian est un modèle d'activiste défenseur du climat, avec le bouton « on » toujours enfoncé. Curieux, décroissant, résiliant, et prenant le temps de vivre et d'apprécier la vie. Tu as été très inspirant dans tes démarches, personnelles et professionnelles. J'ai eu beaucoup de chance de t'avoir dans ce projet, tu as grandement contribué (et contribue encore !) à l'ambiance si chaleureuse du LPCNO, que j'ai tant appréciée. Un grand merci pour tout cela, j'espère te revoir bientôt, autour d'un café ou d'une bonne bière.

Ensuite, Stéphane. Stéphane a été mon principal encadrant pendant mes courtes missions au LPCNO, et m'a énormément assisté pour toutes mes expériences à Toulouse. Ton approche de la recherche m'a vraiment plu. Et, bien sûr, j'ai beaucoup aimé nos nombreuses discussions, portant sur absolument tout. Ta curiosité est merveilleuse, et te pousse à lire et à apprendre toujours plus. Bien sûr, des sujets revenaient régulièrement - le marché du travail est loin d'être juste et méritoire, mais j'espère que tu t'épanouiras au mieux là où tu es et seras. Toi aussi, tu as été une figure très inspirante, et j'espère te revoir bientôt, en compagnie de Julian, autour d'une bonne bière ou d'un café. Merci pour tout.

Enfin, Bruno. Merci pour tes conseils et ton avis sur tous les points de la thèse. Ta hauteur de vue et ton expérience sont impressionnantes ! Merci aussi pour cette superbe atmosphère de travail au LPCNO (le directeur y contribue beaucoup), cette ambiance sud-ouest qui me donne envie de venir m'installer dans la ville rose.

Les membres du jury

Je tiens à remercier très sincèrement Laurent Davoust, Marie-Cécile Péra, Olivier Lottin et Sylvie Bégin, les membres du jury de ma thèse. Merci beaucoup pour avoir pris le temps d'évaluer mon travail, et un grand merci pour ce temps d'échange riche et bienveillant durant la soutenance. Vous avez rendu cet instant inoubliable.

Les collègues-ami.es

J'aime bien l'ordre chronologique, alors je vais commencer par le début, lorsque je suis arrivé en stage au troisième étage du LEPMI, dans l'équipe EIP. J'ai alors rencontré Clémence, Guillaume, et Marine, qui m'ont assuré que l'ambiance dans ce laboratoire était bonne, j'ai compris plus tard que c'était grâce à toutes les sorties organisées par chacun.e, qui permettent une cohésion forte. Puis, passage obligé, mon bureau a été installé en 348, dans celui de Marion et Fabien, qui m'ont accueilli à bras ouverts. Fabien, plein de ressources, merci pour toutes tes réponses à mes nombreuses questions, merci pour ton humour, ta complicité et l'exemple de courage que tu montres. Promis, je finirai l'énigme incroyable que tu as pondu pendant ta rédaction ! Marion, merci pour ton énergie, ton humour et ton franc-parler. J'admire ta force morale ! Clémence, ma collègue écolo, que j'ai rejoint au bureau 323.3 après un an et demi au 348, merci pour toutes ces discussions, que ce soit à propos du climat, du zéro déchet, ou sur

d'autres sujets qui nous ont concernés… cela a grandement aidé à relativiser !! Guillaume, ta passion et ton intuition en électrochimie sont impressionnantes, notamment après quelques pintes… merci pour toutes tes explications, tu as comblé bon nombre de mes lacunes dans ce domaine. Merci pour ton animalerie en origami, notre passion commune des casses-têtes, et ces pauses présidents infinissables ! J'ai aussi rencontré Alix, avec qui nous louons une passion commune pour the Kinks ! Merci pour ces après-midi jeux et à bientôt pour les suivantes ! Marine, merci pour nos discussions, notre bonne entente et ton aide ; j'admire par ailleurs ta droiture d'esprit. J'ai eu la chance, à chaque fois, d'avoir de supers collègues de bureau !

En descendant au rez-de-chaussée, j'ai rencontré François et son humour… bien à lui. Très curieux, fin pâtissier, merci pour toutes ces discussions, ton amitié, tous les nombreux moments que l'on a partagé (je pense notamment au Croisic et cette atmosphère insouciante de l'époque…) et pour les moments qu'on va continuer de partager ensemble ! Maha Rhandi, ta force de caractère m'a impressionné ; Killian Poulet-Alligand, merci pour ces après-midi jeux et ton aide lorsque j'en ai eu besoin. Occasionnellement, j'ai pu rencontrer Juan David Anaya, très bon danseur, toujours le sourire aux lèvres et prêt à rire. Merci pour ces moments partagés et cette soirée jusqu'au bout de la nuit ! Matthieu Gras, merci pour tes conseils et ta sympathie. Raphaël Chattot, le zikos du labo, passionné et très bon à la gratte. Merci pour ton aide dans mon travail, nos discussions, et… je regrette de n'avoir pas osé jouer un peu de guitare avec toi. Merci également à Pierre Bonin et ses Cr^{VI}, David et son accent américain, Vijetha, et Vincent Caldeira, merci pour ta sympathie et tes réponses à mes questions.

Côté LPCNO, j'ai d'abord rencontré Nico Mille. Je me souviendrai toujours, le premier jour, de ta réponse à ma question : « puis-je déjeuner avec vous ? – Y'a intérêt ! » Ca m'a beaucoup touché, et je me suis senti très vite intégré. Nico, c'est en grande partie grâce à toi, alors un grand merci pour cela. Merci aussi pour ton aide, pour les soirées, ta confiance et ta sympathie. J'ai rencontré aussi Alex, féru de physique, Arnaud alias Nono, dont l'humour peut déclencher des fous-rire à tout instant, Nicolas Hallali, merci pour ton accueil, ton partage, ton écoute. Tu as fait un choix de vie singulier que j'admire, quel beau projet tu mènes ! Merci aussi à Sébastien Lachaize qui est un exemple de résilience avec un mode de vie (quasi) durable. Ton engagement est source de courage ! Merci pour tous ces échanges, j'aurais aimé passer bien plus de temps encore à échanger avec toi. J'ai rencontré également Déborah de Masi, je n'aurais pas pu réaliser ma thèse sans tes travaux, merci !! Simon Raffy, Julien Marbaix, Juan Asension Revert - merci pour ta grande disponibilité et ton expertise ! Irene, tu as fait au mieux

pour synthétiser les nanoparticules et me les envoyer, même si je te le demandais en urgence, désolé pour cela et merci beaucoup pour ton aide, ta sympathie et ta disponibilité durant ma thèse !

Puis, d'autres sont arrivés alors que je démarrais la thèse. Au LEPMI, je pense à Eris, dont l'humour, la joie de vivre et le caractère m'ont beaucoup plu et m'ont toujours fait beaucoup rire ! Merci pour ces moments partagés, ton énergie et les photos inoubliables ! Sofyane, un géant très gentil, avec beaucoup d'humour et très bon client. Et, bien sûr, je pense à Jérôme. Le montagnard pure souche, d'une attention et gentillesse rares et très touchantes. Tu es l'ami parfait : à répondre toujours présent, à être toujours de bon conseil, à arrondir les angles lorsqu'il y a besoin, à dire les choses sinon, à proposer un paquet de sorties, à organiser, à aider, à donner ton temps sans sourciller. Merci pour tous ces superbes moments passés et ces découvertes grâce à toi. Bref, merci pour ton amitié, je suis ravi que celle-ci perdure !

Alors que je commençais ma thèse, Kavita est arrivée, toute souriante et toujours de bonne humeur ! Merci pour tous ces moments partagés, surtout en dehors du labo ! J'ai rencontré Ugo en même temps, avec qui le courant est vite bien passé ! Est-ce qu'on va enfin trouver un moment pour faire un peu de zik ?! Youcef est arrivé aussi, discret, très gentil, et si courageux. Tu as traversé tellement de choses pendant ta thèse, je souhaite de tout cœur que tu puisses trouver une opportunité qui te plaise ! Marie, Delphine, je vous garde de la place à la fin des remerciements… La même année, Patricia a fait un stage au LEPMI. Cette nouvelle rencontre a permis de se connaître davantage et d'accrocher. J'ai ensuite rencontré Clément, et passer de plus en plus de temps ensemble à rigoler, jouer, escape gamer, mais aussi skier et fêter un évènement à Méribel, rencontrer une famille si chouette, passer des vacances au bord d'une piscine avec une vue magnifique, et ce n'est pas fini… :D merci à tous les deux pour tous ces moments, et pour tous ceux futurs aussi !

Deux autres vagues d'entrants sont survenues au LEPMI. Raphaël Riasse, très vite intégré, courageux à mettre en place les bancs d'hydrogène et la GDE, merci pour l'organisation des évènements et les moments partagés ! Sédik Illoul, qui a fait un stage et a continué sa thèse. On s'est toujours bien entendu et profité des conseils et de l'humour de chacun. Ricardo Sgarbi, tu es revenu pour un deuxième séjour au LEPMI, j'ai beaucoup aimé ton humour et ta gentillesse, j'espère que tu continueras la musique ! Huong Doan, pleine d'énergie, je suis toujours impressionné par la chef d'équipe et de projet que tu es ! Weverson Capute, tu as appris

le français en 3-4 mois, j'en suis toujours stupéfait ! Merci pour ta gentillesse et ta sympathie. Sans oublier ceux au rez-de-chaussée : Mathilde Perrin, dont le talent d'artiste ne cessera de m'impressionner ! Merci pour toutes ces belles initiatives de soirées ! Parfait Kamara, qui forme la paire avec Mathilde, bon blagueur et toujours prêt à rire. J'aime l'Afrique que tu apportes avec toi et que tu partages au labo.

Ensuite, la deuxième vague est arrivée. Matthieu Tempelaere d'abord, sportif jusqu'au bout des pieds, et des mains aussi. Travailleur organisé à la minute près, tu vas finir par avoir une triple thèse si tu continues d'avancer à cette allure… ! Merci pour tout ces échanges, j'espère qu'on va continuer à se voir à d'autres évènements. Théo Faverge, sportif et toujours blagueur ! J'admire ton courage de mener une thèse tout en étant pompier volontaire ! Pareil, j'espère qu'on se recroisera au bar ou à d'autres évènements. Arthur Bukowski, Quentin Labarde, on n'a pas pu beaucoup échanger en dehors du labo à cause du covid, j'espère que ça se fera quand même un jour malgré les conditions sanitaires. Keyla, who arrived in the 323.3 office while I was finishing my manuscript. Thank you for your smile, it was a pleasure to meet you even for such a short time. Maybe we will see each other during future events! Anne-Claire, que j'ai retrouvé au LEPMI après l'avoir rencontrée à la fin de mon stage à l'INES, en 2017. C'était chouette de te retrouver, cela m'a fait repenser à la première expérience de recherche que j'ai eu, et qui m'a décidé à continuer dans cette voie. Sans doute qu'on se recroisera ! Je pense aussi à Arnaud Viola, qui m'a beaucoup aidé avec les dernières synthèses de nanoparticules, j'espère te rencontrer davantage lors de sorties ou soirées coinche ! Maguy Nahra, discrète et très sympa. Je tiens à remercier également deux stagiaires de Jonathan, Miguel Pinto et Durand Brunel, qui ont contribué significativement à ma thèse. Vous avez fait un super boulot, merci beaucoup ! Jonathan Shilling aussi, qui va poursuivre mon travail pendant un post-doc de 8 mois, je te souhaite bien du courage !

Côté LPCNO, du renouveau s'est fait également : Alvaro Raya Baron and Georgiana Dragomir-Maties, who provided me with new materials which helped enrich my PhD. Thank you for that, but also for your help and your reactivity when I needed emergency information. Sourav Ghosh, thank you for your attention and your help each time I needed it. It is a pity that PANI materials did not work much. Thibault Ourlin, qui s'est montré patient, arrangeant et tant disponible pour m'aider, un grand merci. I think also to Nataliia Marchenko and Gabriel Mencia Berlinches, with who I would have liked to spend more time. Bastien Sanglard, avec qui j'aurais eu plaisir à partager une bière, si les restrictions sanitaires ne nous en avaient pas empêché. Tu

as un sujet de thèse passionnant, et je suis sûr que tu le mèneras au bout en réalisant une superbe thèse !

Les chercheur.ses

Je tiens à remercier également tous les chercheurs et chercheuses que j'ai côtoyés, même si je n'ai pas travaillé avec eux. Au LEPMI, je pense à Frédéric Maillard, Laetitia Dubaud, Isabelle Billard, dont j'admire l'engagement à défendre le droit des femmes dans la science, et son énergie pour plein d'activités ! J'aurais aimé jouer au moins une partie d'échec avec toi. Florence Druart (je me souviens que je t'ai fait danser le rock au Croisic !), merci pour ton aide et merci de m'avoir fait confiance pour encadrer les TPs GP avec toi et Nadine Commenges; Alain Denoyelle qui m'a fait confiance pour encadrer les TPs d'électrochimie avec lui, Eric Sibert, Eric Chainet, Jean-Pierre Magnin.

Au CMTC

Je tiens à remercier vivement Thierry Encinas pour sa patience, sa passion et sa pédagogie. Merci pour tout le temps passé à m'apprendre la DRX. Je remercie également Frédéric Charlot, qui a réalisé toutes les images MEB, merci pour ton temps, les explications et nos discussions.

Les Tech', assistants ingénieur.es et ingénieurs

Ici, il y a de grands mercis à faire… Côté Toulousain, mes remerciements vont à Catherine Crouzet, alias Cathy, notre maman au LPCNO. Nuno et Francis, sur qui j'ai toujours pu compter. Leurs compétences de débrouillard.e et bricoleur.se sont vitales pour toute thèse ! Je remercie tout particulièrement Angélique Gillet et Adeline Pham, qui ont fait tout leur possible pour que mes missions au LPCNO soient réussis. Merci vraiment pour votre aide et votre écoute, malgré la surcharge de travail que vous pouvez avoir. Je remercie également Géraldine Ballon, qui a réalisé toutes les mesures au VSM, et Touati Douar, pour m'avoir chaleureusement accueilli dans votre bureau.

Côté LEPMI, je remercie Vincent Martin, qui a réalisé toutes les mesures ICP-MS. Je suis heureux d'avoir partagé plusieurs moments hors travail avec toi, j'aime beaucoup la

douceur et même la tendresse que tu as face à la vie et pour ce que tu captures en photo. Merci aussi à Laure Lavernot pour son courage à toute épreuve, notamment face au Covid.

Les personnes des équipes administratives

Ici, je remercie grandement Corinne Meunier, Claire Girardi, Claire Benoit et Yasmine Bouhadjar, qui m'ont beaucoup aidé dans toutes les démarches administratives, même lorsque je m'y prenais tardivement, où qu'il y avait des pépins d'envoi de colis, de commandes… Merci ! Vous faites un super boulot !

Côté LPCNO, je remercie Brice Altman qui a géré toutes mes missions et les arrivées/envois de colis.

Il reste quelques personnes…

Je vais commencer par finir avec Delphine Yetim et Marie Minola, les deux mousquetaires avec qui nous avons mené en parallèle une thèse. Notre trio a bien grandi, des premiers pas dans la thèse, en passant par un week-end fabuleux à Marseille, toutes les soirées, sorties bars, escape games, week-end ski, à la rédaction et la soutenance… Nous avons su prendre le temps pour chacun.e, nous écouter, nous aider, durant tout ce marathon ô combien sinueux et vallonné de la thèse. Delphine, je suis admiratif de ton courage et ta bravoure face à l'adversité de la vie. Tu ne te laisses jamais abattre, et cela te permet d'aller jusqu'au bout, même ensevelie dans des situations infernales… Marie, je trouve que tu as beaucoup grandi pendant cette thèse, tant à travers notre rôle de responsables non-permanents qu'à travers la thèse ou les activités extérieures (danse…), tu peux être fière de toi. Ainsi, je suis très fier de nous et vous félicite affectueusement, bravo !

Bien sûr, la réussite de cette thèse est également due à d'autres personnes hors du cadre professionnel, qui m'ont toutes soutenu.

Merci à tous les camarades de promo sur Grenoble, Joris, Etienne, Gwenaël, Lucas, Marie, Josserand, Younes, Maxence, Guillaume, les sorties bar et les fameuses soirées chez Valentin Le Marchand, les descentes des gorges de l'Ardèche, de beaux moments partagés, qui marquent !

Alex, Noémie et leurs ami.es d'école d'ingé, cet EVG et ce mariage… de beaux souvenirs et des temps forts, merci à tous.

Julien, Lorraine et leur bout de chou qui m'ont hébergé à Toulouse, merci.

Naomie et Thibaut, malgré le peu de sorties qu'on a pu faire, celles-ci ont toujours été chouettes !

Mathilde & Julien, notre trio est si fort et m'est très précieux. Que de bons souvenirs depuis la prépa, avec tant de vécus et de rebondissements. Merci d'être et d'avoir été là.

Quentin Provent-Ravenet, c'était un plaisir de suivre le premier livret à travers ton animation, je suis heureux que nos liens tiennent et se renforcent.

Sophie, ton écoute et ta bienveillance sont toujours un précieux cadeau. Samuel, on trouvera du temps pour jouer de la musique ensemble !

Alice Sarrazin, chère Alice, ma Alice. Malgré la distance, notre amitié perdure depuis 15 ans et perdurera, j'en suis sûr. Je suis très heureux de te compter parmi mes amies et aime à me souvenir de tout ce que l'on a partagé, notamment ce traintrip en Europe centrale juste avant ma thèse, et ton séjour sur Grenoble juste après. De tout cœur, merci d'avoir toujours été là.

Léa Fournasson, la vie est surprenante, et voici qu'elle nous a rassemblés en école d'ingénieur deux années après notre première rencontre inopinée en vacances, pour créer une amitié solide, sans faille, que je crois pas prête de s'arrêter ! Tant de souvenirs, des soirées chez toi dans ton appart rue Alsace Lorraine, de ta coloc boulevard Joseph Vallier, lorsque tu m'as hébergé, l'Estonie et ses huskys – je ne détaille pas toutes les péripéties… - le voilier dans le golfe de Botnie… Notre passion commune du piano, la Cantina Band dans l'aéroport… Merci, merci pour cette belle amitié.

Bien sûr, merci à mes ami.es d'enfance, Gwénégan, Cédric, Thibault, Samuel, Yanis, Florian, Pauline, Alice, Romain et toutes leurs copines-copains. 27 ans de souvenirs, et encore tant de partage à venir… Je ne vais pas m'étaler sur notre amitié, ce serait trop long, et ils savent tout l'amour que je leur porte.

Marc-Antoine, un ami d'enfance également. Nos rencontres sont toujours un moment attendu et très riche. Comme notre amitié me fait du bien !

Merci à ma famille éloignée, les nombreux oncles et tantes, Danielle et ses petites attentions, les (petit.es) cousins et cousines, mais aussi mon parrain et ma marraine, qui m'ont tous soutenu.

Merci à mes parents, qui m'ont toujours soutenu dans mes études, quels que soient mes choix. Ils ont toujours été à l'écoute, j'ai toujours pu compter sur eux, je ne pourrais jamais assez les remercier de tout l'amour qu'ils me portent. Je vous aime.

Ma sœur, notre complicité, notre écoute, notre bienveillance, notre amour, merci. Tug, merci pour ton soutien et tous ces moments partagés, à rire, discuter, découvrir de la musique, en apprendre plus sur plein de sujets.

Enfin, la thèse m'a permis de rencontrer celle que mon cœur à choisi, Estelle. Notre amour était inattendu, et c'est là la beauté de la vie. Merci pour ton soutien constant : ton attention, ton écoute, ta patience, notamment pendant mes missions à Toulouse, et ta confiance. Mais aussi, merci pour toutes ces sorties – découvertes – randonnées – séjours – vacances, ces chansons, cette complicité, ces photos, ce confinement, ces bons petits (gros) plats… Merci de me rendre meilleur chaque jour à travers notre amour.

Un grand merci à toutes celles et ceux qui ont pu laisser un petit mot dans le carnet !

J'espère n'avoir oublié personne. Au cas contraire, pardon d'avance…

A toutes celles et ceux de ma famille qui ont travaillé dur
Pour me permettre d'être là où j'en suis

Table of Contents

List of abbreviations

AMF	Alternating Magnetic Field
AST	Accelerated Stress Test
ATO	Antimony-doped Tin Oxide
AWE	Alkaline Water Electrolysis
CCD	Charged Coupled Device
CE	Counter Electrode
CISS	Chiral-Induced Spin Selectivity
CP	Chronopotentiometry
CTC	Charge Transfer Coefficient
CV	Cyclic Voltammetry
CV_C	Cyclic Voltammetry in a capacitive current region
CV_F	Cyclic Voltammetry in a Faradaic current region
DFT	Density Functional Theory
DI	Deionized (water)
ECSA	Electrochemical Surface Area
EIS	Electrochemical Impedance Spectroscopy
Eq.	Equation
ETEM	Environmental TEM
FC	Fuel Cells
FWHM	Full Width at Half Maximum
HAADF	High-Angle Annular Dark-Field
HER	Hydrogen Evolution Reaction
HHV	High Heating Value
HI	Hot Injection
HOR	Hydrogen Oxidation Reaction
HRTEM	High Resolution TEM
ICP	Inductively Coupled Plasma
ICP-MS	ICP Mass Spectrometry
ICP-AES	ICP Atomic Emission Spectroscopy
ILTEM	Identical Location TEM
MF	Magnetic Field
MHD	Magnetohydrodynamic
NP(s)	Nanoparticle(s)
OCP	Open Circuit Potential
OER	Oxygen Evolution Reaction
OGM	Organometallic
ORR	Oxygen Reduction Reaction
PCTFE	Polychlorotrifluoroethylene
PEM	Proton Exchange Membrane
PEMFC	PEM Fuel Cell
PEMWE	PEM Water Electrolysers
PGM	Pt Group Metals
PMMA	Poly(Methyl Methacrylate)
PTFE	Polytetrafluoroethylene
QSEI	Quantum spin(-orbital) Exchange Interaction
RDE	Rotating Disk Electrode
REF	Reference (electrode)
RHE	Reversible Hydrogen Electrode
RT	Room temperature
rms	Root Mean Square
rpm	Rotation Per Minute
SAR	Specific Absorption Rate
SEM	Scanning Electron Microscopy
SOE	Solid Oxide Electrolysers
SPM	Superparamagnetic
STEM	Scanning TEM
STP	Standard Temperature and Pression
TEM	Transmission Electron Microscopy
TGA	Thermogravimetric Analysis
V_{RHE}	Potential referred to the RHE
VSM	Vibrating Sample Magnetometer
WE	Water Electrolysis
WS	Water Splitting
X-EDS	X-ray Energy Dispersive Spectroscopy
XRD	X-Ray Diffraction

List of symbols

$\|.\|$	Absolute value (mathematics)
$\|\|.\|\|$	Standard (mathematics)
$<.>$	Average (mathematics)
Ø	Diameter of a wire/tube
/C	Supported on carbon Vulcan XC72
@Y	Enriched in element Y
$\boldsymbol{X}$	X vector
at.%	Atomic percentage
wt.%	Weight percentage
$^1\Delta_g$	Singlet excited state of dioxygen
$^3\sum_g^-$	Fundamental state of dioxygen
a_s	Activity of the specie *s*
A	Hysteresis cycle area ($m^2.s^{-2}$)
a	Slope of the curve in a Tafel plot
α	Charge transfer coefficient
$\boldsymbol{B}$	Magnetic flux density vector (T)
$B_a=B_{applied}$	Applied magnetic field (T)
$B_{//}$	Parallel to electrode applied magnetic field (T)
$B_\perp$	Perpendicular to electrode applied magnetic field (T)
b	Intercept of the Y axis at the origin in a Tafel plot
$[s]$	Concentration of a given specie *s* ($mol.L^{-1}$ or $mol.m^{-3}$)
$c_{+,-}$	Concentration of cations or anions ($mol.m^{-3}$)
C	Correction factor in the Scherrer equation
C_{DL}	Double layer capacitance (F)
Cp_s	Calorific capacity of specie *s*
C_S	Specific capacity (F)
$\boldsymbol{D}$	Electric displacement field vector ($C.m^{-2}$)
d	distance between the electrodes and the magnet (m)
d_c	Critical diameter (m or nm)
d_{hkl}	Interplanar distance (nm)
$< d_{XRD} >$	Average crystallite diameter
$D_{+,-}$	Diffusion coefficient of cation or anions ($m^2.s^{-1}$)
Δ	Energy to overcome to reverse the spin (J)
ΔX	Variation of quantity X
$\Delta_r G$	Gibbs Free Energy of reaction ($J.mol^{-1}$)
$\Delta_r H$	Enthalpy of reaction ($J.mol^{-1}$)
ΔS	Variation of entropy ($J.mol^{-1}$)
$\boldsymbol{E}$	Electric field vector ($V.m^{-1}$)
E_A	Activation energy (J)
E_{ani}	Anisotropy energy (J)
E_a	Anode Nernst potential of a redox couple (V_{RHE})
$E°_a$	Anode standard potential of a redox couple (V_{RHE})
E_c	Cathode Nernst potential of a redox couple (V_{RHE})
$E°_c$	Cathode standard potential of a redox couple (V_{RHE})
E_{corr}	Corrosion potential (V)
E_{dip}	Dipolar interaction energy (J)
E_{exch}	Exchange energy (J)

E_Z	Zeeman energy (J)
ζ	Dynamic Viscosity of a fluid (Pa.s)
e_{mag}	Electromotive force induced by the magnetic field (V)
η_a	Overpotential at the anode (V)
η_c	Overpotential at the cathode (V)
$\eta_{Faradaic}$	Faradaic efficiency of a system
$\eta_{Thermal}$	Efficiency calculated from the thermoneutral voltage
$\eta_{H2,yield}$ (25°C)	Efficiency with the HHV of hydrogen, accounting for the magnetic power consumed
θ	Incident angle in XRD (rad)
$\boldsymbol{F}_K$	Kelvin force density vector ($J.m^{-3}$)
$\boldsymbol{F}_L$	Lorentz body force vector ($J.m^{-3}$)
$\boldsymbol{F}_{mag}$	Magnetic body force vector ($J.m^{-3}$)
$\boldsymbol{F}_{\nabla c}$	Paramagnetic gradient body force vector ($J.m^{-3}$)
$\mathcal{F}$	Faraday constant ($C.mol^{-1}$)
f	Frequency of the alternating magnetic field (Hz)
g	Gravitational constant ($m.s^{-2}$)
$\boldsymbol{\nabla}$	Gradient vector
$\boldsymbol{H}$	Magnetic field strength vector ($A.m^{-1}$)
H_C	Coercive field ($A.m^{-1}$)
i	Current (A)
iR	Ohmic losses (Ω)
j	Current density ($A.m^{-2}$ or $mA.cm^{-2}$)
j_0	Exchange current density ($A.m^{-2}$ or $mA.cm^{-2}$)
K	Anisotropy constant ($J.m^{-3}$)
k_B	Boltzmann constant ($m^2.kg.s^{-2}.K^{-1}$)
$k°$	Standard rate constant (s^{-1})
k	Attenuation factor in the thermophoretic velocity equation
l	the dimension of the material in the direction of penetration of the field (m)
λ	Wavelength (nm)
M	Magnetization, *i.e.* magnetic moment per volume ($A.m^2.kg^{-1}$)
M_R	Remnant magnetization ($A.m^2.kg^{-1}$)
M_S	Saturation magnetization ($A.m^2.kg^{-1}$)
m	Mass-transport parameter (s^{-1})
m_i	Mass of specie *i* (kg or g)
$\mu°_{X/Y}$	Standard chemical potential of redox couple X/Y ($J.mol^{-1}$)
μ_0	Magnetic permeability of vaccum ($kg.m.A^{-2}.s^{-2}$)
μ_r (X)	Magnetic permeability of a material X
N	Number of bubbles per second (s^{-1})
n(X)	Number of mol of specie X (mol)
n	Number of electrons
pH	Potential of hydrogen
P	Pressure (bar)
$P°$	Standard pressure (bar)
P_i	Partial pressure of gas *i* (bar)
Q_V	Gas flux rate ($L.s^{-1}$)
q_S	Surface charge density ($C.m^{-2}$)
R	Ideal gas constant ($J.mol^{-1}.K^{-1}$)
R	Bubble radius (µm)
R_{anode}	Thermodynamic contribution at the anode
$R_{bubble, H2}$	Resistance due to the H_2 bubbles

$R_{\text{bubble, O2}}$	Resistance due to the O_2 bubbles
R_{bubbles}	Resistance due to the H_2 and O_2 bubbles
R_c	Electric contact resistance
R_{cathode}	Thermodynamic contribution at the cathode
$\text{Re}_{\text{ bubble}}$	Reynold number of bubble plume
$\text{Re}_{\text{ channel}}$	Reynold number of the cell channel of the electrolyte
$\text{Re}_{\text{ mag}}$	Magnetic Reynold number
R_{ions}	Resistance due to the conductivity of the electrolyte
R_{membrane}	Resistance due to the presence of a membrane
ρ_{mass}	Volumic mass ($kg.m^{-3}$ or $g.cm^{-3}$)
S	Entropy (J)
S_{sample}	Surface of the sample (m^2)
$\mathbf{S}$	Total spin angular momentum
s	Scan rate ($mV.s^{-1}$)
σ	Conductivity of the electrolyte ($S.m^{-1}$)
T	Temperature (K or °C)
T_B	Blocking temperature (K)
t	Thickness (mm)
ΔT	Temperature variation (K or °C)
Δt	Time duration (s)
τ_1	Time of the electron transfer (s)
τ_2	Bubble nucleation and growth time until its departure at the electrode surface (s)
τ_B	Brownian relaxation time (s)
τ_{meas}	Measuring time (s)
τ_N	Néel relaxation time (s)
τ_0	factor depending on the anisotropy in the Néel relaxation time expression (s)
U_{cell}	Cell tension (V)
U_{rev}	Equilibrium cell voltage (V)
U_{tn}	Thermoneutral voltage (V)
V	Volume of a particle (m^3 or nm^3)
V_H	Hydrodynamic volume of the nanoparticle (m^3 or nm^3)
φ	Angle between B_a and the magnetization of the particles (°)
$\boldsymbol{v}$	Velocity of the charged specie vector ($m.s^{-1}$)
v	Fluid velocity ($m.s^{-1}$)
υ	Cinematic viscosity ($m^2.s^{-1}$)
w	Instrumental width in the Scherrer equation
χ	Magnetic susceptibility
χ_m	Molar magnetic susceptibility ($cm^{-3}.mol^{-1}$)
ψ	Angle between the easy axis and the magnetic moment (rad)
z	Valence of a specie

Note: As this manuscript is long, short abstracts in English and French are presented at the beginning of each chapter, in order to facilitate the reading.

Chapter I: Energetic context, electrochemistry with SMF/AMF

Abstract of the introduction: The first Chapter introduces the topic by recalling the current global ecologic issue, and presents an alternative energy source: the dihydrogen (H_2). The focus is then made on the H_2 production: the main current water electrolysers are presented, as well as thermodynamics and kinetics notions of the water splitting (WS) reaction. Then, a way to reduce the energy consumption of this reaction is presented: the use of alternating magnetic field (AMF) to heat the catalyst at a local scale by hysteresis losses. Principles of hysteresis losses and some applications are then given.

Résumé de l'introduction : L'introduction s'ouvre sur le contexte actuel de crise écologique mondiale et propose l'utilisation du dihydrogène comme source d'énergie renouvelable - une solution parmi d'autres. L'accent est mis sur les méthodes actuelles de production d'hydrogène, et des voies « vertes » sont illustrées : les électrolyseurs en milieu acide et basique. Quelques notions thermodynamiques et cinétiques sur l'électrolyse de l'eau sont également abordées. Puis, une méthode pour réduire l'énergie nécessaire à la réalisation de l'électrolyse de l'eau est proposée : l'utilisation d'un champ magnétique alternatif permettant de chauffer des nanoparticules à une échelle très locale grâce au phénomène de pertes par hystérésis. Ce principe ainsi que quelques-unes de ses applications sont introduites.

I.1 Global warming, soil degradation, water pollution, mass extinction … the need for an energy transition

At all times, humans have been using energy to live and survive. This energy originally came from their own muscles, from cattle muscles or their close environment, allowing them to travel, to heat and to find the necessary to eat. However, only 20% of the metabolic energy is used for muscle work, the rest is converted to heat: biologic energy conversion are inefficient [1]. Thus, humans rapidly used other primary energy sources like the wind, the sun, the water flow, enabling them to work faster and to extend their range. Since the industrial revolution (XIXth century), humans have extensively been using coal and then oil (petrol). They found in these resources a denser energy than any other [2]. Although some early studies indicated that these fuels may have an impact on health and contribute to the air pollution, humans have been continuing to use them and still do [3,4]. At present, petrol and coal are by far the first energy vectors used in the world, as shows Figure I.1. They allowed humans to consumes increasingly more energy. The energy repartition is a bit different in France than in the world, for since the 1950's, the public policy favoured the intense development of nuclear energy, which accounts for *ca.* 80% of France electricity production [5].

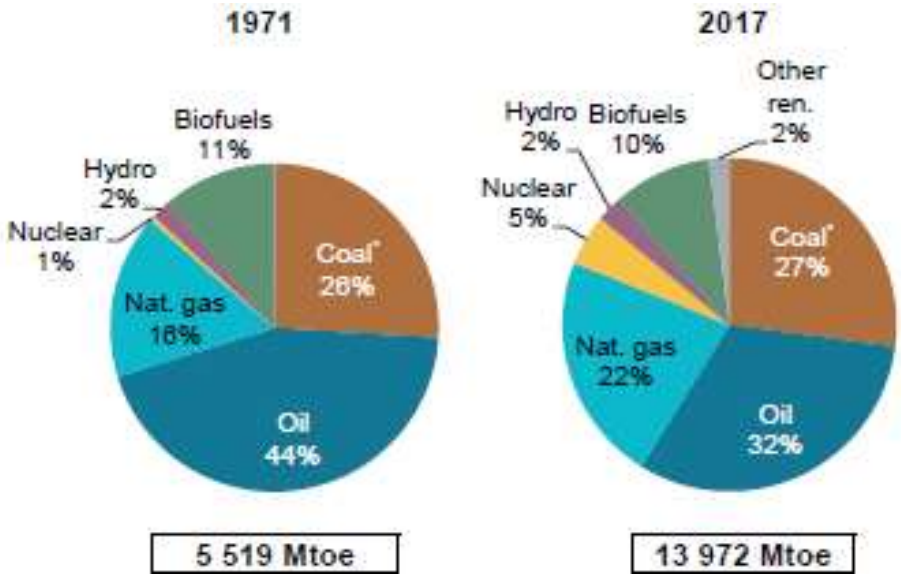

Figure I.1: World total primary energy supply by fuel, expressed in mega ton of oil equivalent Mtoe, 1 toe = 107 kcal. In this graph, oil shale and peat are aggregated with oil. Reprinted with permission from [6].

Nowadays, the energy consumption continues to rise (it more than doubled since 1971 - Figure I.1) to meet the need and demand of the growing human world population (from ~ 3.7 billion in 1970 to 7.8 billion in 2020, up to 10 billion estimated in 2050 [7]). This unlimited consumption, due to our capitalist society and to the large amount of fossil energy available underground, has been done without taking into account some limits of the planet. The dramatic CO_2 accumulation in the atmosphere and the oceans since the industrial revolution demonstrates the human responsibility in climate change, and is the origin of global warming (Figure I.2 and Figure I.3) [8,9]. This triggers severe damages to the environment and living beings, such as global warming, atmospheric pollution, plastic pollution (by-product of petrol exploitation), soil degradation, resources depletion, as well as mass extinction [10].

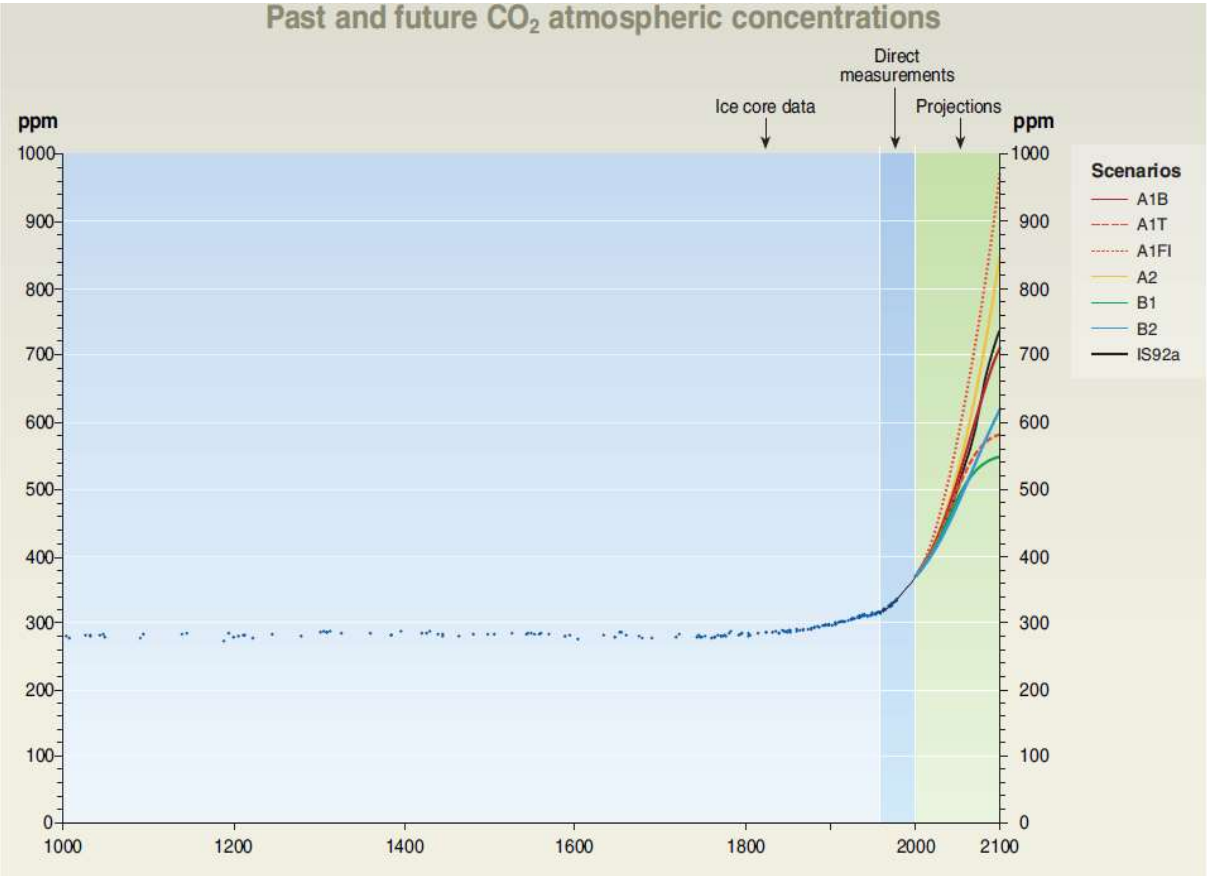

Figure I.2: Atmospheric CO_2 concentration from year 1000 to year 2000 from ice core data and from direct atmospheric measurements over the past few decades. Projections of CO_2 concentrations for the period 2000 to 2100 are based on the six illustrative scenarios from [9]. Scenario A1B corresponds to a balance between the energy sources (fossil or non-fossil); A1T: non-fossil energy source scenario; A1FI: large use of fossil fuels; A2: heterogeneous economic and technologic increase in the world, with a continuous global demographic increase; B1: implementation of global solutions to economic, social, and environmental sustainability, including improved equity, but without additional climate initiatives, and with a demography decline from mid-century; B2: implementation of local solutions to economic, social, and environmental sustainability, with more environmental protection and social equity, and with a smaller global population increase than in A2; IS92a: model with average climate sensitivity.

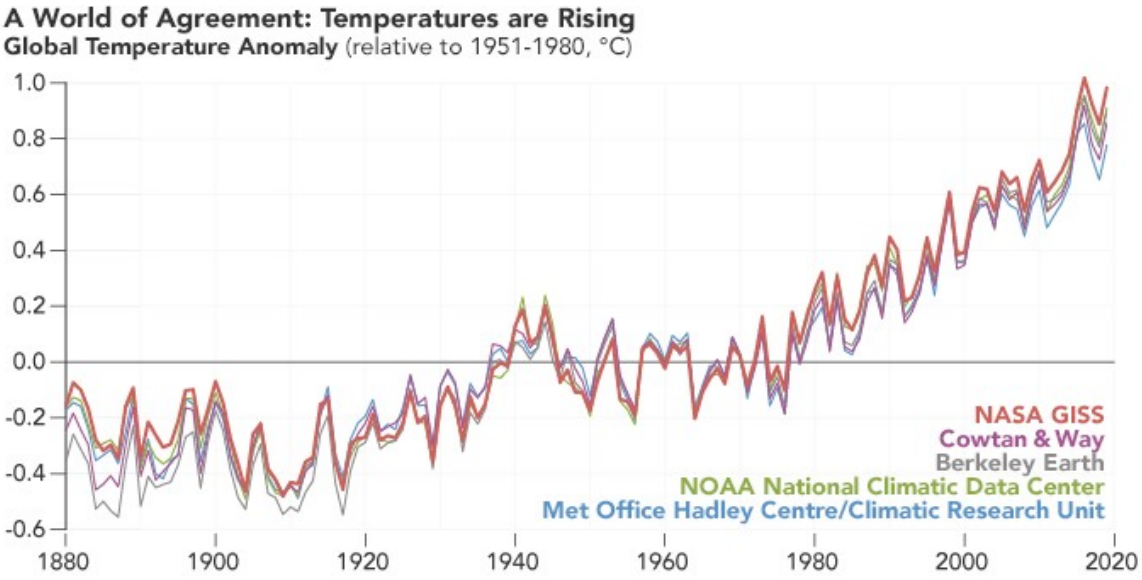

Figure I.3: Yearly temperature anomalies from 1880 to 2019 recorded by NASA, the National Climatic Data Center, the Berkeley Earth research group, the Met Office Hadley Center (United Kingdom), and the Cowtan and Way analysis. Reprinted with permission from [9].

This shows that the current economic system is not viable on the long scale, because it destroys the environment and hugely depends on limited resources [8]. Besides, while huge amount of fossil resources is still available, 80% of these latter should stay in the ground [11] to avoid future disasters, as detailed hereafter.

Since the 1970's, scientists have started to warn governments and companies about the effect of the accumulation of CO_2 on Earth [12], causing its global temperature increase, which could induce a chain reaction: the temperature rise can trigger the melting of the glaciers and ice caps, sparking a global rising sea level, forcing the affected population to migrate. Furthermore, the glaciers' melting can free large amount of methane (from permafrost and from the bottom of oceans), thereby increasingly contributing to global warming via a snowball effect. Nevertheless, no models suggest that water vapour feedback is negative [13]. However, only nonlinear effect could account for the mean state change even in case of the greatest climate variability [14]. In order to evaluate and respond to this dramatic situation, an intergovernmental group called the Intergovernmental Panel on Climate Change (IPCC), has

been established in 1988 by the World Meteorological Organization and the United Nations Environment Programme. It aims to provide relevant scientific information to understand the risks and the possible consequences of climate change on human population and society, in a neutral and objective manner. The IPCC wrote several reports and simulated different scenarios (Figure I.2) indicating the need of an energetic transition from our current high-carbon energy sources to low-carbon energy sources such as hydroelectric power plants, solar panels, wind turbines, geothermal power, biomass and nuclear energy [15]. In 2016, an agreement has been adopted within the United Nations Framework Convention on Climate Change, called the Paris Agreement, which engaged 188 states and the European Union to limit the increase in global average temperature between 1.5 and 2°C by 2100 [16]. This very challenging objective requires to achieve carbon neutrality for anthropogenic emissions by 2050. In this framework, each country has to plan and regularly report the actions undertaken to reach this goal.

Although the low-carbon energy sources cited above are interesting and continue to be deployed [5], some of them require critical elements (Nd, Cu for wind turbine, Si for solar panels, etc [17,18,19]), or create wastes that are dangerous and difficult to handle such as the nuclear energy. Besides, renewable energies heavily depend on meteorological conditions (sunshine, wind…) and need to be coupled with storage systems. When the production from renewable sources exceeds the demand, the spare energy can either be stored in reversible dams (pumped hydro power), or in electrochemical systems (secondary batteries), or in a chemical form (like the power-to-gas process, detailed below), or dissipated through the system or loads (some wind turbines have a system to dissipate the surplus [20]), that latter solution not enabling any recovery. The stored energy can then be released during the discharge of the battery or the turbines downstream the dam. However, the sites available for pumped hydro are already saturated (not speaking from the ecological impact of dams). Moreover, the current batteries are limited by their intrinsically low specific energy, ~ 200 $Wh.kg^{-1}$ in the case of the widely-used lithium-ion

batteries [19,21] in parallel with the fact that each kWh of energy stored scales with a given amount of (usually strategic) metals used in the battery (*e.g.* Li, Ni, Co, etc.). In addition, while it is difficult to know if there is enough of these metals on Earth to only use batteries to store renewable electricity, their mining sparks pollution and greenhouses gases. Another solution is to store the spare energy in the form of energy-dense gaseous compounds, like dihydrogen (H_2) or methane (CH_4); these molecules are easily stored and can be converted back to electricity in fuel cells (FC). This process, called "power-to-gas", is increasingly studied and starts to be used in industry [22]. FC energy and power depend on independently designable parties: the size of the fuel tank and the electrode area, respectively. These technologies can be designed for different power range applications: low power range (< 1 kW) for portable electronics devices (laptop, smartphones, bikes), middle power range (from kW to 100 kW) for transport (cars, buses and trains), and large power range (from kW to MW) for stationary applications (electricity production for cities, industries or as electricity supply system for isolated sites) [23]. In this work, we were interested in H_2, a fuel suited for all range of fuel cells and all types of applications.

I.2 The energy vector H_2, assets and drawbacks

Dihydrogen (H_2, that will be noted hereafter hydrogen), presents numerous advantages. It has the highest energy density (33 $kWh.kg^{-1}$ – 2.5 times that of oil [24]), its combustion generates only water (if well-controlled) and it is a non-toxic gas. However, its use faces three main issues: its production, storage and transport.

Hydrogen as an element is very abundant on Earth, but it is generally not present in the form of molecular hydrogen (H_2); this molecule must then be produced. Nowadays, 99% of the global hydrogen production stems from fossil fuels (mainly steam methane reforming and also

coal gasification) generating a lot of CO_2: a non-ecological route [25]. Besides, the H_2 produced from these techniques contains impurities, such as toxic CO or H_2S gases which do poison the catalyst site, and render mandatory additional purification steps [26]. A cleaner process is water electrolysis, which to date only corresponds to the 1% share left [27]. While this method produces high-purity hydrogen, its deployment is impeded because of its high cost compared to fossil fuel systems (2 to 3 times more expensive, as of today) [28]. Nevertheless, a larger spreading could decrease its price, if the electricity cost decreases as well, or if a sufficient CO_2 tax is adopted.

The storage of hydrogen is complex because of its low boiling point (−253°C) and density (0.08988 $kg.m^{-3}$) [24], requiring high pressure and extensive cooling to achieve its storage in gaseous or liquid form, respectively. A solid storage is possible through adsorption on metal-organic framework, carbon supports, or absorption in metal hydrides (*e.g.* Mg-based alloys) or even via complex chemical hydrides (*e.g.* $NaBH_4$) [29,30], although no satisfactory method exist to-date.

In order to deploy hydrogen as a widespread fuel, it is compulsory to develop its distribution network. Hydrogen can be transported through pipelines or trucks as gas or liquid, to refilling stations for car users for instance, or directly to industrial sites. While the current deployment is limited, several plans are launched to favor its use. In November 2018, the "Zero Emission Valley" project has been launched in the Auvergne-Rhône-Alpes region in France, aiming to set up simultaneously 1000 hydrogen vehicles, 20 refilling stations and 15 electrolysers within 10 years [31]. In the Pas-De-Calais region in France, the first 100% hydrogen French bus line was created in 2019 [32]. It must be noted that, hydrogen being a highly-flammable and explosive gas in contact with air (from 4% air), care is required when spreading systems producing, storing, transporting and consuming hydrogen.

Despite all these hurdles, hydrogen seems to be part of the solution to reduce CO_2 emissions. Governments are increasingly funding research on hydrogen devices, so that their cost is reduced and their performance improved. In the following, we will explain the thermodynamics and kinetics of water electrolysis, and then develop the drawbacks and advantages of the main types of electrolysers.

I.2.1 Water electrolysis: principle, thermodynamics and kinetics

A classical industrial water electrolysis cell consists of two electrodes, an anode and a cathode, immersed in an electrolyte. The electrodes are separated by a membrane or a diaphragm and connected outside the electrolyte to a DC power supply. By applying a voltage between the electrodes, one forces the oxidation of water at the anode, half-reaction called Oxygen Evolution Reaction (OER), producing O_2. The released electrons flow into the electric circuit toward the cathode, where water is reduced to H_2, half-reaction called Hydrogen Evolution Reaction (HER). The released hydroxide ions migrate toward the anode in an alkaline medium (in an acidic medium, proton migrate from anode toward cathode), thus maintaining the electrical neutrality. The diaphragm separates the gas from mixing and recombining [33,34]. The cell and the half-reactions occurring at the electrodes in a basic and acidic medium are summarized in Figure I.4.

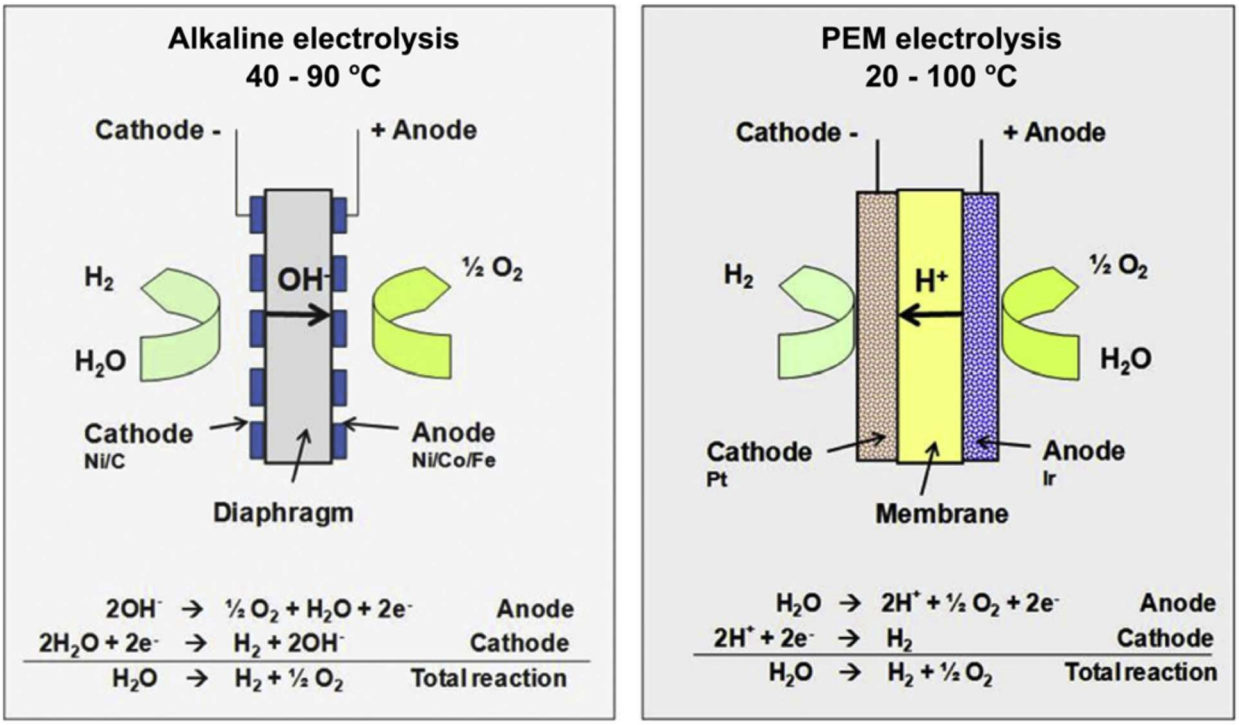

Figure I.4: Schemes of the operating principle of an alkaline and PEM water electrolysis cell. Reprinted from [35] with permission from Elsevier.

In order to enhance the migration of the ions in the solution, electrolytes with high ionic conductivity are used. In industrial alkaline water electrolysis, potassium hydroxide (KOH) is generally employed at a weight fraction between 20-30 wt.%. In acidic medium, where the mostly-used technology is the Proton Exchange Membrane Water Electrolysers (PEMWE), a membrane plays the role of the electrolyte and the separator/diaphragm (*e.g.* Nafion or Fumapen [36]).

Splitting water into hydrogen and oxygen requires a certain amount of energy, which presents three contributions. The electrochemical system can be compared to an electrical circuit, as depicted in Figure I.5.

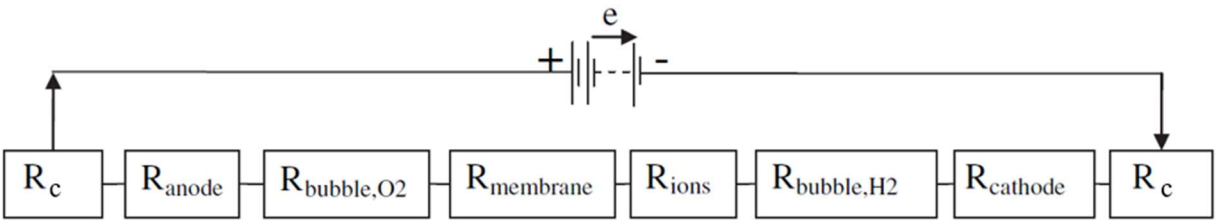

Figure I.5: Electrical circuit analogy corresponding to an alkaline water electrolysis system. Reprinted from [34] with permission from Elsevier.

The main contribution is the thermodynamic energy necessary to split water into H_2 and O_2; the next contribution corresponds to the Ohmic losses due to current flow through different media, and the latest being the bubble coverage issue.

First, thermodynamically, the water molecule is very stable under standard condition of temperature T and pressure P (STP: 25°C and 1 bar). Accordingly, breaking the bonds in the water molecule and creating bonds to produce H_2 and O_2 requires a consequent energy called the Gibbs Free Energy of reaction $\Delta_r G$, in J.mol^{-1}. This amount is the minimum energy to provide for the reaction to happen in a reversible manner. For water splitting (WS), this corresponds to +237.2 kJ.mol^{-1} at 25°C. Its positive sign indicates that the decomposition of water into H_2 and O_2 is unfavourable in STP (thermodynamic convention). Besides, generating two gases from one water molecule creates disorder, chaos, irreversibility, leading to an increase in entropy S (a measure of disorder, $\Delta S > 0$). The Gibbs free energy does not take into account the energy consumption of this phase transition. In contrast, the enthalpy of reaction $\Delta_r H$ in J.mol^{-1} includes the reversible character of the reaction and the irreversible contributions in the form of latent heat, as shown in Equation (Eq.) I.1:

$$\Delta_r H = \Delta_r G + T\Delta S \qquad \text{I.1}$$

At STP: $\Delta_r H$ (25°C, 1 bar) = 285.6 kJ.mol^{-1}.

These energies can be expressed in terms of a voltage to be applied between the two electrodes, Eq. I.2 and I.3:

$$\Delta_r G = n\,\mathcal{F}\,U_{rev} = n\,\mathcal{F}\,(E^\circ_a - E^\circ_c) \qquad \text{I.2}$$

$$\Delta_r H = n\,\mathcal{F}\,U_{tn} = n\,\mathcal{F}\,(E_a - E_c) \qquad \text{I.3}$$

n being the number of exchanged electrons during the reaction (here, 2 *cf* .Figure I.4), $\mathcal{F}$ the Faraday constant which corresponds to the charge of one mole of electrons: $\mathcal{F}$ = 96485 C.mol^{-1}, U_{rev} the equilibrium cell voltage and U_{tn} the thermoneutral voltage in volt, both voltages depending on temperature and pressure. E_a and E_c are the Nernst potentials at the anode and the cathode, respectively, E°_a, E°_c being their value at equilibrium in volt, called standard potentials. In volt, the previous voltage values are: U_{rev} = 1.23 V and U_{tn} = 1.48 V. E_j and E°_j, j standing for an electrode; they depend on the *pH* and are linked by the Nernst equation, hereafter expressed in alkaline medium, at the anode in Eq I.4 and the cathode in Eq I.5:

At the anode
$$E_a = E^\circ_a + \frac{RT}{2\mathcal{F}} \ln\left(\frac{(a_{O_2})^{1/2}(a_{H_2O})}{(a_{HO^-})^2}\right) = E^\circ_a + \frac{RT}{2\mathcal{F}} \ln\left(\frac{{P_{O_2}}^{1/2}}{P^{\circ 1/2}[HO^-]^2}\right) \qquad \text{I.4}$$

At the cathode
$$E_c = E^\circ_c + \frac{RT}{2\mathcal{F}} \ln\left(\frac{(a_{H_2O})^2}{(a_{H_2})(a_{HO^-})^2}\right) = E^\circ_c + \frac{RT}{2\mathcal{F}} \ln\left(\frac{P^\circ}{P_{H_2}[HO^-]^2}\right) \qquad \text{I.5}$$

R is the ideal gas constant, R = 8.3145 J.mol^{-1}.K^{-1}, a_i the activity of specie s, P_i the partial pressure of specie i in bar, P° the standard pressure $P^\circ \approx 1$ bar and [s] the concentration of specie s in mol.L^{-1}.

By considering $\frac{RT}{\mathcal{F}} \ln(x) \approx 0.0591 \log(x)$ at 298 K, Eq. I.4 and I.5 simplify into I.6 and I.7:

At the anode $$E_a = E°_a - 0.0591\ pH = 1.23 - 0.0591\ pH + 0.0148 \log\left(\frac{P_{O_2}}{P°}\right) \quad \text{I.6}$$

At the cathode $$E_c = E°_c - 0.0591\ pH = 0.0 - 0.0591\ pH + 0.0296 \log\left(\frac{P°}{P_{H_2}}\right) \quad \text{I.7}$$

where $E°_a$ = 1.23 V_{RHE} and $E°_c$ = 0.0 V_{RHE}, where RHE stands for Reversible Hydrogen Electrode, an arbitrary but mostly-used reference, the potential of which is independent on *pH*. Thereafter, the potential differences written are always referenced to the RHE and noted "V_{RHE}".

However, further energy is required to enhance the kinetics of the water splitting reaction, which is infinitely slow at STP. From a charge-transfer kinetics viewpoint, an energy barrier has to be overcome with an amount of energy, namely the "activation energy" E_A. For each half reaction at stake (*e.g.* the HER or the OER), E_A is controlled by the electron transfer at the electrodes, and depends on the chemical nature of the catalysts at the electrode surface and its morphology (facets, particles/crystallite size, extent of agglomeration, presence of defects, etc.). In terms of voltage, the activation energy results in overpotential, and is noted η_a and η_c for the anode and the cathode reaction, respectively. These thermodynamic contributions are gathered in the R_{anode} (= (E_a + η_a)/i) and $R_{cathode}$ (= (E_c + η_c) /i) terms in Figure I.5, i being the current.

Secondly, when the two half reactions taking place at the anode and cathode proceed, a flow of electrons is generated into the outer electrical circuit linking the electrodes (from the anode to the cathode), the resulting current corresponding to an ionic flow inside the electrolyte through the diaphragm between the two electrodes (cations migrate to the cathode, anions to the anode). All these flows of charged species require an energy to overcome the different resistances of this system. Two groups of resistances can be distinguished. The first group concerns the electrical resistances, which are the contact resistances between electrodes, current

collectors and wires, and the internal resistivity of these components, that essentially depends on the metal used and their morphology (R_c on Figure I.5). The second group gathers the resistances related to the transport of species inside the electrolyte: the conductivity of the electrolyte (R_{ions}, both in the bulk and in the pores of the electrodes that are filled with electrolyte) and the resistance of the possible membrane to the ionic transfer ($R_{membrane}$). These two contributions are generally called together the Ohmic losses and gathered in an overall term R.

Thirdly, resistances due to bubble formation ($R_{bubble,\ O2}$ and $R_{bubble,\ H2}$) exist. Indeed, during the water splitting reaction, gas bubbles nucleate (*evolve*) at the surface of each electrode, then grow and detach, and flow in the liquid electrolyte until they reach the gas phase. While they are adsorbed at the electrode surface, they prevent any new reactant to reach/adsorb onto the electrode surface, hence blocking subsequent reaction. Accordingly, not all the active sites are available for reactant species, which decreases the efficiency of the reaction. This resistance is generally gathered with R in the literature while it is linked to the mass-transport, and not to real Ohmic loss. We will distinguish these losses and attribute them the term $R_{bubbles}$.

To conclude, the energy necessary for the water splitting reaction is, in volt, U_{cell}, given in Eq. I.8:

$$U_{cell} = E_a - E_c + \eta_a - \eta_c + iR + iR_{bubbles} \qquad \text{I.8}$$

The efficiency of this process can be calculated in the following ways: whether one calculates the ratio of the reversible voltage to the cell voltage (Eq. I.9) or the ratio of the thermoneutral voltage to the cell voltage (Eq. I.10):

$$\eta_{\text{Faradaic}}\,(25°\text{C}) = \frac{U_{\text{rev}}}{U_{\text{cell}}} = \frac{1.23\ \text{V}}{U_{\text{cell}}} \qquad \text{I.9}$$

$$\eta_{\text{Thermal}}\,(25°\text{C}) = \frac{U_{\text{th}}}{U_{\text{cell}}} = \frac{1.48\ \text{V}}{U_{\text{cell}}} \qquad \text{I.10}$$

With the last definition, it is possible to obtain an efficiency greater than 1. This would indicate that the system absorbs the heat from the environment, the reaction being thus endothermic. Otherwise, the reaction is exothermic.

The major causes of efficiency reduction are surface coverage by bubbles, activation energies and the recombination of H_2 and O_2 due to gas crossover. In order to increase the overall efficiency of the reaction, one tries to diminish the different resistance contributions cited above by changing the nature of the wires, the diaphragm and the electrodes, as well as their morphology, and to find more active catalysts toward the HER and the OER. At iso-components, it is also possible to increase the temperature to enhance the overall efficiency: water electrolysis being a thermally-activated process, which means that the reactions at stake are accelerated at higher temperatures. More precisely, the kinetics of the reaction is enhanced while the thermodynamics ($\Delta_r H$) of the reaction is unfavoured [37,38], as testifies the slight thermoneutral voltage increase in Figure I.6. However, the overall effect of a temperature increase is beneficial to the overall system, because the positive kinetics effect overwhelms the negative thermodynamic effects, as showed Miles *et al.*, Figure I.7 [39].

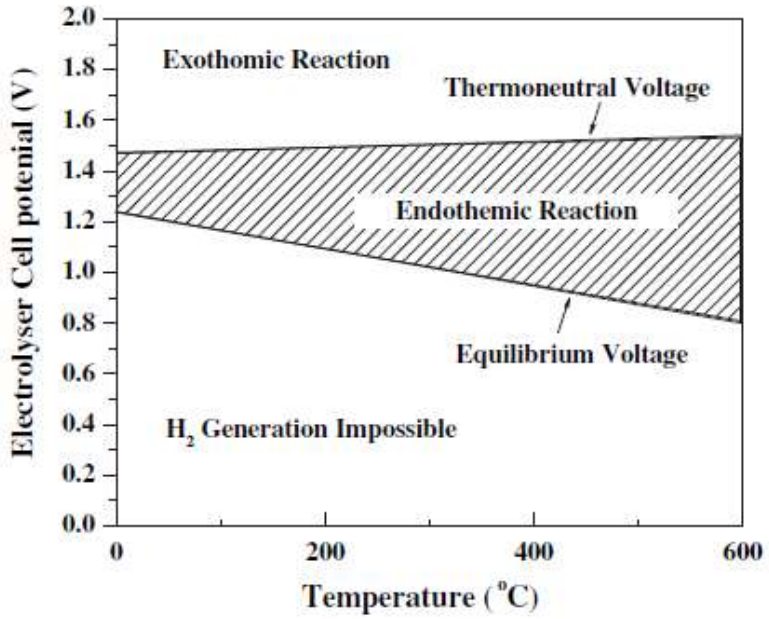

Figure I.6: Theoretical cell voltage of a water electrolysis system as a function of the temperature. Reprinted from [34] with permission from Elsevier.

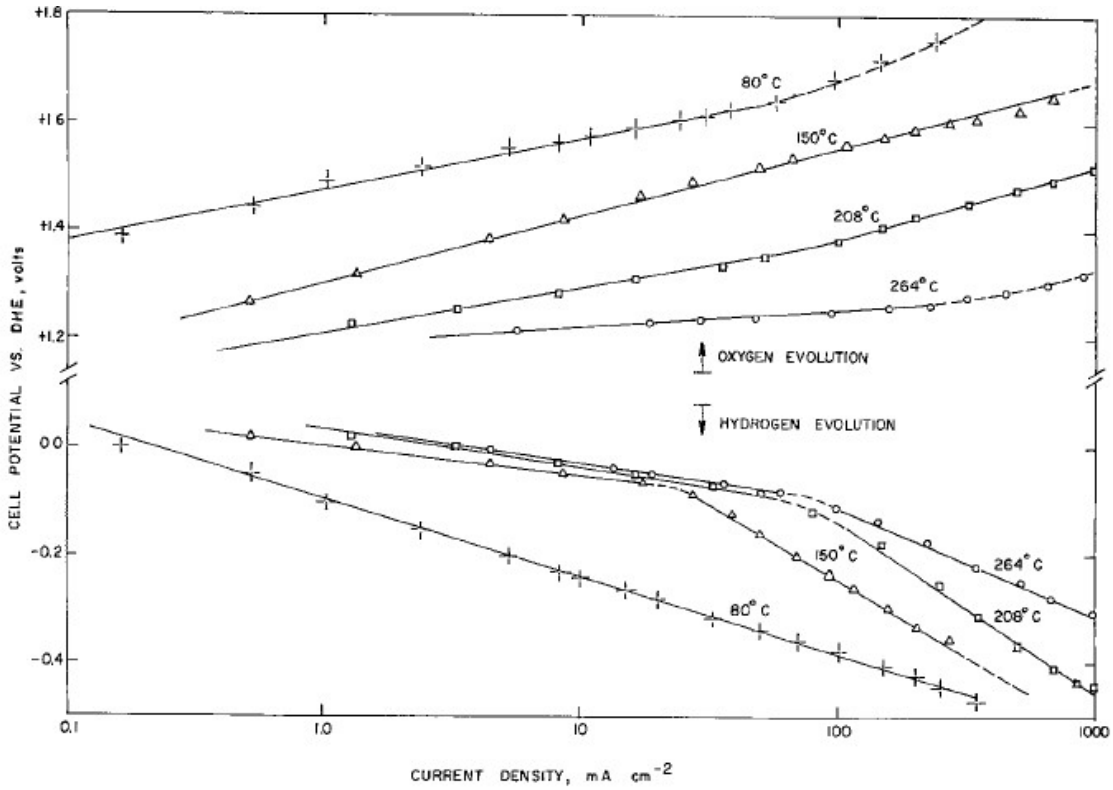

Figure I.7: Cell potential versus (*vs.*) current density for OER and HER on polished Ni electrodes with a geometrical area of 0.2 cm^2 in 50 wt.% KOH solutions at different temperatures.

I.2.2 The different types of electrolysers

Alkaline Water Electrolysers (AWE), Proton Exchange Membrane Water Electrolysers (PEMWE) and Solid Oxide Electrolysers (SOE) are the three main classes of electrolysers.

Figure I.4 gave an overview of the operation of AWE and PEMWE.

PEM electrolysers have received increasing attention since the 1970s. A PEMWE works in an acidic polymer electrolyte medium, which implies to use catalysts stable in the harsh corrosive environment combined with high voltage, especially at high current and for the OER anode (in corrosive potentials). Figure I.8 shows that very few elements are stable in such an environment. In industry, Pt and Ir (in the form of oxides) are generally used. These elements are scarce in the earth crust (0.4 ppb) and their concentration in ores contain amounts similar to 10 ppb. Thus, they are very expensive (~ 50 k$/kg for Pt and ~ 32 k$/kg for Ir, in 2010 [19]), poorly available and produced only by a limited number of countries (South Africa and Russia, mainly). To this must be added the price of the membrane, but also the (usually titanium-based) current collectors and separator plates, which account to 48% of the stack cost [36]. Nevertheless, the use of a solid polymer electrolyte as the membrane in these technologies allows to have a compact system, to reach small cell internal resistance and low gas crossover. The compact and solid-state system prevents the risks of leaks of corrosive liquid, and requires low maintenance. As little hydrogen and oxygen gas cross the membrane and recombine, the current density reachable is high and the hydrogen produced is of high purity. Besides, it enables to operate at high pressures, which presents a triple asset. First, it decreases the volume of the gaseous phase at the surface of the electrode and thus enables to decrease the Ohmic losses and to reach high current density (> 2 $A.cm^{-2}$). Second, it is easier to compress, store and transport the hydrogen produced. Finally, high pressure is suitable for scaling up the system, even if reaching the MW

power range is difficult nowadays. Whatever their advantages, because PEMWE are presently based on Pt group metals (PGM), further research is needed to find other high-performance catalysts not based on PGM, or to diminish the areal loading of PGM at the PEMWE electrodes. Also, developing low cost and corrosion-resistant current collectors and separator plates is necessary, not to speak from the need to increase the durability of PEMWE materials and cells (current industrial lifetime: 10-20 years) [36,40].

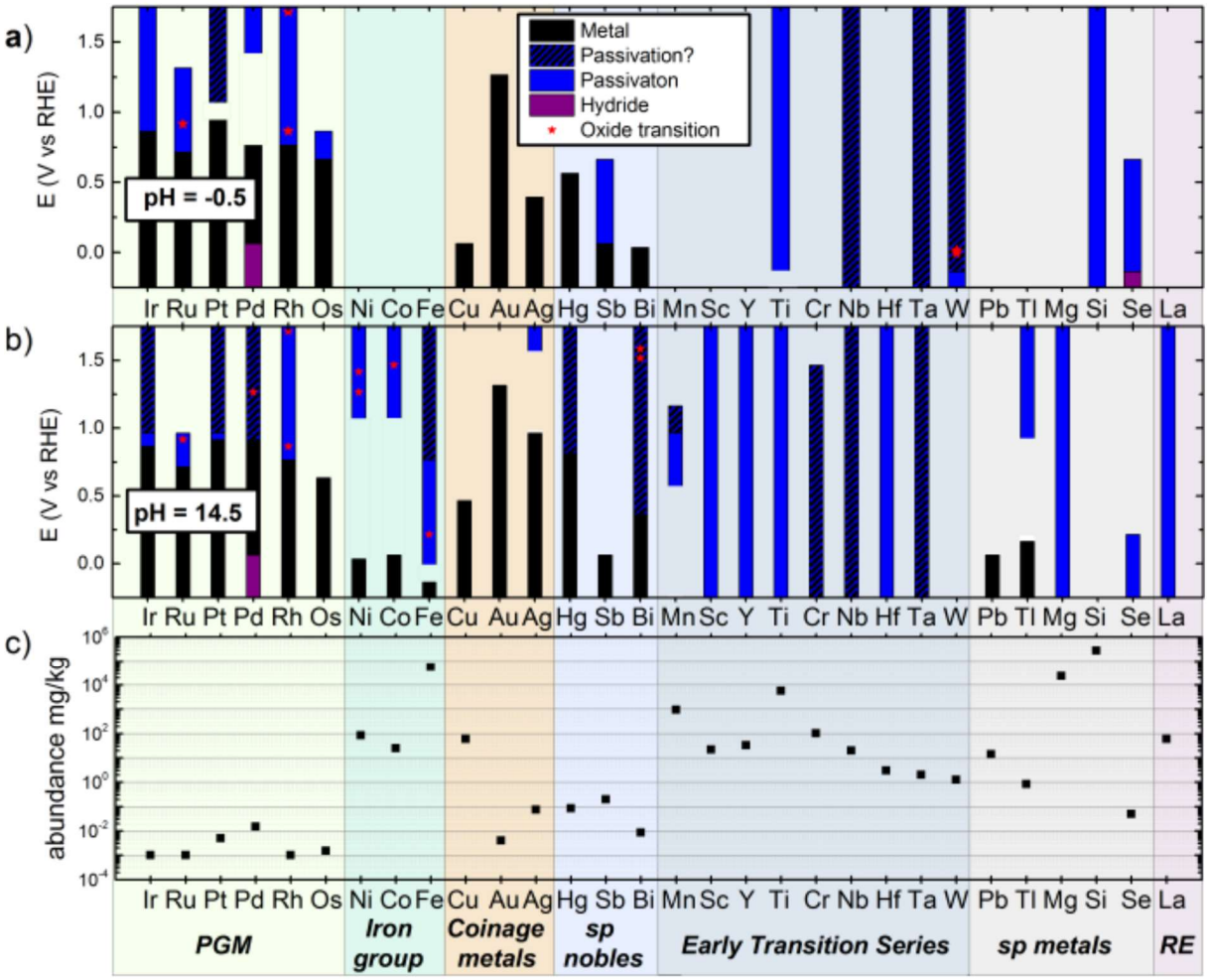

Figure I.8: Chart for metals that shows thermodynamically-stable solid phases at (a) *pH* −0,5 or (b) *pH* 14.5, with reference to a temperature of 25°C and a dissolved metal ion concentration of 10^{-6} mol.L^{-1} or lower (based on the data reported by Pourbaix et al. [41]). The potentials are referred to the reversible hydrogen electrode (RHE). The black area indicates stable metallic phase, blue area: stable oxide, shaded blue area: it is not clarified if the oxide is stable, and purple area indicates stable hydride. Reprinted from [42] with permission from The Electrochemical Society. (c) Mean abundance of the metals in the earth crust (in mg of metal per kg of earth's crust - ppm). Data extracted from [43].

On the contrary, AWE, which has been discovered at the end of the XVIIIth century and is operated since several decades at the industrial scale, is a very mature technology able to reach the MW range at a commercial level. The electrolyte used is generally 20-30 wt.% KOH in water, an affordable chemical product in which more non-PGM elements are stable, such as Ni, an abundant element on earth (Figure I.8). The stability of Ni and its oxohydroxides allows a long lifetime (20-30 years) [36]. However, the Ohmic losses are high due to the high internal resistance of the AWE cells compared to PEMWE (despite a higher conductivity, alkaline electrolytes are impregnated in thick porous diaphragms, leading to larger R_{ions} than for much thinner PEM that exhibit smaller conductivities). Thus, at similar efficiency for PEMWE and AWE, the first system reaches a current density of 1-2 A.cm^{-2}, while the second reaches 0.2-0.4 A.cm^{-2}. In addition, the porous diaphragm cannot separate completely O_2 and H_2, which prevents high pressure operation, causes safety issue and decreases cell efficiency (~ 60% in industrial AWE at same current density as PEMWE, being ~ 80% for this latter [44,45]). Furthermore, the installation costs and the maintenance are high, and this technology is not compatible with an intermittent operation when it operates at 80°C, contrary to PEMWE. Indeed, reaching a stable stationary state for a AWE requires 4-6 hours to increase progressively the current and the temperature of the liquid electrolyte (a necessity to reach stable "bubble regime"), while only few seconds are required for PEMWE to reach the nominal conditions at the same temperature (the solid electrolyte and thin-film electrodes reach their stable conditions within seconds) [36,40,46,47].

SOE work at very high temperatures (600-900°C) and can operate at high pressures owing to the use of a dense ceramic-based solid electrolyte. SOE can reach very high efficiency (~ 95% at a current density of 0.5-1 A.cm^{-2} [48]). However, this technique is still at a laboratory stage and faces high installation costs and very fast degradation due to the harsh conditions and material delamination during temperature cycles experienced at start/stop [36,40,47]. Besides, SOE

should be coupled with an external heat source to be energetically-appealing, like a nuclear power plant [49]. The spreading of SOE can thereby not be generalized and their interest is limited to large installations operating in near-stationary conditions.

To conclude, while AWE is the most mature process, its low current density reachable, congestion and incompatibility with intermittent operation calls for the development of more efficient water splitting devices. PEMWE have assets, and several projects of PEMWE have been launched, *e.g.* the European project HYBalance in Denmark which scales in the MW range. However, PEMWE rely on PGM, which make their wide deployment questionable. One idea, if one wants to keep the real interest of AWE (*i.e.* using non-PGM catalysts), would be to intensify the process and increase its efficiency and compatibility with intermittent operation. To this goal, magnetic field-enhanced AWE operation has some assets, and this is the objective of the present thesis.

I.3 The magnetic heating and its application to water splitting

The concept of magnetically-induced heating comes from the absorption of an electromagnetic energy by a material. If this absorption is irreversible, then the energy is dissipated in form of heat, whatever the mechanism of dissipation. The energy exchanges between an electromagnetic wave and a material had been described by the Maxwell's equations, which can be combined to describe the electromagnetic energetic balance inside the material (Eq. I.11)[1]:

[1] In this manuscript, vectors are written in **bold** fonts (*e.g.* vector ***H)***, and their modulus in normal fonts ($||\boldsymbol{H}||$) = H.

$$-div\,(\boldsymbol{E}\times\boldsymbol{H}) = \frac{\boldsymbol{j}2}{\sigma} + \boldsymbol{E}\,\frac{\partial \boldsymbol{D}}{\partial t} + \boldsymbol{H}\,\frac{\partial \boldsymbol{B}}{\partial t} \qquad \text{I.11}$$

With $\boldsymbol{E}$ the electric field ($V.m^{-1}$), $\boldsymbol{H}$ the magnetic field strength ($A.m^{-1}$), $\boldsymbol{j}$ the current density ($A.m^{-2}$), σ the electrical conductivity ($S.m^{-1}$), $\boldsymbol{D}$ the electric displacement field ($C.m^{-2}$) and $\boldsymbol{B}$ the magnetic flux density (T), which will be called the magnetic field hereafter. On the left side of the equation stands the divergence of the Poynting vector corresponding to the electromagnetic energy; it is a source term. On the right side stand three terms, corresponding to three different energy absorption mechanisms. The first one is the energy transformed as induced currents in the matter, called the eddy currents. This is an irreversible phenomenon leading to heat generation, and is the one called induction and used *e.g.* for cooking applications. The second and the third term correspond to the electric and magnetic losses occurring in matter, respectively. For both interactions, if the work is done in an irreversible manner, then heat is generated [50]. This work focuses on the magnetic heating thanks to an alternating magnetic field (AMF); in that frame, the second term does not intervene.

The magnetic-heating discovery goes back to the XIXth century, when scientists observed that under an AMF, a material releases heat [51]. It has been firstly employed for metallurgic treatments, and then for other domains such as cooking [52], medicine [53] and catalysis [54]. Heating by this technique presents several advantages. First, it heats very fast, and allow to surpass the heat-transfer limit when using a classical reactor [55]. Second, it heats without contact, with an external source: an inductor/a coil (these words are interchangeable, an inductor being a coil designed to heat a system). Third, it heats selectively: only the ferromagnetic or the electrically-conductive materials heat under AMF (depending on the underlying heating mechanism), as will be explained below. Different groups took advantage of this asset to conduct several catalysis reactions in the same reactor, the products of a reaction being the

reactive of the next one for instance, while avoiding side reactions. It has been realized at the millimeter scale [56], the micrometer scale [57] and at the nanometer scale for catalysis reactions or for cancer treatment, especially at the Laboratoire de Physique et Chimie des Nano-Objets (LPCNO) [58,59]. Finally, it has been employed for electrocatalysis, and the results have been published in 2018 [60]. Before explaining deeper this last point, the mechanism by which a nanoparticle (NP) heats is presented. In a first part, basics concepts on magnetism inside matter and NPs, and magnetic heating will be presented, followed by results on the application of magnetic heating to electrocatalytic processes.

I.3.1 Magnetic heating by alternating magnetic field

I.3.1.1 How magnetism can influence the material structure?

In the case of magnetic materials, such as the 3d transition metals (Fe, Co, Ni), the magnetic properties of a macroscopic sample of such material can organize and influence the structure of the matter, even without the application of a magnetic field. The energies governing the different stable magnetic states can be gathered into three contributions (Eq. I.12):

$$E_{\text{total}} = E_{\text{exch}} + E_{\text{ani}} + E_{\text{dip}} \qquad \text{I.12}$$

E_{exch} is the exchange energy (J) and contributes to the magnetic moment alignment in ferromagnetic materials; it has a short range. E_{ani} is the anisotropy energy (J), which tends to align the magnetic moments toward certain crystallographic direction, called “easy axis”. It depends on the volume, the structure and the composition of the material. E_{dip} is the dipolar interaction energy (J), which has a long range and forces the magnetic flux lines to close, to avoid the creation of magnetic poles (div (B) = 0) [61,62].

The competition between these different energies leads to the creation of different magnetic domains inside the material, in which the magnetic moments are aligned, but with a possible different orientation of the adjacent magnetic domains. The frontier between two magnetic domains is called a Bloch wall. A picture of ferromagnetic domains in a single crystal platelet of Ni is given in Figure I.9 Several magnetic domains with different magnetic moment directions result from a trade-off between the three energies listed above [63].

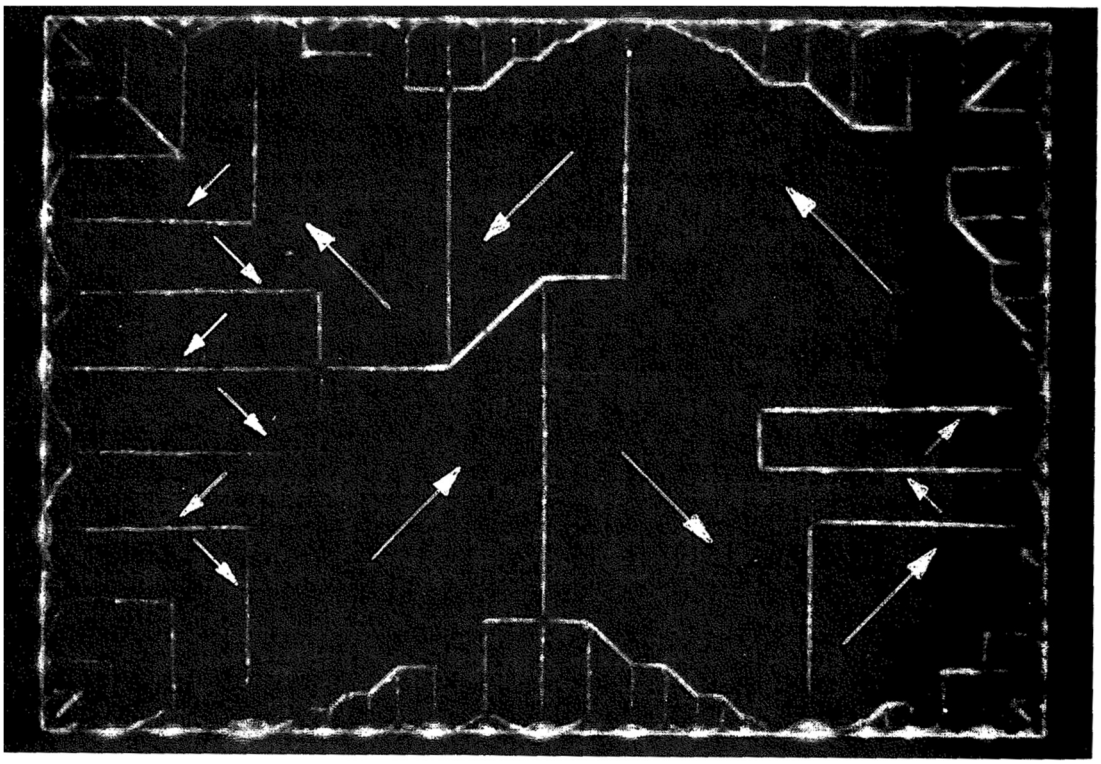

Figure I.9: Ferromagnetic domain pattern on a single crystal platelet of nickel. The domain boundaries are made visible thanks to the Bitter magnetic powder pattern technique. The direction of magnetic moments within a domain is determined by observing growth or contraction of the domain in a magnetic field. Reprinted from [64] with permission from Wiley.

When the size of the particles decreases down to a "critical diameter" d_c, the exchange energy overcomes the dipolar energy, and the particle changes its magnetic configuration from multidomain to single-domain, a stabler configuration. The critical diameter for Fe, Ni and Co are given in Supplementary Figure 1, and it is typically below 100 nm [65,66].

I.3.1.2 Single-domain nanoparticle magnetism

Without magnetic field and for a particle with a diameter inferior to the critical diameter, the magnetic moments (*i.e.* the spins of the particle) align toward the easy axis. Moreover, if the diameter is sufficiently small, the sum of all the spins can be considered as the global magnetic moment of the particle [67]. Magnetic moments of different ions are given in Supplementary Figure 1 as order of magnitude. Two possible directions exist, corresponding to two energy minima: parallel or antiparallel to the easy axis (Figure I.10).

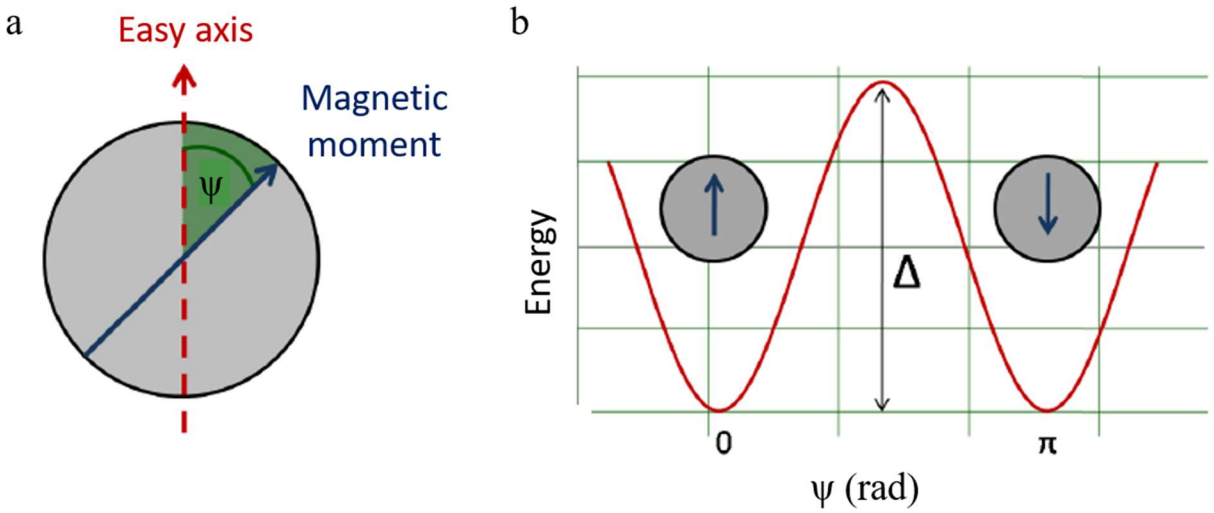

Figure I.10: (a) Schematic representation of the magnetic moment (or spin) of a single-domain nanoparticle (b) energy diagram of the two possible energy states in function of ψ. Reprinted from [66] with permission from INSA Toulouse University.

These states are generally and arbitrarily called “up” and “down” respectively. Due to the thermal agitation, the magnetic moment can present a small angle ψ between its direction and the easy axis, and can flip from one minimum to the other. This requires an energy Δ corresponding to the anisotropy energy (Eq. I.13):

$$\Delta = E_{\text{ani}} = K\,V\,\sin^2\psi \qquad \text{I.13}$$

V is the NP volume (m^3), and K the anisotropy constant ($J.m^{-3}$), which depends on the shape, the structure and the nature of the material. The transition time from one state to the other was described by Néel, and is called the Néel relaxation time τ_N, Eq. I.14:

$$\tau_N = \tau_0\ e^{\frac{\Delta}{k_B T}} \qquad \text{I.14}$$

With τ_0 a complex factor depending on the anisotropy, generally approximated to ~ 10^{-9} s. k_B is the Boltzmann constant ($m^2.kg.s^{-2}.K^{-1}$) and T the temperature (K).

Thus, if an experimenter measures the spin of such a particle during a time τ_{meas}, if $\tau_{meas} < \tau_N$ the magnetic moment will be non-null, and the particle is called ferromagnetic, but if $\tau_{meas} \gg \tau_N$ then the average spin will be zero, and the particle is called superparamagnetic (SPM).

The transition between these two states is also influenced by the temperature. Obviously, if the thermal agitation is higher, the spin fluctuates more rapidly. For a given τ_{meas}, a "blocking temperature" T_B is defined, below which the particle is ferromagnetic, and is SPM otherwise, Eq. I.15:

$$T_B = \frac{\Delta}{\ln\left(\frac{\tau_{meas}}{\tau_N}\right) k_B} \qquad \text{I.15}$$

These phenomena could be reversible as a particle can emit/absorb a phonon to flip its spin.

I.3.1.3 Magnetic heating

At present, let's consider an assembly of single-domain particles under a magnetic field (MF) $B_a = B_{applied}$. If one looks at a sufficiently large scale, the magnetic moments of the particles result in a magnetization M (magnetic moment per volume). The MF adds a new energy in the balance, called the Zeeman energy E_Z, which forces the magnetization to align with B_a, Eq. I.16 and I.17:

$$E_{\text{total}} = E_{\text{ani}} + E_{\text{Z}} \quad \text{I.16}$$

$$E_{\text{total}} = KVsin^2\psi - M_S V B_a \cos\varphi \quad \text{I.17}$$

with M_S the saturation magnetization ($A.m^2.kg^{-1}$) and φ the angle (°) between B_a and the magnetization of the particles. The theoretical model of this type of system has been described in [68].

In this case, two mechanisms exist for the magnetic moment alignment: whether only the spins rotate, which is the Néel relaxation, or the NPs rotate physically, which corresponds to the Brown relaxation. Both mechanisms happen, depending on the timescale at which each mechanism occurs. For the Brown relaxation, the time τ_B between two flips is, Eq. I.18:

$$\tau_B = \frac{3\,\eta\,V_H}{k_B T} \quad \text{I.18}$$

With V_H the hydrodynamic volume of a NP (m^3) and η the dynamic viscosity of the medium (Pa.s). Generally, V_H is superior to V due to adsorbed species or fluid interactions. V_H can be determined by hydrodynamic measurements such as dynamic light scattering [69].

By changing the amplitude of B_a and measuring the magnetization of a material, one gets a hysteresis loop from which magnetic properties of the sample can be extracted. Figure I.11 presents a typical hysteresis loop (red curve).

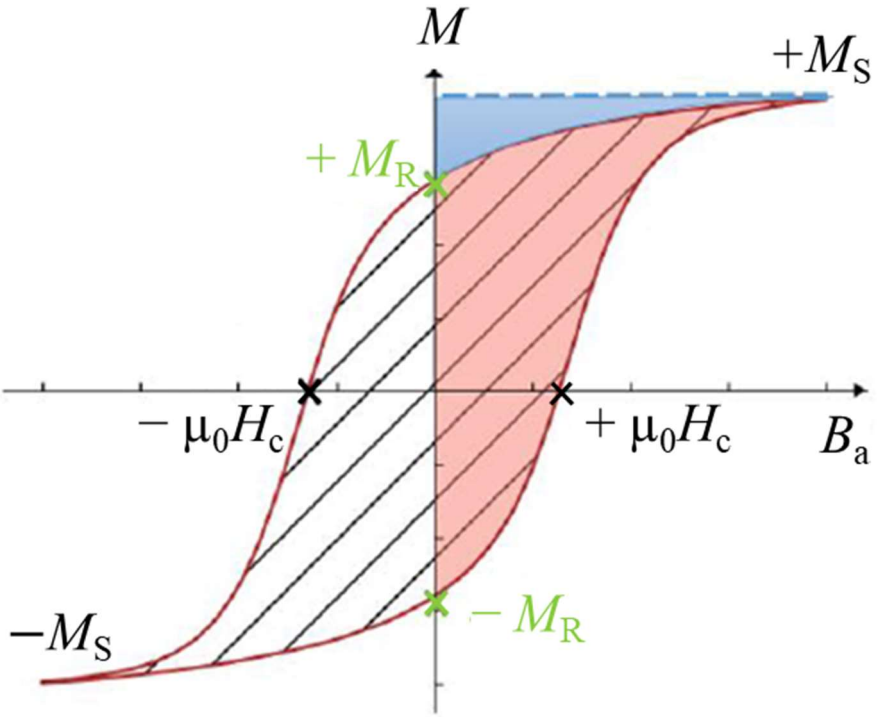

Figure I.11: Hysteresis loop of an assembly of nanoparticles. Modified from [61] with permission from INSA Toulouse University.

From this curve, three parameters can be determined: the saturation magnetization M_S corresponding to the maximum field that a polarized sample (*i.e.* under B_a) can create when all its magnetic moments are aligned, the remanent field M_R which is the residual magnetization of the system when B_a goes back to 0 T, and the coercive field $H_C = B_C/\mu_0$ corresponding to the field required to depolarize the magnetic sample ($\mu_0 = 4\pi\ 10^{-7}$ kg.m.A^{-2}.s^{-2} is the magnetic permeability of vaccum). Let's follow the curve from a state where no field is applied: let's take $(0, -M_R)$. An energy corresponding to the red and blue area on Figure I.11 is necessary to align all the magnetic moments with the B_a direction. When switching off the field, the magnetization of the system goes back to the state $(0, +M_R)$, which frees the energy corresponding to the blue area. Thus, the energy dissipated in form of heat corresponds to the red area. Similarly, the same

amount of energy is dissipated when the field scans the negative part of the hysteresis loop. Overall, the total amount of heat released during the full hysteresis loops corresponds to the loop area. It has to be noted here that, by travelling through the hysteresis cycle, the spins flip in an irreversible manner, as many of them flip, and not just one (as the magnetism of single-domain NP). As a consequence, heat is produced.

The amount of heat generated by an assembly of magnetic NPs is often call the Specific Absorption Rate (SAR), expressed in $W.g^{-1}$ (normalized to the mass of metals). Since each time the particles undergo the hysteresis loop, an energy corresponding to the area of the hysteresis loop A ($m^2.s^{-2}$) is released, the SAR reads, Eq. I.19:

$$SAR = A\,f \qquad \text{I.19}$$

where f is the magnetic field frequency (Hz). High heating materials have a SAR of one to several thousand $W.g^{-1}$, while low heating materials have a SAR below *ca.* 100 $W.g^{-1}$. Such a hysteresis loop can be measure via the Vibrating Sample Magnetometer technique (VSM), which will be deeper explained in subsection II.5.1.

So, we have seen that under a MF, an array of single-domain particles release heat. The issue at present is how to optimize this heat generation, which raises the question of which parameters control the heating.

I.3.1.4 Hysteresis losses and the prominent parameters influencing it

Several parameters influence the heating. Firstly, the magnetic nature of the material is of major importance. We have seen before that the magnetic particle can be whether ferromagnetic or SPM. A ferromagnetic material presents a broad cycle opening, while a SPM's cycle is closed and thus these materials release very little heat (Figure I.12).

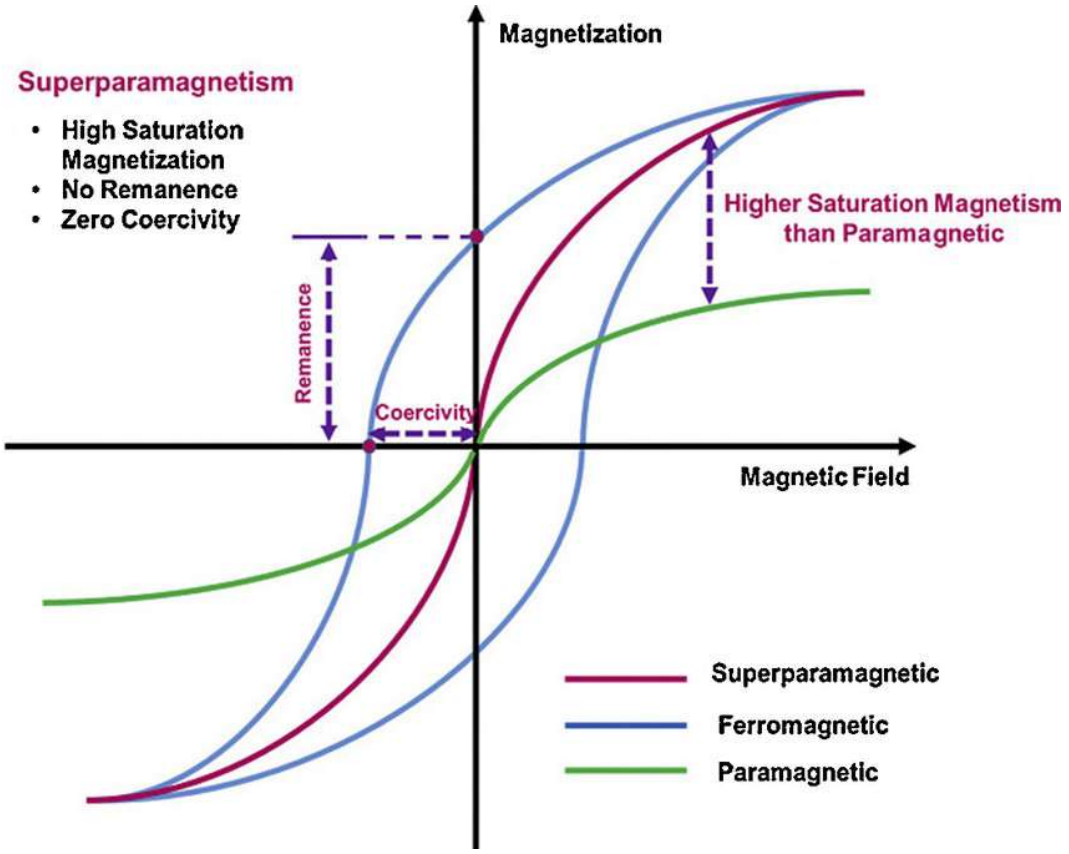

Figure I.12: Schematic hysteresis loop of a superparamagnetic, a ferromagnetic and a paramagnetic material. Reprinted from [70] with permission from Elsevier.

One distinguishes hard ferromagnetic and soft ferromagnetic materials, the former having much higher H_C and M_R values, which makes them suitable for permanent magnet applications. As the SAR is proportional to the hysteresis loop area, one would prefer hard ferromagnetic materials than soft ferromagnetic NPs. However, this implies that the magnetic field applied to flip the magnetic moments is higher, which costs much more electrical energy to generate than a low MF (see Supplementary Figure 2 and Supplementary Figure 3). Thus, soft ferromagnetic materials are better candidates for hysteresis losses.

Moreover, the nature of the material is important, as it influences the M_S value (the higher the *M*s, the higher the hysteresis area).

The frequency is also an important parameter. The SAR is directly proportional to it, but the frequency also influences the hysteresis shape and area as exemplified in Figure I.13 for the case of superparamagnetic particles.

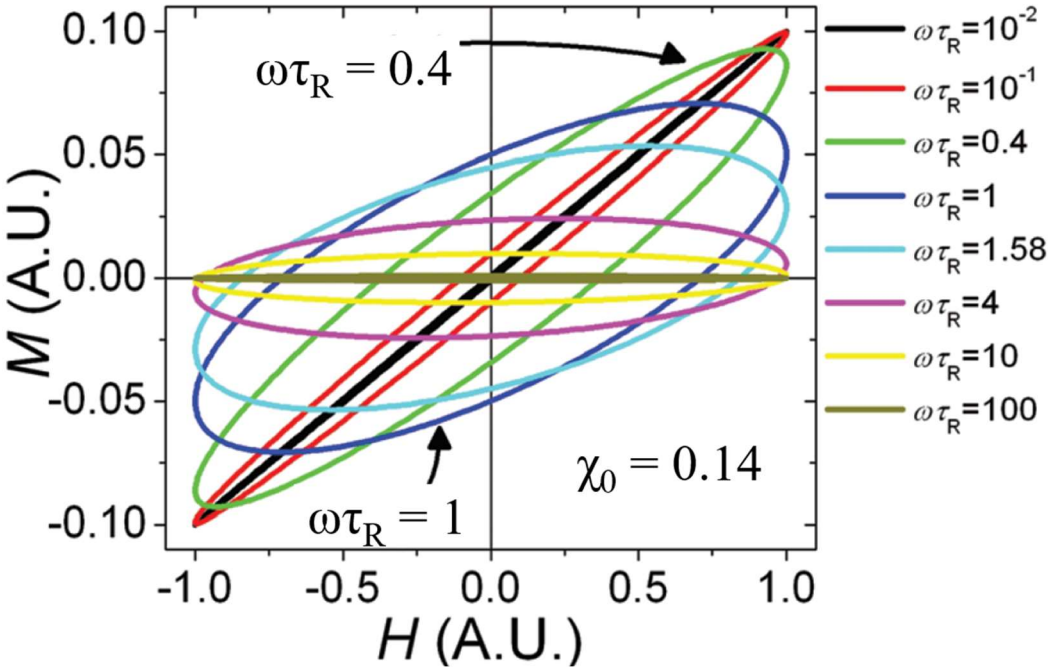

Figure I.13: Numerical evolution of the hysteresis loop as a function of the frequency times the Néel relaxation time. The magnetization and the magnetic field strength are normalized to unity. Reprinted from [71] with permission from AIP Publishing.

At low frequency, the magnetization does follow the MF direction in a reversible manner (one can think in a quasi-stationary evolution), and no heat is generated (black and red curves). When the frequency increases, the magnetization follows B_a but with a delay, which induces an opening of the hysteresis loop. When the frequency is too high, the magnetization cannot follow the applied MF, and no heat is generated (dark yellow curve). This graph has been calculated using the Linear Response Theory model, which will not be described here, but the reader can refer to [71] for more information.

The size of the NPs is also a serious parameter. Bigger particles will have a multidomain configuration. The heating in this case will come from the displacement of the Bloch walls which will change the direction of the domains' magnetic moment. Also, the size of the particle

influences the magnetic transition from superparamagnetic to ferromagnetic, impacting the SAR. It has been proved that single-domain particles heat more than multidomain particles, which show a drop in coercive field and thus SAR [72,73,74].

Finally, the interactions between the particles are very influential. Indeed, because of dipolar interactions, the NPs can form chains or aggregates, as showed Asensio *et al.* [75] (Figure I.14). In this last case, the SAR decreases because the aggregates are harder to magnetize as their magnetic response occur at a larger field than isolated particles [76,77]. When chain formation arises, a decrease as well as an increase of the SAR have been observed [75,78]. The chain creation depends on several parameters, notably the anisotropy and the size of the particles [79], the amount and size of ligands surrounding them, which increases the interparticle distance, lowering the dipolar interactions [80], as well as the magnitude of the applied MF. Mehdaoui *et al.* isolated (by simulation) two criteria characterizing the chain formation, which arises when the NPs do not present a strong anisotropy (in this case, the individual behavior dominates); for NPs with weaker anisotropy, chain formation is possible and it impacts the NP magnetic properties. The first criterion is quantitative, particle chains present a M_R/M_S ratio superior to 0.5 (the hysteresis cycle tends to a square). The second criterion is qualitative: the slope at the coercive field becomes steeper [81], which increases the area of the hysteresis loop. Physically, one can imagine that aligned magnetic moments (chain) under a MF help to align other moments by dipolar interactions, as a domino effect, especially when $\boldsymbol{B_a}$ is along the easy axis on the sample, hence a facilitated or more difficult heating.

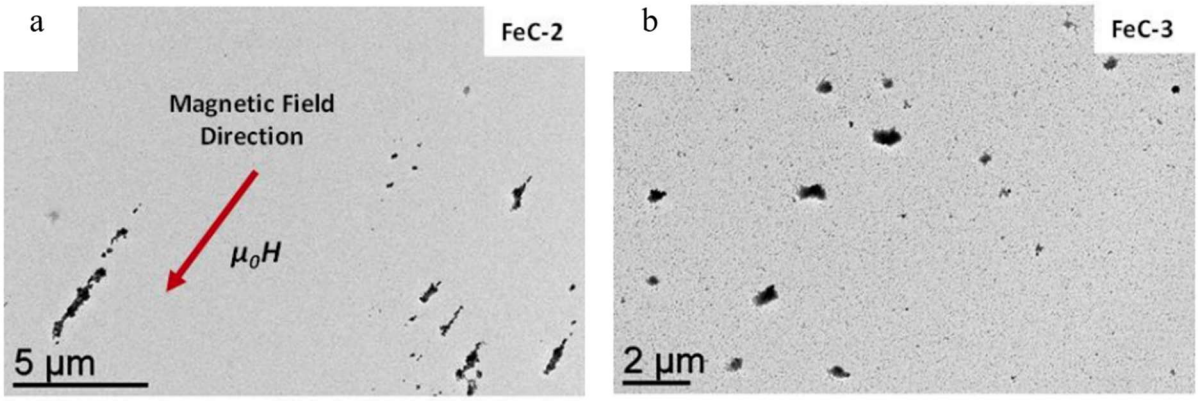

Figure I.14: (a) TEM pictures of $Fe_{2.2}C$ nanoparticles forming chains under a magnetic field (b) while similar particles after heating at 150 °C in mesitylene in the presence of 0.2 equivalents of palmitic acid for 2 hours formed agglomerates, insensitive to the magnetic field orientation.

To conclude, optimizing the SAR of NPs is very challenging and depends on many parameters. What is clear, though, is that soft ferromagnetic NPs are good starting candidates.

I.3.2 Application of magnetic heating by hysteresis losses to water splitting

The use of this heating route to catalyse the Fischer-Tropsch (conversion of CO and H_2 or water gas into liquid hydrocarbons) and Sabatier (CO_2 methanation) reactions was optimized by the use of FeC and core-shell FeC-Ni NPs during a PhD conducted by Alexis Bordet at the LPCNO. Then, the Laboratoire d'Electrochimie et de Physicochimie des Matériaux et des Interfaces (LEPMI) and the LPCNO laboratories applied this technique to the water electrolysis reaction. This work was conducted by Christiane Niether [60]. She used the same FeC-Ni particles deposited on a circular carbon felt support in a three-electrode and two-electrode cells in alkaline medium (KOH, 1 $mol.L^{-1}$). These NPs were of interest, as they *a priori* presented a magnetic sensitive core (SAR > 3000 $W.g^{-1}$), with a protective catalytic shell of Ni. Christiane Niether used an especially-designed cell in poly(methyl methacrylate) (PMMA), which could be inserted inside a 300 kHz coil, with a WE electrode positioned parallel to the MF to limit eddy current generation (generated in the perpendicular plane of $\boldsymbol{B_a}$), and conducted chronopotentiometric (CP) measurements: a constant current was applied and the potential of

the working electrode (WE) recorded (Figure I.15); the cell and the CP technique will be more explained in part II.2.1 and II.2.1.3 respectively.

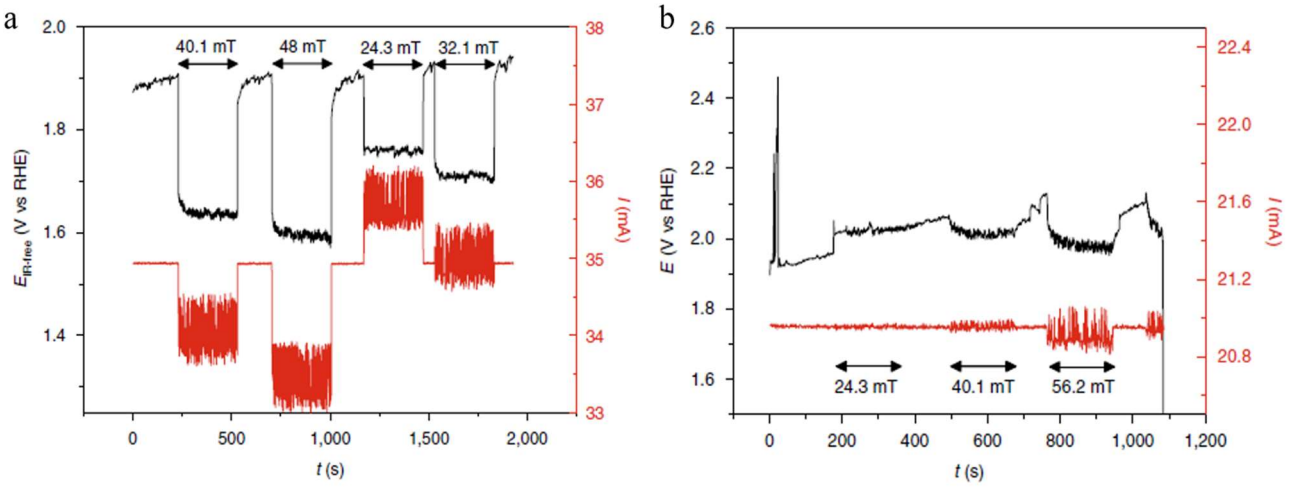

Figure I.15: Chronopotentiometric measurement at 35 mA with an Ohmic drop correction of a working electrode made of a carbon felt with (a) FeC-Ni particles deposited onto it and (b) no particle, under different MF amplitudes. Reprinted from [60] with permission from Springer Nature.

The application of the AMF led to an immediate and significant WE potential decrease up to ca 200 mV at 40.1 mT (Figure I.15 (a)), while its application on the non-catalytic carbon felt support resulted in much less potential decrease (~ 50 mV at 40.1 mT). In both cases, the applied constant current was affected by the AMF, and this created a small shift, which could be explained by Lens's law (induced currents tend to oppose to the cause of its production). Christiane Niether conducted these measurements for HER and OER (Figure I.16).

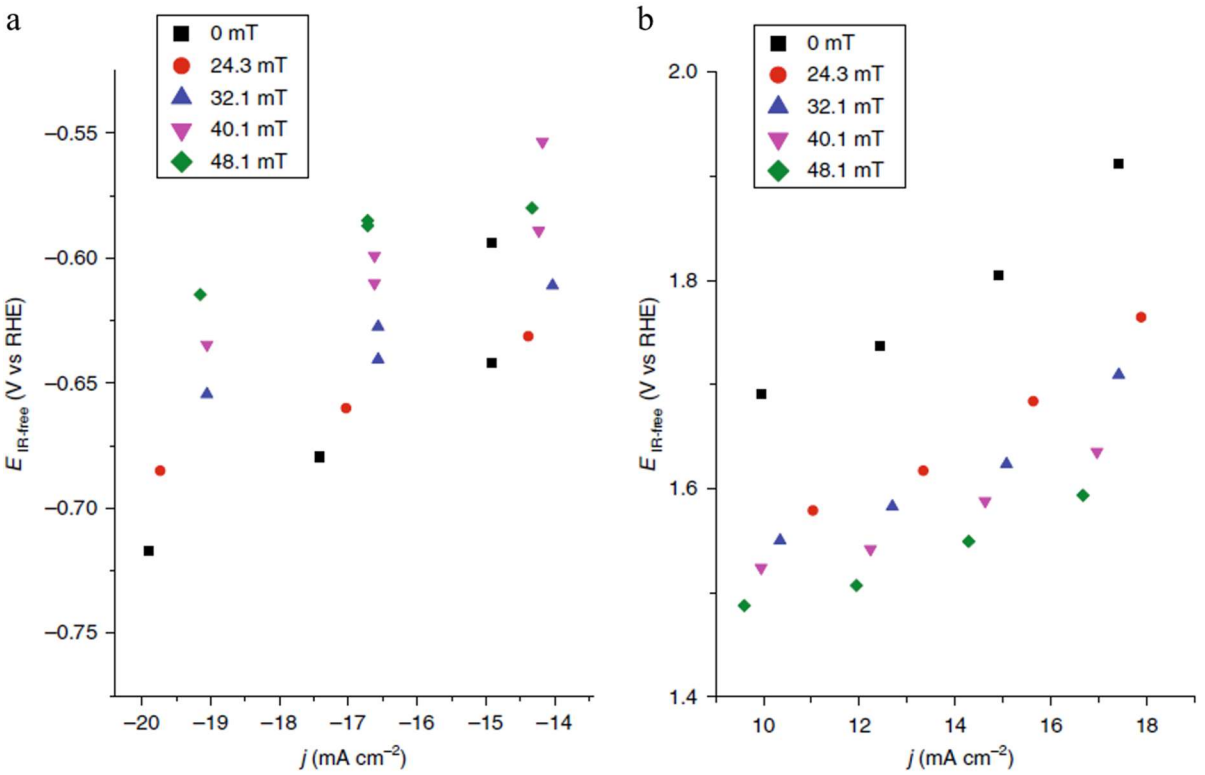

Figure I.16: Quasi-stationary potential values in the HER (a) and OER (b) sides, at different magnetic field amplitudes. The potentials were measured ~ 5 min after each applied current. The values are Ohmic-drop corrected, the high-frequency cell resistance being $R_{HF} = 5 \pm 2\ \Omega$.

The decrease (in absolute values) of the overpotential at both sides is an increasing function of the MF amplitude. This is consistent with the fact that increasing the MF amplitude corresponds to a temperature rise in the vicinity of the NPs, where half-reactions happen. Accordingly, WS is indeed thermally-activated.

This work was a promising proof-of-concept, as it showed that magnetic heating by hysteresis losses was applicable to the WS reaction (through Néel relaxation as the particles are stuck on the support), with all the advantages that this technique brings: an instantaneous positive effect with a remote source, with facile start/stop operation. Furthermore, the energy-efficiency of the system could in principle be improved, as the heating is supplied exactly where the reactions occurs: at the nanocatalyst surface, which are the active sites, and not to the rest of the cell (temperature elevation of the electrolyte remained below a few degrees, as measured

by an infrared camera). This last asset should lead to a better durability, as the other cell components remain at low temperature.

However, several bottlenecks and issues must be considered/resolved in order to optimize this technique. First of all, the mechanisms by which the water splitting reaction was enhanced were unknown: does the magnetic field application improve the kinetics and/or the thermodynamic of the reaction? Are there other magnetic or electrochemical effects which can intervene in this complex environment of applying an AMF on a system being the seat of an ionic and an electric current flow, where charged and gas species are consumed and/or produced? Besides, the FeC-Ni NPs did not prove to be a fast HER catalyst, and was an intermediate OER catalyst. Thus, the catalytic and magnetic properties of the catalyst could be improved.

Disposito: *to unravel these different points, we chose to improve first the catalysts by testing other magnetic materials for alkaline water splitting without an AMF application and characterizing their physicochemical and magnetic properties. The characterization techniques used herein are described in the Chapter II, while the results of this study are gathered in the Chapter III.*

Then, the new materials were tested under AMF, and several different studies were conducted to evaluate the effect of the magnetic field on the structure, the magnetic and catalytic properties of the catalysts. In parallel, a bibliographic work had been realized to learn which phenomena can arise when a magnetic field, static or alternating, is applied on an electrochemical system, which parameters control these effects, and how electrochemical systems are influenced by them. Then, we tried to evaluate these phenomena in our own cell. The bibliographic survey is detailed below, as part of the Chapter I, while the electrochemical tests under AMF, research of the origin of the positive effect observed and post mortem analyses are presented in the Chapter IV.

This PhD falls within the Hy-WalHy project (Hyperthermia-enhanced Water electrolysis for Low-cost Hydrogen production), funded by the French National Research Agency (ANR-1-CE05-0017). Two institutions have been involved, each with different attributed tasks: the Laboratoire d'Electrochimie et de Physicochimie des Matériaux et des Interfaces (LEPMI, Grenoble, France), where the intrinsic electrochemical activities of the materials, and the tests under static magnetic field had been realized, and the Laboratoire de Physique et Chimie des Nano-Objets (LPCNO, Toulouse, France), where the electrochemical tests under AMF were conducted, as well as the SAR and VSM measurements. The physicochemical characterizations were conducted at the LPCNO and at the Consortium des Moyens Technologiques Communs (CMTC Grenoble, France).

Abstract of Chapter I: In the following, four main effects of the application of magnetic fields (generally static - SMF) on electrochemical processes are described. First, the Lorentz force, the most observed and common effect, which increases the limiting current (magnetohydrodynamic effect – MHD), and induces different electrodeposition profiles in function of the direction of the MF: parallel ($B_{//}$) or perpendicular ($B_{\perp}$) to the electrode surface. Then the Kelvin force, which acts on high magnetic susceptibility species, and forces paramagnetic species to go in high MF gradient, and removes diamagnetic species to low MF gradient. Afterwards, the spin polarization, studied since 2000, is said to facilitate the electron-transfer on ferromagnetic and chiral species. Finally, the use of AMF in electrochemistry is reviewed. The review is broad, and could have been more concise, but it gives a global overview on the topic.

Résumé du chapitre I : Dans la suite de ce chapitre bibliographique sont présentés différents effets provoqués par l'application d'un champ magnétique (le plus souvent statique) sur des systèmes électrochimiques. D'abord, la force de Lorentz, bien connue, qui augmente les courants limites des réactions étudiées (effet magnétohydrodynamique) et induit différents profils dans les électrodépôts, selon l'orientation du champ magnétique, parallèle ou perpendiculaire à la surface de l'électrode de travail. Ensuite, l'effet Kelvin est présenté. Il agit sur les espèces chimiques présentant une forte susceptibilité magnétique : les espèces paramagnétiques sont attirées vers les régions de fort gradient de champ tandis que les espèces diamagnétiques sont repoussées vers les régions de faible gradient de champ. L'effet de polarisation de spin est ensuite introduit. Il survient avec des matériaux ferromagnétiques ou chiraux, et permettrait d'améliorer le transfert d'électrons lors de processus électrochimiques. Enfin, l'utilisation d'un AMF en électrochimie dans la littérature est rapportée. Un large éventail d'effets est présenté, ne concernant pas tous ce travail. Néanmoins, cela fournit un aperçu relativement exhaustif des phénomènes observés dans la littérature.

I.4 Effects of magnetic fields in electrochemistry

While the application of a magnetic field on electrochemical systems has been studied for over 45 years [82,83], magnetoelectrochemistry remains a challenging field of research, which involves several domains: electrochemistry, magnetism, hydrodynamics and spintronics. In the literature, most studies focus on the application of a static magnetic field (SMF), being either parallel ($B_{//}$) or perpendicular ($B_{\perp}$) to the electrode surface, and three effects, generally concomitant, have been observed: the Lorentz force, the Kelvin force, and the spin polarization effect. Very few studies report the use of an AMF on electrochemical systems. The phenomena arising under SMF will be firstly presented (part I.4.1 to I.4.3), then those under AMF (part I.4.4) [84]. The bibliographic work on these observed phenomena has been published as a mini-review in the following article:

Gatard V, Deseure J, Chatenet M. Use of magnetic fields in electrochemistry: A selected review. *Curr Opin Electrochem*. 2020;23:96-105. doi:10.1016/j.coelec.2020.04.012

We thank sincerely all the contributors for their participation in this work.

I.4.1 The Lorentz force

The Lorentz force has been the first studied phenomenon, and a huge diversity of effects have been reported [85,86,87]. The literature on this topic is abundant, and the main observed effects will be summarized herein. Its expression is given in Eq I.20:

$$\boldsymbol{F_L} = \boldsymbol{j} \times \mathbf{B} \qquad \text{I.20}$$

With $\boldsymbol{F_L}$ the Lorentz body force (N.m^{-3}), $\boldsymbol{B}$ the magnetic field (T) and $\boldsymbol{j}$ the current density (A.m^{-2}), which is expressed as follows, Eq. I.21:

$$\boldsymbol{j} = \sigma(\boldsymbol{E} + \boldsymbol{v} \times \boldsymbol{B}) - n\mathcal{F}D_{+,-}\nabla c_{+,-} \quad \text{I.21}$$

With $\boldsymbol{v}$ the velocity of the charged species (m.s^{-1}), n the charge number of the electroactive ionic species and $D_{+,-}$ (m^2.s^{-1}), $c_{+,-}$ (mol.m^{-3}) their diffusion coefficient and concentration respectively.

The Lorentz force acts on moving charged ions and depends on their velocity and the MF amplitude. It is maximal when $\boldsymbol{v}$ and $\boldsymbol{B}$ are orthogonal, and null when they are parallel. An order of magnitude is typically ~ 10^3 N.m^{-3} for j = 100 mA.cm^{-2} and B = 1 T, which is comparable to the buoyancy force ($\Delta\rho g = 10^3$ N.m^{-3} [88]).

Its most observed and common effect is to slim the diffusion layer, which improves the mass-transfer toward the electrode: the limiting current is proportional to $B^{1/3}$ and thus enhanced. Several groups have proven this relation theoretically by using the Navier-Stockes equation when including a Lorentz contribution [89,90,91,92], and it has been verified empirically for different electrochemical processes: electrodeposition [93,94], bioelectrocatalysis reactions [92], or for known Faradaic reaction: reduction of nitrobenzene in tetra(n-butyl)ammonium [95]. Concretely, the Lorentz force induces a magnetohydrodynamic (MHD) convection, whose magnitude is higher for $B_{//}$ than for $B_{\perp}$, and depends on the distance d between the electrodes and the magnet (B decreases as $1/d^2$) [96]. Even under a $B_{\perp}$, this effect is visible, since at the edge of the electrodes, the current density lines bend and are no longer parallel to the magnetic field direction. This triggers micro-MHD vortices, impacting especially electrodeposition processes (Figure I.17). In practice, both convections occur, but one can be prominent against the other, depending on the B orientation.

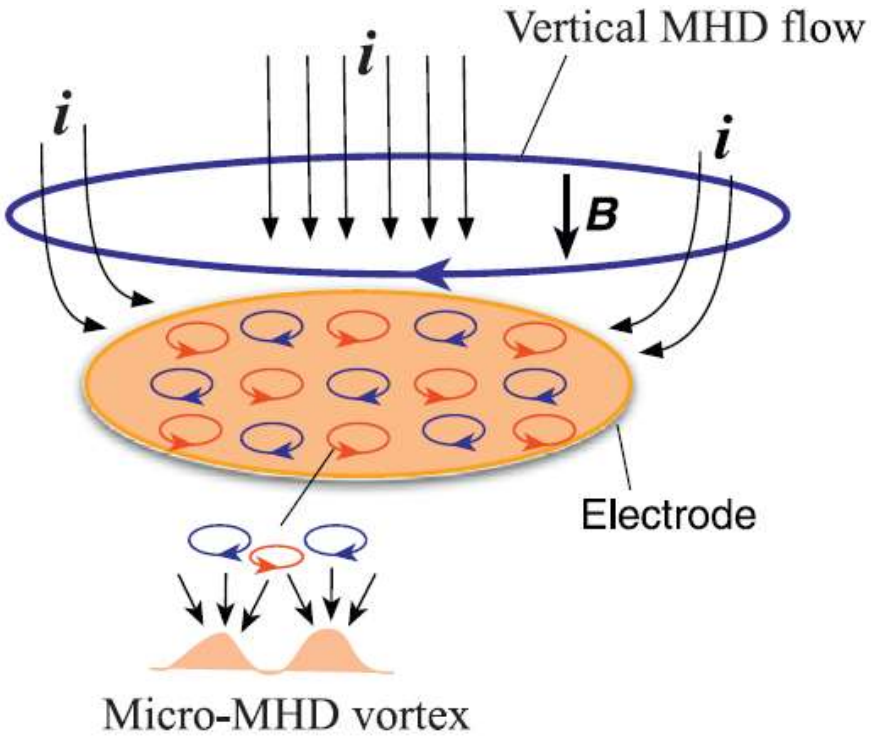

Figure I.17: Current field lines ***i*** and magnetic field direction ***B*** during an electrodeposition process. The current lines bend at the edge of the electrode, creating micro-MHD vortices on the electrode surface. Reprinted from [97] with permission from Elsevier.

Contradictory results were obtained for electrodeposits. In the case of a dominant convection by micro-MHD vortices induced under a $B_{\perp}$, a 2D growth instead of a 3D growth was observed: research groups suppressed dendrite formation [98,99] while others increased the deposit roughness [100]. Besides, preferential crystallographic growth was promoted upon metal deposition, which changed the deposit shape [101]. With a prominent global convection created under a $B_{//}$, rougher deposits were found [102] and dendrite/needle growth was enhanced [102,103], as well as a more homogeneous surface with smoother deposits and finer grains [100,104]. Also, magnetic properties can be altered: smoother deposits of CoFe alloys led to a coercive field reduction [100], and a reduction in the remnant field was observed for $Fe_{0.3}Ni_{0.7}$ deposition under 100 mT [104]. Figure I.18 illustrates the different shapes obtained for a CoFe deposition without a MF, and under a $B_{//}$ and a $B_{\perp}$ of 1 T.

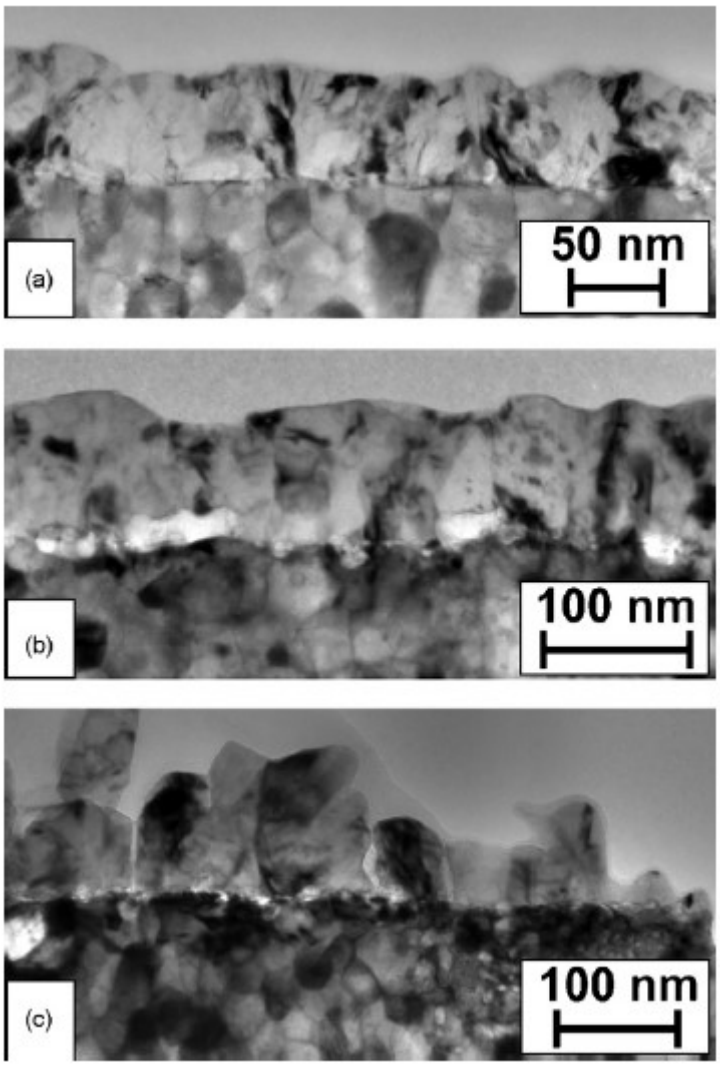

Figure I.18: Cross-sections of CoFe layers (a) without, (b) with $B_{//}$ and (c) $B_{\perp}$ of 1 T. Reprinted from [100] with permission from Elsevier.

Although a mechanical agitation could be more effective, the Lorentz force can induce electrodeposits patterns at a very small scale, which is impossible via mechanical agitation [87].

Moreover, a shift in the rest potential due to facilitated oxidant transport toward the surface by micro-MHD convection was found, leading to enhanced corrosion [105,106,107,108], in both cases of a $B_{//}$ and $B_{\perp}$.

Also, the Lorentz force can be used as an enantioselectivity tool [97]. Magnetically-prepared Cu or Ag electrodes were found sensitive toward certain enantiomers of chiral

molecules such as glucose and amino acids [96]. The magnetic field application favored screw dislocation growth in certain direction, leading to a chirality of the electrode.

In addition, gas-evolving reactions are impacted by MHD convection. Indeed, the bubbles removal, in a clockwise or anticlockwise direction depending on the surface charge of the bubbles, is promoted [109]. Several groups calculated experimentally that the void fraction decreases for both H_2 and O_2 evolution in alkaline medium [110], as well as the surface coverage θ which had been fitted to $B^{-0.5}$ [111]. Charged Coupled Device (CCD) camera observations showed that the bubble diameter decreases by almost half compared to the diameter without a MF, as does the nucleation site number [104,112,113]. The effect has been seen as an imbalance between radial pressure difference and centrifugal force at the electrode surface, leading to a drag force which increases the contact angle and forces the bubbles to detach at earlier stage with a smaller size [114,115,116]. This was supported by numerical simulations, where flow lines velocities were found to increase with a $B_{//}$, leading to enhanced bubble detachment, when the Lorentz force was in the opposite direction of gravity, while the reverse effect was computed and observed when F_L is in the gravity direction for a current density of 1.5 $A.cm^{-2}$ [117]. For electrodeposition processes, this bubble removal effect favors better electrodeposits with fewer vacancies and defects [118,119]. Furthermore, this effect was proven beneficial to enhance water splitting processes, bubbles' removal decreasing the Ohmic drop due to bubbles' coverage [120,121], and the MHD-effect reducing the supersolubility of the gases [122]. Other processes like polymerization [123] and organic reactions [124] presented a better efficiency under a static magnetic field.

While many interesting effects have been observed and simulated, no comprehensive/universal model explaining all phenomena under each condition exists. Efforts are still to be made in this regard.

I.4.2 The Kelvin force

When a magnetic field $\boldsymbol{H}$ is applied to a material of dimensionless magnetic susceptibility χ (defined by the Curie-law [63]), a magnetization $\boldsymbol{M} = \chi \boldsymbol{H}$ is induced. Thus, the energy density of a material under a SMF is, Eq. I.22:

$$E_{\text{mag}} = -\frac{1}{2}\mu_0 MH \qquad \text{I.22}$$

Assuming that the material has a magnetic permeability $\mu_r = 1$ (which is the case for diamagnetic medium like KOH [125]), it comes $B = \mu H = \mu_r \mu_0 H = \mu_0 H$. The force density $\boldsymbol{F}_{\text{mag}} = -\boldsymbol{\nabla} E_{\text{mag}}$ is, Eq. I.23:

$$\boldsymbol{F}_{\text{mag}} = -\frac{1}{2\mu_0}\boldsymbol{\nabla}(\chi_{\text{m}} c B^2) \qquad \text{I.23}$$

Which leads to Eq. I.24:

$$\boldsymbol{F}_{\text{mag}} = -\frac{1}{2\mu_0}\chi_{\text{m}}[\, B^2 \boldsymbol{\nabla} c + c \boldsymbol{\nabla} B^2 \,] \qquad \text{I.24}$$

With χ_m the molar susceptibility of the considered species (assumed invariant, in $m^3.mol^{-1}$), and c its concentration ($mol.m^{-3}$).

The first term is the paramagnetic gradient body force $\boldsymbol{F}_{\nabla c} = -\frac{1}{2\mu_0}\chi_{\text{m}} B^2 \boldsymbol{\nabla} c$, which arises when there is a susceptibility gradient due to a concentration gradient of magnetic materials. It tends to inhibit diffusion and confine ions at the vicinity of the electrode. A typical order of magnitude is ~ 10^2-10^4 $N.m^{-3}$, given $B = 1$ T, $\nabla c = 10^7$ $mol.m^{-3}.m^{-1}$ and $\chi_m = 10^{-11}$-10^{-8} $m^3.mol^{-1}$ depending of the magnetic character of the material.

The second term is the Kelvin body force (also known as field gradient force or magnetophoretic force) $\boldsymbol{F}_{\text{K}} = -\frac{1}{2\mu_0}\chi_{\text{m}} c \ \boldsymbol{\nabla} B^2 = -\frac{1}{\mu_0}\chi_{\text{m}} c B \ \boldsymbol{\nabla} B$, which tends to attract

paramagnetic/ferromagnetic species ($\chi_m > 0$) in regions of high field gradient, and repel diamagnetic species ($\chi_m < 0$) toward regions of low field gradient. Its order of magnitude is ~ 10^3 N.m^{-3} with ∇B = 100 T.m^{-1}.

It is worth mentioning that these magnetic forces are ubiquitous as any electron-transfer redox process involves para/diamagnetic species, such as cations, free-radicals or unpaired spin species such as O_2. However, the huge majority of the species have a low magnetic susceptibility of 10^{-10} m^3.mol^{-1} and only 3d elements from the 4th and 5th raws (or higher when combined with oxides for instance) in the periodic table present a susceptibility of 10^{-7} m^3.mol^{-1} (given at 300 K). Thus, these two forces are generally negligible when compared to the driving force of diffusion $RT\nabla c$ ~ 10^8 N.m^{-3} at room temperature. However, at the micro or nanoscale, magnetic field gradient of 10^6-10^7 T.m^{-1} can be expected leading to a Kelvin force of 10^6-10^7 N.m^{-3} which could influence the diffusion process at a local scale [88,126,127].

Effects on electrodeposits have been observed, leading to direct or indirect patterning. The former is achieved when a metal deposit is realized from paramagnetic cations, like Co^{2+}, Ni^{+2}, Cu^{+2} or Bi^{+2} [128,129]. At the vicinity of the cathode where the magnetic field gradient is the most intense, thicker and rougher deposits have been obtained, with a dendrite-like growth (Figure I.19) [130].

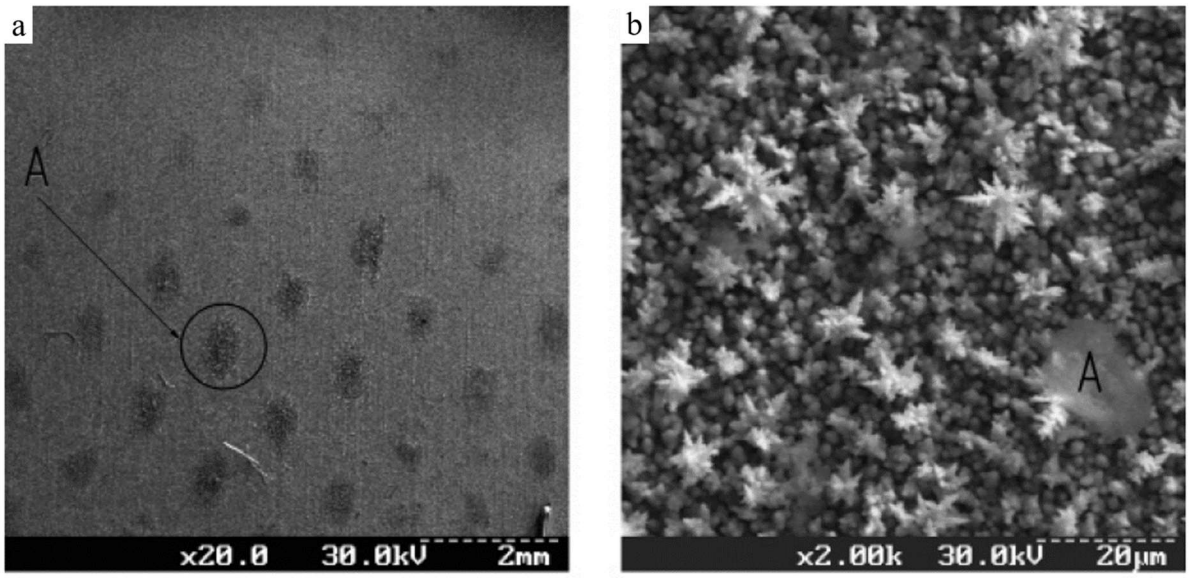

Figure I.19: Ni deposits on a steel gauze spliced of wires with a diameter of Ø = 0.5 mm, obtained under a gradient magnetic field with a $B_{\perp}$ = 100 mT, i = 21 mA during 20 minutes. Reprinted from [130] with permission from the American Chemical Society.

Inverse patterning (with respect to the $|B\nabla B|$ distribution) is obtained when a strong paramagnetic inert specie is added to the solution, with the aim to deposit a diamagnetic specie. The electroinactive paramagnetic ions create a concentration gradient which tends to exclude the diamagnetic ions from the high gradient magnetic field regions. These latter are then deposited on the side in an inverse footprint with a thicker deposit in regions where there are no magnets [131]. In this context, Bi has been deposited with a reversed pattern using an electrolyte composed of 0.01 mol.L^{-1} $Bi(NO_3)_3$ + 0.09 mol.L^{-1} $Mn(NO_3)_2$ in 0.1 mol.L^{-1} HNO_3 (Figure I.20). Figure I.20 (a) shows a homogeneous thick Bi layer, while Figure I.20 (b) presents a thinner Bi layer in regions of high gradient film (we can see the brightness of the gold layer underneath), while a thick gray layer of Bi is deposited around.

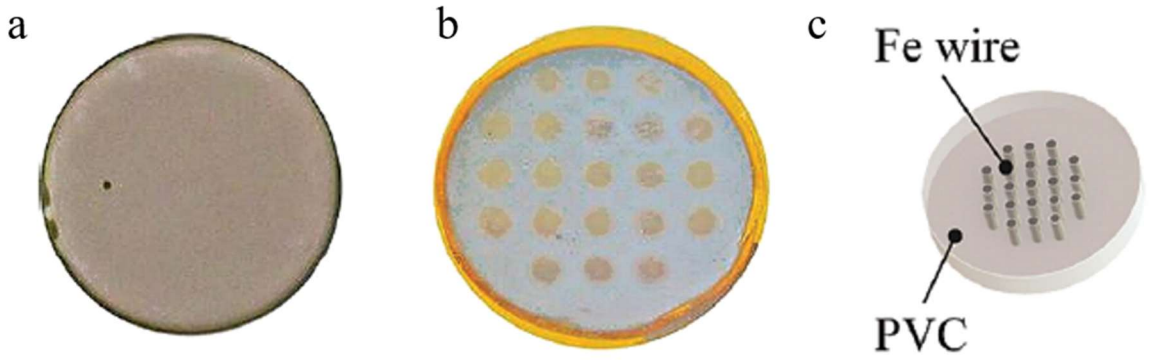

Figure I.20: Optical images of Bi deposits obtained under (a) a homogeneous magnetic of 500 mT, and (b) under a gradient magnetic field induced by the ∇B template containing 21 Fe wires (c). Reprinted from [131] with permission from the American Chemical Society.

Also, when a ferromagnetic anode like Fe was employed, the dissolved Fe ions were retained at the vicinity of the electrode (due to the Kelvin force), preventing hydroxide ions from coming at the electrode, which triggers a local *pH* increase, and a decreased corrosion current as well as a cathodic shift of the rest potential [132,133].

The Kelvin force has also been used to enhance the oxygen reduction reaction (ORR) in a PEMFC. Using an electrode of Pt/C 20 wt.% with Nd/Fe/B NPs magnetized under 4 T, Okada *et al.* succeeded in improving the O_2 transport toward the cathode gas diffusion layer. Indeed, the susceptibility of O_2 is much superior to that of water: χ_m (O_2) = 4.334×10^{-2} $cm^3.mol^{-1}$ >> χ_m (water) = -1.329×10^{-4} $cm^3.mol^{-1}$ at 293 K [127], an effect confirmed by simulations [134]. Similarly, Xu *et al.* found experimentally that the diffusion and transfer coefficients of O_2 increased for an electrode made of Pt/C with $Nd_2Fe_{14}B$/C [135], such improvement being also observed in alkaline medium [136].

Convection of paramagnetic species enhancing mass-transport has also been observed[106,125], likewise the MHD convection effect. Also, the Kelvin effect has been used to enrich a tube zone in oxygen from an air gas flow, by the interception effect of a gradient magnetic field [137,138].

I.4.3 The spin polarization effect

A domain of growing interest is the application of spintronics to oxidoreduction reactions. It deals with the transfer of polarized electrons, which becomes selective, restricted or enhanced [84,139,140,141,142].

It has been used as a tool to investigate the OER and ORR mechanisms. While most studies focus on thermodynamic considerations of the adsorption/desorption of reactant and intermediate species (according to Sabatier's principle, the reactant should adsorb neither to strongly nor to weakly to the catalyst surface), the electron transfer between the active sites and the reactants/intermediates (•OH, •O, •OOH radicals) and the binding strength are crucial factors which can be studied from a spintronic point of view. This analysis is applicable to water splitting (or water formation from H_2 and O_2), because this reaction starts (ends) from a diamagnetic molecule: water, and ends (starts) with H_2 which is diamagnetic and O_2 which is paramagnetic in its fundamental state. Yet, it is known that gas-phase reactions are controlled by a spin-conservation rule (conservation of the total spin $\boldsymbol{S}$ angular momentum: $\Delta S = 0$), that is, if the spin of the electronic wave function of the products differs from that of the reactants, the reaction rate is very weak [143]. In this context, the OER proceeds to the formation of the oxygen in one of its singlet excited state $^1\Delta_g$ (the outer electrons are in the same energy state with their spin opposite, the spin of O_2 is thus null and the molecule is diamagnetic), and not in its fundamental triplet ground state $^3\sum_g^-$ (the outer electrons are in two different energy states, their spins are parallel so that the spin of O_2 equals one, and the molecule is paramagnetic), as sketched in Figure I.21 [144].

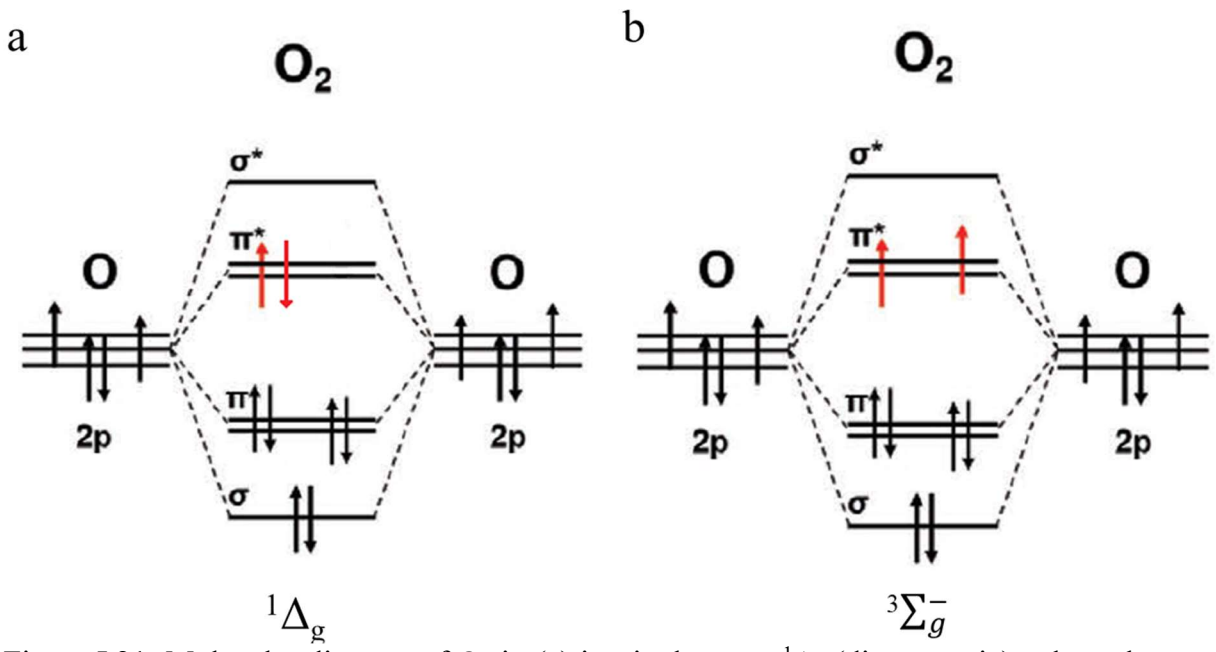

Figure I.21: Molecular diagram of O_2 in (a) its singlet state $^1\Delta_g$ (diamagnetic), where the two electrons are in the same antibonding molecular orbital and (b) its triplet state $^3\sum_g^-$ (paramagnetic) where the two electrons are in different antibonding molecular orbitals (right). Only the p states of O_2 elements are represented.

The difference between these two energy states has been calculated to be 0.98 eV by density functional theory (DFT) computations [145,146,147,148]. This huge difference can be explained by the high value of the Coulomb integral, corresponding to the repulsion energy between two electrons of opposite spin in the same energy state [142]. The transition between these two states is forbidden by the spin selection rule, which results in a very low decay from the singlet to the triplet state [149]. Thus, creating O_2 directly in its triplet state is much more interesting thermodynamically.

This was the thermodynamic point of view, let's continue with the spintronic considerations. Creating triplet O_2 is possible by quantum spin(-orbital) exchange interaction (QSEI) between the reactants/intermediates and the catalyst surface (which is required to present a high spin-orbit coupling, *i.e.* a high spin). Chiral molecules and magnetic materials were used to obtain this effect, which has first been observed in 1999 by Naaman *et al.* who found that chiral compounds act as a spin-filter: one polarization of the spin of the exchanged

electrons is favored against the other when the electrons are transmitted through a chiral molecule [150]. The effect was called Chiral-Induced Spin Selectivity (CISS). This forced spin polarization of the exchanged electrons permits to increase the overlap integral of the catalyst surface atom molecular orbital and the reactants/intermediates molecular orbital, and decreases the Coulomb integral, enhancing the reactivity. Several groups studied the binding of reaction intermediates on ferromagnetic or antiferromagnetic (the direction of the spin is alternating) working electrodes (WE) for the OER/ORR and showed that the binding strength can be controlled by spin polarization: DFT calculations for 3d-element with QSEI indicated that dominant antiferromagnetic QSEI increases the repulsion Coulomb potential and pair localization (lowering electron conductivity) of the electrons in the valence band compared to a nonmagnetic covalent structure. Too strong coupling and pair localization in fully antiferromagnetic orderings may strongly lower the chemisorption of reaction intermediates, which is detrimental to the reactivity. On the contrary, dominant ferromagnetic QSEI decreases Coulomb interactions and pair localization, and lowers the adsorption enthalpies of reactants, yielding milder intermediate adsorption and enhancing OER/ORR activity [151,152,153,154]. The calculations have been sometimes verified experimentally, as did Forslund *et al.* who studied the overlap integral between the Ni and Fe 3d bands and the O 2p band of Ruddlesden-Popper oxides. They found that a sufficient Ni content favored the 4-electron pathway yielding •OH over the 2-electron pathway yielding •OOH in the OER mechanism [155].

Also, this effect has been used by Garcès-Pineda *et al.* to explain the enhanced OER current from 24 to 40 $mA.cm^{-2}$ at 1.65 V_{RHE} when simply approaching a permanent magnet (450 mT) from a $NiZnFe_4O_x$/Ni-foil ferromagnetic WE [156]. Similarly, Ren *et al.* used ferromagnetic $CoFe_2O_4$ under a constant magnetic field (MF) of 1 T to enhance the OER, while with diamagnetic IrO_2 no enhancement was observed. Besides, they found a change in the Tafel slope, going from ~ 120 to ~ 90 $mV.dec^{-1}$, indicating, in their opinion, a change in the rate

determining step and a facilitated electron transfer, supporting the spin polarization effect (Tafel slope will be explained more deeply in subsection II.2.1.2). Moreover, they studied the influence of the temperature and found that the enhancement under the SMF was increasingly less distinguishable at higher temperature, the ordered magnetic moments being thermally disturbed [157]. Indeed, this spin dependence is more significant at low translational energy, but was found to amounts over 40% at thermal energy (ORR on a Ni(111) surface) [158]. Accordingly, Jose Gracia modified the electron transfer constant expression to account for this spin dependency by introducing an electronic entropy term, and an electronic enthalpy term, representing the activation energy required to create an itinerant transition state in the conduction band of the catalyst [159,160,161]. Figure I.22 (a) sketches the formation of triplet O_2 on an antiferromagnetic and ferromagnetic Ni surface. Figure I.22 (b) to (e) shows the OER current-potential curves of OER reaction obtained for $CoFe_2O_4$ and IrO_2, and the associated Tafel slopes.

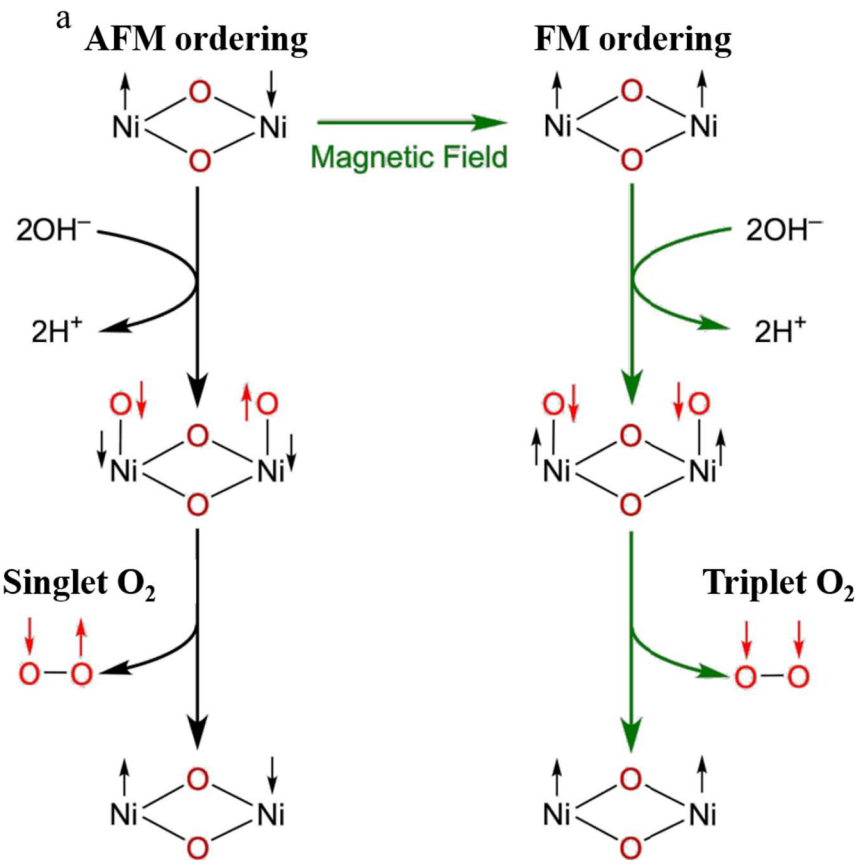

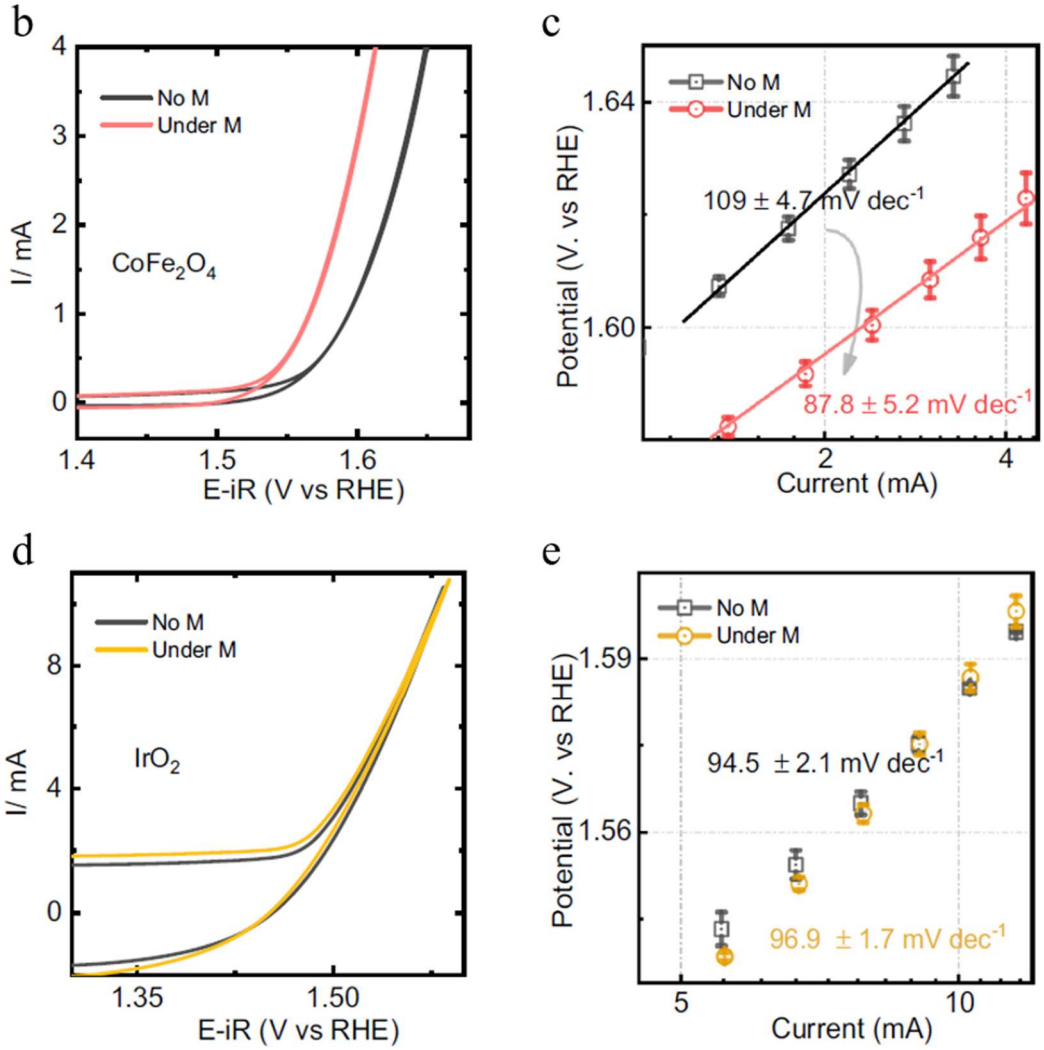

Figure I.22: (a) Schematic representation of the formation of singlet and triplet oxygen on an antiferromagnetic (left) and ferromagnetic (right) Ni surface. Current-potential curves of OER reaction on (b) $CoFe_2O_4$ and (d) IrO_2 and the associated Tafel slope (c) and (e). Modified from [156] for (a) and from [157] for (b)-(e) with permission from Springer US.

Side-reaction inhibition or selectivity was also observed. Mtangi *et al.* succeeded in polarizing the spin through chiral Zn porphyrins and observed an inhibition of the side-reaction of H_2O_2 formation and an enhanced O_2 evolution, the H_2O_2 creation being symmetry-forbidden for a chiral molecule due to the Pauli exclusion principle while it is not for an achiral molecule, as sketched in Figure I.23. Enantioselectivity has also been observed for oxalate oxidation [162].

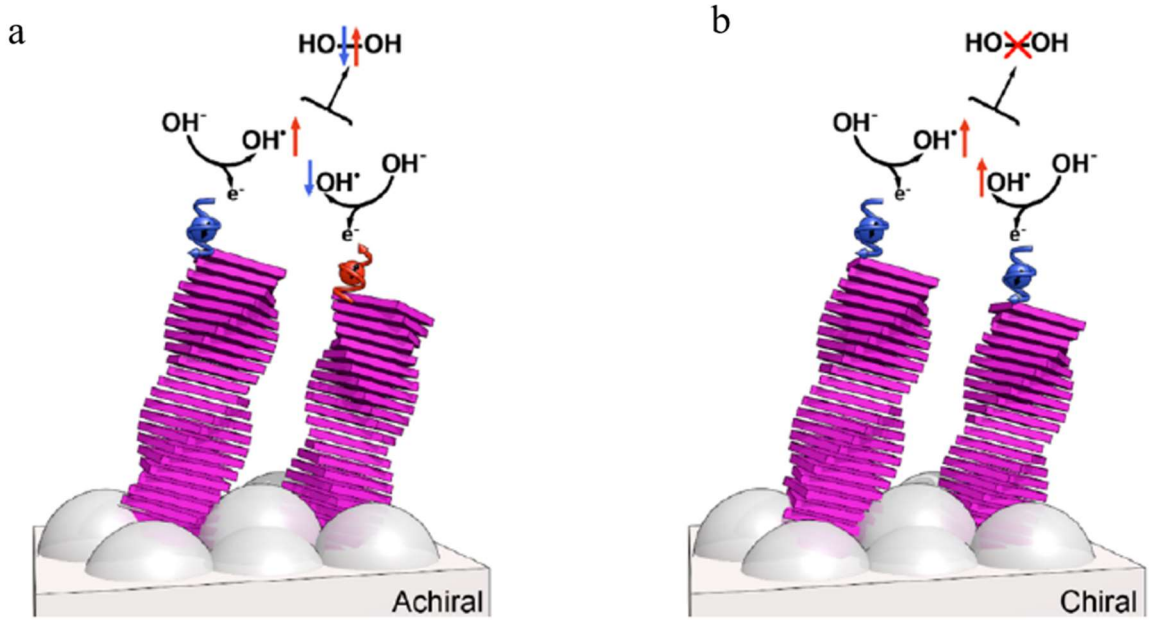

Figure I.23: H_2O_2 formation on an achiral surface with non-defined spin orientation (a) H_2O_2 inhibition on a chiral surface with parallel spins due to the Pauli principle (b). Reprinted from [163] with permission from the American Chemical Society.

While the spin polarization effect seems easy to setup as just abundant and cheap ferromagnetic materials besides with a relatively small magnetic field can be employed to generate it, it faces limitations. Indeed, is it constrained by the distance and the lifetime over which the electrons' spin is preserved. Bullard *et al.* used magnetic-conducting atomic-force microscopy to show that the polarized current created by chiral molecules can flow through achiral molecules over ~ 35 Å, a distance exceeding the length of chiral moieties (~ 15 Å) [164], whereas Mishra *et al.* observed CISS effect through extracellular conduits, over distances above 10 nm [165]. Kumar *et al.* recorded a long lifetime (>10 ms) in an AlGaN/GaN device [166]. In addition, the spin-selectivity may be *pH* dependent for certain reactions, as Garcès-Pineda *et al.* did not observe spin-restriction for WS at *pH* = 11 using Ni-foil-supported 3d-element oxides in 1 mol.L^{-1} KOH electrolyte [156], whereas Tassinari *et al.* observed enhanced Hydrogen Evolution Reaction (HER) with a chiral poly(fluorene-co-thiophene) decorated with CdSe quantum dots in 0.35 mol.L^{-1} Na_2SO_3 + 0.25 mol.L^{-1} Na_2S aqueous electrolyte solutions (*pH* = 9.5) [167]. These results indicate that the rate-limiting step is spin-restricted under different *pH*

conditions or with different catalysts. More studies are necessary to understand well and use the spintronics for catalyst optimization.

I.4.4 Use of an alternating magnetic field in electrochemistry

The use of AMF in electrochemical systems is very scarce. In 2008, Bin *et al.* reported the influence of a 25 Hz AMF on the Cu corrosion in 3.5 wt.% NaCl solution, sea water and magnetized sea water (subjected during 10 days to a 300 mT AMF at 37 mHz). They observed a 10-fold reduction of the corrosion current in magnetized sea water compared to sea water, no explanation being provided [168].

Melo *et al.* used a switchable MF to manipulate single Fe_3O_4 microparticles coated with Prussian blue, and enhanced the oxidoreduction of the one-electron transfer Prussian blue/Prussian white reaction.

Chehade *et al.* studied in 2020 the ammonia synthesis on Ni electrodes in the presence of 10 g Fe_3O_4 NPs under a 49 mT AMF of 30-60 kHz. They recorded a potential reduction from 1.7 to 1.25 V_{RHE} under AMF, at 6.4 $mA.cm^{-2}$ and 197°C. They explained the enhancement by the Joule effect caused by eddy currents, but they do not dwell on this argument [169].

Zheng *et al.* studied the HER on $NiFe_2O_4$ on metal organic framework (metal ions coordinated to organic compounds) under a small AMF [0.5 to 2.8] mT, but they did not precise the working frequency. They found an overpotential reduction of 31 mV at 10 $mA.cm^{-2}$ and 2.3 mT. However, they observed that the current density increases with the AMF amplitude and then decreases. They used an interesting thermodynamic approach to explain this result, considering the Joule effect, the Lorentz force, and the electromotive force sparked by the

induced current. Although very few explanations are given, the global thermodynamic assessment indicates that the Gibbs free energy evolution supports the current density trend [170].

To conclude and focus on this work, influence of the Lorentz force on the current and on bubble could intervene, as well as a Kelvin effect as O_2 is produced. Finally, since ferromagnetic materials are employed, a spin polarization effect can have an impact on the performances toward WS.

Finally, from the scarce reported works on AMF, it seems that it does influence electrochemical systems, but its actions, principles and effects deserve much deeper investigations, which will be attempted in this manuscript.

Chapter II: Materials and methods

Abstract of the Chapter II: In Chapter II are presented the choice and syntheses of the materials used. Then all the electrochemical, physicochemical and magnetic characterization techniques are detailed. Especially, some theory about electrochemistry, double layer interface, capacitive/ Faradaic current, the elementary steps of HER and OER and the Tafel analysis is addressed in the electrochemical section.

Résumé du chapitre II : Le chapitre II développe le choix des matériaux utilisés ainsi que leurs synthèses, et détaille toutes les techniques utilisées pour les caractérisations électrochimiques, physicochimiques et magnétiques. Notamment, des notions électrochimiques telles que l'interface de double couche au niveau d'une électrode, la nature des courants capacitif ou Faradique selon les phénomènes qui surviennent aux interfaces, les étapes élémentaires reconnues pour les réactions HER et OER et l'analyse de type Tafel sont abordées.

In this chapter, the materials and the methods chosen for the studies are described. Firstly, the choice of the studied materials will be justified, and their synthesis presented. Then, the electrochemical techniques and cells used will be presented. Finally, the physicochemical and magnetic characterization techniques will be detailed.

II.1 Materials and their synthesis

II.1.1 Materials used

In this study, magnetic and electrocatalytic materials were required, to mix a magnetic behavior responding to an AMF, with good electrocatalytic properties towards water splitting.

Thus, $FeNi_3$ and $FeNi_3$@Ni (@Ni standing for a Ni enrichment), which were developed by Déborah De Masi at the LPCNO for the CO_2 methanation enhanced by AMF, were first studied. These particles proved to be good heating agents, requiring a lower magnetic field to start heating than the FeC-Ni developed by Alexis Bordet [171,172]. Indeed, the SAR of $FeNi_3$ (resp. $FeNi_3$@Ni) started to increase from 15 mT (resp. 20 mT) while the SAR of FeC-Ni particles started to rise around 30 mT (see Figure II.1). Heating at lower magnetic field is interesting, as it decreases the energy consumption of the coil (see Supplementary Figure 2 and Supplementary Figure 3), and would therefore lower the overall energy consumption of AMF-enhanced water electrolysis.

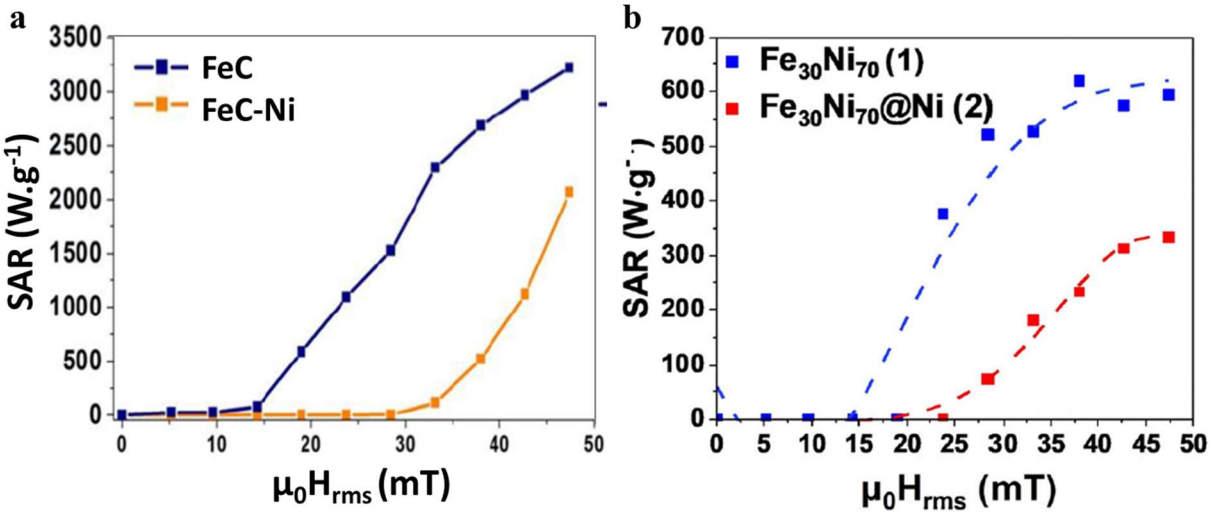

Figure II.1: Specific Absorption Rate of (a) FeC(-Ni) and (b) $FeNi_3$(@Ni) measured at 100 kHz in the [0; 47] mT range. Reprinted from [66] and [172] with permission from INSA Toulouse University and Wiley, respectively.

Regarding the electrocatalytic properties, materials with better activities towards WS than FeC-Ni NPs were targeted, especially in the OER side, where the overpotential is higher than in HER. The FeNi-based particles seemed interesting as this association is among the best catalyst for water splitting in alkaline media. It has been shown by Trotochaud *et al.* that the presence of small Fe quantities in the electrolyte influenced considerably the OER activity on oxided Ni catalyst, as these ions incorporate into the NiOOH matrix during the crystallization process. It seems that Fe exerts a partial charge-transfer activation effect on Ni, similar to that observed for noble-metal electrode surfaces. Besides, the presence of Fe led to a 30 fold increase of the (oxo)hydroxide conductivity [173]. Indeed, the Fe presence could create electrical bridges between the insulating $Ni(OH)_2$ phase and the conducting NiOOH phase, which could explain partly the observed enhancement. While many studies were conducted to understand and optimize the FeNi catalyst activity, no consensus exists currently whether the Fe [174,175,176] or the Ni [177,178] is the actual active site. Different techniques (Synchrotron-based X-ray Absorption Spectroscopy, X-ray Absorption Near Edge Structure and Extended X-ray Absorption Fine Structure) have been employed to scrutinize the oxidation state and the local atomic structure under anodic potential. Bates *et al.* showed that the Fe presence stabilizes the Ni in its +2

oxidation state [179], while other authors reported that Ni oxidizes from +2 to +4 [180,181]. Recently, *operando* Inductively Plasma Coupled-Mass Spectrometry (ICP-MS, technique explained in part II.5.4) conducted by Chung *et al.* revealed that there is a dynamic Fe exchange (dissolution and redeposition on the electrode surface) from the WE and the electrolyte, indicating the existence of a dynamic change of the active sites during the OER process [182]. In that respect, Sun *et al.* used a very interesting spintronic approach to explain the better activity of FeNi oxides compared to Fe oxides [183]. By analyzing the d-electron configurations of Fe and Ni cations, and calculating the bond strength by the number of electrons in the bonding and antibonding molecular orbitals, they showed that $Ni_xFe_{1-x}OOH$ is more active than FeOOH, which they confirmed by density of state computations via DFT simulations. In any case, studies report that $Ni_{1-x}Fe_x$ oxides with x ~ 0.20-0.30 are optimized catalysts for the OER [173,184,185,186,187], and this remains valid for different particles shapes [188] or supported particles [189] for instances. Thus, this $FeNi_3$(@Ni) particles were promising catalysts mainly for OER, but for HER also [190,191].

$FeNi_3$@Mo particle (@Mo standing for Mo enrichment) were also used. Associating Mo (and generally selenide [192,193], nitride [194] or phosphor [195]) to Ni proved to increase the durability of the catalyst, and very good performances were obtained [196]. Besides, interesting heating properties were expected.

In addition, different Ni NPs were employed. Ni is known to be among the best non-noble catalysts for HER when partially oxidized [197,198]. Besides, Ni had already been used in magnetic heating for hydrocarbons reforming (especially methane), at the millimetric size by Koch *et al.* [199], at the nanometer size by Ovenston and Walls [200] and by Varsano *et al.*, the latter using NiCo particles [57].

Finally, benchmarks HER and OER catalysts were used, namely Pt/C 10 wt.% (E-Tek®, Vulcan XC72 carbon black substrate) and unsupported IrO_2 catalyst (99.99 % trace metals basis, Alfa Aesar®) [34,47,201,202].

II.1.2 Synthesis of the materials

The syntheses of the material studied in this PhD had been carried out by several colleagues from the LPCNO and the LEPMI.

Déborah De Masi and Irene Mustieles-Marin did the syntheses of $FeNi_3$ and $FeNi_3$@Ni nanoparticles (NPs) at the LPCNO. The syntheses paths are fully described in [172]. Briefly, unsupported $FeNi_3$ NPs were synthesized by the co-decomposition of two organometallic precursors: $Fe(N(Si(CH_3)_3)_2)_2$) (1 equivalent) and $Ni(iPr\text{-}Me\text{-}AMD)_2$ (5 equivalents, AMD=acetamidinato) under H_2 at 3 bars and T = 150°C for 24 h in the presence of palmitic acid, a stabilizer. The surface can be enriched with Ni through decomposition of 0.5 equivalents of $Ni(AMD)_2$ under H_2 at 3 bar and 50°C during 24 h in the presence of pre-formed $FeNi_3$ NPs in mesitylene. Thermogravimetric analysis (TGA) indicated a total metal content of 94% for $FeNi_3$ and 88% for $FeNi_3$@Ni, the rest being ligands (palmitic acid and toluene).

The $FeNi_3$@Mo NPs were synthesized by Alvaro Raya Baron at the LPCNO. These nanoparticles were prepared by deposition of Mo on previously-synthesized $FeNi_3$ NPs. Inside a glovebox, a Fisher-Porter bottle was charged with $FeNi_3$ NPs (70 mg), $Mo(CO)_6$ (26.4 mg, 0.1 mmol) and a stirring bar. Mesitylene was added (10 mL) and the mixture stirred at room temperature for 30 minutes, resulting in complete dissolution of $Mo(CO)_6$. The bottle was then pressurized with H_2 (3 bar) and stirred within a pre-heated oil bath at 150°C for 72 h. After cooling down to room temperature, palmitic acid (64 mg, 0.25 mmol), followed by $Mo(CO)_6$ (105.6 mg, 0.4 mmol), were added to the reaction medium. The mixture was stirred at room

temperature for 30 minutes, then pressurized with H_2 (3 bar) and placed in a pre-heated oil bath at 150°C for 72 h. It was allowed to cool down to room temperature while decanting with the assistance of a magnet, and the supernatant was removed. The remaining black powder was washed three times with toluene (10 mL) and dried under vacuum (69 mg). A total metal content of 81% was determined by TGA.

Then, different Ni NPs had been synthesized in different ways. At the LPCNO, Georgiana Dragomir-Maties prepared the Ni_{OGM}, OGM standing for organometallic. In a glove box, 136.5 mg (0.4 mmol) of $Ni[iPrNC(CH_3)NiPr]_2$ were dissolved in 6 mL of degassed mesitylene in a Fisher-Porter bottle. Then, 205 mg (0.8 mmol) of palmitic acid dissolved in 7 mL of mesitylene and 97 mg (0.4 mmol) of hexadecylamine dissolved in 7 mL of mesitylene were added under vigorous magnetic stirring. The Fisher-Porter bottle was pressurized with 3 bars of H_2 and heated at 150°C for 48 h under magnetic stirring. The NPs were recovered by magnetic decantation, washed with 3x5 mL of toluene and dried under vacuum. Ni NPs were obtained as a black powder in an Ar glovebox (*ca.* 20 mg). A total metal content of 86% was determined by TGA.

The Ni_{HI} (HI = Hot Injection), Ni_{polyol}, and Ni_{polyol}/ATO had been synthesized by Raphaël Chattot at the LEPMI. Their protocol is fully described in [203]. Pure unsupported Ni NPs were prepared using a slightly modified protocol of the PtNi NPs synthesis, referred to as the "hot injection" method, previously reported in [204]. Briefly, 575 mg of Ni(II) 2,4-pentanedionate (95%, Alfa Aesar®) and 736 mg of 1,2-tetradecanediol reducing agent (90%, Sigma-Aldrich®) were dissolved in a mixture of 120 mL dibenzylether (≥ 98%, Sigma-Aldrich®), 1.2 mL oleylamine (≥ 98%, Sigma-Aldrich®), and 1.2 mL oleic acid (tech. 90%, Sigma-Aldrich®). The mixture was first heated at 80°C under Ar flow for 30 min, then heated to 240°C. As soon as the targeted temperature was reached, 12 mL of a 1,2 dichlorobenzene

(99%, Alfa Aesar®) solution containing 7 mg of Pt(II) 2,4-pentanedionate (48%, Alfa Aesar®) was quickly injected in the reactor. Since Ni alone is not reducing under this reacting condition, a low Pt atomic fraction (0.8 at.%) was maintained in order to initiate the nucleation and growth of the Ni NPs (consequently, these Pt atoms are buried in the Ni NP core). The suspension was heated at 270°C and maintained under continuous stirring for 1 h. After cooling down, 120 mL of ethanol was added to the mixture; then, the product was collected by centrifugation, washed one time with toluene (Roth®, ≥ 99.8%) and 3 times with ethanol, and then freeze-dried. These NPs are noted Ni_{HI} hereafter.

A much easier and scalable approach to produce Ni NPs is offered by the polyol method. Here, 410 mg of Ni(II) chloride hexahydrate (Puratronic 99.995%, Alfa Aesar®) was dissolved in 200 mL ethylene glycol (Rotipuran® ≥ 99.9%, Roth). To induce the nucleation of Ni NPs, 2.5 mL of a 5.8 mM aqueous solution of Pt(IV) dihydrogen hexachloroplatinate hexahydrate was also added (resulting in an overall 0.8 at.% Pt content). The *pH* of the solution was set to 10 by dropwise addition of an aqueous 0.5 $mol.L^{-1}$ NaOH (Suprapur, Merck®) solution. The solution was heated to 160°C under Ar flow for 1 h. After cooling down, the product was collected by centrifugation, washed 3 times with ethanol, and then freeze-dried. It is noted Ni_{polyol} hereafter.

To support these latter NPs on antimony-doped tin oxide (ATO), 8 mg of Ni_{polyol} and 32 mg of SnO_2 aerogel doped with Sb (10 at.%) [205] were mixed in 40 mL toluene (thus targeting a total Ni mass fraction of 20 wt.% on ATO). The product was first sonicated using a SONOPULS HD 3100 series equipped with a MS73 titanium microtip (3 mm diameter) and operated at 33% amplitude for 20 min in an ice bath, then collected by centrifugation, washed 3 times with ethanol, and freeze-dried. It is noted Ni_{polyol}/ATO hereafter.

It has to be noted that all the particles were exposed to air when using them, so that they were all oxidized, at least in surface.

II.2 Electrochemical techniques

In this section, the two cells used to make water electrolysis are described, together with the different electrochemical techniques employed to characterize the materials.

II.2.1 Electrochemical cell & measurement techniques: example of the RDE

In order to study the electrochemical activity of the materials toward water splitting, the rotating disk electrode (RDE) setup has been employed. This RDE constitutes the working electrode on which happens the studied reaction (see Figure II.2 below). It is made of a motor capable to rotate from 400 to 10,000 revolutions per minute (rpm), at the tip of which is connected the WE; the latter is electrically connected to the potentiostat to measure its current and potential. Choosing the rotation speed allows to control the convection and the mass-transport of the reactive species around the WE (quasi-stationary conditions). No membrane is used in this configuration.

II.2.1.1 Cell and inks preparation

The electrochemical cell is composed of three electrodes. The WE, which is a mirror-polished glassy carbon rod embedded in a hollow cylinder made of Kel-f® (polychlorotrifluoroethylene, PCTFE - sustaining most chemical product), onto which a thin-film deposit of an ink containing the catalyst is made. This tip is screwed onto the RDE (Origatrod, Origalys®) and a gold wire enables electrical connection between the glassy carbon

tip and the RDE, which is connected to the potentiostat. The wire is not in contact with the electrolyte to avoid possible dissolution and contamination of gold cations [206]. The counter electrode (CE) was a Pt mesh for short-term experiments (intrinsic catalytic activity measurements) where no consequent dissolution and redeposition of Pt on the WE shall be expected [207]. For long-term experiment (durability tests), the Pt was replaced by a glassy carbon slab (Sigradur®), linked to the potentiostat through a gold wire, not immersed in the electrolyte either. Finally, a hydrogen reference electrode (REF, Gaskatel®) was used. Its stability was checked with a freshly home-made reversible hydrogen electrode (RHE) prior and after each measurement. The RHE is an ideal reference, the potential of which is considered to be 0 V independent on the *pH*. These three electrodes dipped in the alkaline electrolyte (1 mol.L^{-1} KOH aqueous solution, made from 99.98% purity KOH pellets, Alfa Aesar®). The current of the reaction flows through the WE and the CE, and not in the REF, so that this setup allows to measure a potential between the WE and the REF (and between the CE and the REF). This way, one can study the overpotential of the half-reaction happening on the WE, without being disturbed by the coupled associated half-reaction occurring at the CE. Besides, as no current flows through the REF, an accurate potential (not biased by induced current flow Ohmic drop) could be applied. Sometimes, a fourth electrode made of a Pt wire was dipped into the electrolyte and linked to the REF via a capacitor bridge of ~ 100 µF. It served as a low-pass filter to limit the high frequency electrical noise stemming from the LEPMI building [208]. The atmosphere was controlled by bubbling an inert gas (Ar 99.999% purity, Messer®), into the electrolyte at least 10 minutes before each experiment through a tube with a sintered glass at the end. This removes the dissolved O_2 and curbs the current contribution of the Oxygen Reduction Reaction (ORR) to the overall Faradaic current. The temperature of the electrolyte was controlled by a thermostatically-controlled bath (200F, Julabo®) and set at 25°C. Figure II.2 displays a picture of the RDE setup.

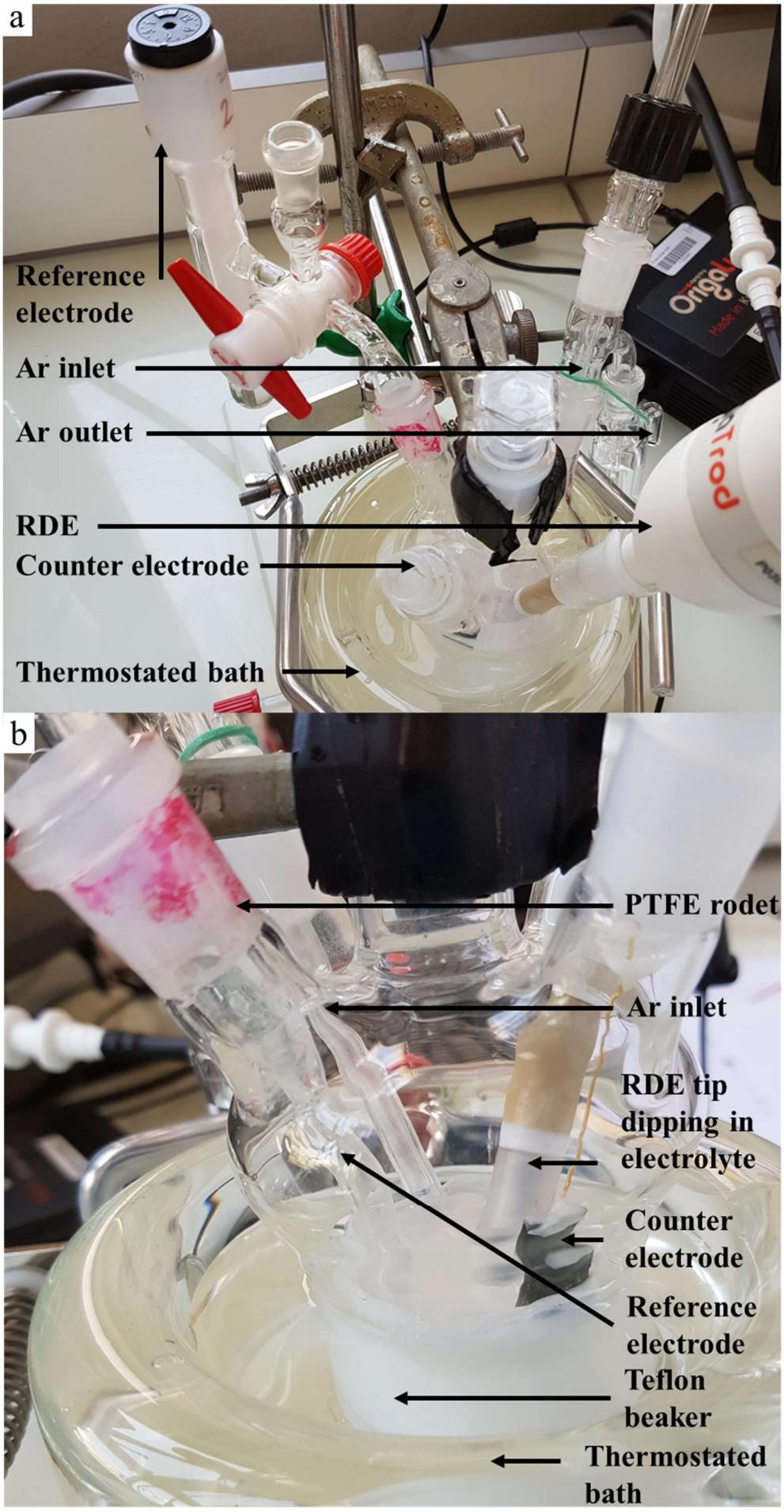

Figure II.2: (a) Rotating Disk Electrode (RDE) setup without the electrical connection (b) close-up of the setup near the electrodes.

As the oxidoreduction reactions are generally very sensitive to any contaminant, it is compulsory to clean properly beforehand all the constituents of the cell and to avoid at maximum any dissolution from the components. In that respect, prior to each measurement, the glass cell (Pyrex®, blown by Verre Equipements®) is immersed in home-made Caro's acid (H_2SO_5, mixture 5:2 of H_2O_2 and H_2SO_4) to remove any organic trace adsorbed on all surfaces, and then thoroughly rinsed with deionized (DI) water (18.2 MΩ.cm, Millipore®). As Pt is corroded by Caro's acid, the Pt mesh CE was pyrolyzed instead (in a butane/air flame) to remove any organic traces [209]. In addition, a previously cleaned in Caro's acid Polytetrafluoroethylene (PTFE) beaker (Teflon®) is placed inside the glass cell and used as an electrolyte tank: the electrolyte is poured in and the three electrodes dipped into it. This prevents the glass from being corroded by the KOH solution, which could be contaminated by Si, B, Al and Pb elements and could lead to distorted results [210]. Similarly, cylindrical sheets of PTFE (Roth®) are inserted around the contact of the electrode and the cell, to avoid KOH vapor from corroding the glass (see Figure II.2 (b)).

In order to characterize the electrochemical activity of the synthesized materials which are in a powder form, inks are elaborated under a nanohood. These inks are composed of a mixture 70:28:2 of DI water, isopropanol, and Nafion® 5 wt.% (Sigma Aldrich®). The isopropanol facilitates the ink homogenisation and shortens the drying time. The Nafion is a cation exchange ionomer which acts as a binder and provides a mechanical stability of the thin-film to the support [211]. A higher Nafion quantity enables higher mechanical stability, but implies a lower electrical conductivity and could block catalytic sites, due to its electron-insulating feature. As the electrical conductivity was a challenge point under AMF (see part II.3.2.1), an ionomer-over-support ratio in the [0.5; 5]% range was chosen. These values are generally seen in RDE studies of Pt supported on Vulcan® XC72 (electron-conductive carbon black) [212] or unsupported IrO_2 [213], which are benchmark HER and OER catalysts respectively, while being

far inferior to the 30% ratio used in PEMFC [214,215] and PEMWE [216,217]. It is worth noting that the aim of this PhD was not dedicated to the optimization of the ink formulation. It was preferred to set the different ratio of the three components, and maintain this ratio while changing the amount of catalyst to vary the loadings. Dispersion and mixing of the inks were realized with an ultrasonic bath (34 kHz, S10 Elma®) for ~ 10 minutes after ink creation.

Inks are then deposited on the glassy carbon RDE tips, thoroughly polished beforehand in order to obtain a mirror-polished surface, considered as a model surface of 0.196 cm^2 (5 mm diameter glassy carbon rod). Mechanical polishing was firstly performed with different silicon carbide disks (Presi®) from high to low grain size: from 800 to 1600 and 2400 $grains.inch^{-2}$. Between each mechanical polishing step, the tips were cleaned in an acetone bath, sonicated during 5 minutes to remove any abrasive grains. Then, the tips were manually polished with diamond pastes (Presi®) with three grain sizes: 6, 3 and 1 µm. The cleaning was composed of a sequence of sonication in three baths: acetone – ethanol – DI water, each for a duration of ~ 10 minutes.

Spin-coating was employed as deposit method. It consists of making a deposit on a rotating RDE tip, wait till the drop flattens and then dry the deposit with a hot hair-dryer to obtain a thin-film deposit, according to the methodology developed by Garsany *et al.* [218,219,220]. Sonication from 10 seconds to ~ 3 minutes maximum were applied before deposition. The sonication time is an important parameter as it could imply catalyst modifications due to cavitation and sonolysis phenomena [221,222]. However, in this study, low frequency, power and duration of sonication were used, and no catalyst modification had been observed.

The electrochemical tests were conducted thanks to two potentiostats: a Biologic® VMP3 at the LEPMI for electrochemical experiments without AMF exposure and under SMF,

and a Biologic® VSP-300 at the LPCNO for tests under AMF. Prior to each test an Ohmic drop *iR* measurement at high frequency (100 kHz) was determined. This resistance accounts for the electrical resistances (contact, resistivity of the wires), and the conductivity of the electrolyte (*cf* I.2.1). An 85% compensation of this Ohmic loss is dynamically applied to all techniques. A higher compensation is not recommended to avoid faulting the device. Typical values of *iR* were comprised between 1 and 10 Ω, depending on the cell used.

Hereafter are presented the electrochemical techniques which have been employed.

II.2.1.2 Cyclic Voltammetry (capacitive/Faradaic current, electrochemical surface area and Tafel analysis)

A lot of phenomena could occur at an electrode interface. The region close to the electrode surface is composed of two domains. The closest one corresponds to a compact layer of solvated species and is called the inner Helmoltz layer (~ 0.3 nm). The next one corresponds to a more diffuse layer of the species, and is called the outer Helmoltz layer (~ 0.1 µm, called the Debye length) [223]. Phenomena of charge accumulation/depletion in the double layer result in a current called the capacitive current. This latter is distinguished to the Faradaic current, which corresponds to the current of the studied reactions, like HER and OER for water electrolysis, where electroactive species are consumed/produced at the electrode surface. Probing potential windows where no Faradaic current occurs allows to record the capacitive current: one can see positive (anodic) or negative (cathodic) current peaks/hills characteristic of the phenomena happening in the vicinity of the electrode (like hydrogen desorption/adsorption for instance). Depending on the catalysts, the medium and the scan rate, the current peaks occur at different potentials. Thus, the cyclic voltammetry (CV) profiles of capacitive currents correspond to the electrochemical signature of a material, at least if no

Faradaic reaction compromises the measurement. On the contrary, probing the potential windows where the studied reaction happens allows to evaluate the intrinsic activity and extract kinetics information of the catalyst used.

Parameters and CV profiles corresponding to capacitive currents will be first described (and noted CV_C hereafter), before ones corresponding to Faradaic current (noted CV_F hereafter). An important parameter is the scan rate s ($mV.s^{-1}$). Varying s changes the electric field applied on the electrode surface, and forces the phenomena happening in the double layer to occur slower or faster with more or less species. A fast scan rate (100 $mV.s^{-1}$) triggers a high capacitive current and allows to clean the electrode from impurities, revealing the characteristics of the electrode surface. At slower scan rate, 20 $mV.s^{-1}$, the capacitive current decreases and the profiles can be biased by Faradaic or capacitive reactions involving electrolyte impurities, but slow processes are better witnessed. To evaluate the capacitive current of the studied materials, three potential regions were chosen: $[-0.2; 0.5]$ V_{RHE} corresponding to the HER onset region, [1.2; 1.6] V_{RHE} corresponding to the OER onset region, both zones being interesting for (Fe)Ni-based metals, and the [0.05; 1.2] V_{RHE} zone corresponding to the stability zone of Pt/C. After *iR* determination and before each WS activity measurement, between 5 to 10 CV_C cycles at 100 $mV.s^{-1}$ followed by 3 to 5 CV_C cycles at 20 $mV.s^{-1}$ were realized (cycling was run until the cycles superimpose). In particular, this pretreatment enables to evaluate the surface oxidation state of the catalyst employed, to stabilize it, and to clean its surface from adsorbates in order to have a similar initial state for all the thin-films of the same catalyst ink.

Taking the case of a Ni electrode as an example, Figure II.3 presents the CV_C of initially metallic Ni in 0.5 $mol.L^{-1}$ KOH at 100 $mV.s^{-1}$ and $T = 293$ K. The experimental conditions are chosen so that Faradaic reactions are not favoured (pure electrolyte, potential range restricted

to the capacitive region: minimal intrusion in the HER region below 0.05 V_{RHE} and the OER region above 1.5 V_{RHE}). Cycling at a potential below 0.5 V_{RHE} leads to the formation and reduction of the α-$Ni(OH)_2$ oxides from metallic Ni (red curve), a reversible process as long as the potential is not scanned above 0.5 V_{RHE}. When potentials higher than 0.5 V_{RHE} are experienced, irreversible phase transition from α-$Ni(OH)_2$ to β-$Ni(OH)_2$ and NiO formation proceed: no reduction peak in [0.5; 1.1] V_{RHE} is visible, while the positive current increases slightly in [0.5; 1.4] V_{RHE} – blue and black curves. Above 1.2 V_{RHE}, the β-NiOOH phase is formed and then reduced. After ten cycles, the thickness of the β-$Ni(OH)_2$ increases and masks the α-$Ni(OH)_2$ formation/reduction. In this PhD work, the Ni-based materials studied were all too oxidized to clearly observe the α-$Ni(OH)_2$ peaks below 0.5 V_{RHE} (see section III.2.1.2 on the durability of the materials). This set of CV_C peaks gives information about the surface roughness and electrochemical surface area of the electrode, as explained below.

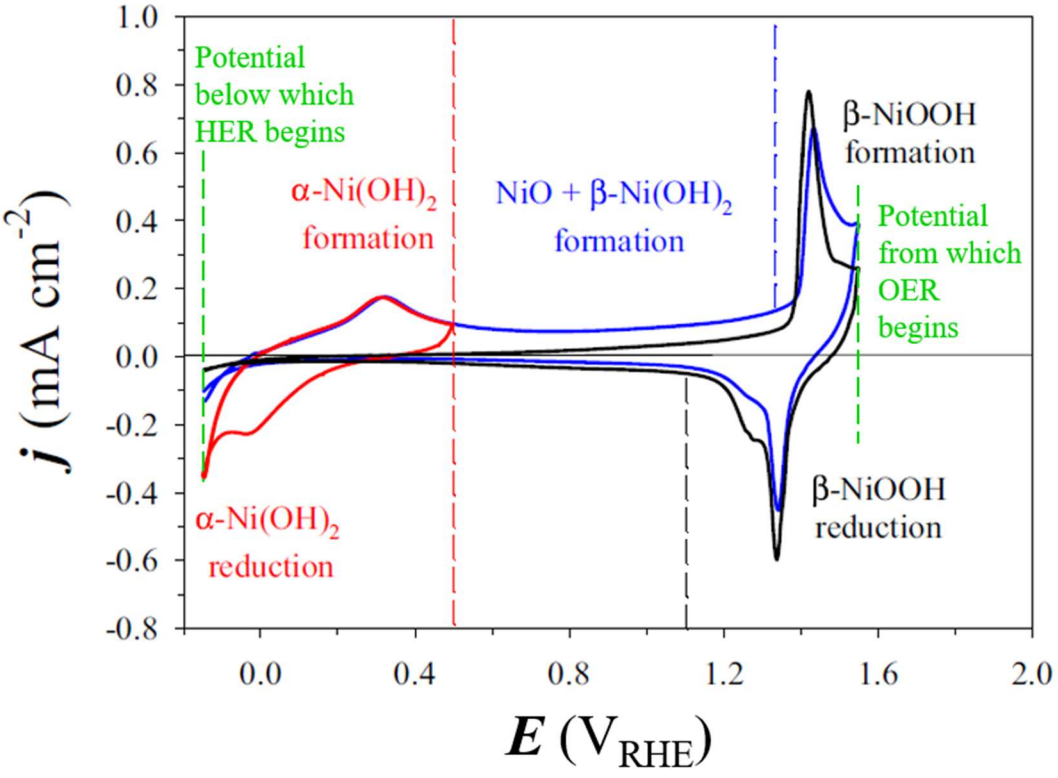

Figure II.3: CV_C of Ni(poly) electrode in 0.5 $mol.L^{-1}$ KOH obtained at 100 $mV.s^{-1}$ and room temperature. The red curve covers the [−0.15; 0.5] V_{RHE} potential range, while the blue and black curves correspond to the first and tenth cycle of the [−0.15; 1.55] V_{RHE} potential range. The dashed green lines indicate the potential from below which the HER starts (left) and above which the OER starts (right). Reprinted from [224] with permission from Springer.

The electrochemical active surface area (ECSA) can be estimated from CV_C. As the water electrolysis reactions are surface reactions, meaning that they occur on active sites on the catalyst surface, it is interesting to increase the surface area of the electrode so as to increase the number of active sites. One way is to increase the surface roughness. This one is defined by the ratio of the ECSA by the geometrical surface area of the support. The ECSA corresponds to the surface which takes part in the oxidoreduction reactions, *i.e.*, the surface occupied by the catalyst sites, compared to the geometrical surface. Thus, it is important to measure the ECSA as not all the sites are available and reactive.

Many techniques have been studied to measure the ECSA [225]. A classical method, used for the ORR on Pt catalyst for instance [226], is to integrate the charge resulting from the adsorption of a single monolayer of CO on the catalyst surface, assuming that one CO molecule adsorbs on one Pt active site. Then the charge is divided by the scan rate ($mV.s^{-1}$) and the specific charge (in $\mu C.cm^{-2}$ - charge density associated to the adsorption of one monolayer of species) to get the ECSA (in cm^{-2}). A similar methodology could be applied to the formation of α-$Ni(OH)_2$ assuming a specific charge of 514 $\mu C.cm^{-2}$ [227,228]. However, this technique considers only the metallic Ni sites, so that the surface fraction covered by stable oxides (β-NiOOH or NiO, see Figure II.3) is not taken into account, and the ECSA is then under-estimated if the sample is initially (partly) oxidized [229]. As said above, the Ni-based catalysts studied herein were all in an oxidized initial state (see section III.2.1.2), so that this method is questionable. Use of X-ray photo-electron spectroscopy was proposed to estimate the amount of oxidized species and apply a correcting factor to the ECSA [230]. However, the XPS measurements were *ex situ*, so that the oxidation degree of the Ni catalyst is likely to change during the transfer to the XPS chamber due to of air contact. So, *in situ* measurements are necessary, and were not possible at LEPMI. Using the α-$Ni(OH)_2$ reduction peak is not relevant because it generally overlaps with the HER current, leading to uncertainties in the charge integration (the same issue

arises for the anodic Ni^{2+} to Ni^{3+} transition with OER Faradaic current). Another technique employed is the double layer capacitance C_{DL} determination by electrochemical impedance spectroscopy (EIS) or CV_C at different scan rates. C_{DL} is proportional to the amount of species in the double layer. Compared to a tabulated specific capacitance C_S characteristic of the studied material, one can get the ECSA value from the C_{DL}/C_S ratio [231]. However, discrepancies among the specific capacitance were obtained, and no tabulated C_S value was found for the FeNi-based material studied herein. Other techniques have been developed [232,233], but were not easy to implement. Therefore, determining an accurate value of the ECSA is very challenging. Eventually, in the case of this work, it was chose to integrate the area under the anodic peak of α-$Ni(OH)_2$, assuming a specific charge of 514 $\mu C.cm^{-2}$ in the HER side, and to integrate the area under the cathodic peak of Ni^{3+} to Ni^{2+}, assuming a specific charge of 257 $\mu C.cm^{-2}$ in the OER side. This value serves as a reasonable "universal accepted standard" to evaluate the oxidized part of Ni-based catalysts [191,229,234,235]. It has to be noted that this value was only used to compare $FeNi_3$(@Ni) catalysts between them, and not with the literature. Indeed, the value of 257 $\mu C.cm^{-2}$ corresponds to a Ni surface only (not with Fe). It was used here as a reasonable value since the CV_C and the XRD data of FeNi-based catalysts were very similar to Ni's ones.

Two potential windows were probed to evaluate the electrochemical activity toward HER and OER: CV_F from 0 to maximum -1 V_{RHE} for HER and from 1 to maximum 2 V_{RHE} for OER. Mass-transport has a marked influence on the overall performances as these reactions consume/produce species from the electrolyte, so that the Faradaic current is limited by the diffusion of these species toward/from the electrode. The rotation of the RDE was set to ω = 1600 rpm. This value was chosen to permit the comparison of current densities of the catalysts studied herein with those published in the literature, where ω = 1600 rpm is generally chosen. Indeed, the mass-transport is optimized at this revolution rate [236]. The scan rate of these CV_F is chosen generally low from 5 to 10 $mV.s^{-1}$, to limit the capacitive current and observe accurately

the Faradaic contribution. Too low scan rates (1 $mV.s^{-1}$) are likely to create a bubble poisoning effect and active layer detachment [237]. Figure II.4 displays typical CV_F curves of $FeNi_3$@Ni catalyst, in the HER and OER regions, made with the RDE setup.

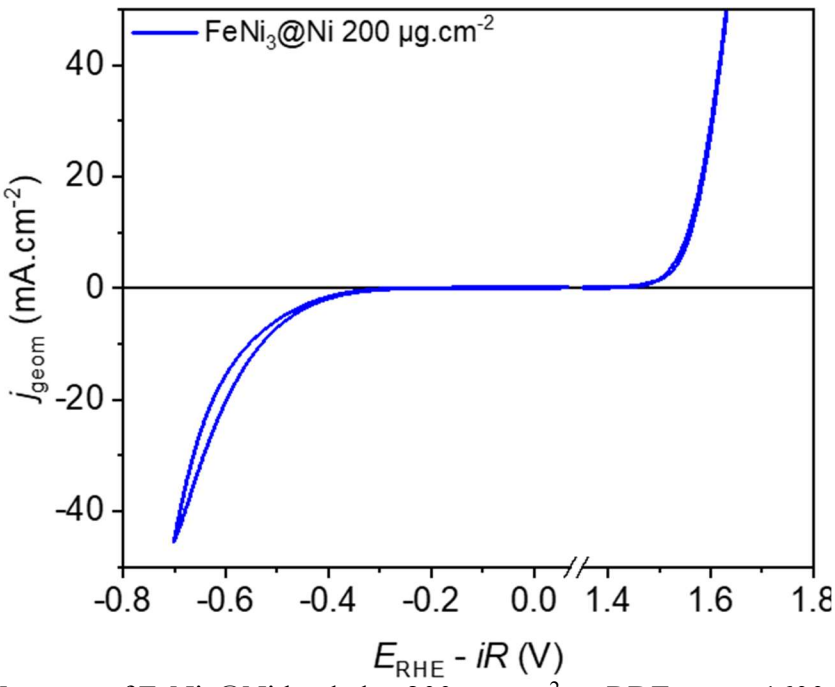

Figure II.4: CV_F curve of $FeNi_3$@Ni loaded at 200 µg.cm^{-2} on RDE setup: 1600 rpm, scan rate: 5 $mV.s^{-1}$, in KOH 1 $mol.L^{-1}$, T = 25°C, corrected from Ohmic drop iR.

The increase of the absolute value of the current corresponds to HER at low potentials and OER at high potentials. From this curve, one can note the overpotential at a certain current density j. Generally, 10 $mA.cm^{-2}$ is used to evaluate the catalytic performance of a new material. This criteria comes from the current density expected in an integrated solar-to-fuels device operating at 10% efficiency under one sun illumination [231,238]. Besides, by plotting $\log|j|$ versus the overpotential η, one can have access to intrinsic kinetic parameters of an electrochemical reaction. It is based on the Tafel equation stemming from simplified Butler-Volmer equation (Eq. II.1), assuming electron-transfer control around the standard potential of an oxidoreduction couple [239]:

Butler-Volmer $$j = j_0(e^{+\alpha\frac{\mathcal{F}}{RT}\eta} - e^{-(1-\alpha)\frac{\mathcal{F}}{RT}\eta})$$ II.1

with j the current density, j_0 the exchange current density associated with a reversible electrolysis reaction, $\alpha \in [0; 1]$ the charge-transfer coefficient (CTC) characterizing the kinetics of a half-reaction, $\alpha = ½$ = indicates that the kinetics of one half-reaction is the same for the oxidation and the reduction. $\eta = E – E°$ the overpotential at the studied electrode. This equation is theoretically for one elementary step, but is also applied for half-reactions. By assuming a large positive overpotential at the anode (which is the case for WS), the Butler-Volmer equation simplifies and the use of the logarithm leads to the Tafel equation, Eq. II.2:

Tafel equation $$\eta = a + b \log|j|$$ II.2

with $a = -\frac{2.3RT\, log(j_0)}{\alpha\mathcal{F}}$ and $b = \frac{2.3RT}{\alpha\mathcal{F}}$.

This equation indicates that a higher current density induces a higher overpotential. In electrocatalysis, one is looking for material with high exchange current density (a high) and low Tafel slope (b low). The determination of the Tafel slope gives insights about the rate determining step for a half-reaction and its mechanism thanks to the CTC parameter. Indeed, let's consider the different elementary steps of the HER [240] and OER (while the OER elementary steps on Ni are debated [33,241], the commonly accepted steps are presented herein):

HER	$H2O + e^- + M^* \rightleftharpoons M\text{-}Hads + HO^-$ (Volmer step)	II.3
	$H2O + e^- + M\text{-}Hads \rightleftharpoons H2 + HO^- + M^*$ (Heyrovsky step)	II.4
	$2\ M\text{-}Hads \rightleftharpoons H2 + 2\ M^*$ (Tafel step)	II.5
OER	$M^* + HO^- \rightleftharpoons M\text{-}OHads + e^-$ (Volmer step)	II.6
	$M\text{-}OHads + HO^- \rightleftharpoons M\text{-}Oads + H2O + e^-$	II.7
	$M\text{-}Oads + HO^- \rightleftharpoons M\text{-}OOHads + e^-$	II.8
	$M\text{-}OOHads + HO\text{-} \rightarrow M\text{-}OO\text{-}ads + H2O$	II.9
	$M\text{-}OO^-ads \rightleftharpoons M^* + O2 + e^-$	II.10
Or from II.8	$M\text{-}Oads + M\text{-}Oads \rightarrow M^* + O2$	II.11

With M* being an available catalyst site. When is considered the X^{th} elementary step, α is replaced by (n+α), n being the number of transferred electrons before the X^{th} step. Thus, if the rate determining step involves one electron transfer with a CTC of 0.5, and if the overall reaction presents a Tafel slope of $2RT/\mathcal{F}$ ~120 mV at 298 K for n = 0, the studied reaction could be the HER Volmer step (II.3), or if $2RT/3\mathcal{F}$ ~ 40 mV for n = 1, the reaction could be the HER Heyrovsky step (II.4). If the rate determining step involves zero electron transfer with the CTC of 0 (HER Tafel step II.5), the overall reaction displays a Tafel slope of $RT/\mathcal{F}$ ~ 60 mV for n = 1, or $RT/2\mathcal{F}$ ~ 30 mV for n =2.

In order to have solid CTC values, the CV must be obtained in near-steady state conditions, so at low scan rate and with a properly-controlled mass-transport (*e.g.* using an RDE setup, with $\omega \neq 0$). However, even at 1 $mV.s^{-1}$, the current is not a true steady-state current. In addition, appropriate fitting assumes that the ($\log|j|$ *vs*. η) plot is linear, which means that mass-transport and Ohmic drop are not (at all) limiting, which is not perfectly true in practice, even less for WS reactions (the evacuation of bubbles induces biases). While this method seems very powerful, the Tafel slope determination on the plot could vary a lot. Another complementary method is by EIS, which consists of applying an alternating potential to an electrode and measure the dynamic current response, being characteristic of the phenomena occurring in the double layer (diffusion, adsorption, charge transfer). Nyquist plot of EIS were plotted, but the obtained CTC values suffer from huge discrepancies [241], making its credit questionable. This method was nonetheless tried one time qualitatively (see section IV.2.2).

II.2.1.3 Chronopotentiometry and chronoamperometry

Two other electrochemical methods had been used for the experiments under AMF and under SMF. The first one is the chronopotentiometry (CP) technique, where a constant current

is applied, and the potential of the WE and the CE are recorded. In this case, the reaction regime is set, *i.e.* the number of consumed/produced species per unit surface area and time. The slope of the concentration profile at the interface for different time of the experiment is constant and, assuming constant the internal resistance of the cell during the measurement, it leads to constant (hence easily corrected) Ohmic drop. This method was a very direct and readable technique to see the effect of the application of an AMF/SMF on the overpotential at a given current and was thus often employed (Figure II.5 gives an example for the OER side).

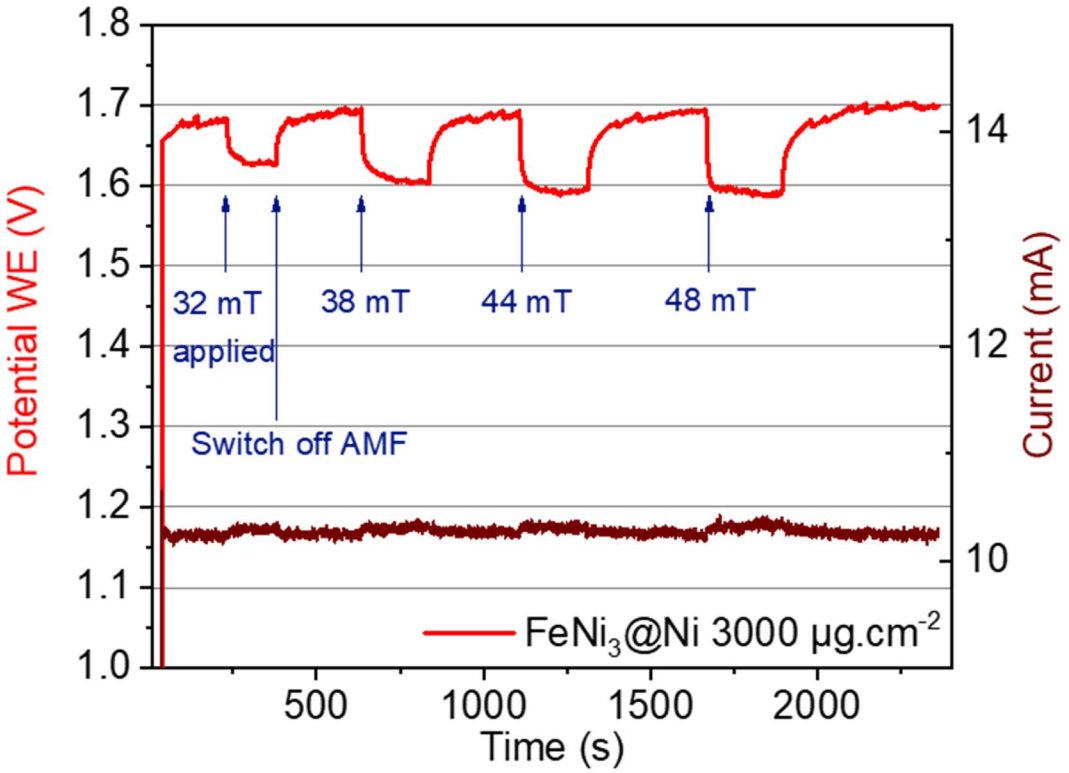

Figure II.5: Chronopotentiometry measurement at i = 10 mA (j_{geom} = 10 mA.cm^{-2}), with FeNi$_3$@Ni catalyst loaded at 3000 µg.cm^{-2}, OER side under different AMF values.

In Figure II.5, applying an AMF triggers an immediate decrease of the WE potential, and the drop increases with the MF amplitude increase. Note that under AMF, the potentiostat was sometimes biased by the AMF (in Figure II.5, the current applied was ~ 10.3 mA, while the targeted value was 10 mA), but the difference was always small enough to be considered non-impactful on the final result.

Another used technique was the chronoamperometry, where a potential is applied, and the current is recorded. This method was especially employed for the estimation of the efficiency of the system. Indeed, in this case, the amount of reactive species is not set, and the Faradaic current can increase or decrease under AMF exposure. More or less hydrogen (oxygen) can then be produced, and the different quantities measured to estimate the added efficiency due to AMF activation. Figure II.6 depicts a typical WE measurement for the HER: the current under AMF jumps to higher absolute values, indicating a higher H_2 production rate.

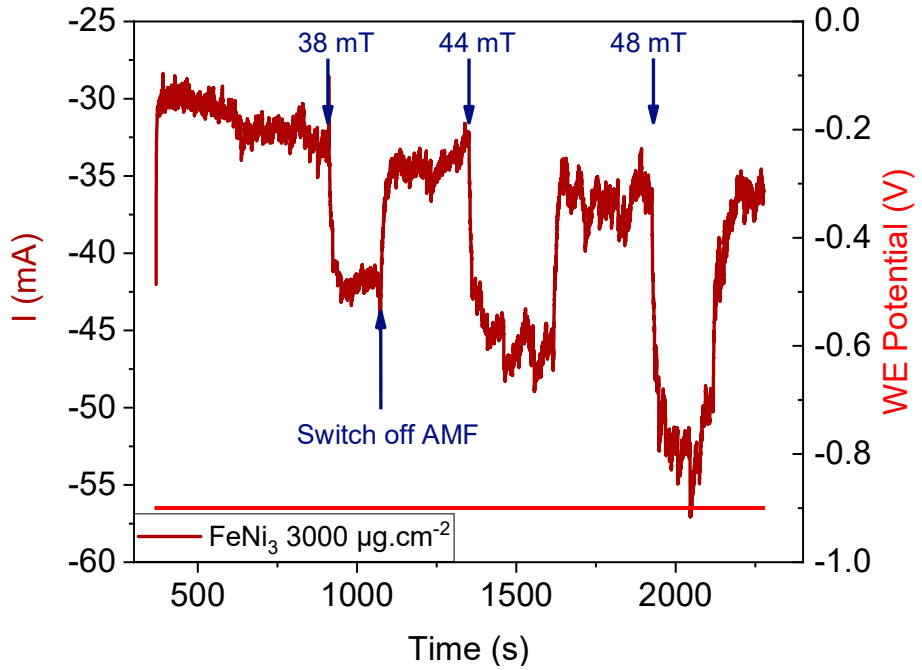

Figure II.6: Typical chronoamperometry measurement at −0.9 V_{RHE} on $FeNi_3$ at 3000 µg.cm^{-2}, HER side under AMF.

II.2.1.4 Accelerated stress test

Finding active catalysts toward the WS reaction is a prerequisite, but characterize their stability is necessary also. Potentiodynamic accelerated stress test (AST) were used to simulate the non-constant operation of an electrolyser occurring with a renewable energy source coupling [242]. It consists of alternating constant voltage steps between two values, during 3 s for each value (an AST cycle lasts 6 s). For the HER AST, potentials at −0.7 and 0 V_{RHE} were

applied, while for OER AST, potentials at 1.2 and 1.6 V_{RHE} were applied. 5000 cycles were made, and characterization measurements were made (CV_C and CV_F) after 200, 500, 1000, 2000 and 5000 cycles. Also, after each of these measurements, an electrolyte sample of 1 mL was extracted to measure by inductively coupled plasma mass spectrometry the amount of catalyst potentially dissolved in the electrolyte. No fresh electrolyte was added to the medium to keep a constant volume as the extracted sample volume was small with respect to the electrolyte's one (85 mL). A typical AST measurement is displayed on Figure II.7, for the OER.

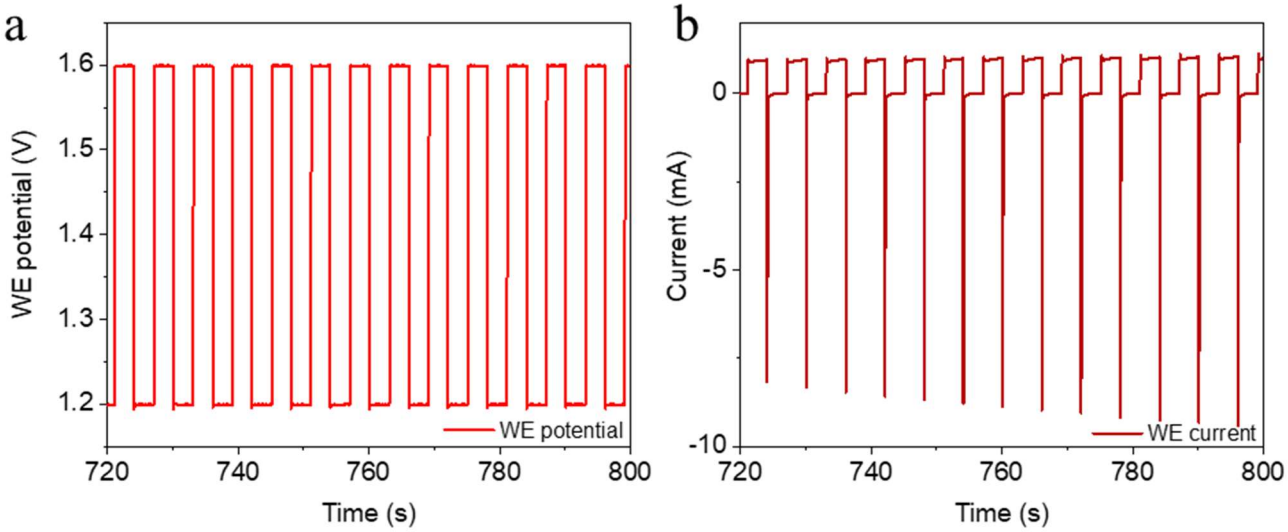

Figure II.7: Typical OER AST measurement on $FeNi_3$ 100 µg.cm^{-2}, with (a) the potential steps at 1.2 and 1.6 V_{RHE} and (b) the current response in function of the time. Electrolyte: KOH 1 mol.L^{-1}, under Ar atmosphere, at 25°C, RDE at 1600 rpm.

AST were performed on Ni_{HI} and $FeNi_3$(@Ni) catalysts. ECSA determinations were realized on these three catalysts in HER and for $FeNi_3$(@Ni) catalysts in OER. The HER ECSA was nevertheless difficult to determine, as it corresponds to the metallic part of the catalysts, while the studied ones were very oxidized.

To summarize, the RDE has been widely used to study the intrinsic activity of the catalyst as it is a rapid method. However, it suffers from limitations. Indeed, the operating conditions are far from industrial fuel cell and water electrolyser systems: in RDE, there is generally no membrane used and the current densities are usually kept low to avoid hindrances

by bubbles generation (~ 100 mA.cm^{-2} maximum, while AWE work at 300 mA.cm^{-2} [36]), even though bubbles' coverage is an issue as soon as j > 10 mA.cm^{-2} [237]. In addition, the forced convection applied (rotation) does not necessarily match with the industrial devices, and most of all, it is practically impossible to apply an AMF on an RDE cell. Gas Diffusion Electrode and Floating Electrode, displaying conditions closer to industrial devices and increasingly used at the lab scale [243,244,245,246] are themselves not compatible with AMF characterizations. For these reasons, dedicated flow cells were developed.

II.2.2 Use of a specific cell designed for measurements under AMF

Applying an AMF on an electrochemical system triggers lots of issues. Specific cells had to be designed to enter into the 300 kHz and 100 kHz coils used for tests under AMF.

II.2.2.1 Cell designed for the 300 kHz coil

The first cell was designed to study the magnetic heating due mainly to hysteresis losses (not by eddy currents), and was the one used by Christiane Niether. The chosen material for the cell (Figure II.8 (a)) was the poly(methyl methacrylate) (PMMA, machined by Technico-Plast®) as it resists concentrated KOH electrolytes, is easy to machine and is transparent, so that the bubble formation is visible, and surface temperature measurements with an infrared camera are rendered possible. Under AMF, eddy currents are nevertheless created and dissipate through Joule effect in the current collector wire and the support. Moreover, hysteresis losses increase the sample temperature. So, an electrolyte convection was applied to cool the system, and was beneficial to remove the nucleated bubbles also. The choice of the flux rate is given below. The support for the catalyst is a carbon felt disk of 16 mm diameter (Ø) and 410 µm thickness (Optiveil 20301A, University of Reading, NCBE®). The support is placed at the centre of the cell, located at the middle of the coil where the magnetic field is the more homogeneous, and

maintained thanks to a silicon seal. The carbon felt was chosen because it does not heat too much (and neither burns) under AMF, compared to other tested supports such as Ni felt/grid/foam, gold sheet and Pt plate (see Supplementary Figure 4). The advantage of heating less leads to a drawback: a lower electrical conductivity ($<\sigma_{elec}$ (carbon felt)$>$ ~ 500 $S.m^{-1}$). Gold and silver capping of different thicknesses were tested to improve the conductivity, but were likely to dissolve and contaminate the solution. A gold wire of Ø = 200 µm diameter was placed under the carbon support to connect the WE to the potentiostat. Several shapes of this wire were tested: a single strand, two twisted strands with a final fork shape and two twisted strands with a final rake shape. A picture of the different current collectors is given in Figure II.8 (c-e). The idea of increasing the number of strands in contact to the carbon felt was to improve the electrical contact. However, it could create more eddy current loops and spark more Joule heating. Nevertheless, the rake shape was finally chosen as it led to much reproducible results. The diameter is a compromise between having a sufficient electrical contact and avoiding the skin effect (the skin depth is 137 µm at 300 kHz, leading to Joule heating). A lower wire diameter like 125 µm < 137 µm was commercially available, but too fragile for practical current collection. The CE was a carbon felt (plain Toray paper TGP-H-120, E-Tek®), connected to the potentiostat via the same gold wire, made of two twisted strands, sewn in the Toray paper (Figure II.8 (b)). The CE is located outside the coil (at a distance of ~ 3 cm above) so that no magnetic effect (especially heating) is triggered at the CE, allowing to study solely the AMF influence at the WE. A luggin capillary located at 1 cm from the WE enables the ionic connection with a Gaskatel® reference RHE. The reference was delocalized via a Luggin capillary to avoid any noise creation due to electromagnetic waves sparked by the AMF. The cell is closed thanks to 4 Nylon screws at each corner of the cell, and sealed with a glue gun. No contamination from the glue had been observed for all experiments.

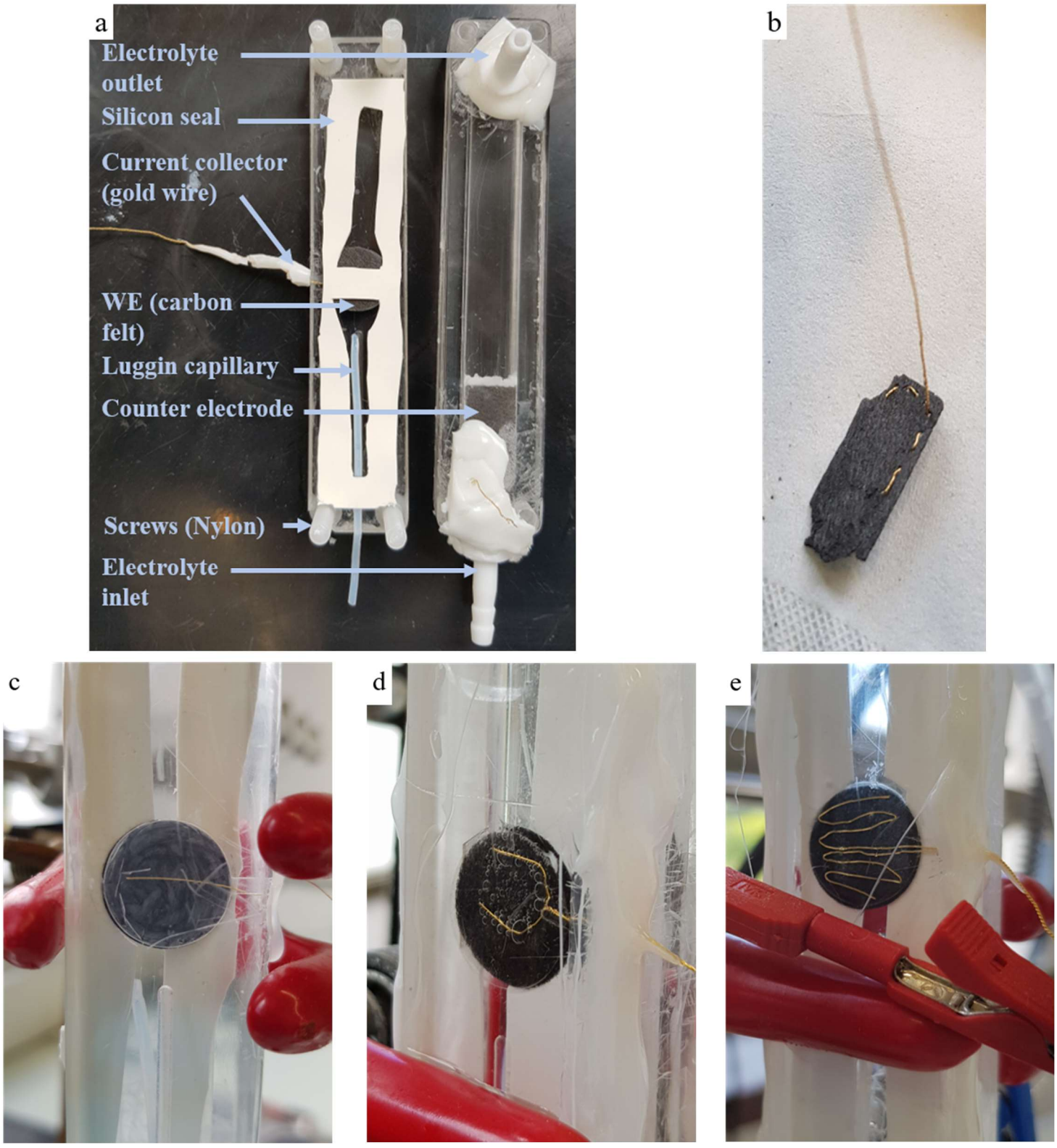

Figure II.8: (a) PMMA cell (b) Counter-Electrode with the sewn gold wire electrical contact (c), (d), (e) the carbon felt working electrode with the single, fork and rake shape gold wire current collector, respectively.

Besides, the PMMA cell with carbon felt WE with the ink deposit was placed vertically inside the coil, so that the magnetic field was applied parallel to the WE surface, in order to minimize the eddy currents (Figure II.9). Indeed, the eddy currents are induced in the plane perpendicular to the magnetic field. One can refer to the elementary “right-hand rule” (Figure II.10) to get easily the eddy current loop plane and direction.

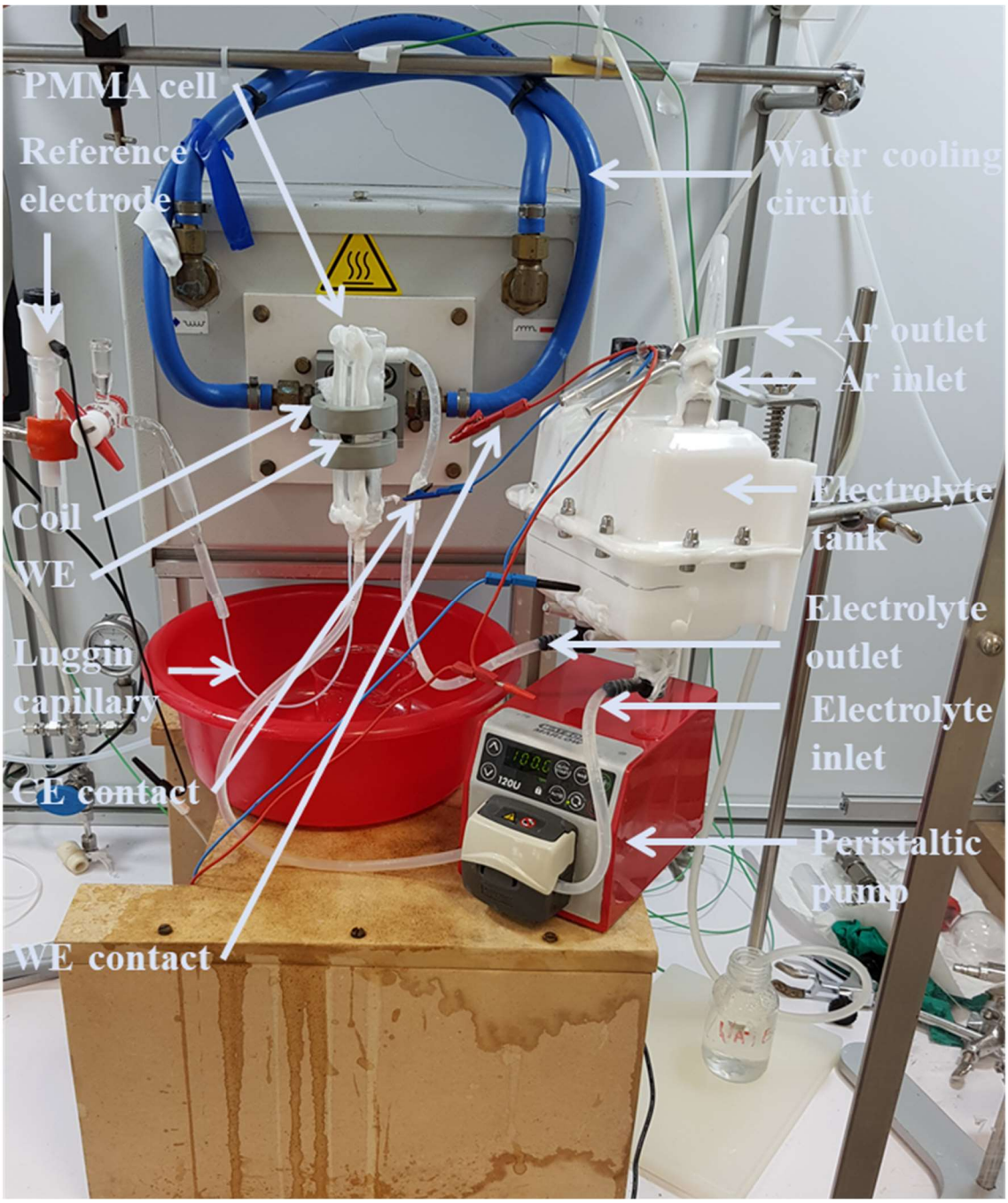

Figure II.9: Setup of the electrochemical test under AMF.

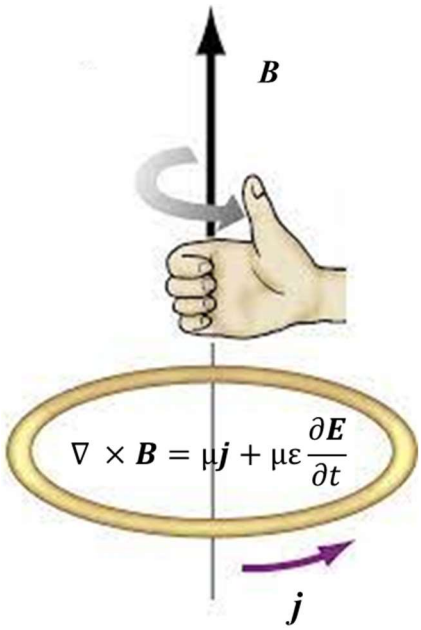

Figure II.10: Right hand rule illustration, with the fourth Maxwell law (Ampere's circuital law). The rotational of ***B*** gives rise to a current density ***j*** in the perpendicular plane of the ***B*** direction.

A peristaltic pump (120U, Watson Marlow®) was used to create an electrolyte flow. The flow has been chosen by calculating the necessary flow to cool down a sample which presents a temperature heating of ΔT = *3*°C in the coil under an AMF of 48 mT (as measured by Christiane Niether with an optic probe located on the surface of the working electrode in the cell filled with electrolyte [247]), with a condition of cell temperature elevation of 1°C. The power *P* generated by such heating is, Eq. II.12:

$$P = h\, S_{\text{sample}}\, \Delta T_{\text{sample}} \qquad \text{II.12}$$

The convection coefficient *h* of KOH was estimated to ~ 1000 $W.m^{-2}.K^{-1}$. The surface *S* of the sample was taken as the whole surface, not only the deposit area: $S_{\text{sample}} = 2*\pi*0.008^2 = 4.02\ 10^{-4}\ m^{-2}$. Thus, a power *P* of ~ 1.2 W is generated and has to be cooled down. The electrolyte flow is then calculated with equation II.13:

$$P = q_m \, c_p \, \Delta T_{condition} \qquad \text{II.13}$$

With c_p the calorific capacity of potassium hydroxide at 1 mol.L^{-1} considered as water: c_p (water, 28°C) = 4.18 kJ.kg^{-1}.K^{-1}. The necessary electrolyte flow q_m is thus ~ 17 mL.min^{-1}. A much larger value of ~ 85 mL.min^{-1} was chosen, to ensure proper cooling.

The inks used for the deposit are the same than the ones described in part II.2.1.1. The spin-coating deposit method had been adapted for the carbon felt. A small support was created to attach the carbon felt and allow its rotation (Figure II.11). 10 µL of ink was deposited at the center of the carbon felt, similarly as for the RDE setup. After one minute of rotation, the carbon felt was heated in an oven at 100°C during 4 minutes, and cooled down in air.

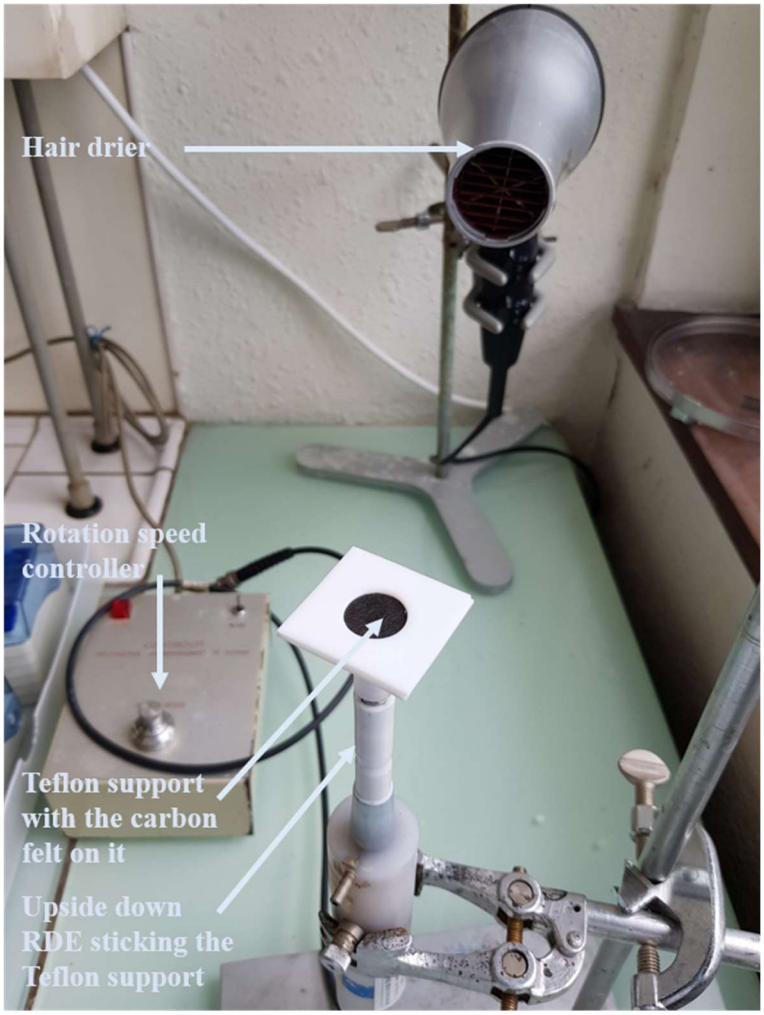

Figure II.11: Picture of the deposit setup for the carbon felt setup.

II.2.2.1 Cell designed for the 100 kHz coil

The second cell was designed to optimize the eddy current generation inside the working electrode, and to reduce the electric consumption of the coil by using an air-cooled coil with a smaller gap (3 cm inner diameter, 12 cm height, ID Partner®). Thus, the working electrode was placed horizontally in the cell, and was constituted of Ni foams of different thicknesses (1.0 and 1.6 mm), and a Ni felt, all of 6 mm diameter. A plain Toray paper was chosen as CE. A capillary allows the connection to the reference electrode (Figure II.12). No nanoparticle is used in this setup.

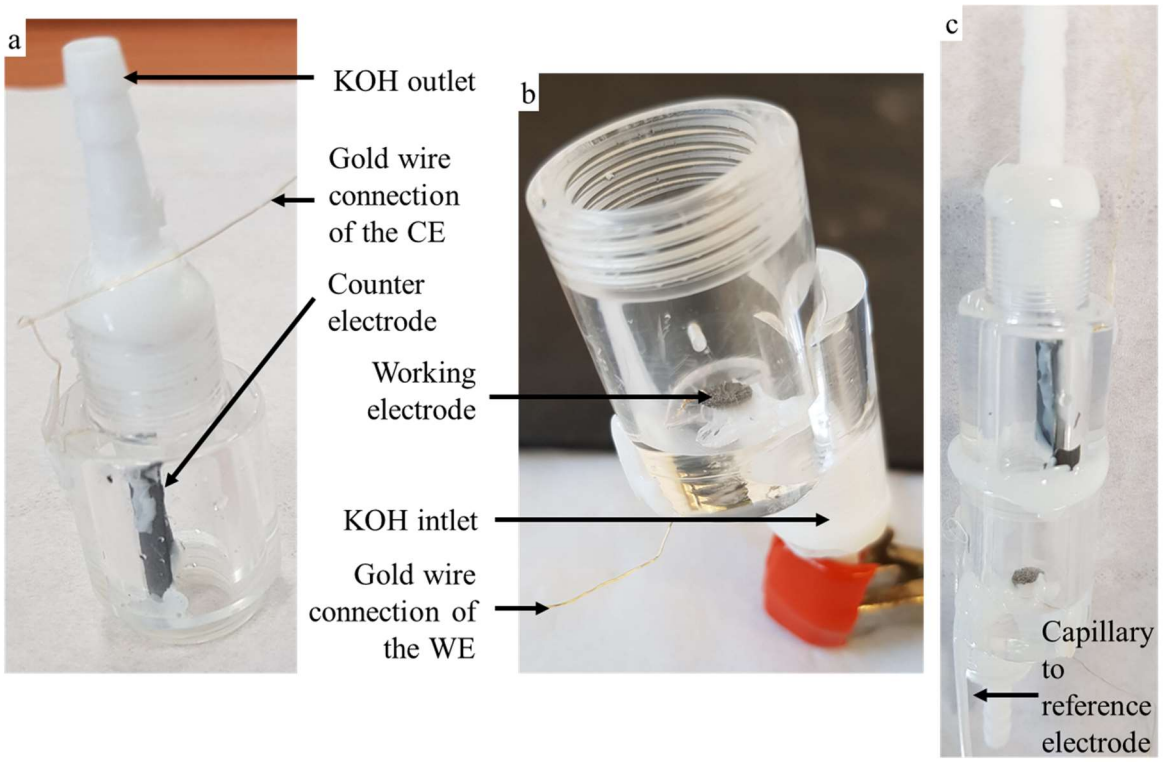

Figure II.12: Experimental setup of the cell designed for eddy current generation: (a) upper part of the cell, (b) lower part of the cell and (c) mounted cell. The working electrode is placed horizontally in the cell. The inner diameter of the cell is inferior to 3 cm to enter into the air-cooled coil.

The complete setup in the 100 kHz coil is displayed in Figure II.13.

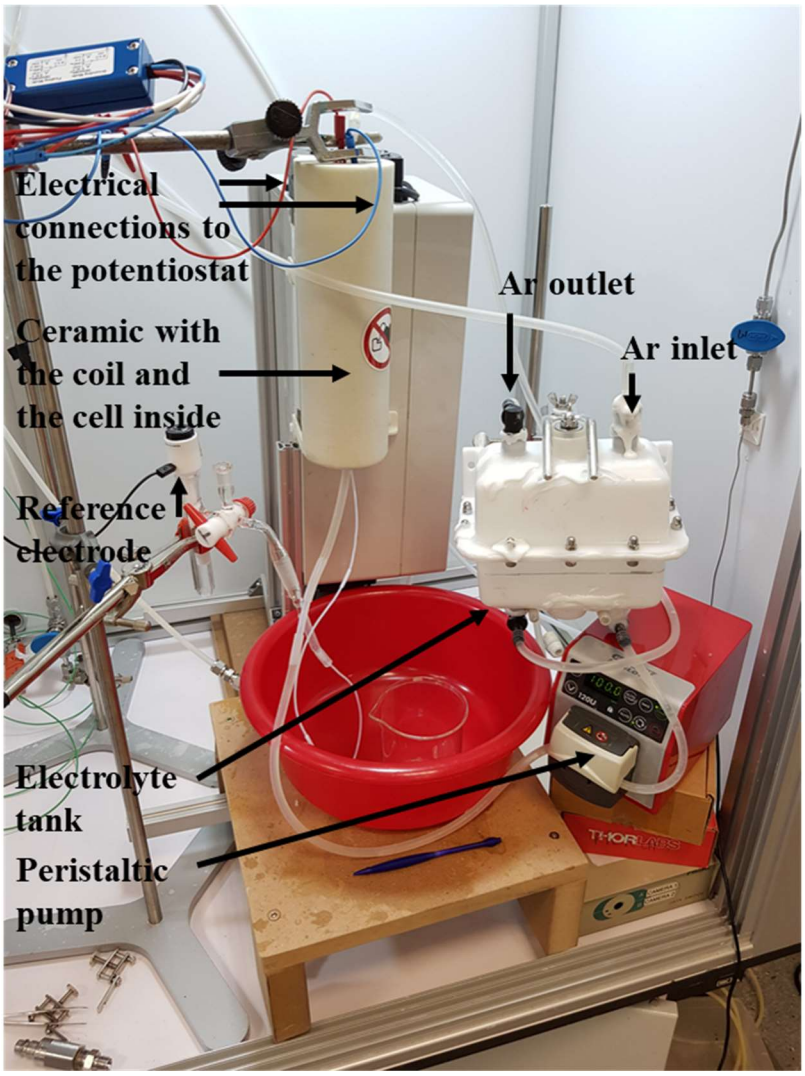

Figure II.13: Electrochemical setup in the 100 kHz air-cooled electrochemical setup in the 100 kHz coil water-cooled.

II.3 Physicochemical characterizations

In order to analyze and/or check the structure, the composition, and the shape of the catalyst and the carbon felt WE, several techniques were employed.

II.3.1 Microscopy techniques

II.3.2 Scanning electron microscopy

Scanning electron microscopy (SEM) allows to observe the topography of a sample surface. A thin electron beam is created under high vaccum by an electron gun and accelerated toward the sample thanks to a voltage between 0.1 and 30 keV. This beam interacts with the sample and ionizes electrons of the surface atoms of the sample. These electrons (called secondary electrons) are detected (either by an in-lense detector: chemical and topographic contrast or a side detector: topographic contrast) and shown on a screen. The number of collected secondary electrons depends on the surface variations. By scanning a surface, one gets the topography of the sample. Generally, SEM enables a magnification up to 10^5, with a resolution up to 10 nm, and a field depth up to ~ 1 mm at 10^3 magnification [248,249]. In this PhD, all the SEM pictures were imaged by Frédéric Charlot at the CMTC; a FEG SEM ULTRA 55 from Carl Zeiss operating at 3 keV was used in all cases. Typical pictures of SEM are given in section IV.4.1.

II.3.3 Transmission electron microscopy (TEM), Scanning TEM and Identical Location TEM (ILTEM)

The magnification of a SEM is not enough to properly image nanoparticles; so, the transmission electron microscopy technique can be employed. Similarly, an electron gun creates an electron beam directed toward the sample, but at a higher voltage (between 100 and

400 keV). Transmitted electrons through the samples are collected, (possibly treated to correct from the objective aberrations) and sent toward an imaging device [250]. The resulting contrast originates from local differences of thickness, atomic number or crystallinity of the sample. For TEM imaging, the sample has to be sufficiently thin (< 100 nm) so that electrons can go through. Thus, special grids designed for TEM devices are used to image nanoparticles. In this study, gold grids (Au, 300 mesh, Ted Pella®) composed of a carbon mesh stabilized by a carbon film were used. Its preparation is as follows: the grid is firstly cleaned with ethanol, dried with a precision wipe (Kimtech Science®) and a small drop of an ink is deposited onto it, and let dried in air. Marian Chatenet did the TEM pictures of FeNi-based, Ni_{HI}, Ni_{polyol}/ATO and Ni_{polyol} catalysts at the Laboratoire des Matériaux et du Génie Physique (LMGP, Grenoble-INP, France) with a LaB6 Jeol 2010 TEM, operating at 200 keV with a 0.19 nm resolution. The TEM pictures of the $FeNi_3$@Mo and Ni_{OGM} NPs were realized by Alvaro Raya Baron and Georgiana Dragomir-Maties respectively with two 100 kV JEOL microscopes, 1011 and 1400, working at 100 kV and 120 kV, respectively.

Some apparatuses are equipped with a magnetic lens system enabling to scan the surface of the sample. Scanning TEM (STEM) graphs of FeNi-based materials were performed by Pier-Francesco Fazzini using a Jeol 2100F- 200 kV microscope, equipped with a field-emission gun, which was operated at 200 kV (point-to-point resolution of 0.23 nm). In addition, high-angle annular dark-field (HAADF) imaging has been employed. This technique allows to record incoherently scattered electrons and is very sensitive to the variations in the atomic number of atoms in the sample (Z-contrast). STEM-HAADF was performed at the LPCNO by Pier-Francesco Fazzini for $FeNi_3$(@Ni) particles, by Alvaro Raya Baron and Georgiana Dragomir-Maties for $FeNi_3$@Mo and Ni_{OGM} nanoparticles respectively. The diameters of the imaged particles were measured with the ImageJ® software, and average on *ca.* 200 isolated particles when possible.

Identical Location TEM was used to observe catalyst zones before and after an electrochemical test. This technique is useful to see the degradation (dissolution, detachment, sintering, aggregation, agglomeration, corrosion…) caused by a given electrochemical or chemical treatment. Different grids had to be used. Indeed, the gold grids can dissolve after an OER treatment [251]. Thus, Ti grids (Ti, 300 mesh, Ted Pella®) were used, as they sustain corrosive environment in highly-oxidizing conditions (*e.g.* during OER operation) [41]. The deposit method is the same as previously. After this latter, different zones of the grid are imaged, and located thanks to the mesh pattern of the grid. Then, they undergo an electrochemical treatment in the same cell as the one described for RDE measurements. However, the RDE is replaced by an electrode made of crocodile clamp holding two glassy carbon plates in which the grid in inserted, as depicted in Figure II.14. The grid is dipped into the electrolyte, then slightly taken out so that the glassy carbon plates are as less in contact with the electrolyte as possible (meniscus configuration). The clamp is covered with a PTFE film to prevent consequent corrosion. Marian Chatenet did the ILTEM of FeNi-based materials at the LMGP.

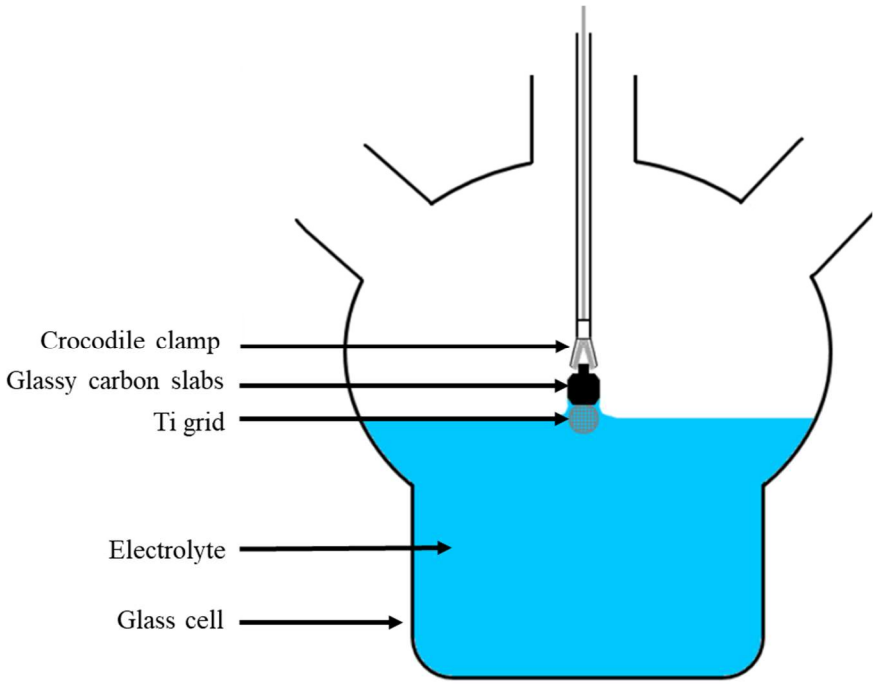

Figure II.14: Scheme of the WE composed of a crocodile clamp holding two glassy carbon plates in which the grid in inserted. Reprinted from [252] with permission from Grenoble Alpes University.

After the electrochemical test, the grid is cleaned in ultrapure water, dried on a precision wipe, and imaged again. Typical pictures of ILTEM are given in section III.2.1.3.

II.3.4 Environmental transmission electron microscopy

TEM pictures are made in an ultra-high vacuum (~ 10^{-7} Torr ≈ 10^{-10} bar). This environment is obviously not the one in electrochemical cells (and neither under AMF). In order to study the effect of the temperature and the H_2/O_2 atmosphere on the main catalysts, we had the chance to have access to an Environmental TEM (ETEM). With this apparatus, it is possible to heat the sample up to ~ 800°C, and to insert different gases into the chamber where the sample ($FeNi_3$@Ni was chosen) is located. The pictures were imaged by Mimoun Aouine in the Institut de Recherche sur la Catalyse et l'Environnement de Lyon (IRCE, Lyon France) with an ETEM FEI Titan G2 corrected from objective spherical aberration, operating at 300 kV maximum with a 1 Å resolution. Special grids (Widlfire S5 heating holder from DENS Solutions®) are used to heat the samples. The chips are able to heat the sample with a very fast temperature ramp (few milliseconds to heat at any temperature), mimicking the heating sparked by the AMF. Besides, it was possible to insert H_2 and O_2 gases up to 20 mbar. While one does not have any estimation of the H_2/O_2 pressure at the vicinity of the electrode under AMF, being under a reductive/oxidizing pressure gave information about the possible catalyst evolution in practical operation.

II.4 Structural and compositional characterization

II.4.1 X-ray Energy Dispersive Spectroscopy (X-EDS)

The electron beam stemming from a SEM or a TEM can also ionize the atoms of the sample and spark the emission of X-ray photons when the atom decays. This phenomenon is called fluorescence. The energy of the X-rays depends directly on the electronic structure of each element of the periodic table, allowing an elementary composition analysis of the sample. A quantitative composition analysis necessitates specific conditions [253]. Only qualitative analyses were realized in this PhD. The X-EDS analyses were performed by Frédéric Charlot at the CMTC, thanks to a Zeiss® Gemini SEM-500 operating at 3 keV.

II.4.2 High Resolution (HR)TEM with Fast Fourier Transform analysis

Without going into details, it is possible to obtain the crystal structure of a sample with a TEM [249]. By calculating the fast Fourier transform of the picture numerically, one gets a diffraction image characteristic of the crystallographic structure of the sample. From the diffraction pattern (reciprocal network), indexing the diffracted points gives the interplanar distances and the angles of a crystalline cell. By comparing the experimental values with tabulated ones of known and analyzed compounds, the structure of the sample can be fitted. The advantage of doing this compared to X-ray diffraction (see section II.4.3 below) is that the analyzed part of the sample is very small – corresponding to the beam diameter, while XRD gives structure information of the whole sample. The two techniques are therefore complementary.

Local fast Fourier transform HRTEM analyses were performed by Mimoun Aouine at the IRCELyon with the same apparatus. This study was very helpful to evaluate the change of the catalyst studied at different temperatures and under H_2/O_2 atmospheres.

II.4.3 X-ray diffraction

The average crystallinity of the catalysts has been studied by X-ray diffraction (XRD). An X-ray beam provided by an X-ray source of wavelength λ hits the sample (generally in a powder form) with an incident angle θ. Depending on the incident angle, the planes of the studied crystal can diffract (elastic diffusion) if the diffraction conditions defined by the Bragg's law are verified (Laue conditions), Eq. II.14:

$$2d_{\mathrm{hkl}}\sin(\theta) = n\lambda \qquad \text{II.14}$$

With d_{hkl} the interplanar distance, *i.e.* the distance between two diffracting planes in the crystal, and *n* the diffraction order.

X-ray emitted by the elastic diffusion interfere and are collected by a detector. By plotting the signal intensity versus the incident angle, one gets a diffractogram, resulting from the constructive/destructive interferences, and characteristic of the crystal structure of the sample. The shape of the peaks (height, width, half width at maximum, profile) depends on the sample's crystallographic properties. For instance, a very crystallized sample leads to very narrow and tall peaks, while a more amorphous structure broadens and shortens the peaks. The Scherrer equation enables the determination of the average crystallites size, Eq. II.15:

$$< d_{\mathrm{XRD}} > = \frac{C\lambda}{\sqrt{FWHM^2 - w^2}\cos(\theta)} \qquad \text{II.15}$$

With $< d_{XRD} >$ the average crystallite diameter, C a correction factor (= 0.89), *FWHM* the Full Width at Half Maximum, and s the instrumental width.

Furthermore, a temperature XRD study on $FeNi_3$@Ni catalyst, collecting XRD diffractograms at {25, 100, 200, 300, 400, 500, 600, 50}°C under air with a temperature ramp of 12.5°C.min^{-1} was carried out, in order to evaluate the evolution of this material at different temperatures. Typical diffractograms are displayed in section III.1.

The measurements of the FeNi-based, Ni_{HI}, Ni_{polyol}/ATO and Ni_{polyol} particles have been carried out by Thierry Encinas at the Consortium des Moyens Technologiques Communs (CMTC Grenoble-INP, France), with a X'Pert Pro MPD (PANalytical) equipped with a copper anode. The K_α-Cu wavelength (1.5419 Å) was chosen for the measurements. The diffraction patterns were collected in reflection mode using the Bragg-Brentano geometry. The *in situ* temperature XRD study was realized with a High Temperature Oven Chamber HTK1200N (Anton Paar) with an automatic adjustment in z.

The XRD diffraction patterns of the $FeNi_3$@Mo and Ni_{OGM} NPs were realized by Alvaro Raya Baron and Georgiana Dragomi-Maties respectively with a PANalytical Empyrean diffractometer using K_α-Co radiation (λ=0.1789 nm) at 45 kV and 40 mA.

II.4.4 Inductively coupled plasma mass/atomic emission spectrometry

In order to analyze the composition of the catalysts or to quantify the dissolution after accelerated stress tests, inductively coupled plasma mass spectrometry (ICP-MS) or ICP atomic emission spectroscopy (ICP-AES) measurements were conducted. In this method, a plasma is created by a plasma burner. The sample is nebulized into the plasma and then ionized. A mass

spectrometer analyzes the plasma which contains the components of the sample. This technique allows a deep accuracy of *ca.* hundredth of parts per billion (ppb).

Sofyane Abbou and Vincent Martin carried out the ICP-MS measurements with a Perkin Elmer, model NexION 2000c operated with Syngistix for ICP-MS software v2.3. The standard and the collision mode (kinetic energy discrimination) were employed. The calibration curve was drawn by using metal standard solutions (Sn, Sb, Ir, Pt, Fe, Ni, Au) of 2, 5, 10, 20, and 50 ppb with an intern standard (2 ppb of Rh), in nitric media (2% HNO_3). Analyzed masses of the studied elements were calculated regarding the dilution and the calibration curve with a minimum R^2 of 0.9999 and an overlapping percentage of the intern standard of 100 ± 5%. However, for the electrolyte sample analyses during AST tests (realized with an intern standard in KOH 1 $mol.L^{-1}$), an overlapping ranging down to 80 up to 100% was found. It probably comes from the potassium ionization, which consumes a significant part of the torch energy, but the reason is not certain. It was observed for all the electrolyte samples. Thus, the values given have to be considered with caution in this specific study.

The composition of $FeNi_3$@Mo and Ni_{OGM} catalysts were studied by Alvaro Raya Baron and Georgiana Dragomir-Maties respectively, by the use of thermogravimetric analysis (TGA) performed in a TGA/DSC 1 STAR System equipped with an ultra-microbalance UMX5, a gas switch GC200 and DTA and DSC sensors, and by ICP-AES (Pascher laboratory). TGA measurements allow to obtain the metallic percentage of the sample, the rest being attributed to organic ligands.

II.5 Magnetic characterizations

This section presents the devices used to measure the magnetic properties/heating of the materials, to apply an alternating magnetic field, or to measure the magnetic field (MF) produced by permanent magnets. The provided MF values are the root mean square (rms) values and not the peak amplitude values, as the former is more representative of the consumed energy by the coils.

II.5.1 Vibrating Sample Magnetometer

The magnetic properties of the samples were measured by the vibrating sample magnetometer (VSM) technique. It consists of placing a sample inside an electromagnet which applies a MF $B_{applied}$. As the sample is moved up and down (vibrating), its leakage field creates an AMF which is recorded by pickup coils, and is proportional to the sample magnetization. One gets a hysteresis loop, as described in subsection I.3.1.3. This type of measurements can be conducted in the temperature range 2-400 K. The samples were under powder form (catalyst nanoparticle aggregates). The magnetic moment is normalized by the mass of the sample. Usually, the magnetic moment is given in "emu".g^{-1}, which is not a S.I. unit, but 1 emu.g^{-1} = 1 A.m^2.kg^{-1} (S.I.). Figure II.15 shows a hysteresis loop measurement of a $FeNi_3$@Ni sample.

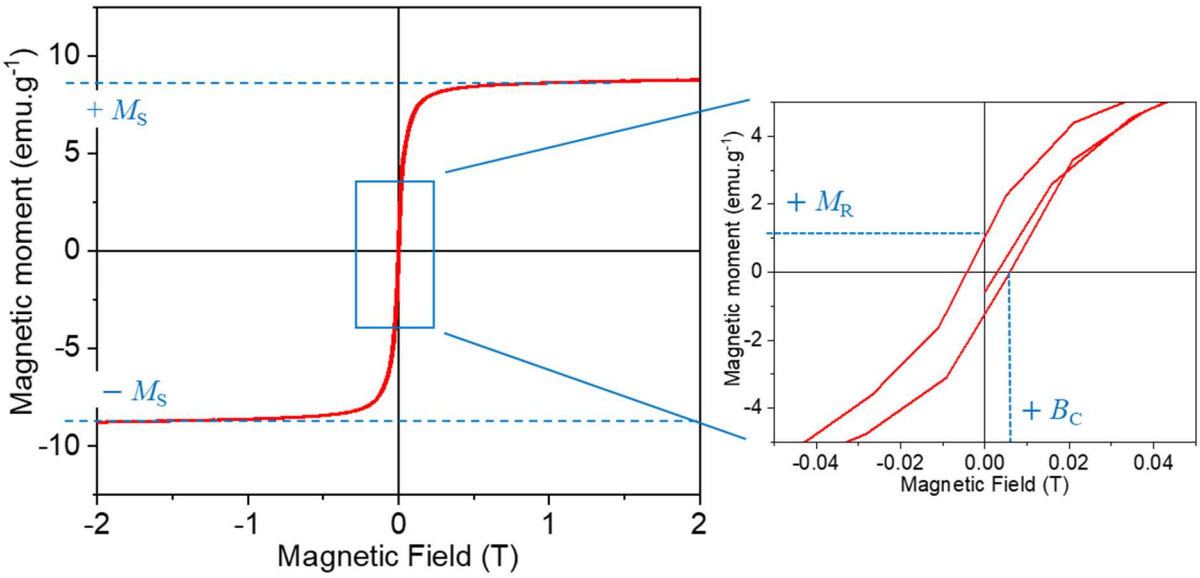

Figure II.15: Hysteresis loop of a $FeNi_3$@Ni sample at 3000 µg.cm^{-2} deposited on a carbon felt.

Arnaud Hillion, Géraldine Ballon, Déborah De Masi, Alvaro Raya Baron and Georgiana Dragomir-Maties conducted the VSM measurements on a Quantum Device PPMS Evercool II.

II.5.2 Specific Absorption Rate

The heating capacity of the material under AMF is characterized by the Specific Absorption Rate (SAR). Measuring it consists of applying an AMF at a known magnitude and frequency during a defined time, and to measure by different ways the temperature elevation of a known mass of material. It had been carried out in two different ways during this PhD.

Firstly, the employed procedure was a calorimetry method developed at the LPCNO. A weighed mass of material (generally around 10 mg) is deposited in a glass tube (borosilicate glass, Avitec®) with 0.5 mL of mesitylene, and sonicated during 2 minutes. The tube is then placed in a one hole drilled Teflon cylinder (3 cm height, 1 cm diameter) filled with 2 mL of water, which is put at the center of a 100 kHz induction coil generating a field in the range [0; 47] mT. Two optical probes (Reflex 4, Neoptix®) measure the temperature elevation inside the cylinder, at the bottom tip of the tube, and at its center (Figure II.16).

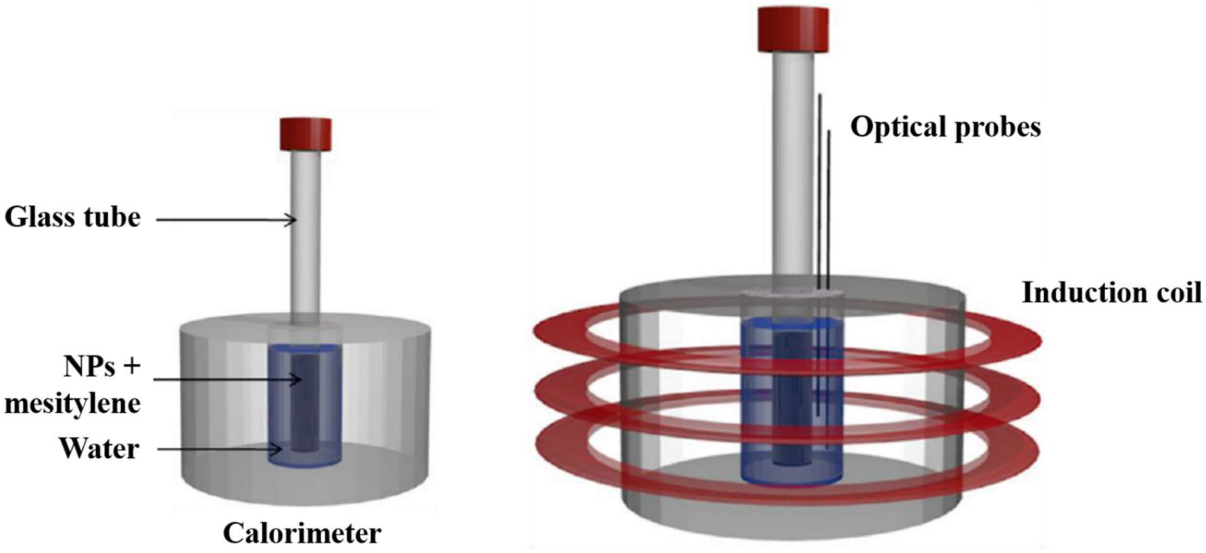

Figure II.16: SAR measurement calorimeter setup. Modified from [66] with permission from INSA Toulouse University.

The heating is monitored in real-time thanks to a LabView program. The AMF is applied during a precise time, between 20 and 40 seconds. After this exposure, the AMF is switched off and the tube is agitated to homogenize the water temperature of the calorimeter (Teflon cylinder). The temperature difference ΔT, before and after AMF exposure, allows to determine the SAR value at a given AMF amplitude, according to the following formula:

$$SAR = \frac{\sum_s Cp_s m_s}{m_{mag}} \frac{\Delta T}{\Delta t} \qquad \text{II.16}$$

With Cp_s the calorific capacity of element s, m_s the mass of element s, m_{mag} the mass of magnetic material (generally the iron mass), ΔT the temperature elevation or heating, and Δt the AMF time exposure. The mass and calorific capacity of the different elements of the setup (mesitylene, water, glass) are taken into account in Eq. II.16. (used values are indicated in Supplementary Figure 5).

Obviously, the calorimeter is not perfectly adiabatic, and calorific losses occur during the measurement. In order to improve this method, the calorimeter losses were calibrated by the corrected slope method, where the heating phase slope is corrected by subtracting from it

the slope of the corresponding cooling phase (*i.e.*, at the same temperature value). Then, a correction factor is applied to all SAR measurements (the values are given in Supplementary Figure 6) [254]. Short time SAR measurements are closer to the real SAR value, but the exposure time incertitude is higher, as the AMF switching is done manually. Thus, Δt of 30 seconds was generally used, although the temperature continued to increase for 1 minute (1') more. It is very important to note that this technique allows the measurement of two contributions of the heating power of a material: the hysteresis losses (due to the magnetic properties of the NPs) and the Joule heating due to the eddy currents induced by the AMF into the sample (including the support).

In addition, as the samples used for electrochemical tests under AMF are very different from a colloidal suspension, another heating measurement method was also employed. Indeed, the particles in suspension can form chains, which enhances the heating power (see subsection I.3.1.4), while the sample used herein were dried and stuck on a carbon felt. Besides, most of the electrolysis experiments were performed on a 300 kHz coil, instead of a 100 kHz one. Eddy currents increase at the square of the AMF frequency [255], and the SAR increases linearly with the frequency [71], so that the measured SAR heating contributions are under-estimated. Thus, it was chosen to measure the system {carbon felt support + deposit} on the 300 kHz coil, in the same position that in the PMMA cell, but under air. The heating of the system was measured by a pyrometer (RAYMMLTSSF1L, Raytek®) targeting the center of the deposit (Figure II.17).

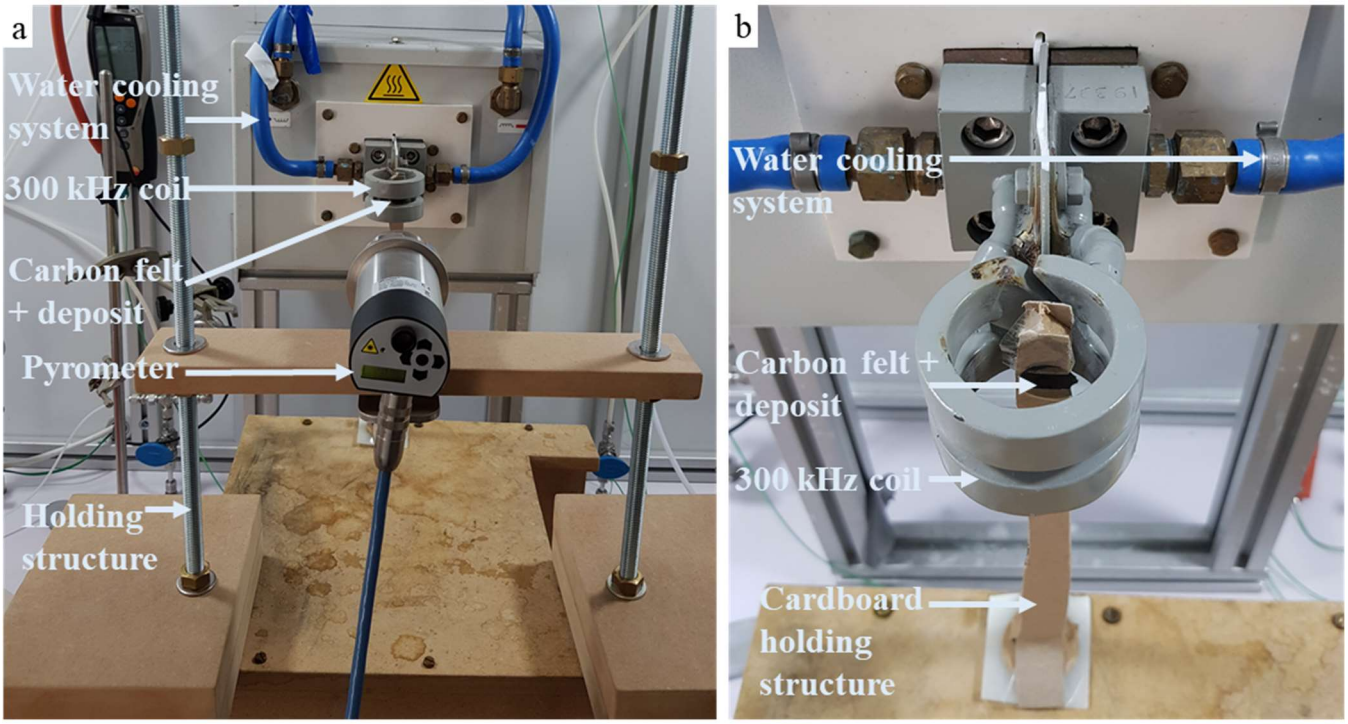

Figure II.17: (a) SAR measurements setup with the pyrometer (b) close-up on the system {carbon felt + deposit}.

Again, the system is not perfect, it is not adiabatic and does not correspond to the electrochemical environment, as the system is not in the cell filled up with electrolyte. It was not possible to measure accurately the system elevation temperature in the PMMA cell as its thickness (5 mm) distorts the ΔT values. Besides, it was tried to measure the system in the electrolyte (beaker), but the latter was rapidly boiling, rendering the measurements difficult.

Another way to obtain the SAR of a material is by the measure of the high-frequency hysteresis loops (under an AMF). The LPCNO developed a setup for this type of technique, which is described in [256]. The SAR is then calculating by integrating the area under the curve A and multiply it by the working coil frequency f, as explained in I.3.1.4. One test was performed by Stéphane Faure, but unfortunately, the electric signal of the system {carbon felt + deposit} was too noisy. A higher catalyst mass could have helped increasing the signal-to-noise ratio, but at higher loading (> 3000 $\mu g.cm^{-2}$) the ink was impossible to homogenize. Another way could have been to make several deposits on the support to reach enough mass, but this would

have implied to make 20 deposits to reach ~ 10 mg of catalyst (the commonly used mass for this measurement), which would have been very time consuming. Nevertheless, this would be a very interesting characterization to conduct in the future, especially because this measurement gives the value of the SAR heating due to hysteresis losses SAR_{hyst} only. Thus, it is possible to estimate the amount of heat generated by induced eddy current $SAR_{\text{eddy current}}$ by subtracting the SAR_{hyst} value given by the hysteresis loop from the SAR_{calo} value obtained by the calorimeter technique, Eq. II.17:

$$SAR_{\text{eddy currents}} = SAR_{\text{calo}} - SAR_{\text{hyst}} \qquad \text{II.17}$$

II.5.3 Electrochemical experiments under an alternating magnetic field

Two coils were employed to conduct electrochemical tests under an alternating magnetic field. The first one was dedicated to study the influence of hysteresis losses on different magnetic materials. The coil (4 cm height, 5 cm wide, Fives Celes®) worked at 300 kHz, with an amplitude varying from 0 to 65 mT (Figure II.17). This coil was convenient for fundamental purpose experiments, as it was easy to control the magnitude, especially because it allows recipes implementation. However, this coil is oversized for our application. Indeed, the energy necessary to create a magnetic field of 43 mT at 300 kHz is 5.5 kW (Supplementary Figure 2). In order to reduce this power, another coil was used, operating at 100 kHz. Reduction of frequency decreases the coil heating and decreases the energy consumption (Supplementary Figure 3). The small diameter coil (3 cm inner diameter, 12 cm height, ID Partner® - Figure II.13 (a)) is a hollow pipe (maximal skin effect) and is cooled by an air flow. Accordingly, a much lower power of 722 W is necessary to produce an AMF at 42 mT, at 100 kHz.

II.5.4 Magnetic field measurements with a Hall probe

Several experiments were conducted under a static magnetic field in order to see a possible influence of Lorentz/Kelvin/spin polarization effects. Two types of NdFeB magnets were used: ring shape magnets (70x30x5 mm^3, INEA0044, IMAgnet®) and parallelepiped magnets (50.8x50.8x25.4 mm^3, Q51-51-25-N, Supermagnetete), both with an axial magnetization. The magnetic field of the magnets has been measured with a Gaussmeter and a transverse Hall probe (GN106, MM®) as shows Figure II.18.

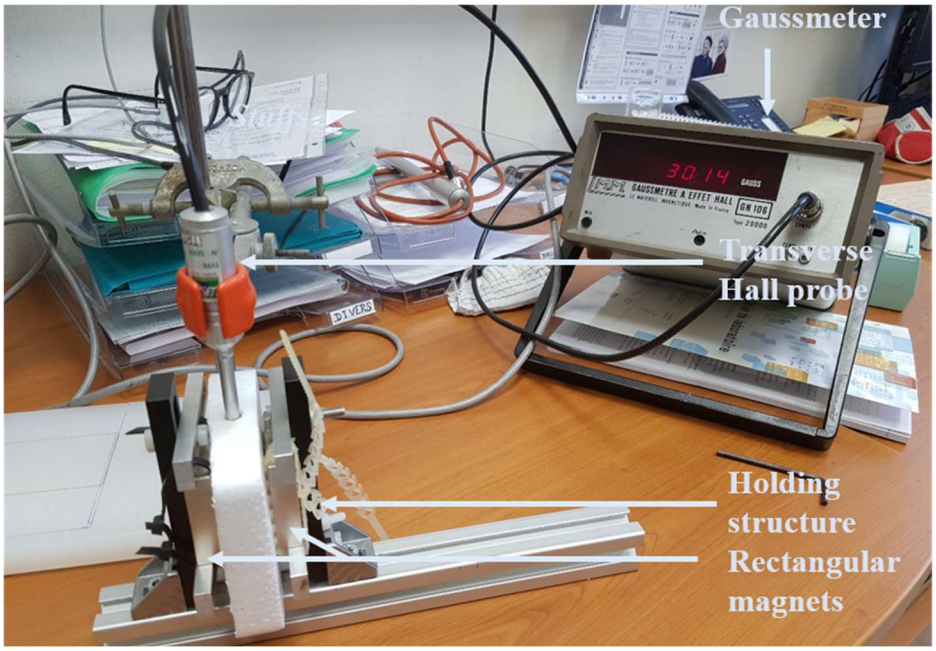

Figure II.18: Static magnetic field measurement setup between two rectangular magnets.

Figure II.19 presents the calibration curves of the magnets in different configurations.

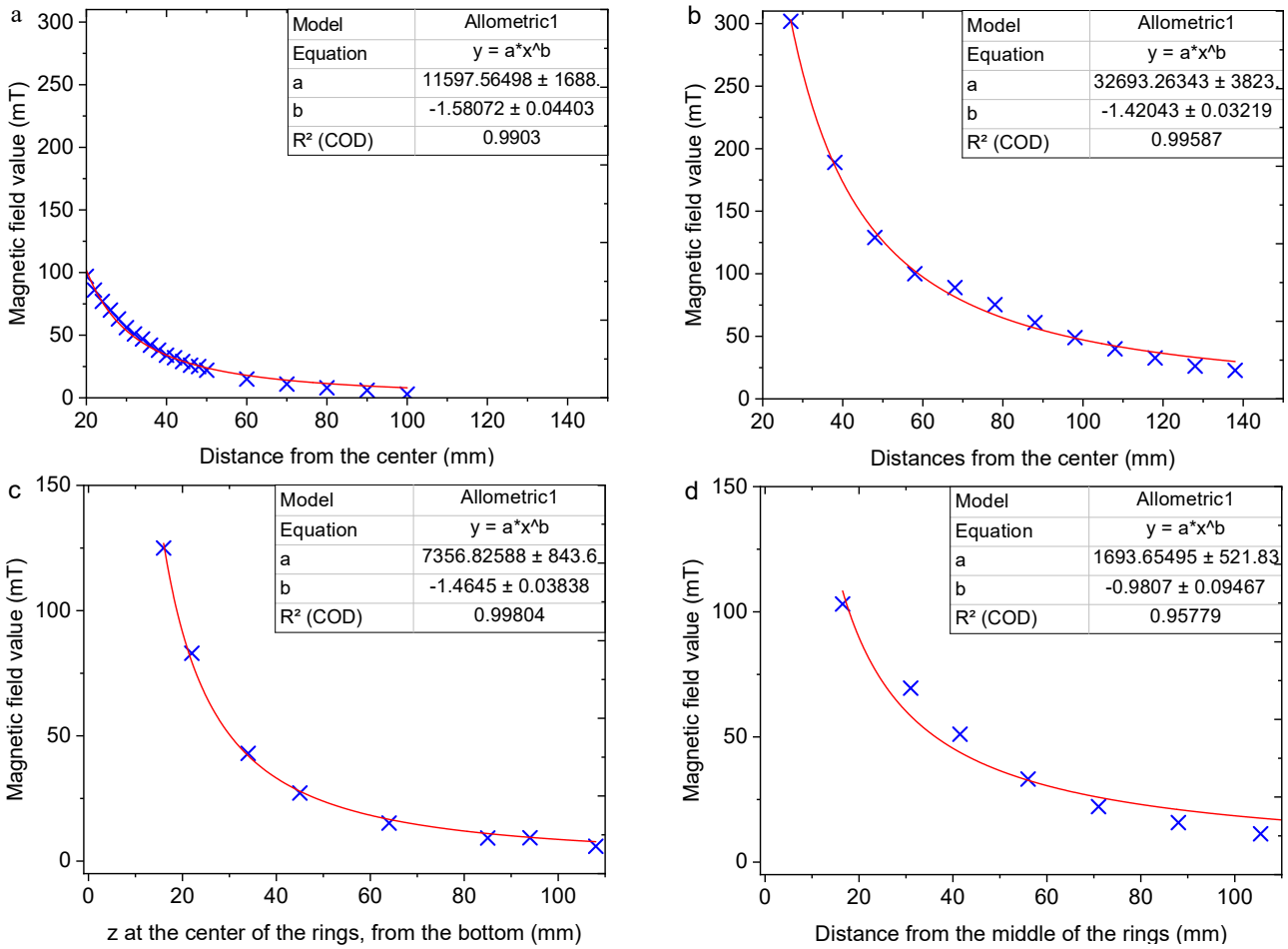

Figure II.19: Permanent magnets calibration using a Gaussmeter with a transverse Hall probe. (a) calibration of a single parallelepiped magnet, magnetic field measured at its center, in the z direction perpendicular to its face (b) two parallelepiped magnets facing each other, magnetic field measured at the center of the faces between the magnets (c) piled ring magnets (same axis) with magnetic field measured along the ring axis z from the bottom of the piled magnets, (d) two rings magnets with different axes in the (Oxy) plane, at the same z level (same horizontal place), the magnetic field is measured between the two rings, when approaching one ring to the other.

The two main setups used when static magnetic fields were applied on the WE in the PMMA cell are displayed in Figure II.20.

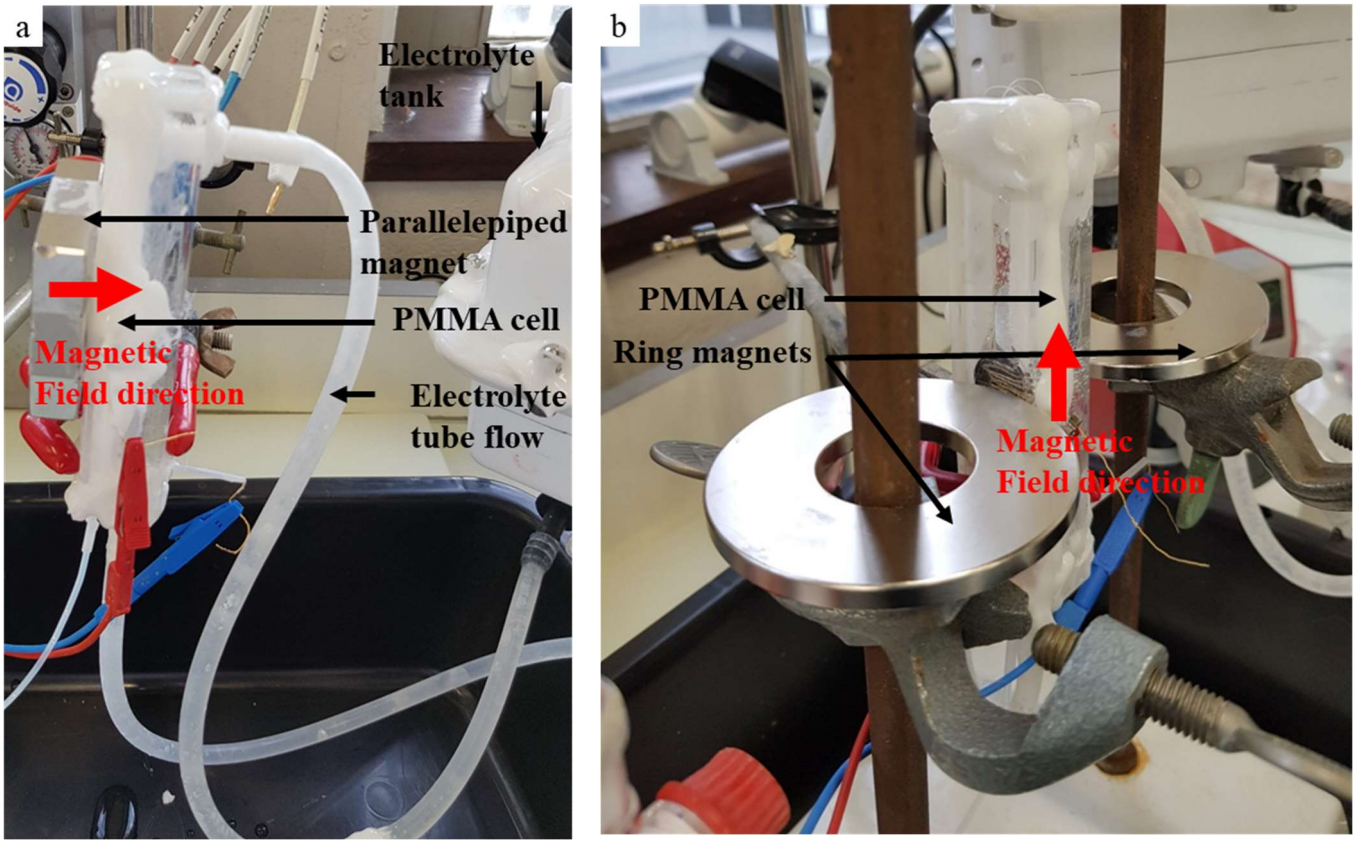

Figure II.20: (a) Setup where a perpendicular-to-electrode magnetic field of ~ 200 mT is applied on the WE in the PMMA cell (b) Setup where a parallel-to-electrode magnetic field of ~ 80 mT is applied on the WE in the PMMA cell.

Also, experiments with SMF were conducted with a beaker filled with KOH, which allowed to approach closer the magnets, and reach accordingly a higher magnetic field applied on the samples.

Chapter III: Physicochemical, electrochemical, and magnetic characterizations of the studied materials

Abstract of Chapter III: The intrinsic electrochemical activity of the studied materials in the rotating disk electrode (RDE) setup is presented in Chapter III. The newly active materials reveal more active than the previous FeC-Ni NPs. An ink loading study indicates one limit of the RDE setup (too thick layer is detrimental to the activity). Durability study in RDE on the most active materials ($FeNi_3$(@Ni) and Ni_{HI}) indicates that they suffer from Fe dissolution and layer detachment. Then, the activity toward WS in the cell designed for AMF tests is evaluated. It changes compared to the RDE setup because of the different working conditions (electrolyte flux and different electrode support). Nevertheless, $FeNi_3$(@Ni) catalysts remain among the most active materials. A loading study in this setup indicates that the higher the loading, the better the activity (more active sites). Finally, magnetic characterizations show that these latter materials present a high heating capacity (SAR), while Ni-based nanoparticles exhibit a low SAR, and the other do not heat.

Résumé du chapitre III : L'activité intrinsèque des matériaux par rapport aux réactions HER et OER est étudiée dans un montage en électrode à disque tournant (RDE). Des catalyseurs plus actifs que celui utilisé au début de ce projet (FeC-Ni) ont été obtenus. L'influence du chargement du matériau dans l'encre est évaluée, et montre une limite du système RDE (couche catalytique épaisse préjudiciable à l'activité). Des mesures de durabilité montrent que les matériaux les plus actifs ($FeNi_3$(@Ni) et Ni_{HI}) sont dégradés, notamment par détachement de la couche active et dissolution de Fe. Ensuite, les performances des matériaux sont évaluées dans la cellule conçue pour les mesures sous AMF. Ces dernières changent par rapport aux mesures en RDE car les conditions de travail sont différentes (flux d'électrolyte, support d'électrode différent). Toutefois, les catalyseurs $FeNi_3$(@Ni) restent parmi les matériaux les plus actifs. Une nouvelle étude du chargement indique que plus l'encre est chargée, meilleure est l'activité (plus de sites actifs). Enfin, des caractérisations magnétiques montrent que les nanoparticules $FeNi_3$(@Ni) chauffent (SAR élevé), les catalyseurs à base de Ni beaucoup moins, et les autres ne chauffent pas.

In this chapter are presented first the physicochemical properties of the studied materials, then their intrinsic activities toward the HER and OER, and their possible modifications after electrochemical tests. Finally, the magnetic properties of the catalysts are reported. These experiments enable to determine the nature and the structure of the catalysts and compare their electrochemical activity in the RDE setup together and with the former catalyst employed by Christiane Niether at the beginning of this project (FeC-Ni). Accordingly, the most active materials toward HER and OER were selected and tested for their durability. The activities in the RDE setup are compared to the performances in the PMMA cell. Finally, the performed magnetic characterizations enable to determine the intrinsic magnetic properties of the catalysts and evaluate their heating capacity.

The physicochemical properties and the RDE tests of $FeNi_3$(@Ni) and Ni NPs synthesized by Raphaël Chattot have been published in the following article:

V. Gatard, D. De Masi, R. Chattot, I.M. Marin, J. Manuel, A. Revert, F. Fazzini, $FeNi_3$ and Ni-Based Nanoparticles as Electrocatalysts for Magnetically Enhanced Alkaline Water Electrolysis, Electrocatalysis. 11 (2020) 567–577. https://doi.org/10.1007/s12678-020-00616-9.

We thank sincerely all the contributors for their participation in this work.

III.1 Physicochemical characterizations

The physicochemical characterizations consisted of TEM imaging with STEM-HAADF, elemental X-EDS analyses, XRD and ICP-MS measurements.

III.1.1 FeNi-based nanoparticles

Figure III.1 shows representatives TEM, STEM-HAADF images and X-EDS mapping of $FeNi_3$ ((a) to (e)), $FeNi_3$@Ni ((f) to (k)) and $FeNi_3$@Mo ((l) to (r)) particles.

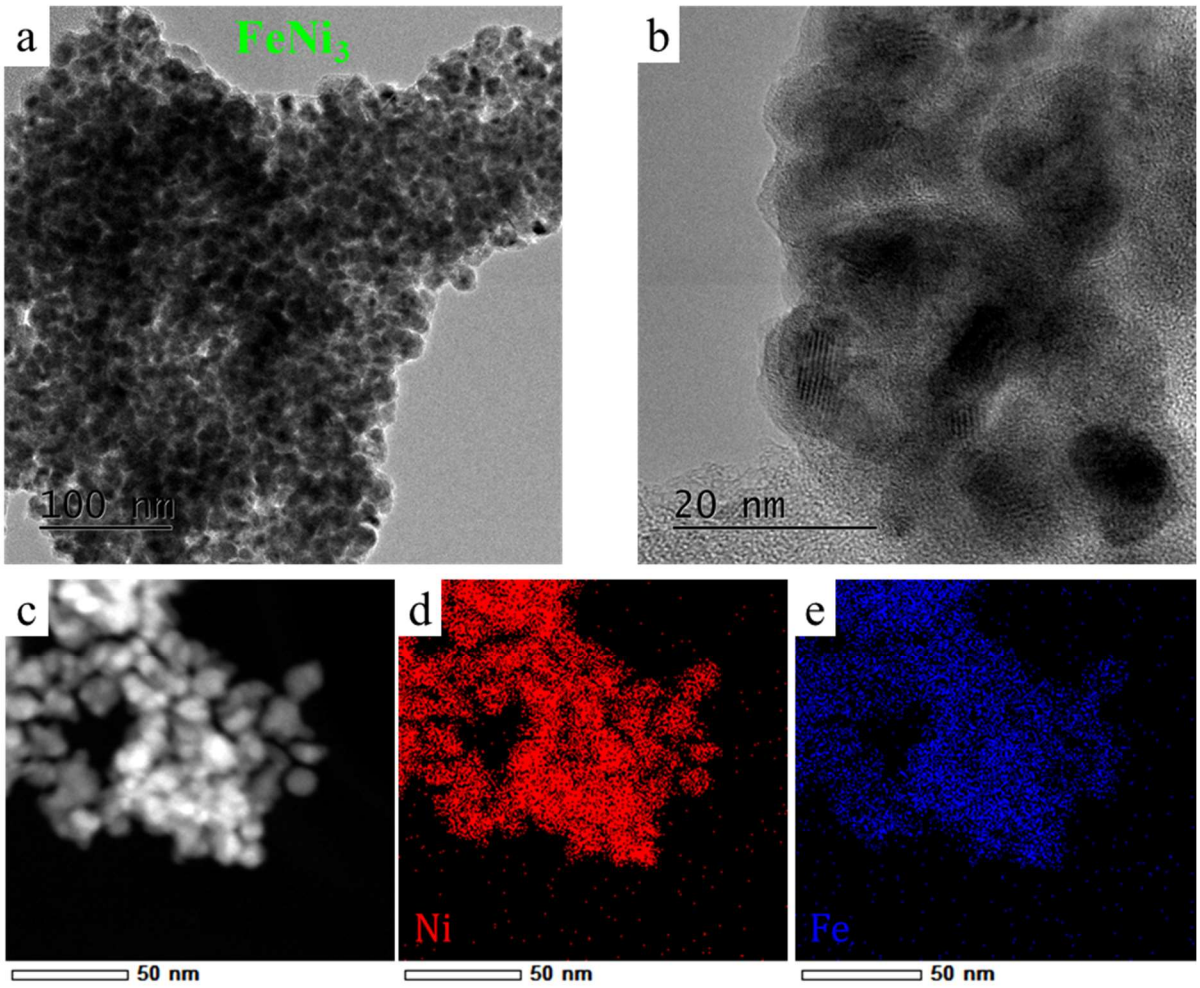

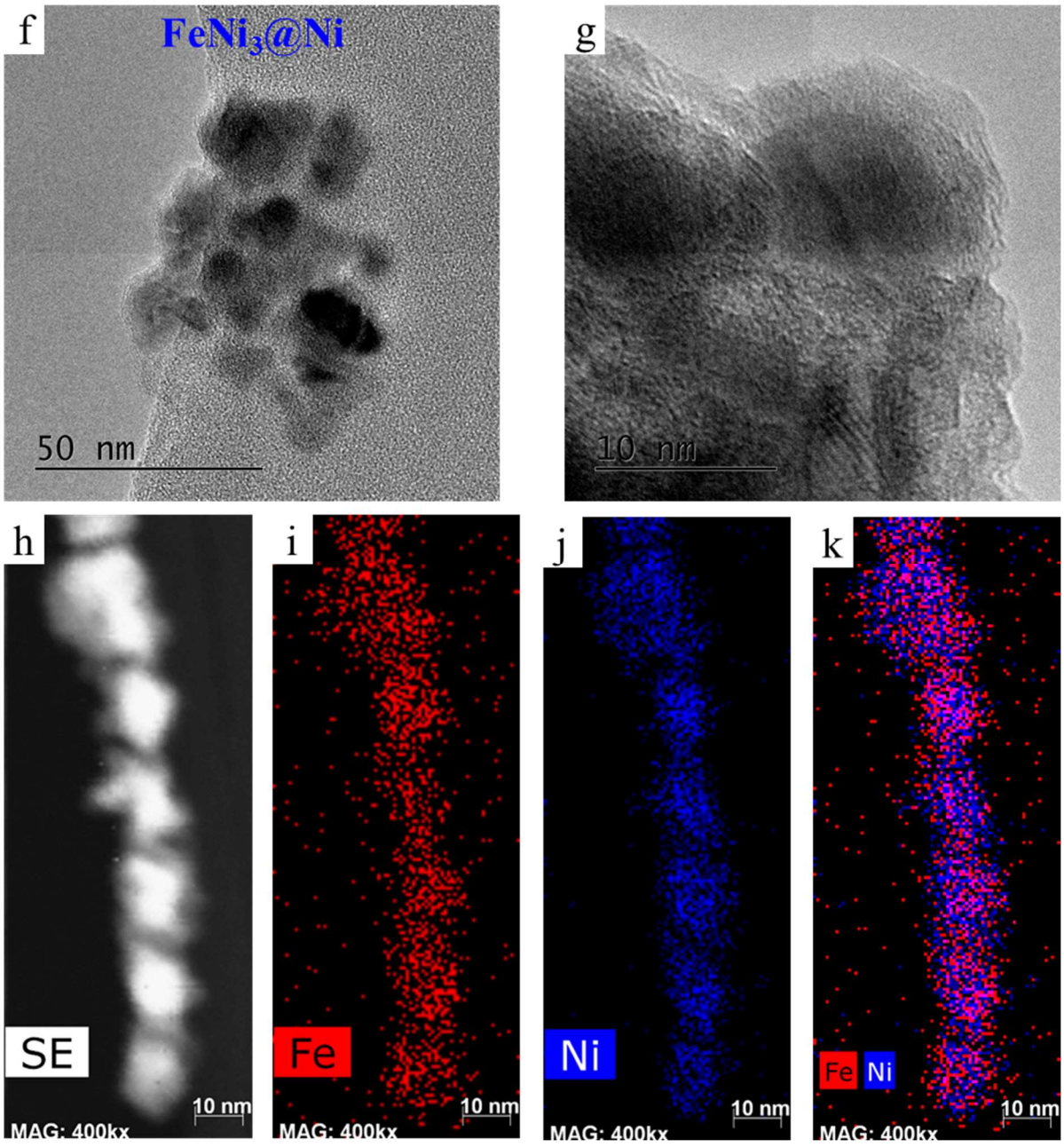
f
FeNi3@Ni
50 nm
g
10 nm
h
SE
10 nm
MAG: 400kx
i
Fe
10 nm
MAG: 400kx
j
Ni
10 nm
MAG: 400kx
k
Fe Ni
10 nm
MAG: 400kx

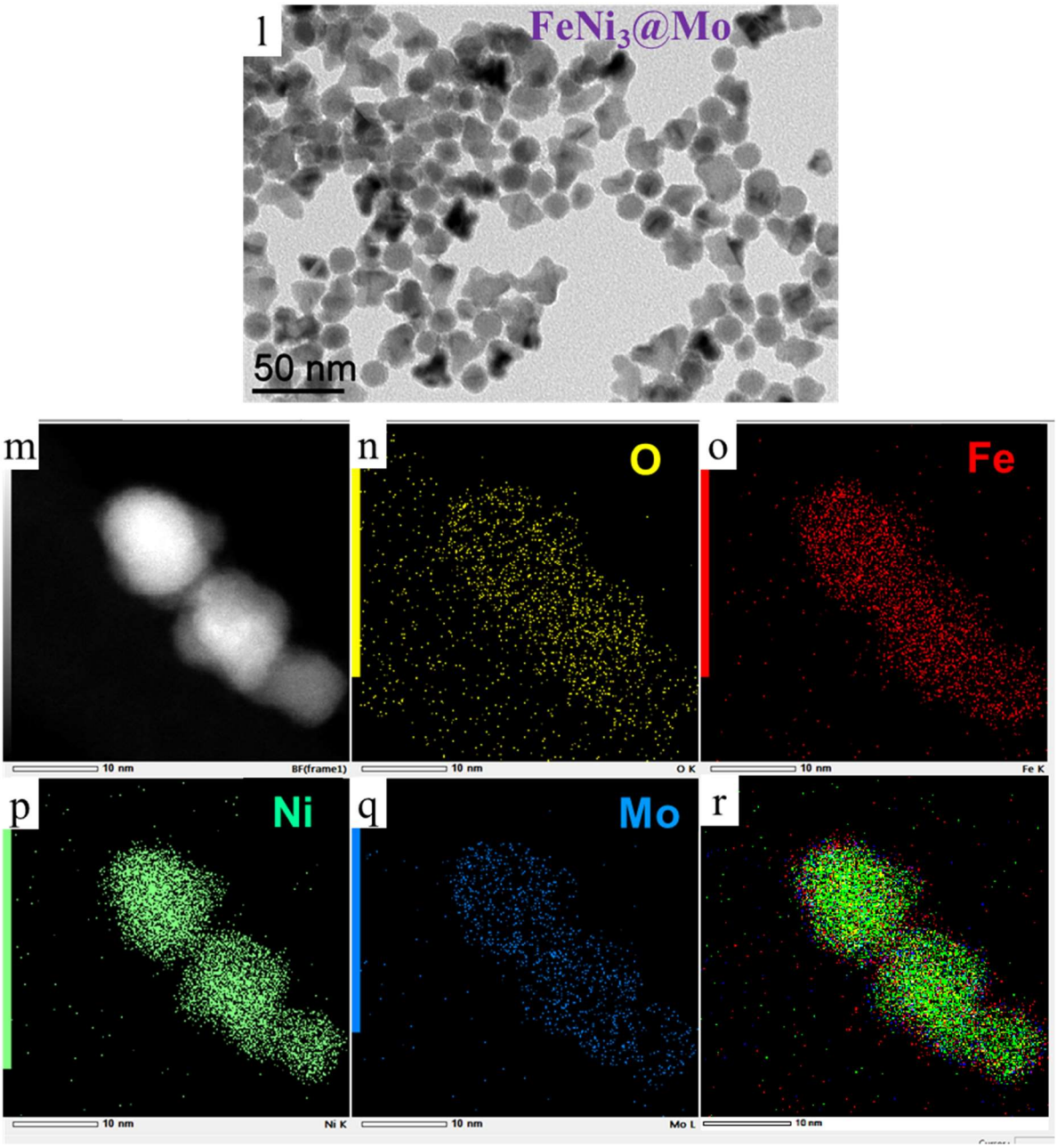

Figure III.1: TEM pictures of (a-b) $FeNi_3$ NPs, (f-g) $FeNi_3$@Ni and (l) $FeNi_3$@Mo. STEM-HAADF and X-EDS for (c-d) $FeNi_3$, for (h-k) $FeNi_3$@Ni, and (m-r) $FeNi_3$@Mo.

The TEM micrographs indicate round-like shape polycrystalline particles having an average diameter of 17.3 nm for $FeNi_3$, 18.6 nm for $FeNi_3$@Ni and 14.4 nm for $FeNi_3$@Mo (values based on the measurement of *ca.* 200 isolated particles); the cores of the nanoparticles are even smaller for $FeNi_3$(@Ni), as grain boundaries and individual crystallites are visible. A thin brighter amorphous layer is visible around the particles, characteristic of surface oxides, and also corresponding to the remaining ligands of the syntheses, both for $FeNi_3$ and $FeNi_3$@Ni

NPs. The solvent on the $FeNi_3$@Mo NPs TEM grid has been evaporated slowly, which permit to have a plane distribution of the particles (Figure III.1 (l)). Moreover, the particles are generally agglomerated, which is standard for unsupported catalysts. While the HAADF technique is sensitive to the atomic number of the elements, the Fe and Ni are too close in the periodic table to visualize a clear difference. Complementary X-EDS elemental mapping (STEM) was conducted: these two elements are evenly distributed in all the NPs core. A stoichiometry of 31% Fe and 69% Ni was found for $FeNi_3$, 22% Fe and 78% Ni for $FeNi_3$@Ni and 22% Fe, 68% Ni and 10% Mo for $FeNi_3$@Mo, corresponding to the target. Figure III.2 presents the X-ray diffractograms of these NPs.

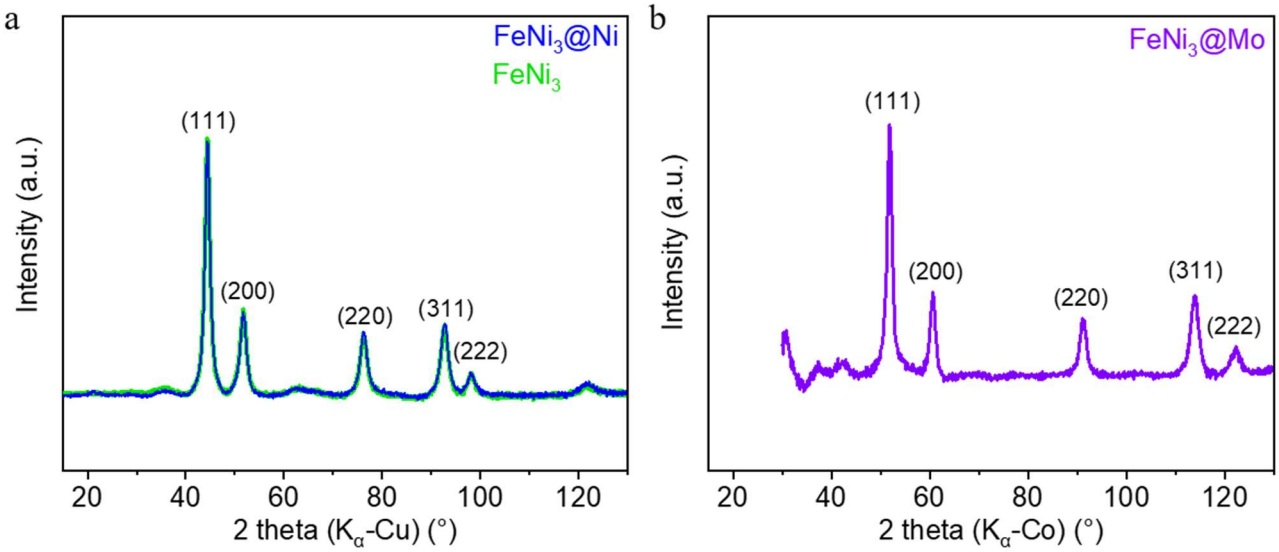

Figure III.2: X-ray diffractograms of (a) $FeNi_3$ in green and $FeNi_3$@Ni in blue (b) X-ray diffractogram of $FeNi_3$@Mo in purple. The planes correspond to the peaks of the PDF card 00-038-0419 of $FeNi_3$ for a (a) K_α-Cu wavelength for (b) and a K_α-Co wavelength for. The backgrounds have been purposely removed.

All the particles fit with a face-centered cubic $FeNi_3$ phase (PDF card 00-038-0419). According to the Scherrer's equation (Eq. II.15), the crystallite sizes are of 4.6 ± 0.3 nm for $FeNi_3$, 4.1 ± 0.9 nm for $FeNi_3$@Ni and 6.3 ± 1.4 nm for $FeNi_3$@Mo. The small broad peaks correspond to surface oxidation, in agreement with the TEM observations. Complementary Mössbauer measurements conducted by Déborah De Masi further confirm the catalysts' structure [65].

Table III.1 summarizes the physicochemical data of the $FeNi_3$-based materials, including ICP-MS/AES measurements, which are consistent with the X-EDS values.

Table III.1: Physicochemical features of $FeNi_3$-based materials.

Materials	**Diameter** (nm)	**Crystallite size** (nm) **(Planes of the peaks used)**	**X-EDS** (atomic %)			**ICP-MS** (atomic %)		
			%Fe	%Ni	%Mo	%Fe	%Ni	%Mo
$FeNi_3$	17.3	4.6 ± 0.3 (111), (220)	31	69	/	29	71	/
$FeNi_3$@Ni	18.6	4.1 ± 0.9 (110), (214)	22	78	/	24	76	/
$FeNi_3$@Mo	14.4	4.6 ± 0.3 (111), (200)	22	68	10	19	73	8

III.1.2 Ni-based nanoparticles

TEM, STEM-HAADF images and X-EDS mapping of Ni NPs synthesized by different routes are displayed in Figure III.3.

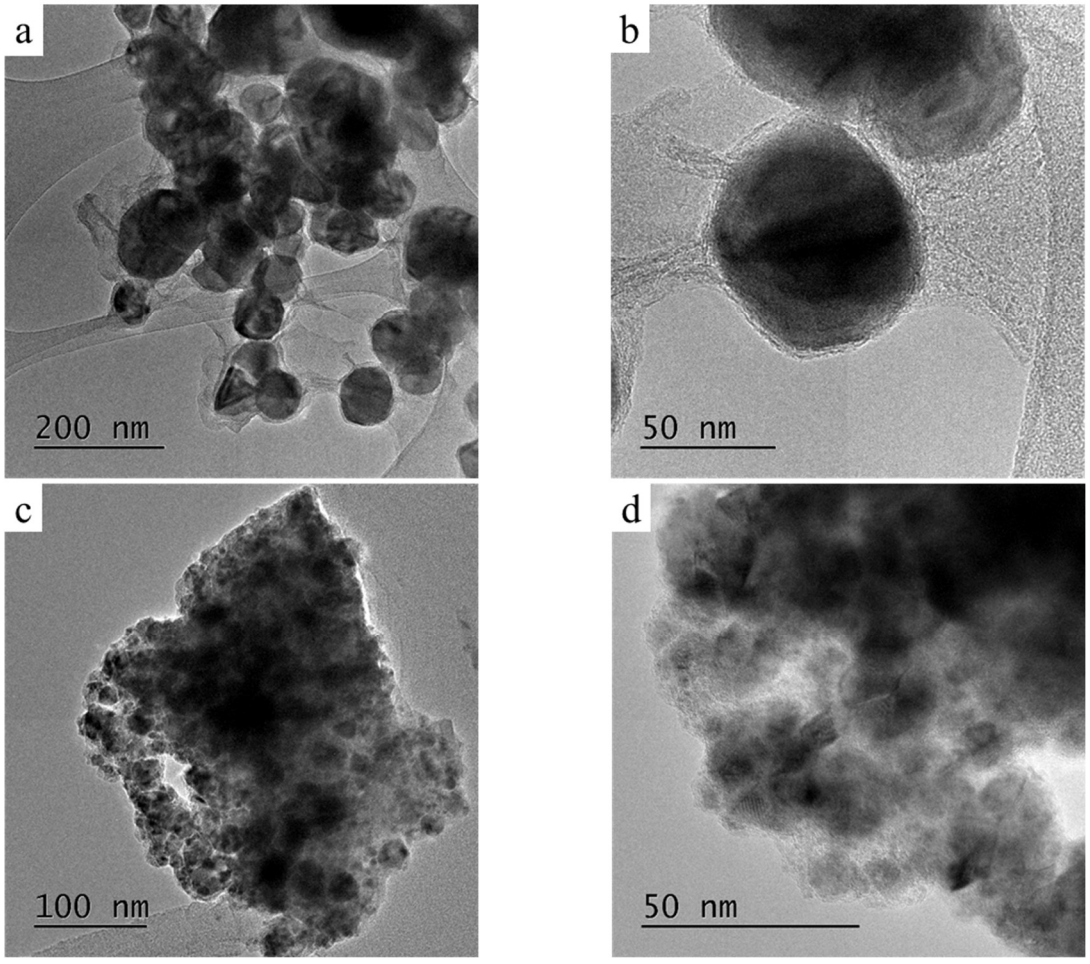

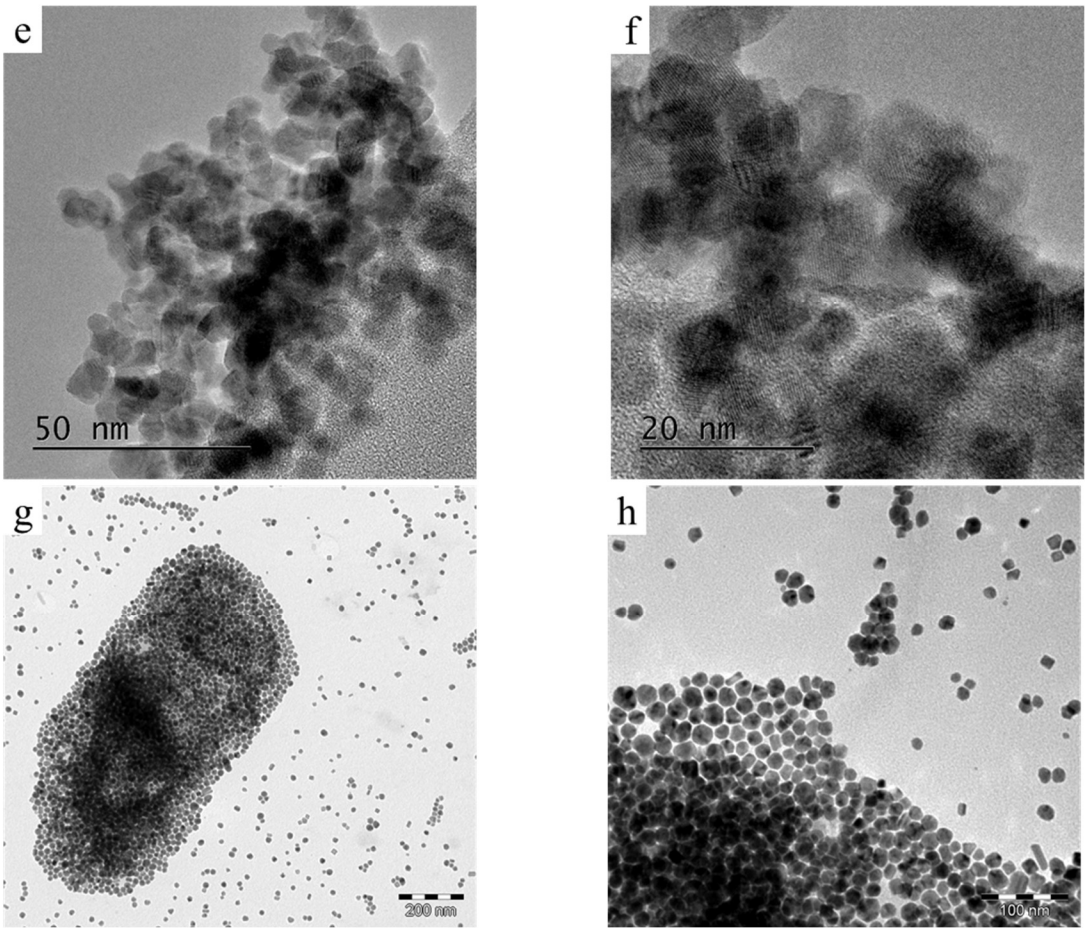

Figure III.3: TEM pictures of (a-b) Ni_{HI} particles, (c-d) Ni_{polyol}, (e-f) Ni_{polyol}/ATO and (g-h) Ni_{OGM}.

The Ni_{HI} particles (Figure III.3 (a-b)) are well-crystallized, spherical-shaped, and of 69 nm mean diameter size, based on the measurement of *ca.* 30 isolated particles. While this value is based on few measurements, low magnification TEM pictures display similar NPs size for all type of Ni particles. Polycrystalline contrast is visible on most particles, with twins and internal grain boundaries. Ni_{polyol} particles are much smaller, *ca.* 12 nm, while Ni_{polyol}/ATO 20 wt.% ones present a mean diameter of 5 nm (both values based on the measurements of 50 distinguishable particles); the smaller size is attributed to the presence of the ATO support (Figure III.3 (c-d) and (e-f) respectively). High-magnification imaging was not possible for the Ni_{polyol} material, as the oxidized particles and ligands surrounding them were changing (being reduced) rapidly under the electron beam: a bright disk is visible for Ni_{HI}, Ni_{polyol} and Ni_{polyol}/ATO NPs. Ni_{polyol}/ATO NPs look polycrystalline and it is difficult to distinguish the Ni

particles from the substrate, owing to their too close average atomic number (the same observation had already been noticed for Pt/ATO NPs [205]). Similarly to $FeNi_3$@Mo particles, the solvent on the Ni_{OGM} NPs TEM grid has been evaporated slowly, which allowed to have a planar distribution of the particles (Figure III.3 (g-h)). These are spherical and polycrystalline, with an average diameter of 17.4 nm (based on the measurement of *ca.* 300 particles); again, the NPs are organized in large agglomerates.

X-ray diffractograms in Figure III.4 indicate that Ni_{HI} particles are composed of a cubic and a hexagonal Ni phase, while the other Ni particles present a cubic Ni phase. ATO is composed of a tetragonal SnO_2 phase. The crystallite sizes for Ni_{HI} are *ca.* 11.9 ± 1.5 nm for the cubic phase and 12.9 ± 2.9 nm for the hexagonal phase, much smaller than the apparent TEM-based particle size for this material, which confirms the observations derived from the TEM analyses (polycrystalline NPs). Ni_{polyol} presents crystallites of 7.2 ± 1.9 nm in cubic phase - consistent with TEM observation, while after being supported by ATO, the crystallites grew up to 10.2 ± 1.7 nm. The supported Ni_{polyol} NPs are bigger probably because Ni NPs act as a reducing agent compared with the ATO, so that the Ni_{polyol} NPs get oxidized and grow in size. In any case, both NP size values are within the error bars. Tetragonal SnO_2 phase shows smaller crystallites of 4.8 ± 0.3 nm. Ni_{OGM} particles fit with a cubic Ni phase (same PDF card but for the K_α-Co wavelength), and display a crystallite size of 6 nm. All the crystallite sizes computed from the Scherrer's equation are inferior to the mean diameter measured from TEM pictures, confirming the polycrystalline structure of the particles and their surface oxidation. The physicochemical data of the different Ni particles are summarized in Table III.2.

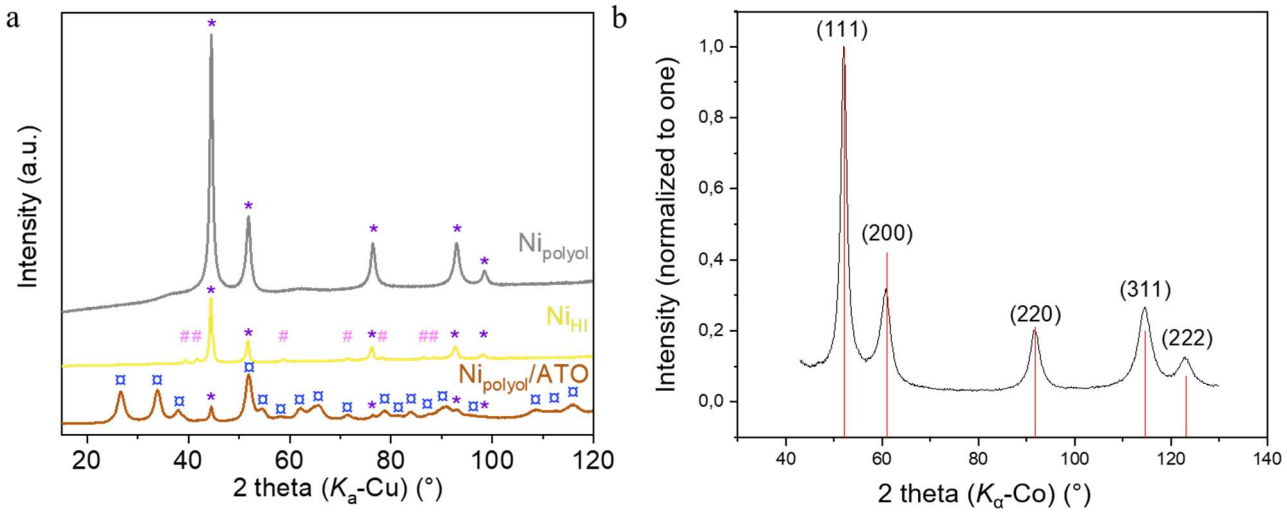

Figure III.4: (a) XRD patterns of Ni_{HI}, Ni_{polyol} and Ni_{polyol}/ATO obtained with a K_α-Cu X-ray source. The star, the hash and the circle symbols correspond to cubic Ni (PDF card 00-004-0850), hexagonal Ni (PDF card 01-089-7129) and tetragonal SnO2 (PDF card 04-003-0649), respectively. (b) XRD pattern of Ni_{OGM} obtained with a K_α-Co X-ray source. The plane corresponds to the cubic Ni phase.

Table III.2: Physicochemical features of Ni NPs.

Materials	**Diameter (nm)**	**Crystallite size (nm) (Planes of the peaks used)**	**ICP-MS (atomic %)**		
			%Ni	**%Pt**	**%other**
Ni_{HI}	69	11.9 ± 1.5 (111), (200) cubic phase 12.9 ± 2.9 nm (100), (102) hexagonal phase	97.2	2.8	/
Ni_{polyol}	12	7.2 ± 1.9 (111), (200)	98.6	1.4	/
Ni_{polyol}/ATO	5	10.2 ± 1.7 (111), (220) cubic Ni 4.8 ± 0.3 (110), (101) tetragonal SnO_2	23.8	/	67.7% Sb 8.5% Sn
Ni_{OGM}	17.4	6 (111), (220) cubic Ni	81.2	/	/

III.1.3 Benchmark catalysts

The benchmark catalysts used, Vulcan XC72-supported Pt (Pt/C 10 wt.%) for HER and unsupported IrO_2 for OER had been characterized by Gwenn Cognard [257] and Fabien Claudel [252,258] respectively: Pt/C 10 wt.% consists of spherical NPs of 2.5 nm (based on the measurement of *ca.* 200 isolated particles) with similar crystallite sizes; IrO_2 NPs are crystalline round-shape particle with a large crystallite size of 101 ± 48 nm (based on the measurement of *ca.* 200 distinguishable particles), surrounded by an oxide layer.

Thus, TEM micrographs performed in this thesis allowed to observe the shape, the diameter and evaluate the crystallinity of the particles. These latter are oxidized and a layer of ligands surround them. The crystal structure determined by XRD, and X-EDS, ICP-MS measurements confirmed the stoichiometry of the materials. The intrinsic electrochemical activity of these materials was determined using the RDE technique, and durability surveys were conducted on the most active catalysts. Their HER and OER activities were compared to the performances in the PMMA cell afterwards.

III.2 Electrochemical activity toward HER and OER

III.2.1 Measurements with the RDE technique

The activity toward water splitting was evaluated by cyclic voltammetry measurements, as described in part II.2.1.2.

III.2.1.1 Cyclic voltammetry measurements

Figure III.5 presents the electrochemical activity of the materials used toward HER. Each cyclic voltammetry cycle in the Faradaic potential region (CV_F) displayed is representative of the other cycles, all recorded at 5 $mV.s^{-1}$. The current is normalized to the geometric surface area of the glassy-carbon support (0.196 cm^2). Ni_{polyol} voltamperograms are not shown, as its activity was very weak, due to extensive surface oxidation, in accordance with its severe reduction under the electron beam during TEM imaging. The potential *E* is expressed versus the RHE and compensated from the Ohmic drop. It is noted hereafter $E_{RHE} - iR$.

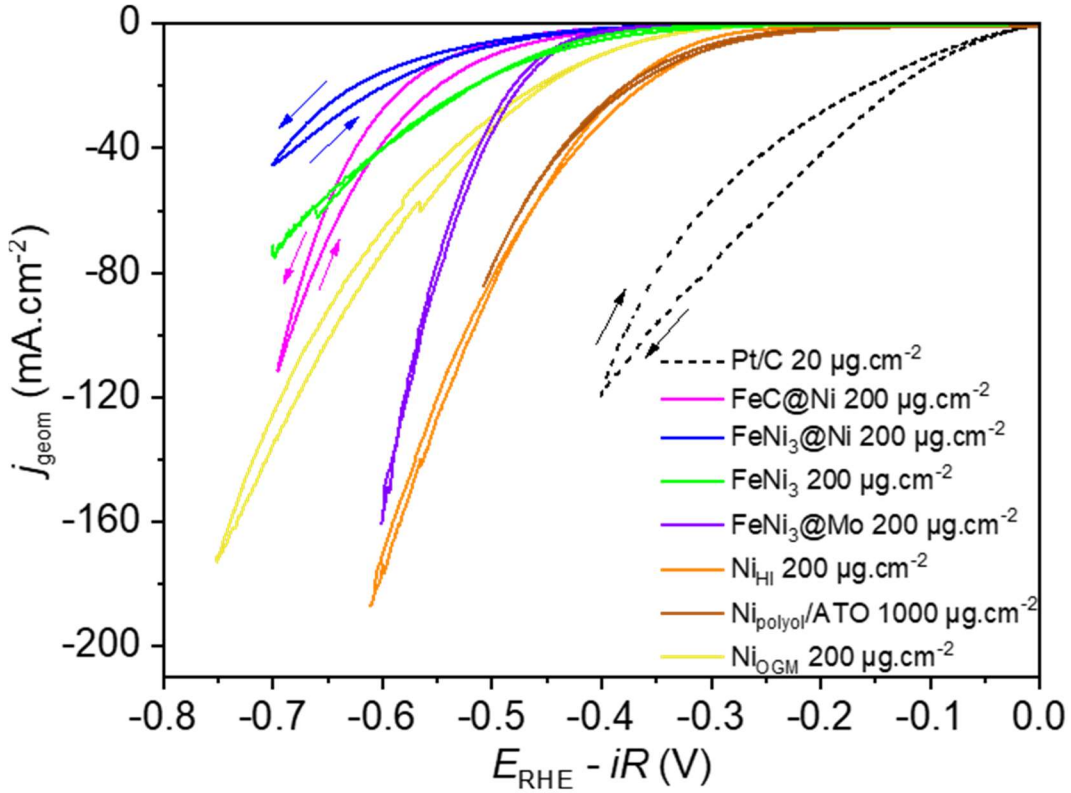

Figure III.5: Electrochemical activity toward the HER in 1 mol.L^{-1} KOH at 25°C of different non-PGM materials compared to the current benchmark Pt/C catalyst in a RDE setup. One representative (and stable) cycle is represented, recorded at a scan rate of 5 mV.s^{-1} and at ω = 1600 rpm. Arrows indicate the scan direction.

The materials are not equivalent in terms of activity. The HER performances decrease in the following order (considering the overpotential at 10 mA.cm^{-2}): Pt/C >> Ni_{HI} > Ni_{polyol}/ATO > Ni_{OGM} > $FeNi_3$@Mo > $FeNi_3$ > FeC-Ni > $FeNi_3$@Ni. The non-PGM inks were loaded at 200 µg.cm^{-2}, tenfold those of Pt/C. The loading of the non-PGM electrodes was chosen higher as the activity was weak at 20 µg.cm^{-2}. Nevertheless, as they do not belong to PGM materials, a larger amount of matter can be employed without compromising the practical applicability of the catalysts. Table III.3 presents the overpotentials of the catalysts at −10 mA.cm^{-2}.

Table III.3: Overpotentials of the studied catalysts at -10 mA.cm^{-2}, in the RDE setup.

Catalysts	Pt/C	Ni_{HI}	Ni_{polyol}/ATO	Ni_{OGM}	$FeNi_3$@Mo	$FeNi_3$	FeC-Ni	$FeNi_3$@Ni
Overpotential (mV) at −10 mA.cm^{-2}	80	310	320	400	450	450	500	530

Small activity decrease was recorded after *ca.* 10 cycles, indicating little initial degradation of the materials (which is classical in alkaline WE [259,260]), except for Ni_{polyol}/ATO, which is due to its initial surface oxidation. The current densities increase exponentially with the potential, in accordance with the Butler-Volmer law (Eq. II.1), which indicates that the reactions are essentially kinetically limited by charge-transfer under these conditions.

It was decided to focus the research on Ni_{HI}, as it is the best non-PGM HER catalysts among those studied. Ni_{polyol}/ATO was excluded due to its fast degradation. Inks with different catalyst loadings were prepared by maintaining the same DI water-Nafion/IPA ratios. Figure III.6 shows that the activity increases first up to 200 µg.cm^{-2} then decreases to 1000 µg.cm^{-2}. An explanation attempt could be a detrimental effect of the active layer thickness: a thin layer results in too few active sites, while too thick layers could prevent hydroxide ion access to all active sites, and larger active site masking due to bubbles. Ni_{polyol}/ATO shows similar activity to Ni_{HI} at an equivalent metal loading, before its dissolution.

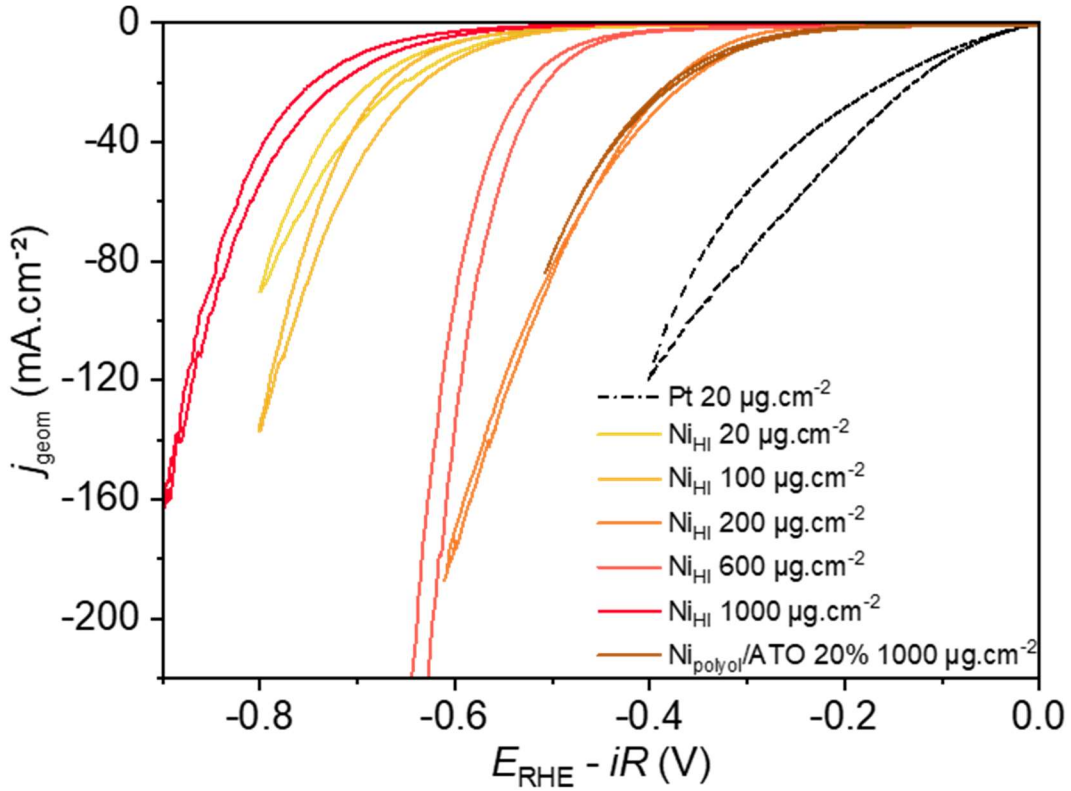

Figure III.6: Nickel loading study on Ni_{HI} in the HER side; voltamperograms recorded at 5 mV.s^{-1} and at ω = 1600 rpm in 1 mol.L^{-1} KOH, T = 25°C.

Figure III.7 displays the CV_F of the same non-PGM materials for the OER, compared with the unsupported IrO_2 (commercial) reference catalyst. Similarly, the loading of the non-PGM material is ten times that of IrO_2, as the activity of the former were weak at 20 µg.cm^{-2}.

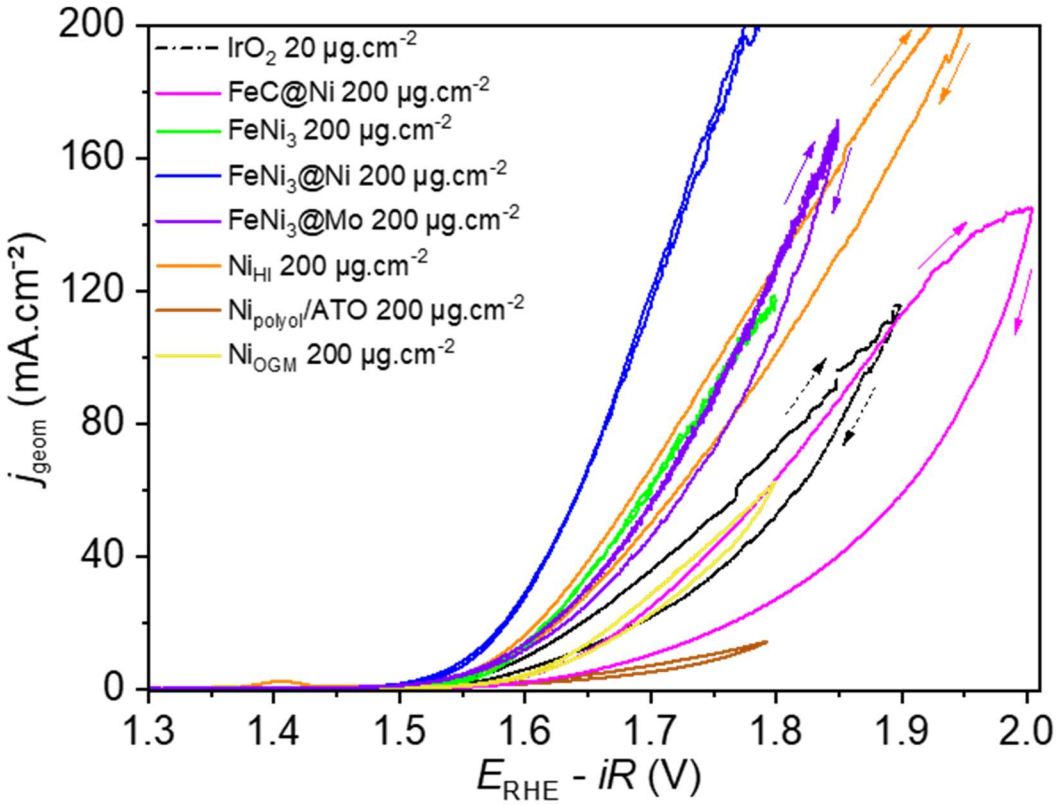

Figure III.7: Electrochemical activity toward the OER in 1 mol.L^{-1} KOH at 25°C of different non-PGM catalysts loaded at 200 µg.cm^{-2} compared to the commercial reference IrO_2 catalyst loaded at 20 µg.cm^{-2} in a RDE setup. One cycle is represented, recorded at a scan rate of 5 mV.s^{-1} and at ω = 1600 rpm.

The OER performance decreases in the following order: $FeNi_3$@Ni > Ni_{HI} > $FeNi_3$ > $FeNi_3$@Mo > IrO_2 > Ni_{OGM} > FeC-Ni > Ni_{polyol}/ATO. Again, several catalysts prove to be more active than FeC-Ni, and, more surprisingly, also more active than IrO_2. The best catalysts are $FeNi_3$@Ni and $FeNi_3$, indicating that the Ni enrichment does enhance the activity, as was thought and discussed in section II.1.1. Table III.4 displays the overpotential of the catalysts at +10 mA.cm^{-2}.

Table III.4: Overpotentials of the studied catalysts at +10 mA.cm^{-2}, in the RDE setup.

Catalysts	$FeNi_3$@Ni	Ni_{HI}	$FeNi_3$	$FeNi_3$@Mo	IrO_2	Ni_{OGM}	FeC-Ni	Ni_{polyol}/ATO
Overpotential (mV) at +10 mA.cm^{-2}	320	350	350	350	370	400	410	510

Again, the reactions are essentially kinetically limited by charge-transfer in these conditions (Butler-Volmer behavior). A higher degradation of the active layers after *ca.* 10 cycles is observed upon OER: small pieces of the deposited layer which detached and fell down in the bottom of the Teflon beaker were visible. This is classical, durability issues are more significant in the intense oxidizing conditions experienced at the oxygen electrode [261].

A loading survey was also conducted, but with $FeNi_3$ catalyst, rather than with $FeNi_3$@Ni (Figure III.8). The former was preferred, as its synthesis is twice shorter and it presents better heating properties under AMF (Figure II.1).

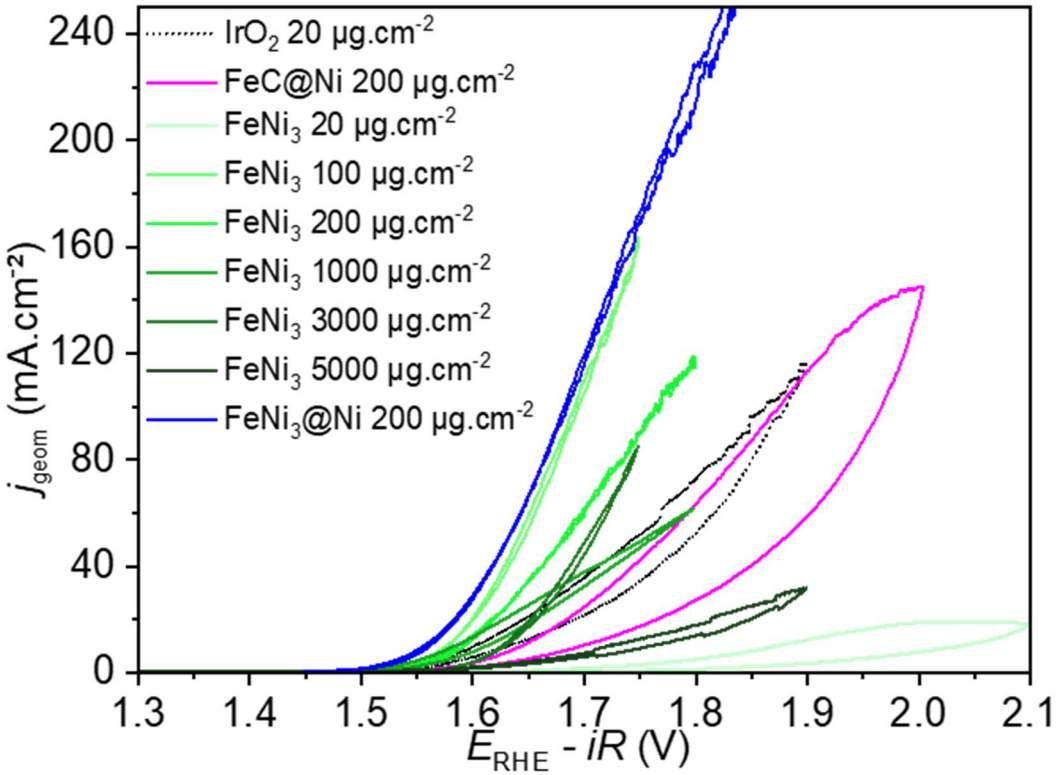

Figure III.8: Loading study on $FeNi_3$ in the OER side, voltamperograms recorded at 5 mV.s^{-1} and at ω = 1600 rpm in 1 mol.L^{-1} KOH, T = 25°C

The OER activity increases from 20 to 100 µg.cm^{-2} and then decreases continuously up to 5000 µg.cm^{-2}. The highest activity was thus observed at 100 µg.cm^{-2}, equivalent to the one of $FeNi_3$@Ni at 200 µg.cm^{-2}. Again, increasing the loading creates more active sites, but at too high loading, detrimental effects occur: a more pronounced resistive effect within thick layers inducing potential gradients and preventing all active sites to operate homogeneously, bubbles entrapment and detachment of the active layer due to bubble growth and departure [237].

To conclude on these first results, almost all the catalysts studied proved to be more active than FeC-Ni on the HER side (except for $FeNi_3$@Ni), which was an objective of this first study, although their activity remains far below those of Pt/C. On the OER side, $FeNi_3$-based and Ni_{HI} catalysts exhibit better activity than FeC-Ni, and outperform IrO_2, although for a loading 10 times higher. Better catalysts for water splitting have thus been obtained.

As stability issues were observed, especially in the high potential region, ageing stress tests were conducted on $FeNi_3$(@Ni) and Ni_{HI} for HER and on $FeNi_3$(@Ni) for OER to evaluate the durability of the most active catalysts. While $FeNi_3$(@Ni) catalysts were not good HER catalysts, the AST study was conducted on them also, because it was known at this time that their SAR was high, while the SAR values of the other catalysts were unknown. Thus, even if the HER $FeNi_3$(@Ni) performances were not good, they could be enhanced by an AMF exposure.

III.2.1.2 Durability study on the most active catalysts

The activity changes of Ni_{HI} at 200 µg.cm^{-2}, $FeNi_3$ at 100 µg.cm^{-2} and $FeNi_3$@Ni at 200 µg.cm^{-2} was evaluated through accelerated stress tests, the methodology of which has been described in subsection II.2.1.4. Besides, the CV_C were analyzed to determine the ECSA and its evolution. The determination of the ECSA has been described in part II.2.1.2. The ECSA

determination in the HER side was not really relevant as the catalysts were oxidized, (Figure III.9), leading to a masking of the α-Ni(OH)$_2$ peaks, as explained in Figure II.3. It was nevertheless realized to get free from the different catalyst loadings used.

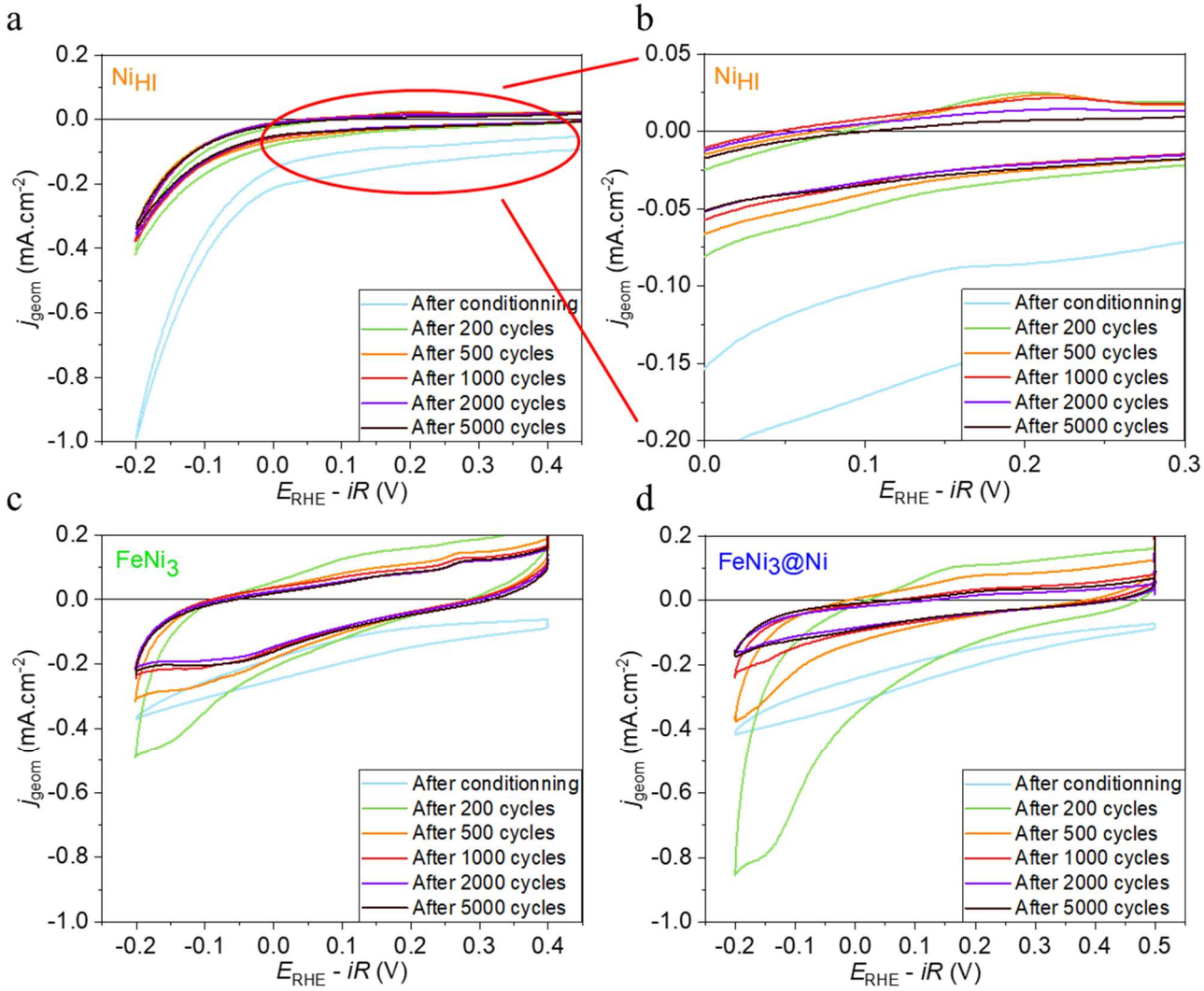

Figure III.9: CV$_C$ profiles in the HER region of three catalysts: (a) Ni$_{HI}$ 200 µg.cm^{-2} with a closer look in (b), (c) FeNi$_3$ 100 µg.cm^{-2} and (d) FeNi$_3$@Ni 200 µg.cm^{-2}. The CV$_C$ were conducted in KOH 1 mol.L^{-1} at a scan rate of 20 mV.s^{-1} and at T = 25°C.

On all graphs, a small and continuous reduction (cathodic peak at 0.06 V$_{RHE}$ and anodic peak at 0.26 V$_{RHE}$) is visible. The first cycles (bright blue curve) are always below 0 mA.cm^{-2} and the curves are tilted, which is characteristic of an O$_2$ presence, although an Ar bubbling of 10 minutes was realized before each measurement; it appeared that the CE was not gastight, which explains this observation. Nevertheless, the next CV$_C$ after the several AST cycles are around 0 mA.cm^{-2}, indicating that the O$_2$ was progressively purged by the Ar bubbling. Besides,

one remarks that for all catalysts, the first cycle exhibits very small current and does not present the characteristic cathodic/anodic peaks of α-$Ni(OH)_2$, while after 200 cycles, the cycles do. This is probably due to the remaining ligands present around the three catalysts after their syntheses (visible in TEM - see part III.2.1.3) and/or to a progressive (partial) reduction of the oxide layer by the prolonged potential cycling inside "reducing" conditions. This has been recently showed by Ferreira and Jerkiewicz [262]. It can be noted that the double layer contribution (area under the curves) is different for the catalysts, being the smaller for Ni_{HI} and the bigger for $FeNi_3$, which could indicate a higher surface roughness with more active sites for $FeNi_3$. Hence, the activity of $FeNi_3$ should be higher than $FeNi_3$@Ni. This comparison between the catalysts is possible because their structure and composition are very close, while it is not possible to compare $FeNi_3$(@Ni) and Ni_{HI}.

The current density normalized by the geometrical area and ECSA recorded at the lowest potential recorded, $-0.7\ V_{RHE}$, the overpotential at $-10\ mA.cm^{-2}$ and the dissolution of the catalysts (compared to the initial catalyst mass deposited onto the glassy carbon support) determined by ICP-MS throughout the cycles are presented in Figure III.10. The blank reference for the ICP-MS was the KOH electrolyte, as this latter contains traces of impurities, especially Fe and Ni.

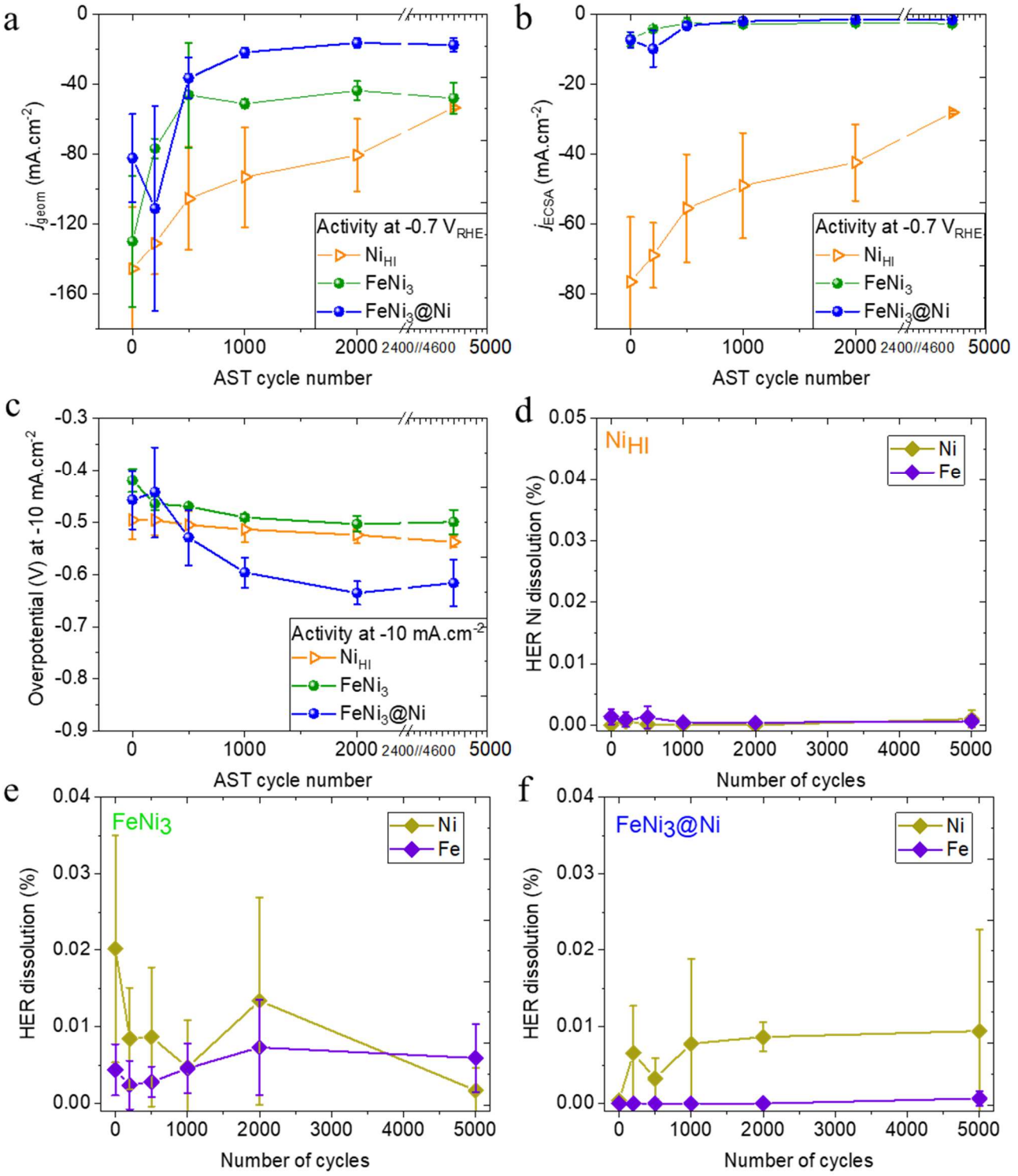

Figure III.10: (a) Geometrical current density at −0.7 V_{RHE} *vs.* AST cycle number, (b) ECSA current density at −0.7 V_{RHE} *vs.* AST cycle number, (c) Overpotential at –10 mA.cm^{-2} *vs.* AST cycle number. Dissolution percentage of Fe and Ni *vs.* AST cycle number for (d) Ni_{HI} 200 µg.cm^{-2}, (e) $FeNi_3$ 100 µg.cm^{-2} and (f) $FeNi_3$@Ni 200 µg.cm^{-2}.

The activity change of the catalysts is different in Figure III.10 (a). Ni_{HI} performance decreases progressively down to –54 mA.cm^{-2}, $FeNi_3$ activity decreases abruptly after 500 cycles and remains quite constant at –48 mA.cm^{-2} up to 5000 cycles, while $FeNi_3$@Ni activity reaches a maximum after 200 cycles after falling down far below $FeNi_3$ activity, at –17 mA.cm^{-2}, as expected from the double layer observations. The activity peak of $FeNi_3$@Ni is explained

as follow: at the beginning of the experiment, the remaining ligands cover the catalyst surface, which prevents the active sites from being available. Then, the KOH electrolyte destroys the ligands, so that more active sites are (transiently) available, before being degraded. TGA analysis indicated that more ligands are present in $FeNi_3$@Ni (88% of metal content while $FeNi_3$ presented a 94% metal content), which explains why no activity peak is visible for $FeNi_3$. TGA on Ni_{HI} indicated only a 62% metal content, which goes against the previous explanation, although this does not take into account the oxide mass. However, as the catalyst is different, it is difficult to rely on it. Figure III.10 (b) presents the current density normalized by the ECSA calculated from the second cycle (after 200 AST cycles) from 0.05 V_{RHE} to 0.3 V_{RHE} and using a specific charge of 514 $\mu C.cm^{-2}$. The calculated ECSA were 0.373, 3.63 and 2.22 cm^{-2} for Ni_{HI}, $FeNi_3$ and $FeNi_3$@Ni respectively. As the CV_C flattened throughout the AST cycles, the ECSA of the other curves became irrelevant, and was not calculated. So, Ni_{HI} exhibits a much higher specific activity, but its ECSA is lower. Two hypotheses can be put forward to explain the bad activity and degradation of Ni_{HI}. First, the major part of the catalyst thin layer is irreversibly oxidized, which is not an active oxidation state; if a small fraction of its surface was reduced to metallic Ni, the activity would not be any better, as an active Ni state for HER is partially oxidized [263]. These two arguments apply also for $FeNi_3$(@Ni) catalysts. The overpotentials at $-10\ mA.cm^{-2}$ in Figure III.10 (c) follow the same trends than the current densities in (a). Almost neither Fe nor Ni dissolutions were recorded by ICP-MS for the three catalysts, although higher values have been found for $FeNi_3$ than Ni_{HI} and $FeNi_3$@Ni. These latter could stem from particle detachments which would have been pipetted and measured. Indeed, small dark aggregates were visible at the bottom of the Teflon beaker and these ones were generally not pipetted for ICP-MS measurements, except for $FeNi_3$. Moreover, the electrolyte was probably not homogeneous, which accounts in part to the huge error bars on Figure III.10 (d-f) (all the measurements were conducted on three independent samples). The electrolyte could have been

ultrasonicated for homogenization and aggregates breaking, but this would have implied to disassemble the cell and break the Ar atmosphere, which was likely to disrupt the measurements. Finally, it has to be noted that the overlapping percentage of the intern standard for the ICP-MS was 80 ± 5%, instead of 100 ± 5%, indicating that the measured values are trustful at 80%. This could be due to the presence of potassium (from KOH), which consumes a part of the flame energy (see part II.4.4). Nevertheless, the values are far below those of KOH, indicating that there is no dissolution of the catalysts (but catalyst layer detachment), and that the electrolyte gets purified of Ni/Fe initially present in KOH [182].

The OER CV_C profiles of $FeNi_3$(@Ni) catalysts are displayed in Figure III.11.

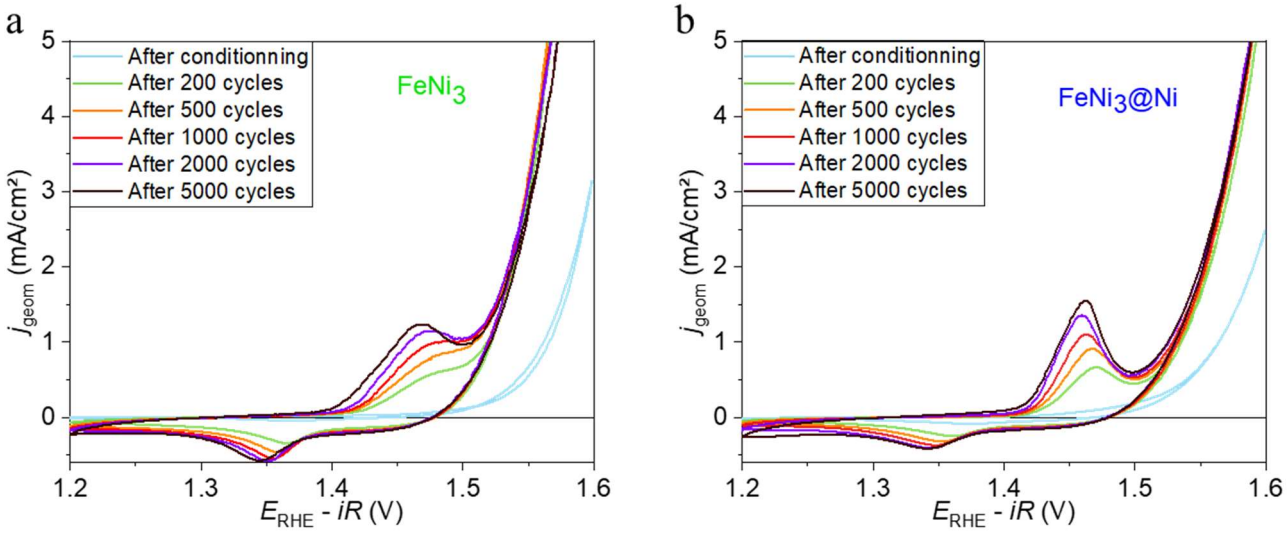

Figure III.11: CV_C profiles in the OER region of (a) $FeNi_3$ 100 µg.cm^{-2} and (b) $FeNi_3$@Ni 200 µg.cm^{-2}. The CV_C were conducted in KOH 1 mol.L^{-1} at a scan rate of 20 mV.s^{-1}.

For both catalysts, the first CV_C cycle shows that the material is not active while the following cycles display much better performances. The OH^- adsorption is prevented by the adsorbed impurities and the remaining ligands, which progressively get oxidized. After cycling the oxides grow: β-NiOOH are formed and β-$Ni(OH)_2$ continues to grow. The last oxide is irreversible and its presence is confirmed as the cathodic peak at 1.35 V_{RHE} is not as big as the anodic one at 1.47 V_{RHE}; it saturates from 2000 cycles, so that all oxides are not reduced [224]. Besides, it shifts towards lower potentials, indicating that it is harder to reduce the oxides (the

oxide layer is thicker). In the case of $FeNi_3$@Ni, it seems that more irreversible oxides are created, which could explain its much lower activity at 1.8 V_{RHE} (factor 2 compared with $FeNi_3$) shown in Figure III.12.

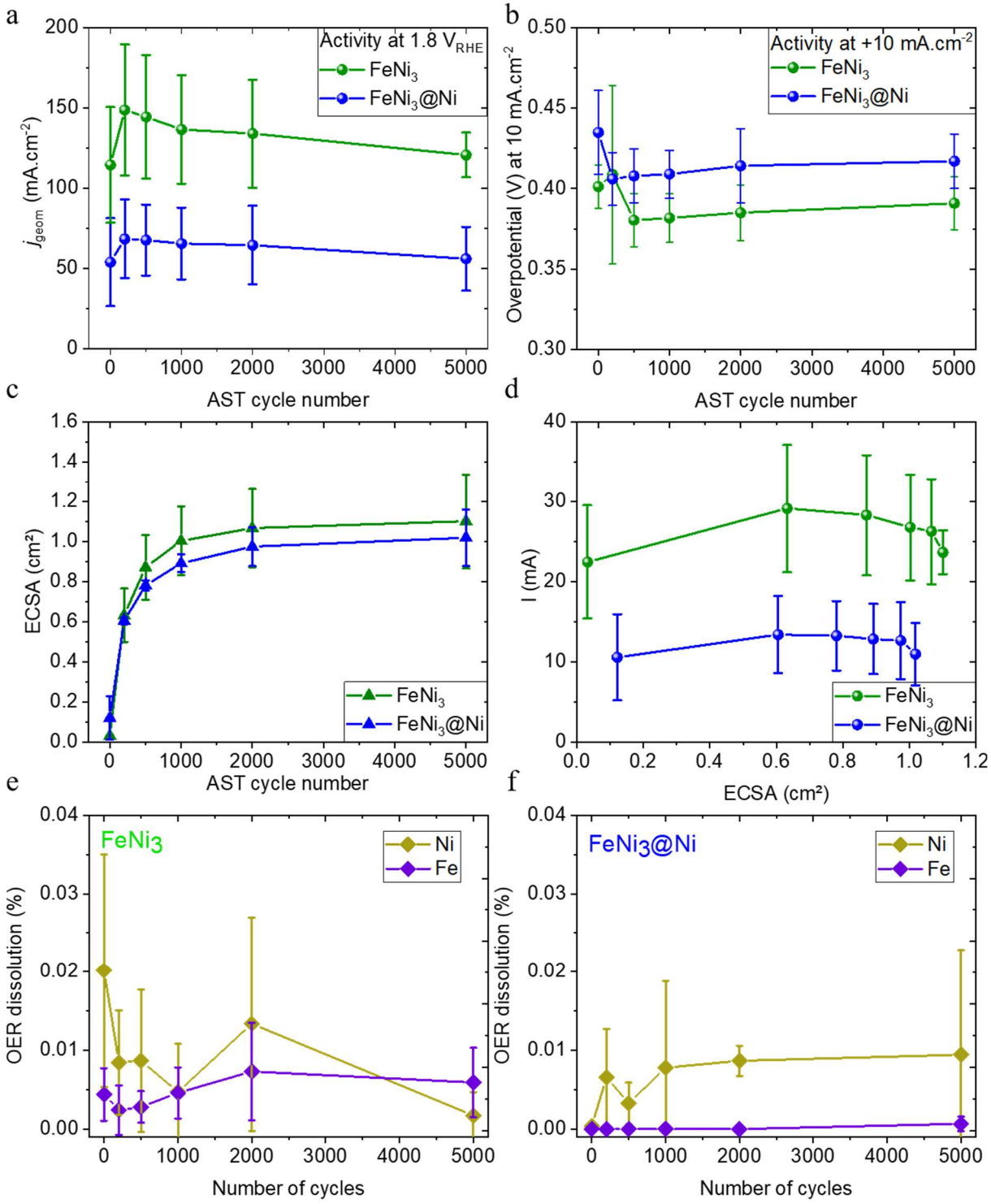

Figure III.12: (a) Geometrical current density at +1.8 V_{RHE} *vs.* AST cycle number, (b) Overpotential at +10 mA.cm^{-2} *vs.* AST cycle number, (c) ECSA evolution *vs.* AST cycle number, (d) current at +1.8 V_{RHE} *vs.* ECSA. Dissolution percentage of Fe and Ni *vs.* AST cycle number for (e) $FeNi_3$ 100 µg.cm^{-2} and (f) $FeNi_3$@Ni 200 µg.cm^{-2}.

For both catalysts, a peak of current density is registered after 200 cycles (Figure III.12 (a)), after which the performances decrease monotonously and slightly; they remain above the initial current density values after 5000 cycles. This trend shows that the catalysts are firstly activated, because the adsorbates and ligands initially present after their synthesis are progressively oxidized/stripped, as testified the very low initial ECSA presented in Figure III.12 (c); this "cleaning" is however accompanied by their progressive and detrimental surface oxidation, hence the OER deactivation. The overpotentials on Figure III.12 (b) follow the same trend than the current densities (but inversed obviously): the overpotentials decrease when the peak in current density is reached, then they keep increasing gently. The activity of $FeNi_3$@Ni is twice lower than that of $FeNi_3$, as expected, and in accordance with the higher quantity of irreversible oxides observed for $FeNi_3$@Ni in the CV_C curves. Figure III.12 (c) displays the ECSA calculated from the cathodic peak at 1.35 V_{RHE}, within the potential range [1.25; 1.45] V_{RHE} of the first CV_C cycle (generally three were made). It is reminded that the specific charge used to calculate the ECSA is normally applied for pure Ni material, and was employed here as an indicator to compare the $FeNi_3$(@Ni) catalysts. Using this methodology, $FeNi_3$ presents a higher (nickel) ECSA than $FeNi_3$@Ni, consistently with the two previous graphs, but the ECSA increases upon AST cycling, in contradiction with the activity decrease. Actually, the activity varies little with the ECSA (Figure III.12 (d)), which indicates that it is the nature of the active sites more than their number which governs the activity, in line with the previous observations about the detrimental material surface oxidation. Again, very little dissolution of Fe and Ni is measured (Figure III.12 (e-f)), but particle detachments were clearly visible, as for HER.

These AST show that the durability of these materials is not perfect, especially because of particle detachments in the RDE configuration (thin active layer deposited on a glassy-carbon tip). Using a more adapted support with better mechanical/electrochemical stability and a better ink formulation to create the active layer (*e.g.* using more binder or another one) could enable

to prevent such degradation mechanism, but it was beyond the initial objectives of this work to study so. Instead, it was chosen to spend more time on the electrochemical activity under AMF, for which the support of choice was dictated by its low heating under AMF. Nevertheless, this point requires necessary development for the future of this project. Further study was conducted on these catalysts with the aim to understand more precisely the activity change and the cause of the degradation. To that goal, ILTEM was performed, which renders possible the observation of different zones of the catalysts deposited on a Ti grid, before and after electrochemical tests. The possible change of local microscopic/nanometric shape and composition of each catalyst can thus be scrutinized.

III.2.1.3 ILTEM $FeNi_3$ and $FeNi_3$@Ni

The Ni_{HI} ILTEM micrographs were imaged but the hard disk containing the data has been lost or stolen. So, no data are available on Ni_{HI}, unfortunately.

Figure III.13 displays similar pictures for $FeNi_3$ and $FeNi_3$@Ni particles, obtained in identical regions prior AST (fresh) and after 500 cycles (aged); only 500 AST cycles were conducted, to be in the situation of the steep decrease in current density observed in Figure III.12 (a). Low and high magnification micrographs are presented in each case.

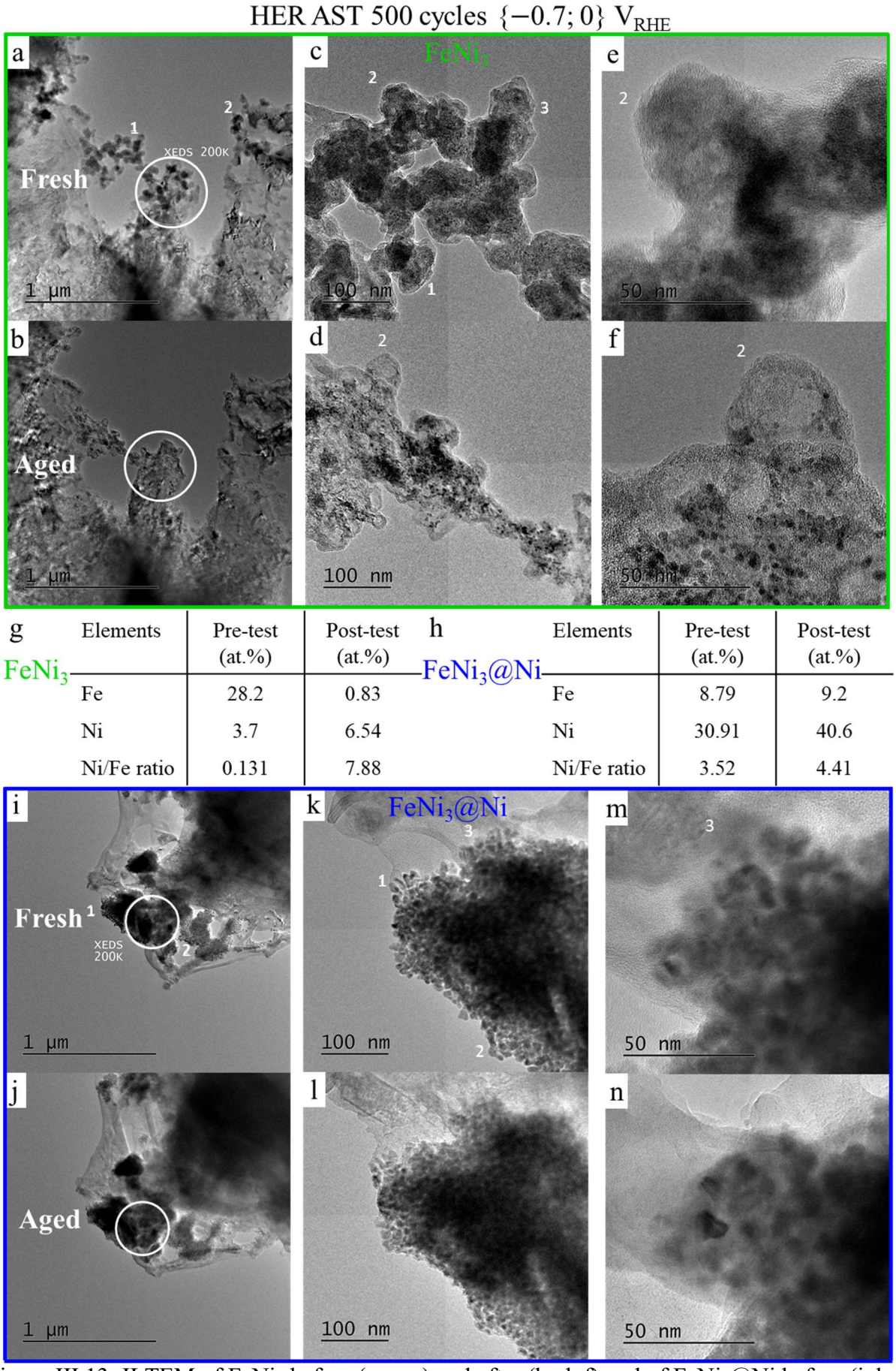

g FeNi$_3$

Elements	Pre-test (at.%)	Post-test (at.%)
Fe	28.2	0.83
Ni	3.7	6.54
Ni/Fe ratio	0.131	7.88

h FeNi$_3$@Ni

Elements	Pre-test (at.%)	Post-test (at.%)
Fe	8.79	9.2
Ni	30.91	40.6
Ni/Fe ratio	3.52	4.41

Figure III.13: ILTEM of $FeNi_3$ before (a, c, e) and after (b, d, f) and of $FeNi_3$@Ni before (i, k, l) and after (j, l, n) the 500 HER AST cycles of durability test. X-EDS analyses of $FeNi_3$ (g) and $FeNi_3$@Ni (h).

The pictures displayed are representative pictures of the three zones observed. The numbers indicate the different parts observed in one zone, and three zones had been scrutinized at the largest magnification (200 keV). The $FeNi_3$ sample underwent much more degradation than $FeNi_3$@Ni. For both materials, the gangue around the particles corresponding to the remaining organic ligands of the synthesis seems "dried" and flattens after the HER test and this effect is enhanced for $FeNi_3$. While the structure of the gangue is quite maintained for $FeNi_3$@Ni, it shrank/shriveled for $FeNi_3$, probably leading to less available active sites, hence its activity decrease. The X-EDS analyses on the displayed zone indicates a huge Fe dissolution for $FeNi_3$, whereas Fe at.% increased in the case of $FeNi_3$@Ni, and Ni at.% increased for both catalysts. However, taking into account the three zones observed for each catalyst, the X-EDS analyses showed a Fe dissolution for both materials, being much more prominent for $FeNi_3$ (confirmed by ICP-MS measurement); while this catalyst showed also a Ni loss, $FeNi_3$@Ni presented a Ni enrichment (no Ni was found by ICP-MS measurement). The Ni^{x+} species being less soluble that the Fe^{x+} ones, the former precipitated more (Ni is nobler than Fe) [264]. Due to the different Fe dissolution rate, more Ni is visible for $FeNi_3$@Ni. This Fe degradation is not in accordance with the dynamic evolution of FeNi catalyst studied by Chung *et al.* by operando ICP-MS, who showed that there is a dynamic Fe exchange (dissolution and redeposition on the electrode surface) from the WE and the electrolyte, indicating the existence of a dynamic evolution of the active sites during the OER process [182] as noted in section II.1.1. In our case, there is an imbalance: the Fe dissolved but did not redeposit at the same rate (if it did).

The evolution of $FeNi_3$(@Ni) catalysts in the OER side is presented in Figure III.14.

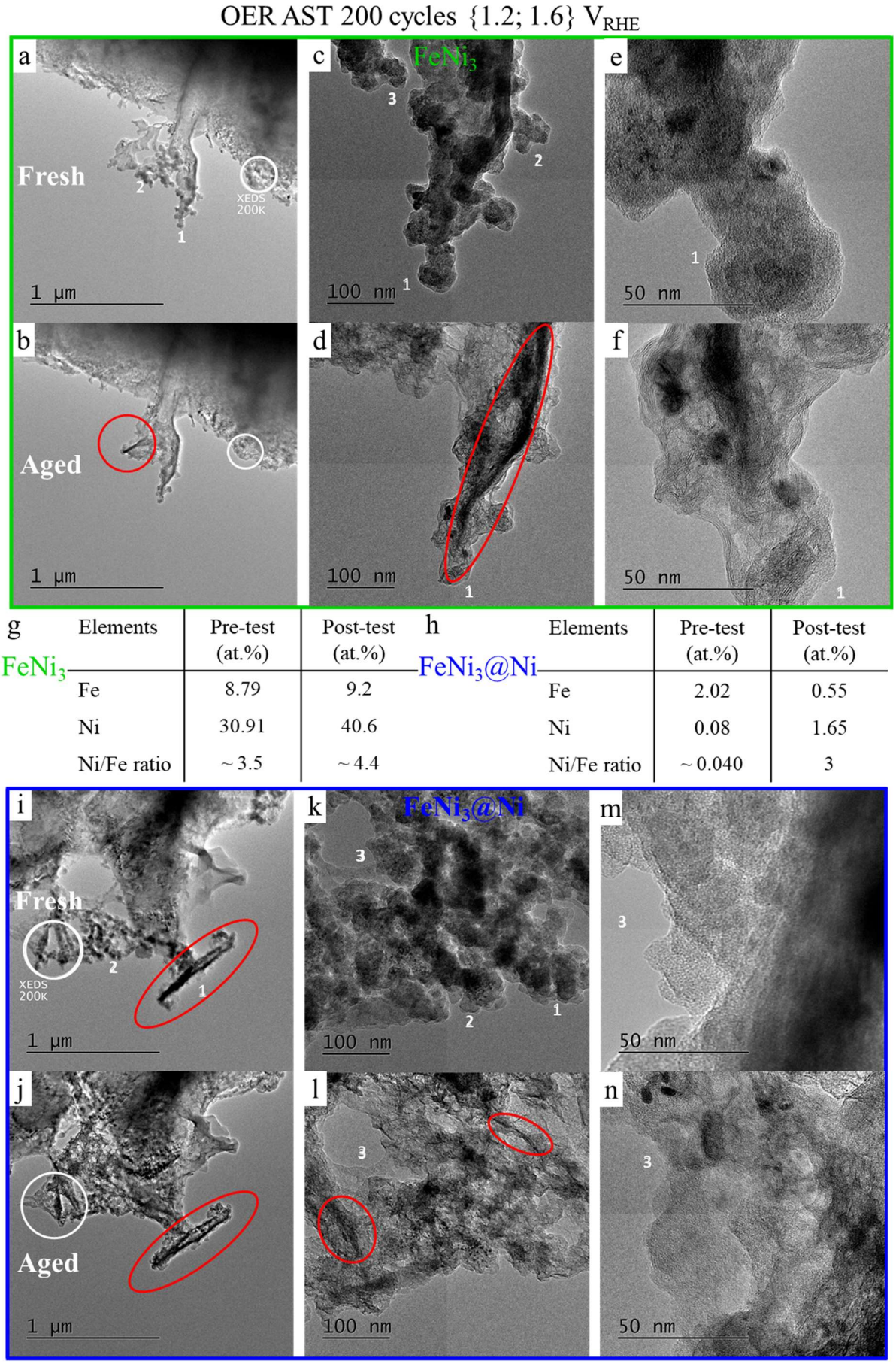

g

FeNi$_3$	Elements	Pre-test (at.%)	Post-test (at.%)
	Fe	8.79	9.2
	Ni	30.91	40.6
	Ni/Fe ratio	~ 3.5	~ 4.4

h

FeNi$_3$@Ni	Elements	Pre-test (at.%)	Post-test (at.%)
	Fe	2.02	0.55
	Ni	0.08	1.65
	Ni/Fe ratio	~ 0.040	3

Figure III.14: ILTEM of FeNi$_3$ before (a, c, e) and after (b, d, f) and ILTEM of FeNi$_3$@Ni before (i, k, m) and after (j, l, n) the 200 OER AST cycles of durability test. X-EDS analyses of FeNi$_3$ (m) and FeNi$_3$@Ni (n).

Again, representative micrographs are displayed, although for $FeNi_3$@Ni, two zones out of three were lost (the remaining zone is presented), and one zone of $FeNi_3$ grid was lost. These losses are surely caused by the harsher (more oxidizing) conditions of OER than of HER, even if similar effects of bubble detachments or grid manipulations can also by mentioned. Again, the structure of the ligand network seems flatten and shriveled, especially for $FeNi_3$. Moreover, NiO_x needles are visible, characteristics of oxidizing electrochemical treatment: dark lines on the picture encircled in red: one appeared on the left tip in Figure III.14 (b), more precisely defined lines are visible in Figure III.14 (b), (d), (j) and (l). Such NiO_x needles are also visible for HER samples, but were present before the AST test, and no further needle were observed after ageing. In addition, graphene planes appeared, as testifies Figure III.14 (f) (parallel lines characteristic of the planes are visible). They probably come from the crystallization of the remaining ligands, which are carbon rich (palmitic acids and toluene). Less graphene planes were visible for $FeNi_3$@Ni, while its TGA values are lower (88%) than $FeNi_3$ (94%), indicating a larger presence of ligands. The X-EDS analyses of the white circled zones in Figure III.14 (a) and (i) leads to the same conclusion as for HER: an Fe dissolution is measured after OER treatment for both catalysts, and enhanced for $FeNi_3$, leading to a Ni dissolution for $FeNi_3$ and Ni enrichment for $FeNi_3$@Ni. ICP-MS measurements confirmed this dissolution for $FeNi_3$, but not for the Ni-enriched catalyst, while no Ni is found by ICP-MS measurements (not shown).

These results tend to show that Fe is an important element in the activity of FeNi-based catalyst, but it gets significantly dissolved in the electrolyte upon HER and OER operation. A Ni enrichment, and so a lower Fe content apparently reduces the activity, as must do the irreversible oxidation of the Ni-surface. The decrease in activity for $FeNi_3$@Ni is limited compared to $FeNi_3$, probably because there is less Fe to dissolve (the Ni-rich outer layer of this material is more robust towards electrochemical operation in these conditions).

The activity of these catalysts was also evaluated in the PMMA cell. As the conditions are different: the support is a carbon felt instead of a glassy-carbon, and an electrolyte flux rate is applied. Thus, the performances could vary. The Ohmic drop was determined and corrected in the same manner than for the RDE experiments, and was in the same range of magnitude.

III.2.2 Electrochemical activity in the PMMA cell

The same catalyst activity toward the HER were tested, except for Ni_{polyol}-based materials, as they suffer from fast dissolution. The performances toward the HER are presented in Figure III.15. The geometrical area was estimated to 1 cm^{-2}, by measuring the diameter of many deposits on the carbon felt, and considering both faces of the carbon felt, although one is pressed against the cell wall, hindering bubble removal.

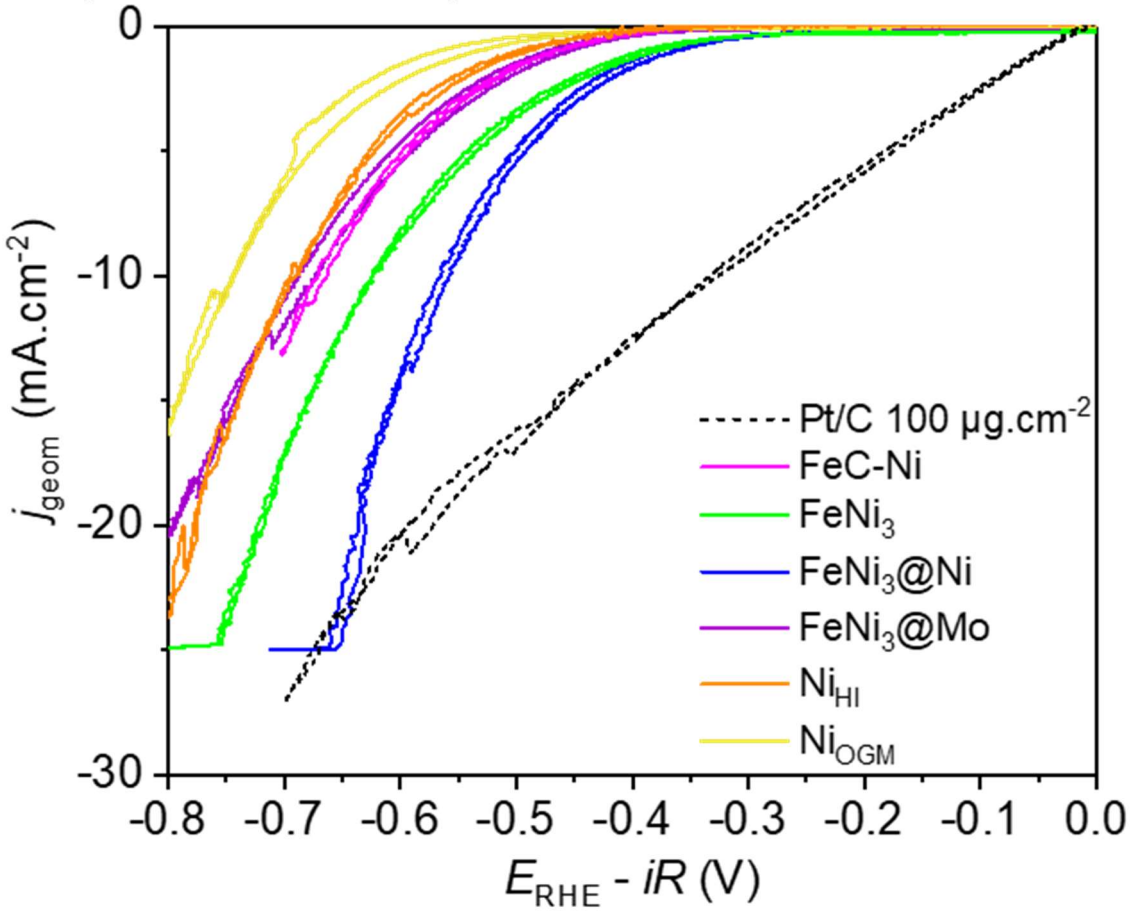

Figure III.15: Electrochemical activity toward the HER in 1 mol.L^{-1} KOH at room temperature (~ 25°C) of different non-PGM materials loaded at 1000 µg.cm^{-2} compared to the current benchmark Pt/C catalyst loaded at 100 µg.cm^{-2} in the PMMA cell. One representative cycle is represented, recorded at a scan rate of 10 mV.s^{-1} and at a flux rate of 83 mL.min^{-1}.

The activity of the catalysts decreases in the following order: Pt/C >> $FeNi_3$@Ni > $FeNi_3$ > FeC-Ni > $FeNi_3$@Mo > Ni_{HI} > Ni_{OGM}. The trend changes from RDE to PMMA cell, probably due to the different conditions cited above, although it is especially significant for Ni_{HI} and Ni_{OGM}. The current was normalized to the geometrical area of the catalyst layer (drop spot), which was similar for all catalysts (the deposition method was identical). However, it is important to note that the support is a felt (the drop could spread inside the felt structure), so that the assumed geometrical area may be underestimated, and the current density may be overestimated. The loading[2] of the non-PGM catalysts are 1000 µg.cm^{-2} while Pt/C was loaded at 100 µg.cm^{-2}. A higher loading was chosen compared to the values used in RDE, because the activity was weak at 200 µg.cm^{-2}. This can be explained by three significant factors: the seal which maintained the WE in place could block catalytic sites; the bubbles issue was important as those located between the cell edge and the carbon felt were blocked and difficult to remove, even at high electrolyte flux rate (see Figure II.8); the last factor is the position of the current collector. The latter should be placed at the center of the carbon felt, where the NPs deposit is; otherwise, the electron conduction is hindered. Therefore, the activity was lower. The overpotentials at –10 mA.cm^{-2} are given in Table III.5:

Table III.5: Overpotentials of the studied catalysts at −10 mA.cm^{-2}, in the PMMA cell.

Catalysts	Pt/C	$FeNi_3$@Ni	$FeNi_3$	FeC-Ni	$FeNi_3$@Mo	Ni_{HI}	Ni_{OGM}
Overpotential (mV) at −10 mA.cm^{-2}	330	560	620	660	680	690	740

A loading study was also conducted on $FeNi_3$ and $FeNi_3$@Ni. $FeNi_3$@Mo was not chosen as its magnetic properties were less interesting (see part III.3 below). Three loadings were tested: 100, 1000 and 3000 µg.cm^{-2} (Figure III.16).

[2] Expressing the loading in µg.cm^{-2} could surprise the reader, as this unity indicates a loading optimized for a glassy carbon support of 5 mm diameter. Nevertheless, keeping this unity when using a different support allows to compare the loadings used in the RDE setup and in the PMMA cell.

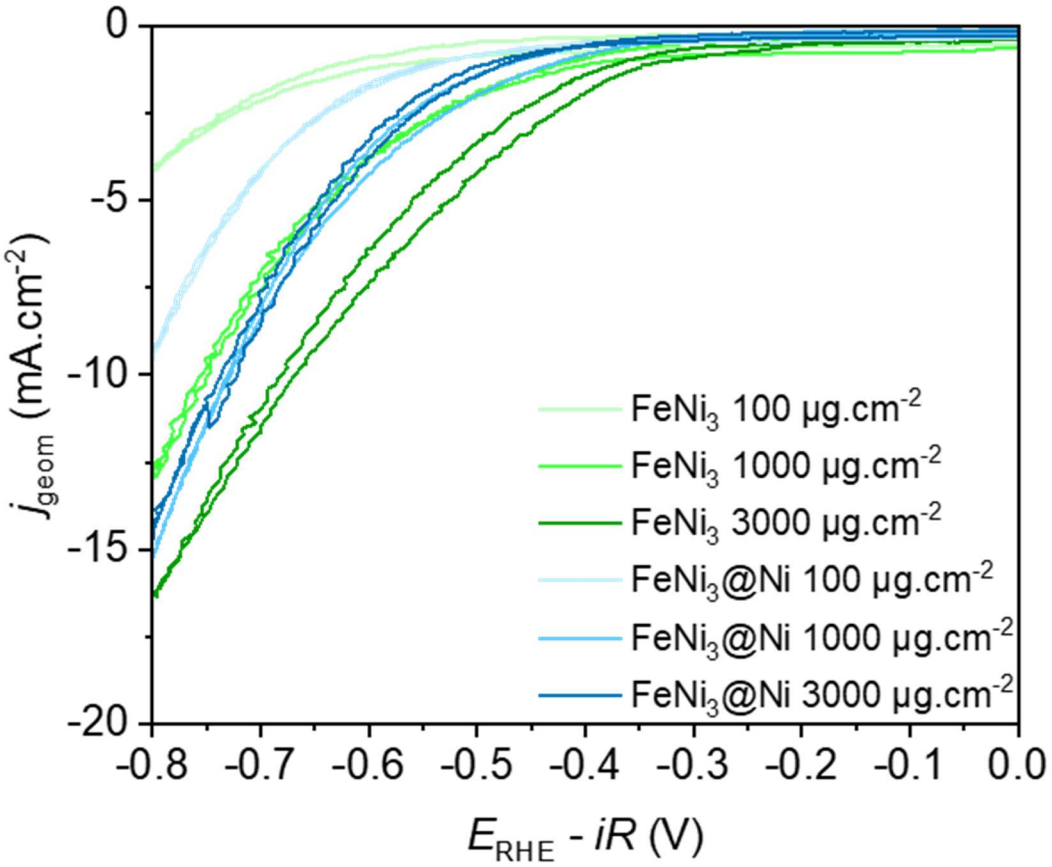

Figure III.16: Loading study on $FeNi_3$ and $FeNi_3$@Ni in the HER side, voltamperograms recorded at 10 mV.s^{-1} and at a flux rate of 83 mL.min^{-1} (PMMA cell).

In the PMMA cell, the trend regarding the loading changes compared to the one observed with the RDE: the higher the loading, the higher the activity (except for $FeNi_3$@Ni where the 1000 and 3000 µg.cm^{-2} curves overlap). The difference with the RDE setup is that the electrode surface area is not limited, as the support is a carbon felt with much bigger geometric area and non-negligible porous volume. Accordingly, the thickness issue with blocking sites encountered in the RDE setup is less significant. Thus, a higher loading leads to more active sites not mutually blocking each other. One remarks that the performances displayed in Figure III.16 are below those of Figure III.15. Indeed, the loading study was conducted before testing all the catalysts in the PMMA cell, and at that time, the current collector was a one-strand Au wire. The Ohmic-losses were higher, and the setup was improved by employing subsequently a rake shape current collector wire, as explained in section II.2.2, which reduced the Ohmic contributions in the cell.

The performances toward the OER are displayed in Figure III.17.

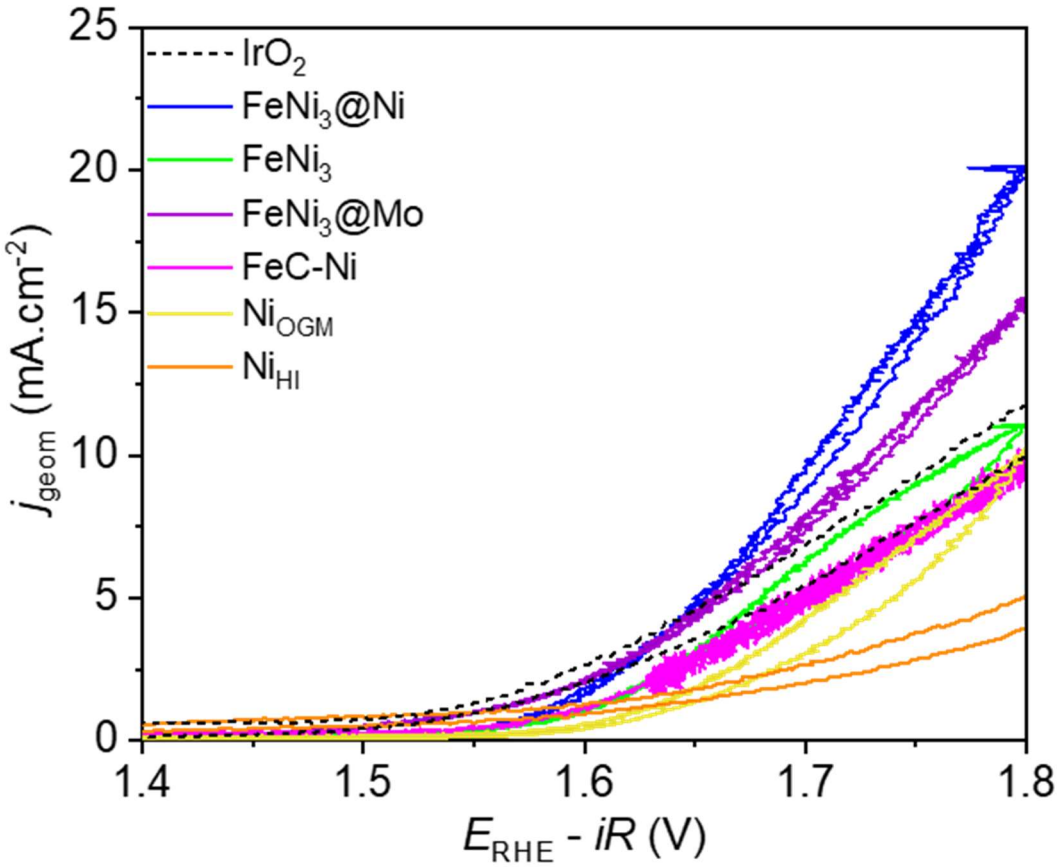

Figure III.17: Electrochemical activity toward the OER in 1 mol.L^{-1} KOH at room temperature (~ 25°C) of different non-PGM materials loaded at 1000 µg.cm^{-2} compared to the current benchmark IrO_2 catalyst loaded at 1000 µg.cm^{-2} in the PMMA cell. One cycle is represented, recorded at a scan rate of 10 mV.s^{-1} and at a flux rate of 83 mL.min^{-1}.

The activity order changed also compared to the RDE setup: $FeNi_3$@Ni > $FeNi_3$@Mo > IrO_2 > $FeNi_3$ > FeC-Ni > Ni_{OGM} > Ni_{HI}. This time, the loading of IrO_2 is similar as the non-PGM material (1000 µg.cm^{-2}), as its activity was too weak at lower loading. Especially again, the activity of the Ni-based materials changed a lot. While the working conditions varies a lot, this discrepancy is strange. The overpotentials at +10 mA.cm^{-2} are given in Table III.6.

Table III.6: Overpotentials of the studied catalysts at +10 mA.cm^{-2}, referred to the RHE, in the PMMA cell.

Catalysts	$FeNi_3$@Ni	$FeNi_3$@Mo	IrO_2	$FeNi_3$	FeC-Ni	Ni_{OGM}	Ni_{HI}
Overpotential (mV) at +10 mA.cm^{-2}	477	500	534	540	570	570	/

A loading study was also performed at three loading: 100, 1000 and 3000 µg.cm^{-2}, on $FeNi_3$(@Ni) for the same reasons cited previously.

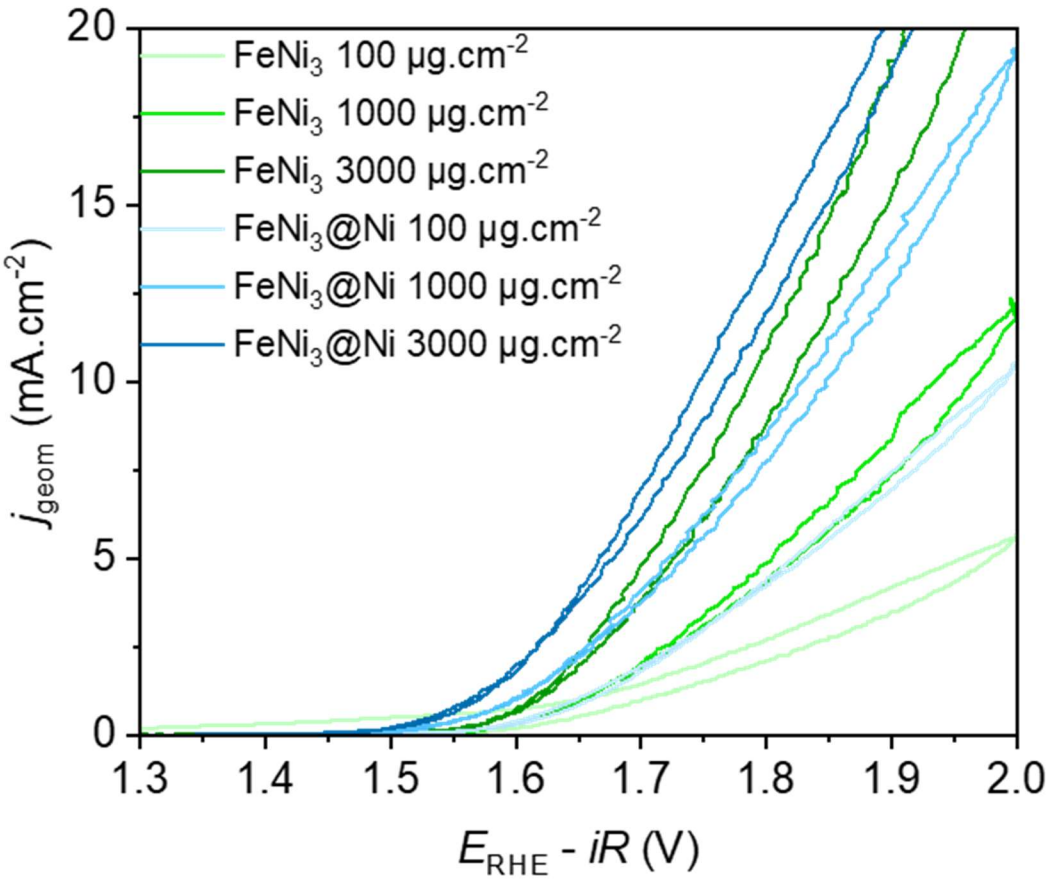

Figure III.18: Loading study on $FeNi_3$ and $FeNi_3$@Ni in the OER side, voltamperograms recorded at 10 mV.s^{-1} and at a flux rate of 83 mL.min^{-1} (PMMA cell).

The same trend is observed than in the OER side, even clearer: the higher the loading, the more active sites are available, the better the performances. Similarly, the performances displayed in the graph above are below those of Figure III.17, for the same reason than for HER measurements.

In conclusion of this section, the electrochemical activity in the PMMA cell was evaluated for the different studied catalysts. The trend is different from the RDE setup due to the different conditions (electrolyte flux rate, nature of the support, position of the working

electrode and the seal, position of the current collector). Especially, determining the ECSA was impossible, as the redox peaks were barely visible in this setup. The experiments nevertheless showed that $FeNi_3$(@Ni) materials behave correctly in the PMMA cell, in particular for the OER, where the performance reached are impressive (outperforming those of the IrO_2 benchmark). A loading study on them indicated that no limitation exists in the large support geometric area used, so that the higher the loading, the better the performances.

III.3 Magnetic properties of the studied catalysts

The magnetic properties of the catalysts were determined by VSM measurements, while SAR measurements indicated their heating power.

III.3.1 VSM measurements

Figure III.19 presents the hysteresis curves of the studied materials measured at 300 K.

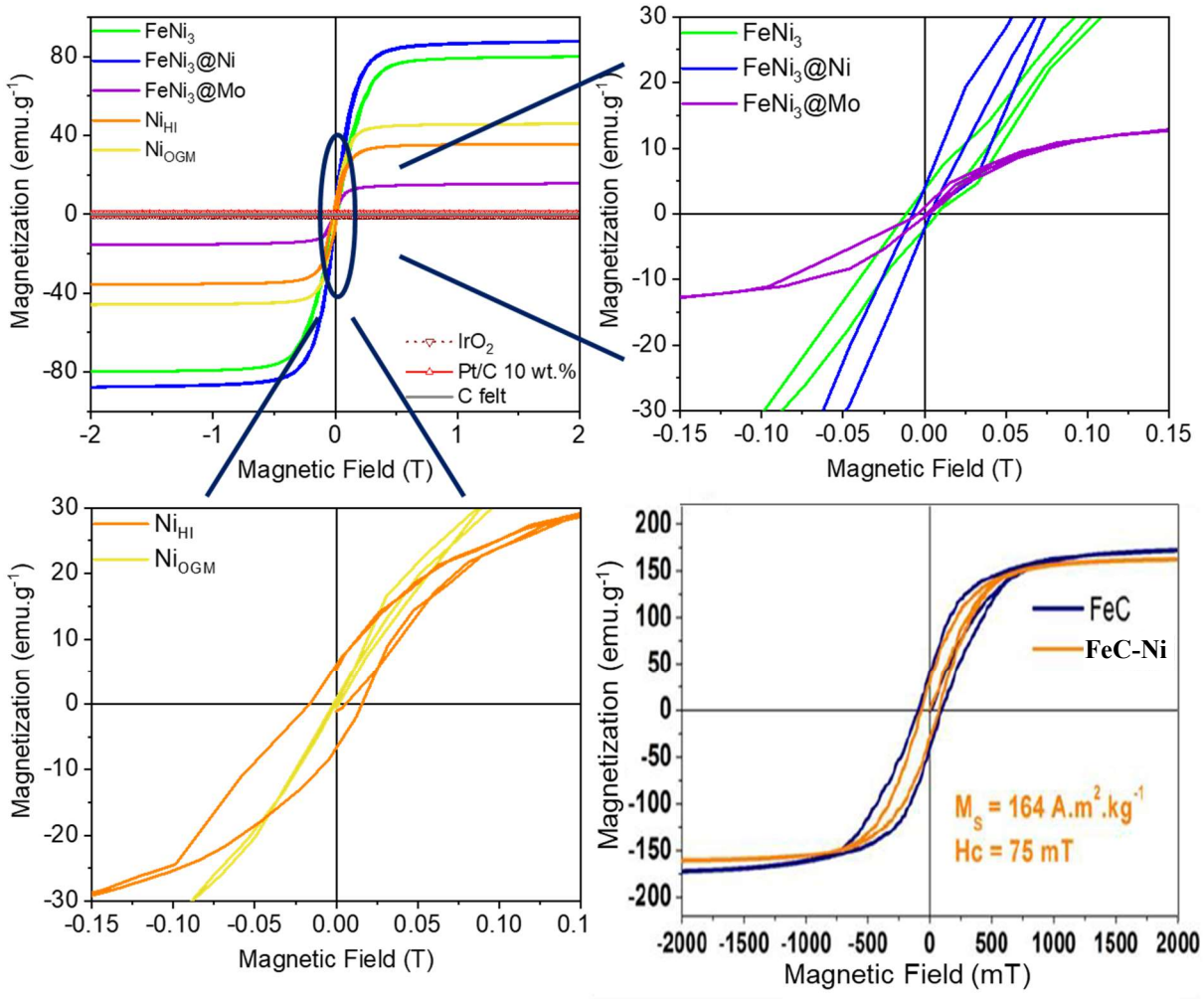

Figure III.19: Hysteresis loops of the studied catalysts, realized at 300 K. The curves of FeC and FeC-Ni are reprinted with permission from [66].

The main magnetics parameters are summarized in Table III.7.

Table III.7: Saturation magnetization M_S, remanent magnetization M_R and coercive field $\mu_0 H_C$ of the materials, at 300 K.

Catalysts	FeC-Ni	$FeNi_3$	$FeNi_3$@Ni	$FeNi_3$@Mo	Ni_{HI}	Ni_{OGM}	IrO_2, Pt/C, C felt
M_S **(A.m^2.kg^{-1})**	160	80	88	15.8	36	46	Negligible
M_R **(10^{-3} A.m^2.kg^{-1})**	30 000	3.0	3.1	0.8	6.4	0.6	Negligible
$\mu_0 H_C$ **(mT)**	80	9.6	5.5	0.22	16	1.6	Negligible

According to the hysteresis cycles and the values in Table III.7, it was deduced that FeNi-based catalysts are soft ferromagnetic materials, with a cycle openness decreasing from $FeNi_3$ to $FeNi_3$@Ni. Surprisingly, $FeNi_3$@Mo presents a very small hysteresis cycle, while it was expected to be ferromagnetic also. The long reaction time (2*72h at 150°C) could have

caused agglomeration or increased the crystallinity, reducing the magnetic properties of this catalyst. Ni-based catalysts tend to be superparamagnetic, with a very small cycle openness, while benchmark catalysts and the carbon felt support present a very close cycle, without surprise, as they are non-magnetic materials. Besides, one can remark that the M_R/M_S ratio is far inferior to 0.5, for all catalyst, so that no chain formation should appear and influence the SAR of the catalysts.

Therefore, it is expected that the SAR of $FeNi_3$(@Ni) is superior to Ni-based particles, being much bigger that $FeNi_3$@Mo and the reference catalysts.

III.3.2 SAR measurements on powder catalysts

The SAR measurements were conducted with ~ 10 mg of catalyst powder, as described in section II.5.2. The following curves were obtained at 100 kHz (Figure III.20):

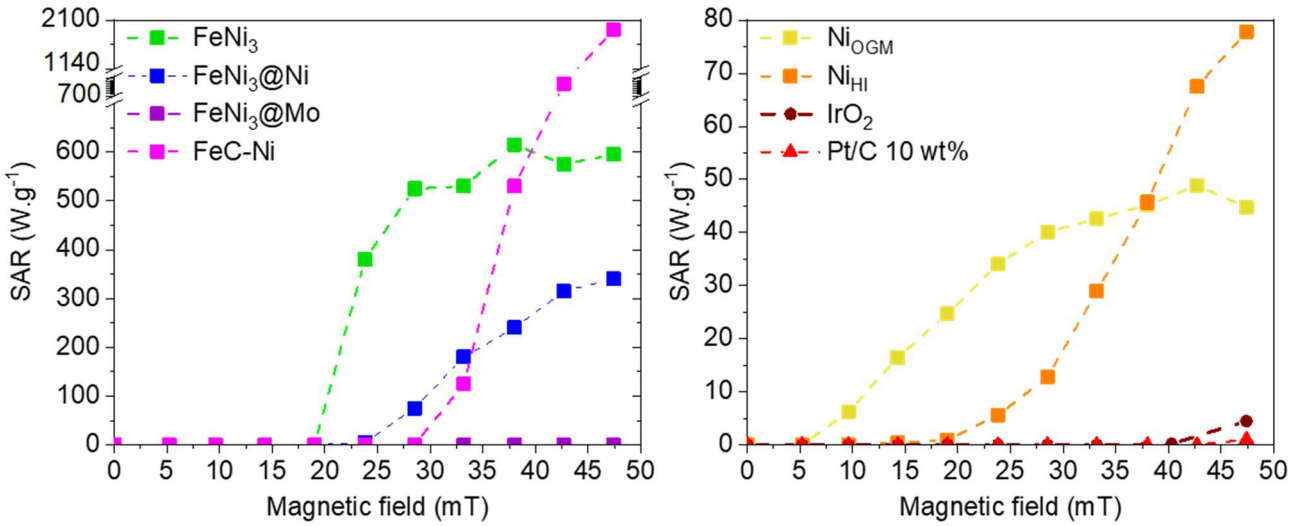

Figure III.20: SAR measurements realized on catalyst powders at 100 kHz.

It has to be noticed that the SAR values given here are at 100 kHz while most of the experiments under AMF were conducted at 300 kHz. The setup used for these measurements was not settable in the 300 kHz coil. Nevertheless, it gives good indications of the heating

power of the materials, and allows to compare the SAR of the studied catalysts. Especially, the heating is expected to be greater at 300 kHz than 100 kHz. It is thus expected that $FeNi_3$(@Ni) catalysts heat more than the Ni-based ones, which should heat more than the reference catalysts and $FeNi_3$@Mo which do not heat, in accordance with the VSM conclusions. Besides, $FeNi_3$ should present much higher magnetic activation than the other catalysts at 25 mT, and Ni_{OGM} could present a magnetic activation from 10 mT while the other should not. Especially, $FeNi_3$@Mo was expected to heat. Nevertheless, it will serve as witness to the AMF influence on the WS activity, compared to $FeNi_3$(@Ni) materials (their composition being close).

In conclusion of this first experimental chapter, the intrinsic electrochemical performances of different materials were measured in an RDE setup. Catalysts with better performances than the previously used FeC-Ni material were prepared and characterized, both for the HER and OER. A loading study allowed to know at which ink concentration the catalysts are the most active in practice for the setups used. Durability and ILTEM surveys indicated that the stability of the catalyst is not perfect on a glassy-carbon support, and that degradation essentially proceeds via layer detachment (durability tests) and Fe dissolution (ILTEM), leading to a reduction of the active sites and a surface enrichment in Ni oxides. While almost no Fe dissolution was detected after durability tests, the ICP-MS values are possibly minimized, as the overlapping percentage of the intern standard was lower than expected (80 ± 5%) whereas after ILTEM, the overlapping was better (100 ± 10%). Thus, the dissolution measurements of the ILTEM survey are probably more trustful. Then, the electrochemical activity of the materials was studied in the PMMA cell. Due to the different operating conditions, the performance trends differ from the activity measured with the RDE setup, especially in the HER side. A loading study indicated that the higher the loading, the better the performances. Finally, magnetic characterizations indicated that while the new materials SAR are far below FeC-Ni's one, they heat at lower MF amplitude, which was one aim of the catalyst optimization.

Chapter IV: AMF influence on the alkaline water electrolysis

Abstract of Chapter IV: In chapter IV, CV_F and chronopotentiometry (CP) tests under AMF are presented. The AMF impacts positively the activity by decreasing the onset potential (CV_F) and decreasing the overpotential (CP), whatever the loading, in both HER/OER side. Surprisingly, null SAR materials are also positively impacted, which raises the question of another contribution to the heating mechanism: eddy currents, while all was set up to minimize them. Further heating measurements confirm their presence. Then, discussions are carried out to understand the effect of the AMF. It seems that it enhances mainly the mass-transport in HER, and the charge-transfer kinetics in OER, while both effects are present. Then, the phenomena under SMF presented in Chapter I section I.4 are evaluated, besides with the Soret, Marangoni and Maxwell stress effect (temperature gradient, surface tension change). Only these three latter, besides with the Kelvin force may intervene. Finally, *post mortem* analyses are conducted. An ILSEM survey indicates that no aggregation of the catalytic NPs occurs, and that the catalyst is not homogeneously distributed onto the carbon felt support. Then, XRD and ETEM study evaluate the influence of the temperature (up to 600°C) and the atmosphere (reductive or oxidant) on $FeNi_3$@Ni catalyst. Several phase changes occur, which are likely to impact its activity toward WS.

Résumé du Chapitre IV : Ce chapitre présente des tests CV_F et CP sous AMF. Le champ alternatif améliore les performances de tous les catalyseurs, en diminuant le potentiel de départ (CV_F) et la surtension (CP), que ce soit en HER ou en OER, et quel que soit le chargement de l'encre. Etonnamment, même les matériaux qui présentaient un SAR faible ou nul sont améliorés. Il est ainsi déduit que les courants de Foucault jouent un rôle non négligeable, bien que tout a été mis en œuvre pour les minimiser. Des mesures de chauffe confirment leur présence. Ensuite, des discussions sont menées pour comprendre comment l'AMF améliore les performances. Il semble que le transport de matière soit particulièrement facilité côté HER, et que la cinétique de transfert d'électrons soit améliorée côté OER, et les deux effets toujours présents. Puis, les phénomènes pouvant survenir sous SMF et abordés au Chapitre I section I.4 sont évalués, ainsi que les effets Soret, Marangoni et Maxwell (gradient de température, variation de tension de surface). Seuls ces trois derniers effets, ainsi que la force de Kelvin, pourraient intervenir dans le système. Enfin, des analyses *post mortem* sont présentées. Une étude en ILSEM montre qu'aucune agrégation survient, et que les agglomérats sont mal répartis sur le feutre. Des mesures XRD et ETEM en température (jusqu'à 600°C) et sous atmosphères réductrice (H_2) et oxydante (O_2) sur $FeNi_3$@Ni montrent que les phases cristallographiques de ce matériau évoluent, ce qui peut modifier sa réactivité par rapport à l'électrolyse de l'eau.

This chapter presents the electrochemical activity of the selected catalysts toward HER and OER under alternating magnetic field. The thermodynamics and kinetics of the reactions under AMF is addressed. Then, the possible effects described in section I.4 are evaluated in the system (Lorentz, Kelvin, spin polarization) and other effects are discussed. Afterwards, the change of the structure and the morphology of $FeNi_3$(@Ni) samples upon operation under AMF was studied by ILSEM. Finally, the influence of the temperature and the atmosphere on $FeNi_3$@Ni material are scrutinized by ETEM observations, as well as by *in situ* XRD measurements performed at several temperatures. In this chapter, only the results obtained with the 300 kHz coil are presented.

IV.1 Electrochemical activity under AMF

The PMMA cell described in section II.2.2 was selected for this study, to characterize the potential effect of magnetic activation by hysteresis losses on the electrochemical activity of the new catalysts. The experiments consisted of CP measurements - as Christiane Niether did, but on a broader magnetic field amplitude range and various catalysts - and CV_F measurements. The results led to question of the heating capacity of the samples, and further magnetic characterizations were conducted to elucidate this point.

IV.1.1 CV_F measurements

A CV_F survey was conducted on $FeNi_3$ and $FeNi_3$@Ni at three different loadings: 100, 1000, 3000 $\mu g.cm^{-2}$ both in the HER and OER side. This study aimed to confirm the conjecture presented in the supplementary figure S12 of Ref. [60], presented below (Figure IV.1). It proposes that the magnetic activation influences the kinetics of the reactions, leading to a change in the

onset potential. Indeed, Christiane Niether observed a decrease in FeC-Ni overpotential of *ca.* 100 mV in HER, and *ca.* 200 mV in OER when applying a 40 mT AMF during CP experiments. Applying these drops in overpotential when conducting cyclic voltammetry test would lead, by conjecture, to a shift of the curve onset toward lower potential in the OER side, by *ca.* 200 mV, as indicated in Figure IV.1. The RuO_x/C (supported on carbon) activity at different temperatures is displayed to indicate the influence of the temperature when heating the whole electrolyte, compared to the hypothetical performance of the FeC-Ni particles under AMF at 40 mT. The change in onset for these latter would correspond to a temperature of 200°C to obtain such shift, according to Arrhenius extrapolated law [60]. Thus, the application of the AMF would lead to a very prominent temperature increase at the catalyst active sites, according to this law.

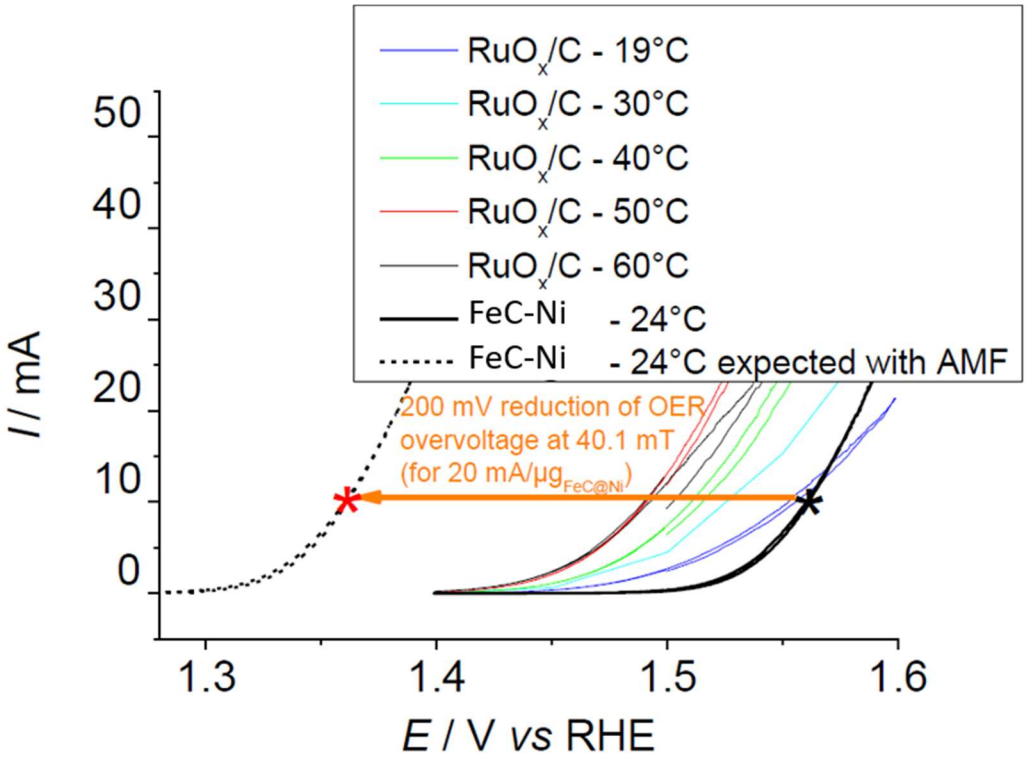

Figure IV.1: OER activity of the FeC-Ni versus RuO_x/C. Representative cyclic voltamperograms of OER measured in 1 mol.L^{-1} KOH on electrodes of 0.2 cm^2 geometric area with 20 µg.cm^{-2} RuO_x/C at various temperatures (19-60°C; coloured thin lines) and 37.8 µg.cm^{-2} FeC-Ni at 24°C without AMF (black bold line). Tentative prediction of the trace of the 37.8 µg.cm^{-2} FeC-Ni electrode in a 40.1 mT AMF, *i.e.* with a decrease of the OER overpotential by *ca.* 200 mV (bold dotted line). The ★ and ★ symbols correspond to an OER current of 20 mA.$\mu g^{-1}_{\text{FeC-Ni}}$ (or of *ca.* 50 µg.$cm^{-2}_{\text{geometric}}$), as measured in the RDE setup at 24°C and calculated after decrease of the OER overpotential by 200 mV, respectively. One would note that the calculated prediction is a theoretical construction, as AMF-heating is not possible on a classical RDE setup; it nevertheless enables to highlight the significant acceleration of the OER using a FeC-Ni electrode under an AMF. Reprinted from [60] with permission from Springer Nature.

Christiane Niether did not succeed in doing CV_F tests because bubbles continuously evolved at the WE, which sporadically cut the ionic contact between the WE and the reference electrode. This problem got solved during this PhD by beveling the tip of the Luggin capillary and improving its sealing. Thus, CV_F tests were conducted with an overall protocol similar to the one for the RDE setup, but under AMF of different amplitudes ranging from 32 to 48 mT. Two cycles were made without the AMF, then two cycles were realized under AMF. The CE potential was also recorded, to see if the plausible positive magnetic activation observed at the WE was not balanced by a negative effect at the CE. Only $FeNi_3$(@Ni) were tested, as they were among the best catalysts tested.

Figure IV.2 displays representatives CV_F cycles of the WE (solid lines) and the CE (dashed lines) in the HER side without AMF (black curves) and under AMF (red curves), for $FeNi_3$ (left) and $FeNi_3$@Ni (right), both loaded at 100 $\mu g.cm^{-2}$.

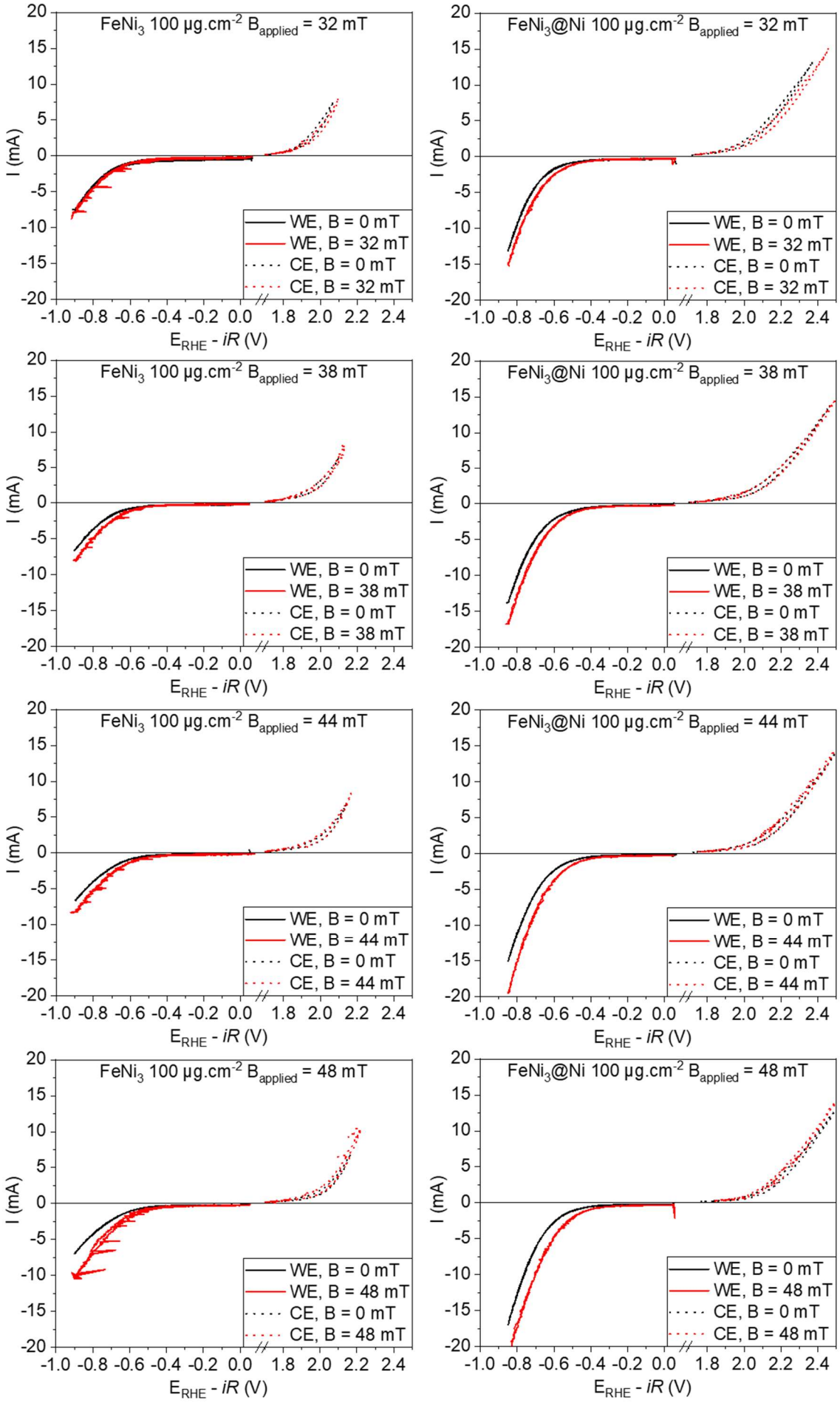

Figure IV.2: CV_F of $FeNi_3$ (left) and $FeNi_3$@Ni (right) loaded at 100 µg.cm^{-2} without AMF (black curve) and under AMF (red curve), for the WE polarized in HER (solid lines) and CE in OER (dashed lines). The AMF amplitude increases from top to bottom.

It is obvious that the AMF positively impacts the WE potential for both catalysts: the current starts at lower overpotential, whereas the CE potential remains essentially unchanged (the counter electrode was purposely located 3 cm above the coil edge, so that it experienced a very small magnetic field only). The WE curves are noisy, which is due to electromagnetic noise generated by the AMF, as measured by an oscilloscope (Supplementary Figure 7). Indeed, no low-pass filter was applied at that time. Noise is also visible at the CE (especially for $FeNi_3$ at 48 mT). Besides, one remarks that the activation is an increasing function of the AMF amplitude. This seems to be the case at loading 100 and 1000 $\mu g.cm^{-2}$, while at the highest loading tested (3000 $\mu g.cm^{-2}$), the magnetic activation seems to saturate above a certain AMF amplitude (see Supplementary Figure 8 and Supplementary Figure 9). This could be due to two reasons at least. First, at higher loading and thus higher active site number, bubbles can conceal the real activity trend (mass-transport issue). Second, a higher loading probably leads to bigger agglomerates of catalyst grains, the size of the agglomerates and aggregation being detrimental to the SAR (see subsection I.3.1.4). These two hypotheses are supported by the fact that the AMF activation seems more significant at lower loading. The aggregation is probed in an ILSEM investigation presented in subsection IV.4.1. Nevertheless, it seems consistent that the increase in magnetic field amplitude, which means a temperature increase, leads to an improved activity - the WS half-reactions being thermally-activated. Besides, these graphs confirm that $FeNi_3$@Ni is more active than $FeNi_3$ under these conditions, even under AMF (a factor 1.5 to 2 is found when comparing the maximum current reached). One can notice that the CE curves do not always overlap. This is due to a continuous degradation of the counter electrode, which was a Pt-mesh at this time of the experiments [207]. Figure IV.3 illustrates this deterioration, where the CE cycles represented in the different $FeNi_3$@Ni graphs of Figure IV.2 are summarized in a single one.

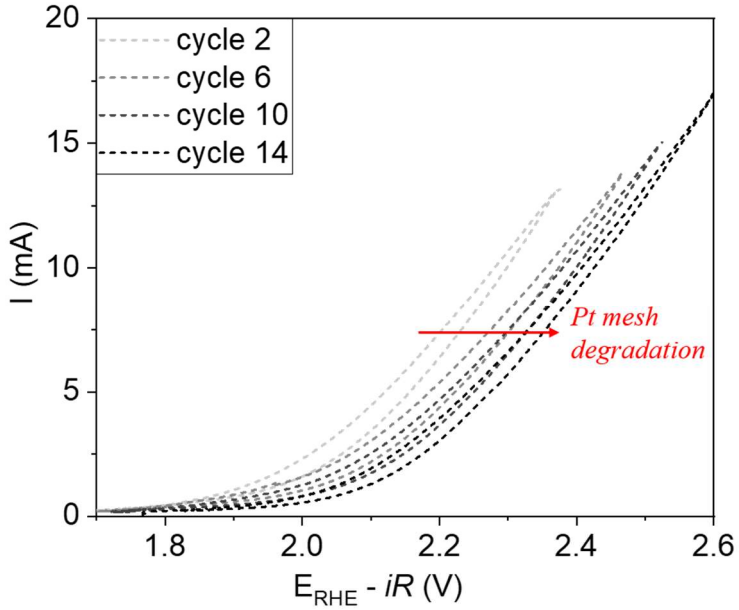

Figure IV.3: Counter electrode cycle degradation in OER during the CV_F experiment with AMF exposure for $FeNi_3$@Ni at 100 µg.cm^{-2}. The cycles displayed are those without AMF.

This effect led to a Pt contamination of the WE as measured by ICP-MS after mineralization in aqua regia, but remained very low (in the accuracy range of the ICP-MS – not shown). Accordingly, a plain Toray carbon paper was preferred afterwards as CE; even if it is likely to corrode as well, its degradation products would not affect the activity of the WE catalyst – contrary to Pt for HER. Finally, the activity of $FeNi_3$@Ni without AMF continuously and slightly increases, while $FeNi_3$ activity remains the same, as Figure IV.4 exemplifies.

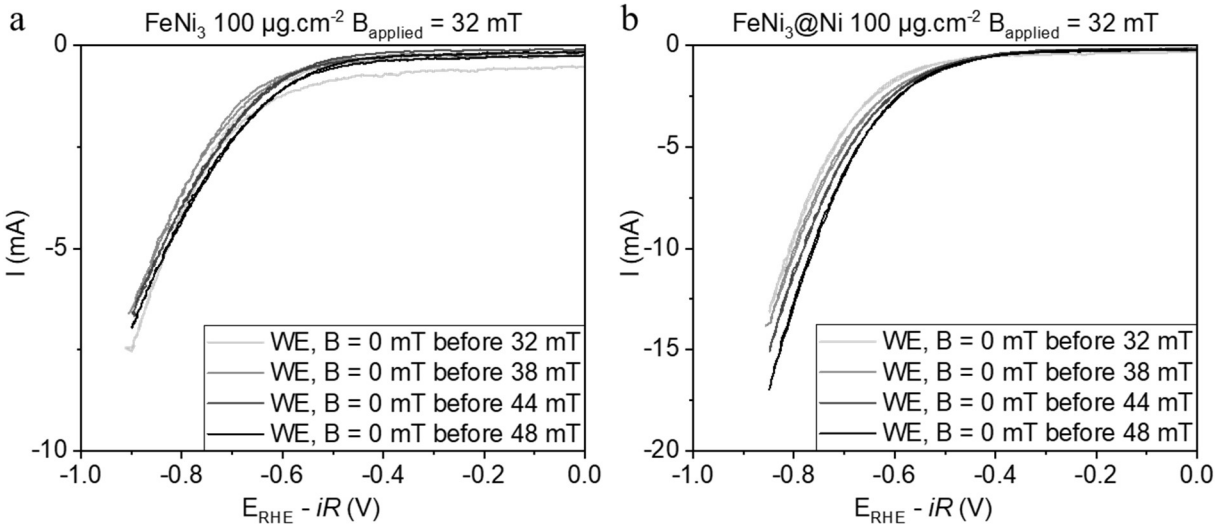

Figure IV.4: CV_F cycles without AMF, before the different applications of AMF, for (a) $FeNi_3$ and (b) $FeNi_3$@Ni, both loaded at 100 µg.cm^{-2}.

This is in accordance with the durability observation for $FeNi_3$@Ni after 200 cycles, where an activity increase was recorded for this latter, and not for $FeNi_3$ (even if the error bar is huge - Figure III.10 (a)). It is possible that before 200 cycles, the $FeNi_3$ activity increases,

due to the progressive degradation of the ligands (from the precursors), which frees more active sites. In parallel, magnetic effects could influence the activity of the catalysts, even when switching off the AMF (section I.4). Indeed, a convection induced by the Lorentz force can improve mass-transport toward the electrode, diminishing the bubble coverage issue, whose effect could be intensified when increasing the AMF and remains by inertia when the AMF is switched off. Besides, very local magnetic gradients can be triggered, paving the way to Kelvin force and spin polarization. The influence of these phenomena is addressed in section IV.3.

Figure IV.5 shows the overpotentials at -5 mA.cm^{-2} of $FeNi_3$ (green) and $FeNi_3$@Ni (blue) for the different tested loadings. A smaller current density was chosen as the catalyst performances did not always reach -10 mA.cm^{-2}. These graphs confirm that (i) for all loading the HER kinetics is improved under AMF, (ii) the higher the AMF, the greater the magnetic activation (iii) the magnetic activation seems more significant at lower loading, (iv) the activity without AMF is an increasing function of the loading, (v) the activity increases throughout the cycles without AMF, except for $FeNi_3$ at 100 µg.cm^{-2}. Especially, the activity increase without AMF cannot account for the more intense increase under AMF, proving its positive effect.

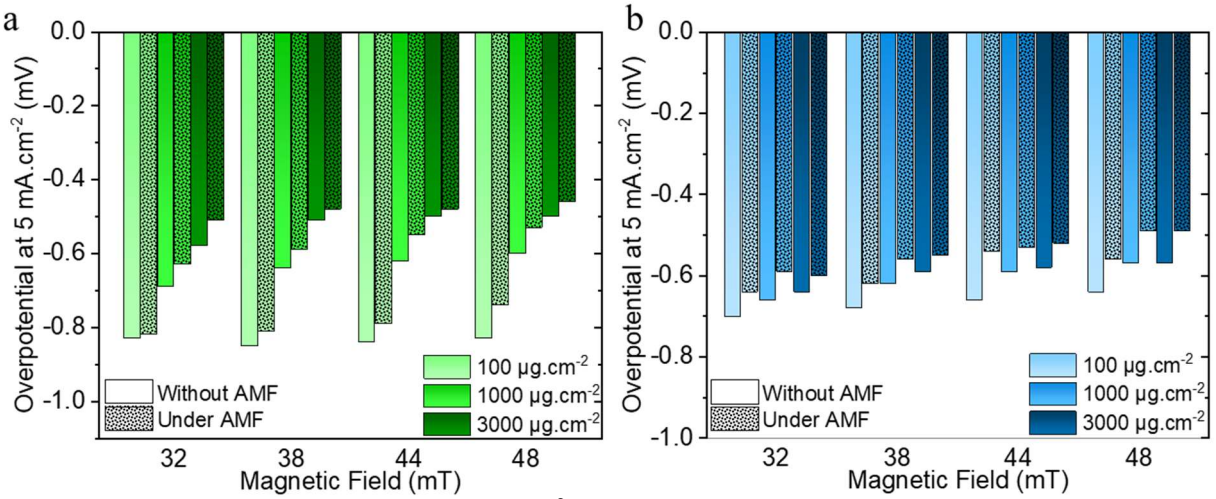

Figure IV.5: Overpotentials at -5 mA.cm^{-2} for (a) $FeNi_3$ in green and (b) $FeNi_3$@Ni in blue, for three different loadings: 100, 1000 and 3000 µg.cm^{-2}, without or under AMF. Darkest colour indicates a higher loading, a filled bar indicates a value under AMF.

The CV_F for the same catalyst at 100 µg.cm^{-2} in the OER are shown in Figure IV.6.

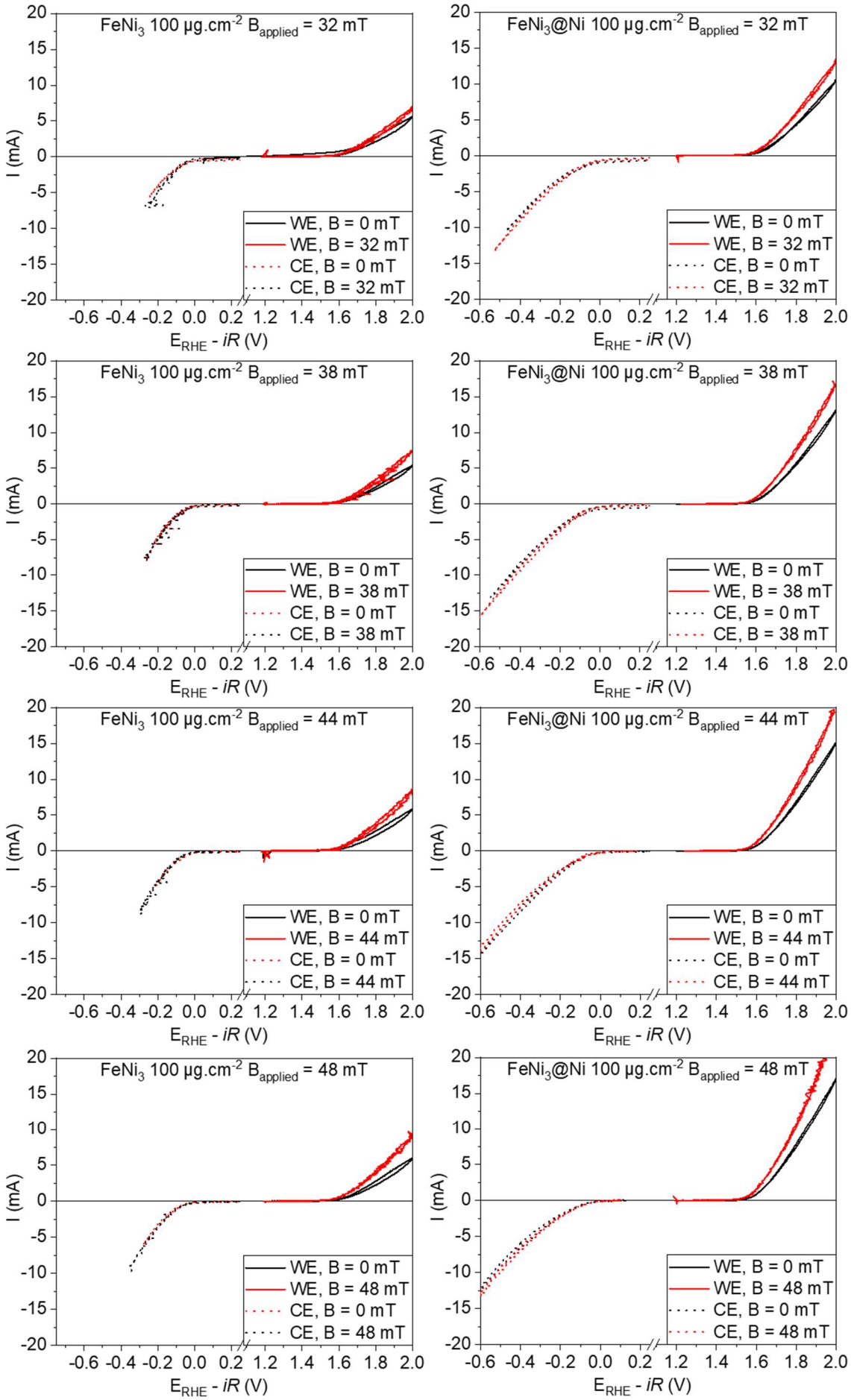

Figure IV.6: CV_F of $FeNi_3$ (left) and $FeNi_3$@Ni (right) loaded at 100 µg.cm^{-2} without AMF (black curve) and under AMF (red curve), for the WE polarized in OER (solid lines) and CE in HER (dashed lines). The AMF amplitude increases from top to bottom.

The same conclusions than for the HER can be drawn. The magnetic activation positively impacts the WE activity, whereas the CE potential is not affected by the AMF, although its degradation also occurred. The magnetic activation is an increasing function of the AMF amplitude (clearer in the OER side), and this is so for 1000 and 3000 µg.cm^{-2} (Supplementary Figure 10 & Supplementary Figure 11), although its activation is more prominent at lower loading. Moreover, $FeNi_3$@Ni exhibits higher performances than $FeNi_3$ (factor 1.5 to 2 again). The activity without AMF decreases for both catalysts (except at 100 µg.cm^{-2}). The ligands are likely to be much more degraded in the oxidizing potentials, and this is amplified by the AMF application (higher temperature), hence the degradation of the activity observed in the durability tests after 200 cycles.

Figure IV.4 shows the OER overpotentials at +5 mA.cm^{-2} for the different tested loadings and for the two catalysts. These graphs confirm that (i) for all loadings the OER kinetics is improved under AMF, (ii) the activity is an increasing function of the loading, and (iii) the magnetic activation is an increasing function of the AMF amplitude (except for $FeNi_3$@Ni at 3000 µg.cm^{-2}) as for HER. The decrease in activity (overpotential increase) throughout the CV_F cycles without AMF is visible, except at 100 µg.cm^{-2}.

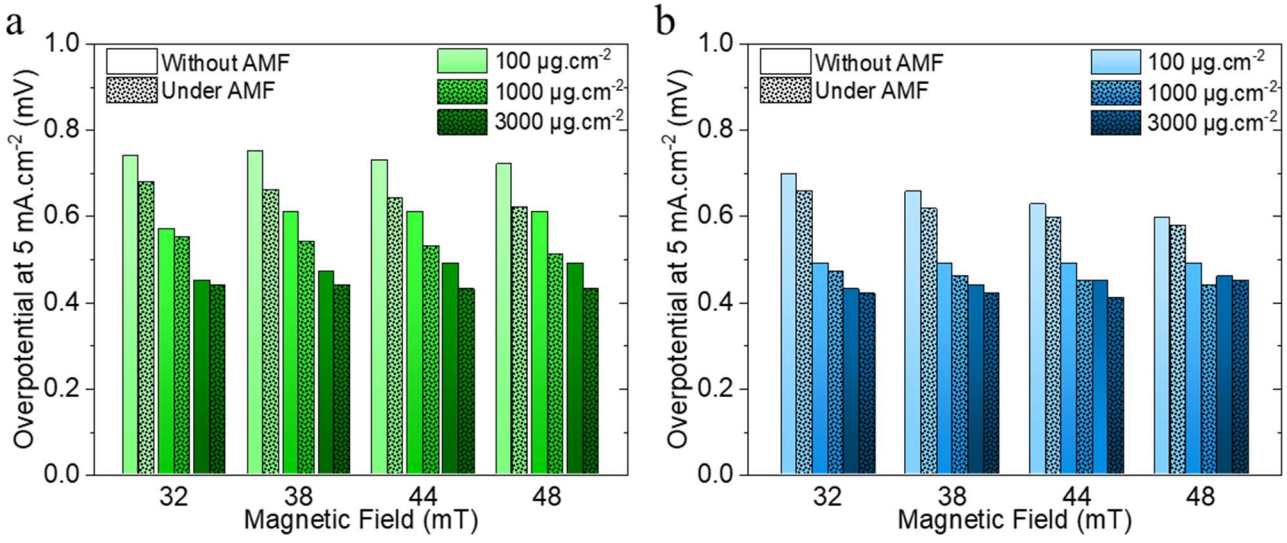

Figure IV.7: Overpotentials at +5 mA.cm^{-2} for (a) $FeNi_3$ in green and (b) $FeNi_3$@Ni in blue, for three different loadings: 100, 1000 and 3000 µg.cm^{-2}, without or under AMF. Darkest colour indicates a higher loading, a filled bar indicates a value under AMF.

Therefore, this study does indicate that applying an AMF impacts the kinetics of the water splitting, both for HER and OER, confirming the hypothesis in [60]. Moreover, even better results have been obtained (with a bigger potential onset shift, especially in the OER side), for both $FeNi_3$ and $FeNi_3$@Ni catalysts, but these experiments were not reproduced. The CV_F cycles are nevertheless presented in Supplementary Figure 12 and

Supplementary Figure 13 for $FeNi_3$@Ni. These results could indicate that the setup is not optimized, and that the magnetic activation can be further improved. A kinetics analysis of $FeNi_3$ at 3000 µg.cm^{-2} curves based on the Tafel method is presented in subsection IV.2.2. Finally, the Ohmic drop during these tests was high as the current collector was a single gold strand. Accordingly, different gold current collector shapes were tested (see section II.2.2), and the rake shape adopted for the following experiments.

IV.1.2 CP measurements at ± 10 mA.cm^{-2}

Then CP measurements of the different catalysts were conducted. For those tests, as described in sub-section II.2.1.3, a current of 10 mA (corresponding to a geometric current density of ~ 10 mA.cm^{-2} - in absolute value) was applied, and the potential recorded in function of time. Magnetic field of different amplitudes were applied in the broadest range possible: from 11.8 mT (lowest AMF applicable on this setup) to 48 mT (above, the sealing glue began to melt due to the heating, sparking leaks). The AMF was switched on only after the potential stabilized at a given CP step; the AMF was generally maintained for 1-2 minutes before turning off the field. Indeed, the overpotential under AMF kept diminishing (in absolute value) following the continuous temperature increase of the felt, where a typical example of the curve obtained in the HER is given in Figure IV.8 (in the OER side, a typical curve is given in Figure II.5). The CE potential was checked and seemed never affected by the AMF. At least two measurements were conducted for reproducibility. In all graphs, the error bars represent the standard deviation based on these reproduced measurements, although sometimes the error bar

is absent, some measurement suffered from a potentiostat overload because of the electromagnetic noise from the AMF.

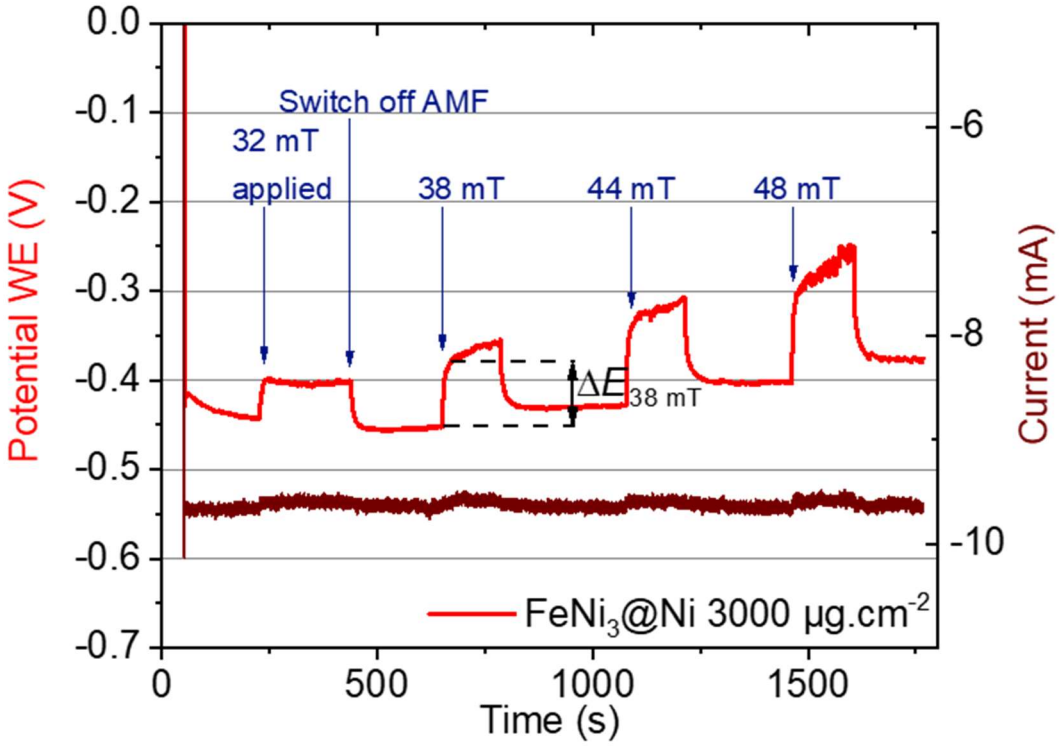

Figure IV.8: Chronopotentiometry measurement at $i = -10$ mA ($j_{geom} = -10$ mA.cm^{-2}), of $FeNi_3$@Ni catalyst at 3000 µg.cm^{-2}, in the HER side under AMF ranging in [32; 48] mT. $\Delta E_{38\ mT}$ corresponds to the "potential gain at 38 mT", *i.e.* the absolute difference of the potential without AMF exposure, minus the potential under AMF, corresponding to the decrease in overpotential at 38 mT.

In such measurements, the absolute difference of the potential without AMF exposure, minus the potential under AMF was extracted, called hereafter the potential gain ΔE, as indicated for an AMF of 38 mT in Figure IV.8. The potential under AMF was chosen just after the AMF ignition, and not after the 2 minutes exposure. This way, the eddy current contribution (heating) to the magnetic activation was minimized, and mainly the activation due to the hysteresis losses was accounted. Figure IV.9 displays the potential gain in function of the magnetic field amplitude, for the studied catalysts in the HER side. It has to be noted that the $FeNi_3$(@Ni) undergone a pretreatment of 500 AST cycles and 200 AST cycles in the HER and

OER side respectively, so that their activity was stable for CP measurements. This reduced a lot the error bars for these materials.

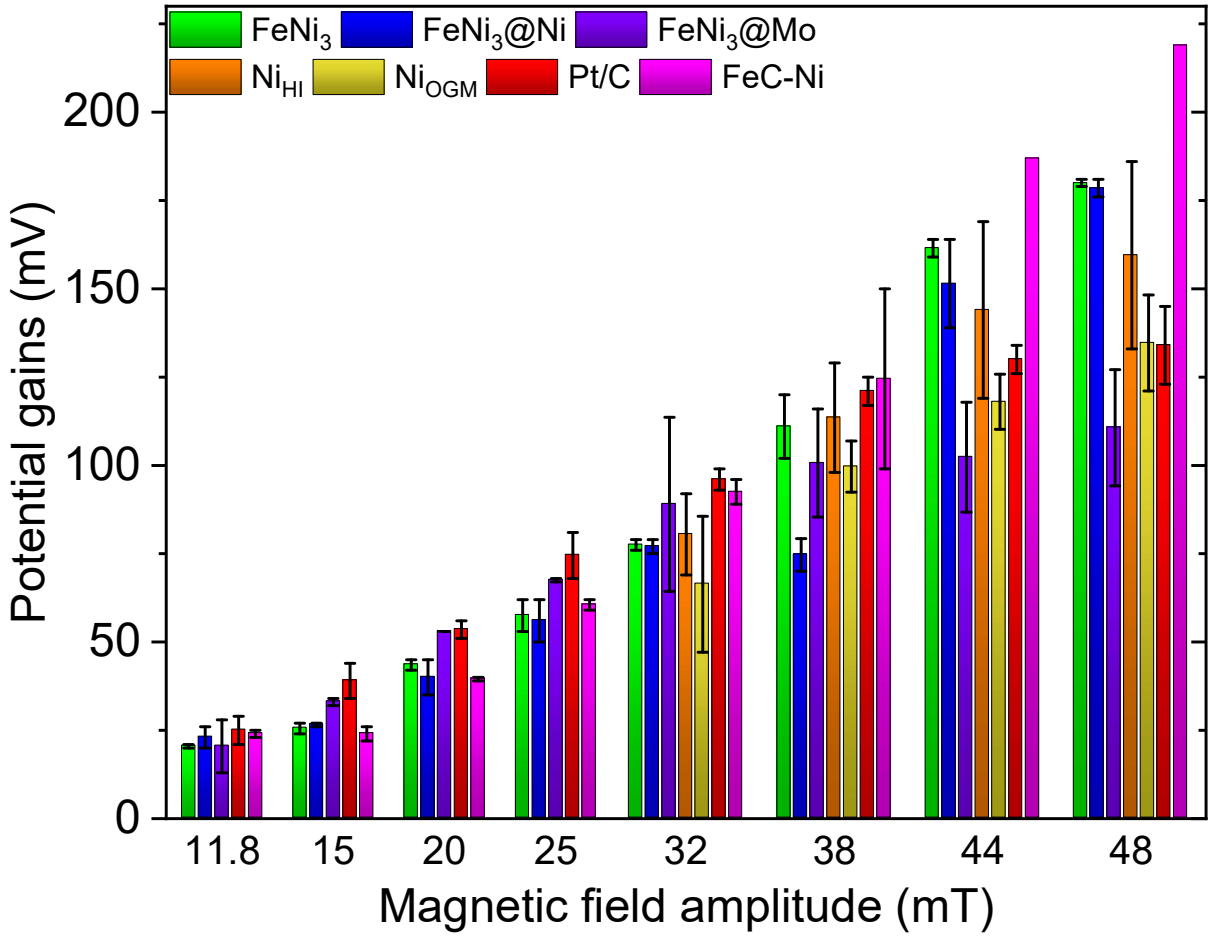

Figure IV.9: Potential gains in the HER side, *i.e.* the absolute difference of the potential without the AMF, minus the potential under AMF, at −10 mA.cm^{-2} *vs.* the magnetic field amplitude at 300 kHz, for the studied materials: non-PGM materials loaded at 1000 µg.cm^{-2}, and Pt/C loaded at 100 µg.cm^{-2}. No data in the [11.8; 25] mT range for Ni-based materials are available.

Figure IV.9 shows that the different catalysts follow a similar magnetic activation, and that it is not truly consistent with the SAR measurements (Figure III.20). The non-PGM catalysts were all loaded at 1000 µg.cm^{-2} to permit their comparison at a same loading, and the benchmark catalyst Pt/C was loaded at 100 µg.cm^{-2} as almost no activity was recorded at 20 µg.cm^{-2}. The catalysts were not loaded at the highest loading possible, as it necessitated more material while their amount was limited (the batches generally led to 30-50 mg of material). Moreover, CP tests in the [11.8; 25] mT range were conducted on the Ni-based materials, but

the results were not obtained due to technical reason. So, no data are available, unfortunately. In any case, what is striking is that materials which presented a low or null SAR (Ni_{OGM}, Ni_{HI}, Pt/C and $FeNi_3$@Mo,) display similar potential gains as higher SAR materials ($FeNi_3$(@Ni), FeC-Ni), except at magnetic fields superior to 44 mT, where these latter exhibit higher ΔE consistently with their heating capacity. Besides, the potential gain of $FeNi_3$ and $FeNi_3$@Ni are very similar, which does not reflect their SAR difference. Similarly, the potential gains of FeC-Ni are close to $FeNi_3$(@Ni), while its SAR is much superior (1125 $W.g^{-1}$ for FeC-Ni compared to 315 $W.g^{-1}$ for $FeNi_3$@Ni at 42.7 mT). Furthermore, the potential gains of Ni_{HI} is always superior to Ni_{OGM}, while its SAR is lower than Ni_{OGM} up to 38 mT. A normalization by, for example, the mass, the density, or the ECSA/$g_{catalyst}$ ($cm^{-2}.g$) which is of use in electrochemistry [265,266,267] was tried but not presented. Indeed, the analysis did not help to the understanding of the results, especially because the catalyst characteristics (NPs diameter, density) are too different. In summary, the application of the AMF does decrease the overpotential of all the catalysts, but its relation with their SAR is blurred. This contradiction was unexpected, but a look at the overpotentials at which HER occurs gives hint to understand this finding (Figure IV.10).

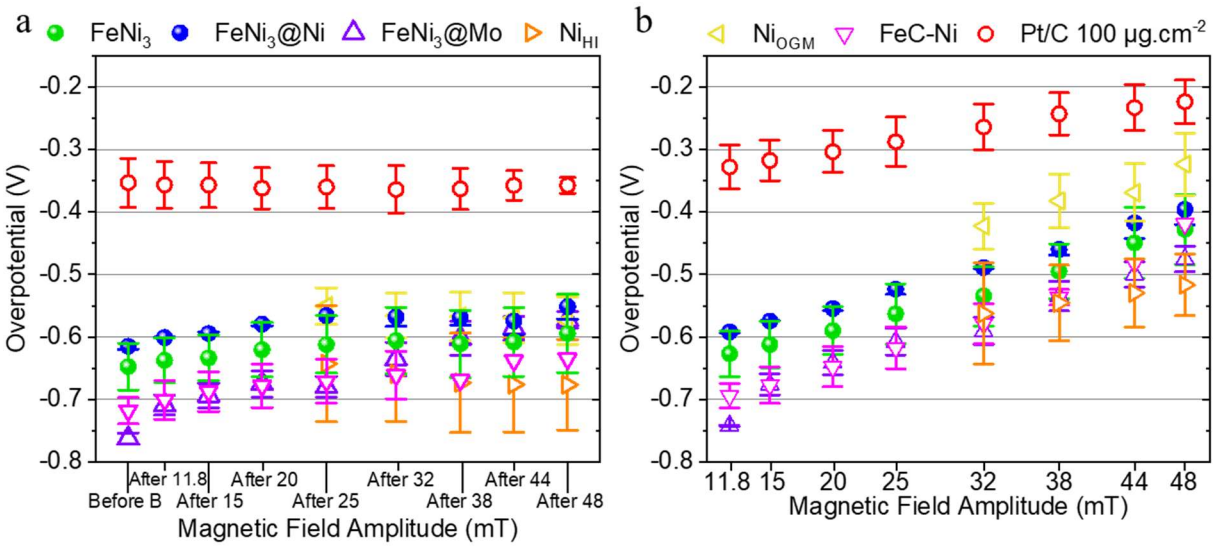

Figure IV.10: Overpotentials at −10 mA.cm^{-2} of the different catalysts (non-PGM loaded at 1000 µg.cm^{-2} and Pt/C loaded at 100 µg.cm^{-2}), (a) without AMF and (b) under AMF. "Before B" and "After X" indicate the overpotentials before the AMF exposure, and after the AMF exposure at X mT, respectively.

It seems that the non-PGM catalysts which present higher potential gains are also those who exhibit the higher overpotentials ($FeNi_3$, Ni_{HI}, and FeC-Ni compared to Ni_{OGM} and $FeNi_3$@Ni), except for $FeNi_3$@Mo. Nevertheless, Pt/C presents similar potential gains as the other materials, but its overpotential is much lower (as it is a benchmark catalyst), while its SAR is null. Thus, the AMF enhances the HER kinetics on this catalyst in another way than by hysteresis losses. Besides, the mass-transport kinetics is also certainly impacted, as the increase in temperature can facilitate the bubble departure (so-called Soret or thermophoresis effect, but also Marangoni, Maxwell stress or simply Brownian motion). The overpotential without AMF of $FeNi_3$(@Ni/@Mo) and FeC-Ni catalysts decreases (in absolute value) up to "After 25 mT". This is probably due to the continuously deterioration of the ligands, unleashing more active sites. Figure IV.11 shows the potential gains of the materials in the OER side.

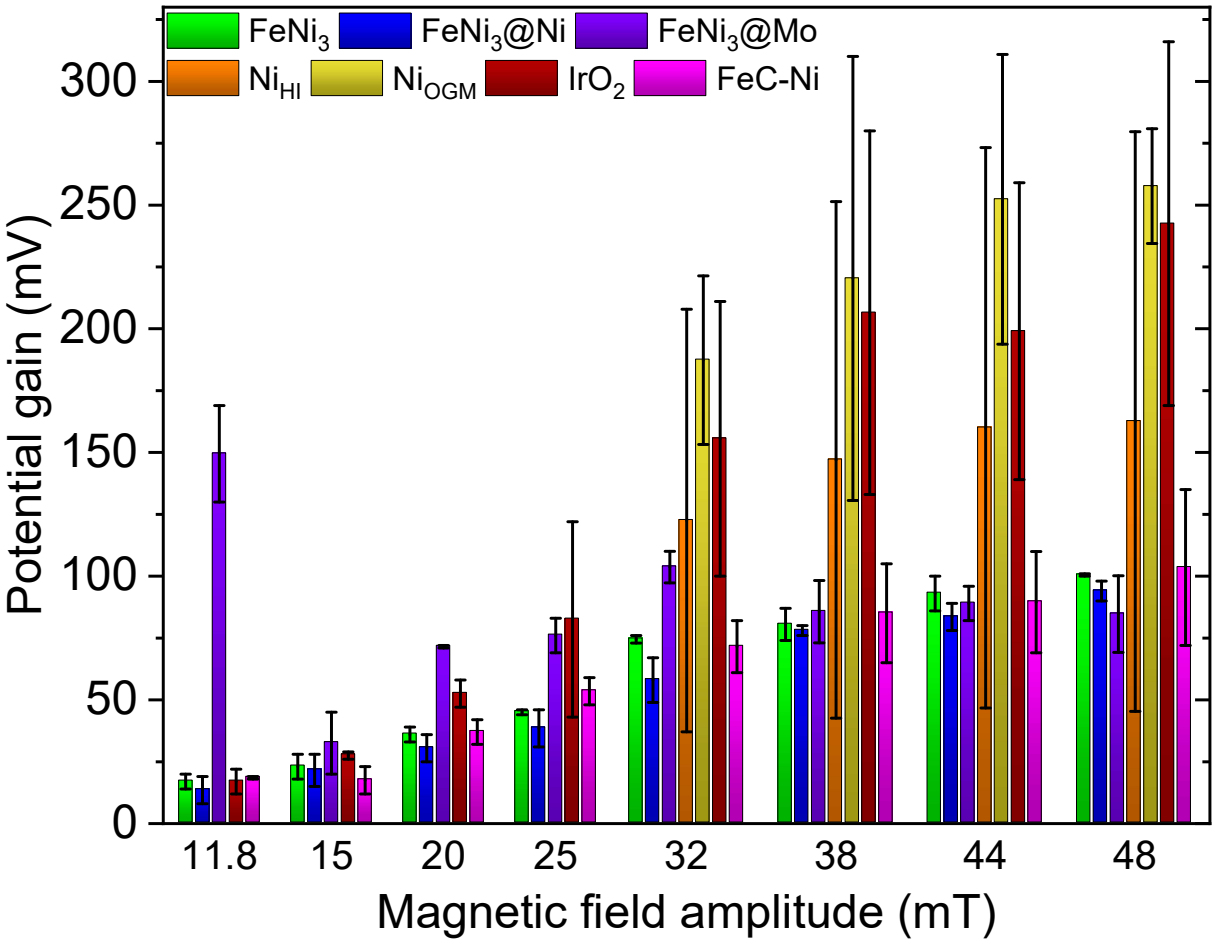

Figure IV.11: Potential gains in the OER side, *i.e.* the absolute difference of the potential without the AMF, and the potential under AMF, both at +10 mA.cm^{-2} *vs*. the magnetic field amplitude at 300 kHz, for the studied materials, all loaded at 1000 µg.cm^{-2}.

Again, the magnetic activation does not agree (only) with the SAR of the colloidal catalyst suspension (Figure III.20). The first potential gain of $FeNi_3$@Mo is very high, probably because the ligands gets rapidly removed by the temperature increase (19% of ligands by TGA measurement), unleashing more active sites, as suggests the drop of 150 mV in overpotential without AMF after 11.8 mT in Figure IV.12 (a) below.

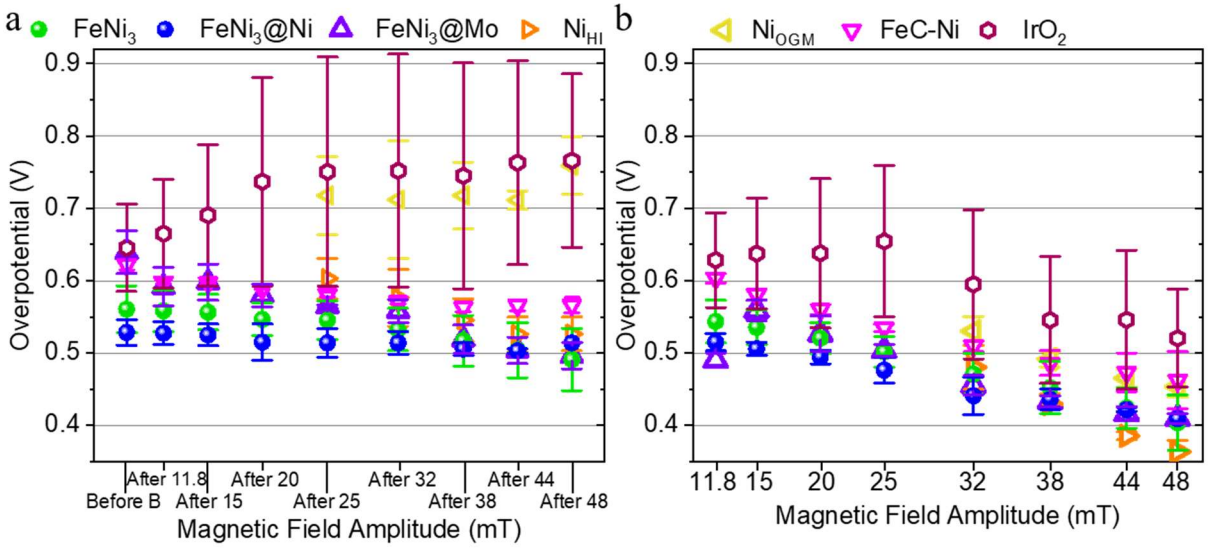

Figure IV.12: Overpotentials at +10 mA.cm^{-2} of the different catalysts (all loaded at 1000 µg.cm^{-2}), (a) without AMF and (b) under AMF. "Before B" and "After X" mT indicate the overpotentials before the AMF exposure, and after the AMF exposure at X mT, respectively.

When looking at the overpotentials, the same observation is made: the higher the overpotential without AMF, the higher the potential gain upon AMF application (for Ni_{OGM}, IrO_2, and Ni_{HI} compared to $FeNi_3$(@Ni/@Mo) - even if the error bars are huge). In the OER side, the Ni_{OGM} is much less active than Ni_{HI}, in disagreement with the CV_F measurements in the PMMA cell. The reason is not known. The operating conditions between a CP or CV_F techniques are different: the activity during a CV_F experiment could be much higher, as the mass-transport issue is less significant, but this argument seems not sufficient to explain such discrepancy (difference of 100 mV on the overpotential between the two techniques). In any event, the kinetics seems also enhanced by the AMF application in the OER side, as well as the mass-transport kinetics. Which of the two effects is prominent is an open question. Let's suppose that the carbon felt and the catalyst on its surface are perfectly wetted (the carbon felt is indeed very hydrophilic), so that the reaction rate of HER/OER is governed whether by the charge-transfer kinetics of the reaction, or by the mass-transport due to the bubble issue, which prevents new reactants to adsorb. Let's call τ_1 the time necessary for the reaction to happen, *i.e.* the electron transfer (inversely proportional to the standard rate constant of the reaction at stake, k°), and τ_2 the nucleation time and the growth of the bubble until its departure (inversely

proportional to the mass-transport parameter $m = D / \delta$ of the reacting species, D being the diffusion coefficient and δ the diffusion layer thickness). Considering cases where a material is more or less active, and where the AMF influences mainly the charge-transfer kinetics (τ_1 decreases more than τ_2, $k°/m$ increases) or the mass-transport (τ_2 decreases more than τ_1, $k°/m$ decreases), one can draw the following Table IV.1:

Table IV.1: Different scenarios where the influence of the AMF impacts more the charge-transfer or the mass-transport, on catalysts being more or less active.

AMF influences mainly	**Very active material ($\tau_1 << \tau_2$)**	**Active Material ($\tau_1 < \tau_2$)**	**Weakly active material ($\tau_1 > \tau_2$)**	**Almost inactive material ($\tau_1 >> \tau_2$)**
Charge-transfer kinetics ($\tau_1 \downarrow\downarrow$ - $\tau_2 \downarrow$)	ΔE_1 small as τ_2 is limiting (case of $FeNi_3$@Ni and Ni_{OGM} in HER)	ΔE_2 intermediate (case of $FeNi_3$ and $FeNi_3$@Mo in OER)	If τ_1 still > τ_2, ΔE_3 intermediate (case of $FeNi_3$@Mo in HER and FeC-Ni in OER) If τ_1 becomes < τ_2, ΔE_{3bis} huge (case of FeC-Ni in HER)	ΔE_4 bigger than $\Delta E_{2/3}$ (case of Ni_{OGM} in OER, Ni_{HI} and IrO_2)
Mass-transport kinetics ($\tau_2 \downarrow\downarrow$ - $\tau_1 \downarrow$)	ΔE_1, high (contradiction with $FeNi_3$@Ni and Ni_{OGM} in HER)	If τ_1 still < τ_2, ΔE_2, intermediate (case of $FeNi_3$@Mo in OER) If τ_1 becomes > τ_2, $\Delta E_{2,bis}$ huge	ΔE_3, small (contradiction with and Ni_{HI} in OER)	ΔE_4, very small (not consistent with, FeC-Ni in HER, Ni_{HI} in HER, Ni_{OGM} in OER and IrO_2)

Let's consider the case where the material is very active ($\tau_1 << \tau_2$) and that the AMF influences mainly the charge-transfer kinetics (second case on the second raw from the left). In this situation, the potential gain ΔE_1 should be small, as the limiting step would be the bubble nucleation, growth and desorption time τ_2, being not as much reduced as the electron-transfer time τ_1. Let's consider now the case of a weakly active material ($\tau_1 > \tau_2$), where the AMF influences mainly the charge-transfer (fourth case on the second raw from the left). In this example, if τ_1 remains superior to τ_2, even after the AMF activation, the potential gain ΔE_3 should be intermediate, the reaction being limited by τ_2; but, if τ_1 becomes inferior to τ_2, then the potential gain ΔE_{3bis} should be higher than ΔE_3, the reaction being more activated by the

AMF. In the first scenario (second raw), where the AMF influences mainly the charge-transfer kinetics, the potential gains increase from ΔE_1 to ΔE_4, *i.e.* low overpotential materials (active materials) present a low ΔE, and high overpotential materials (weakly active) exhibit a high ΔE. In the second scenario (third raw) where the AMF influences mainly the mass-transport kinetics, it is the reverse (the potential gains decrease from $\Delta E_{1'}$ to $\Delta E_{4'}$ *i.e.* from low to high overpotential).

To conclude from this analysis, the scenario where the AMF impacts more the charge-transfer kinetics than the mass-transport kinetics is the one which fits more with the measured results. This analysis fits quite well in OER but is less relevant in HER (especially for Pt/C material which is not taken into account).

This being said, in order to explain the discrepancy between the potential gains and the SAR, new magnetic characterizations were conducted. Indeed, the first SAR measurements did correspond to the catalysts in suspension, which is not the working environment in the PMMA cell, where the NPs are immobilized on the carbon felt support; this could probably change the NP heating behaviour. Besides, the SAR measurements were conducted at 100 kHz, while the coil used for CP tests works at 300 kHz.

IV.1.3 Magnetic characterizations of the working electrode samples

Therefore, temperature elevation measurements were made in air on the system {carbon felt + NP deposit} corresponding to the "final" sample, in the 300 kHz coil, by targeting the deposit with a pyrometer, as described in the second part of section II.5.2. By doing so, the heating sparked by eddy currents generated inside the felt was measured as well. Also, a blank measurement corresponding to the temperature elevation of a carbon felt without deposit was realized, as well as measurement of the current collector wire alone: the gold wire with a rake

shape (Figure II.8 (e)). The temperature elevation ΔT instead of the SAR is presented on the y axis, because the SAR values would have not been comparable to the previous one. Of course, this setup is not ideal as it is non-adiabatic, and the ΔT are those in air and not in KOH, not reflecting truly the behaviour of the WE in the cell under AMF.

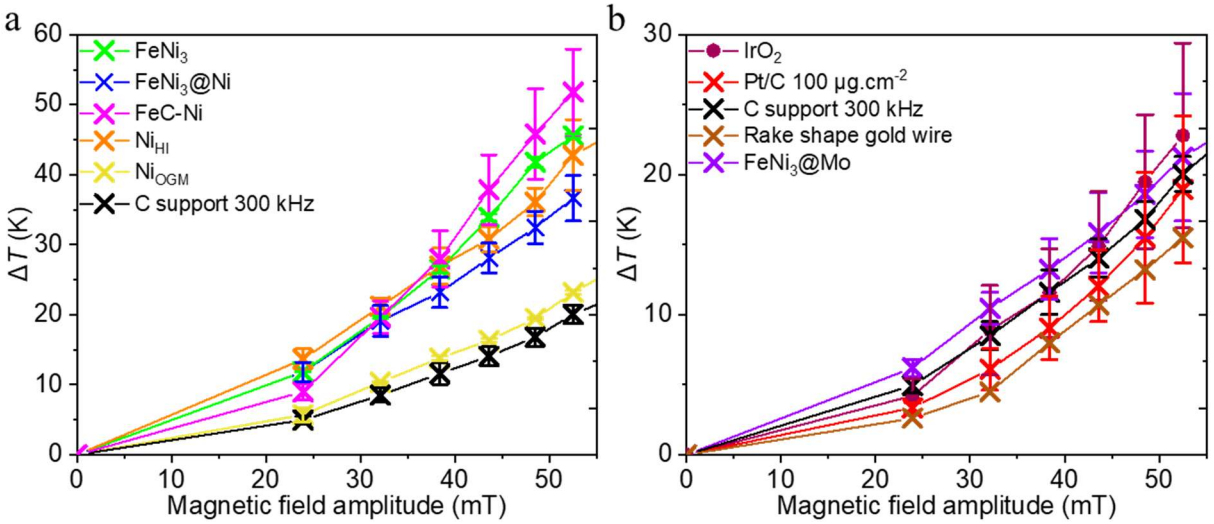

Figure IV.13: Temperature elevations in air as measured by a pyrometer targeting the NP deposit in the 300 kHz coil. Catalyst which heating is (a) superior to the carbon felt's one and (b) Catalyst which temperature elevation issimilar or below the carbon felt's one. When error bars are present, it indicates the standard deviation among 2 measurements.

What is astonishing is that the temperature elevation of the carbon felt is high, indicating that eddy currents are non-negligible in this support, and may thus be a non-negligible heating source for certain catalyst. The ΔT of the carbon felt is equivalent to $FeNi_3$@Mo, IrO_2 and Pt/C, which is in accordance with the near-zero SAR and very low magnetic properties (especially M_S low) of these materials at 100 kHz, and explains their activation under AMF. FeC-Ni and $FeNi_3$(@Ni) exhibit a higher ΔT than the single carbon felt, with ΔT (FeC-Ni) > ΔT ($FeNi_3$) > ΔT ($FeNi_3$@Ni), consistently with the colloidal suspension's SARs. However, ΔT (Ni_{HI}) > ΔT ($FeNi_3$@Ni) from 32 mT, in contradiction with their SAR. This result could possibly indicate that the heating by hysteresis losses is a heating source for these catalysts, although it has to be noted that the eddy current generation is higher when it is through a magnetic material, apart from being conductive. Indeed, eddy currents are proportional to the magnetic flux inside the

material. This latter is higher for a magnetic material, so that eddy currents are heightened [255]. The ΔT of Ni_{OGM} is a bit higher than the carbon felt, but much lower than Ni_{HI}. This is strange, as the Ni_{OGM} SAR is superior to Ni_{HI} SAR up to 38 mT. The difference could be due to a change in conductivity of the materials, which will influence the eddy current generation. However, no such difference was noticed between the samples, as measured by a potentiostat (being more accurate than an ohmmeter). On another note, suggesting that the MF frequency is closer to the inverse of the Néel/Brown relaxation time for Ni_{HI}, and further for Ni_{OGM} is difficult (the difference in diameter could play, 69 nm for Ni_{HI} and 17.4 nm for Ni_{OGM}). But the determination of these parameters is difficult and was not realized, especially because the particles are agglomerated (subsection IV.4.1), so that their behavior should be closer to a magnetic film than to isolated magnetic particles. In summary, the heating observed is also due to eddy currents. Especially, as these latter are enhanced through magnetic materials, it is difficult to know if hysteresis losses are at skate. In any case, the SAR of the materials seems not the good indicator to characterize the heating capacity of the catalysts. These results paved the way to other tests; namely, CP measurements in both the HER and OER side were conducted for the carbon felt without NP deposit with the rake-shape Au wire ("C felt+rake Au wire"), the carbon felt without NP but with a single strand gold current collector wire (similarly to Christiane Niether's setup configuration – "C felt+single Au wire"), and the rake-shape gold wire only ("Rake Au wire only"): Figure IV.14.

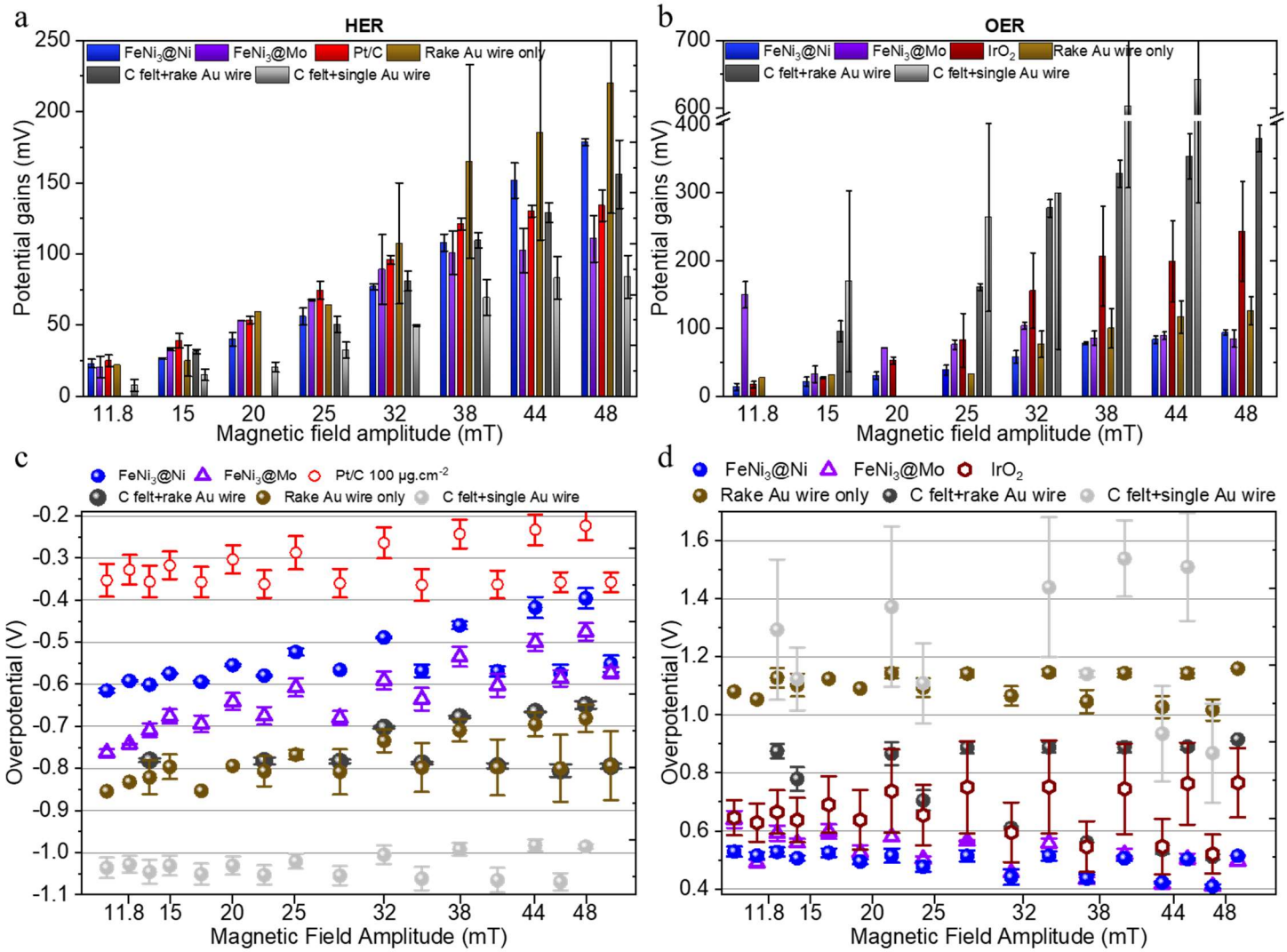

Figure IV.14: Potential gains at 10 mA.cm^{-2} in the (a) HER and (b) OER side of certain catalysts: $FeNi_3$@Ni, $FeNi_3$@Mo, Pt/C and IrO_2, besides with a carbon felt with a rake-shape gold wire, a carbon felt with a single strand gold wire, and the rake-shape gold wire only. Corresponding overpotentials (c) at −10 mA.cm^{-2} in the HER side and (d) at +10 mA.cm^{-2} in the OER side without and with AMF. Only the labels corresponding to the AMF amplitudes are displayed, the points between these labels correspond to the overpotentials without AMF, *i.e.* before or after AMF application.

The first observation is that every material is positively impacted by the AMF. This is consistent as once again, WS is a thermally-activated process. Secondly, it supports the conjecture whereby the higher the overpotential without AMF, the higher the potential gain under AMF, but only in the OER side, except for the Au wire. Indeed, gold is recognized and hence appreciated for its electrochemical inertness towards the WS reaction. In any case, these graphs indicate that the heating generated by the eddy currents is non-negligible: by example, ΔE ($FeNi_3$@Mo) ~ ΔE ($FeNi_3$@Ni) in both HER and OER sides (up to 44 mT in HER). Besides, the application of the AMF on the carbon felt without NP deposit, and with a single strand Au current collector significantly impacts the overpotentials in the OER side (ΔE > 1 V at 44 mT).

This high enhancement is probably also accounted for by enhanced carbon corrosion at high temperature and high potential. Indeed, carbon heavily corrodes above 2-2.2 V_{RHE}, and the carbon felts were indeed very damaged at the end of these OER tests.

CP measurements were also conducted at 10 mA.cm^{-2} on $FeNi_3$(@Ni) at 3000 µg.cm^{-2}, and at higher current density (30 mA.cm^{-2}) on $FeNi_3$@Ni, $FeNi_3$@Mo, Pt/C and IrO_2.

IV.1.4 Loading study on $FeNi_3$(@Ni) with CP measurements

Figure IV.15 presents the potential gains and the overpotentials obtained for $FeNi_3$(@Ni) at 1000 and 3000 µg.cm^{-2}, in the HER side (left) and OER side (right).

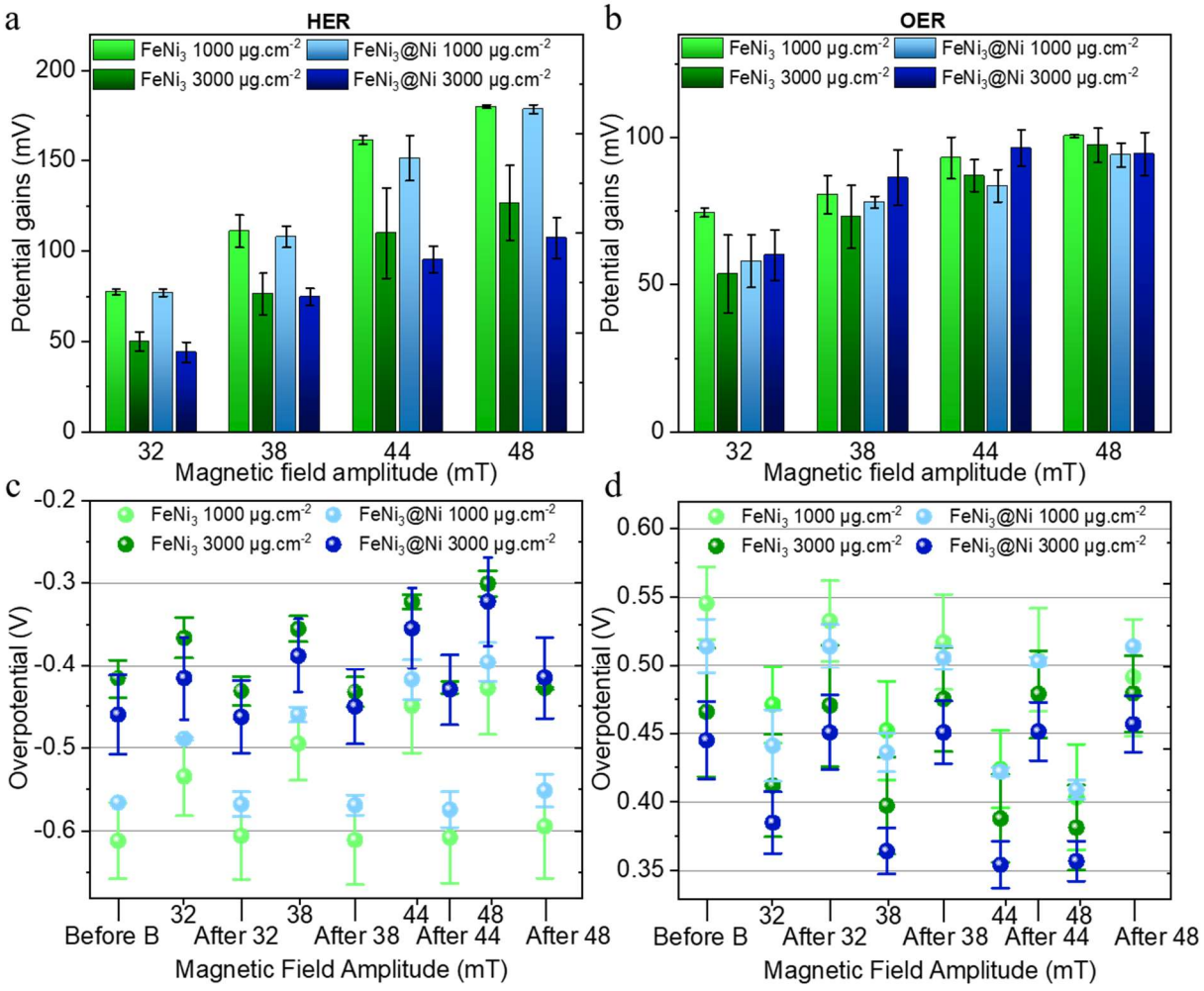

Figure IV.15: Loading study on $FeNi_3$(@Ni) at 1000 and 3000 µg.cm^{-2}: potential gains in (a) the HER and (b) the OER side, at AMF ranging from [32; 48] mT, corresponding overpotentials in (c) the HER and (d) the OER side.

First of all, the overpotentials are much lower at 3000 than at 1000 µg.cm^{-2} (difference of *ca.* 200 mV for $FeNi_3$ and 100 mV for $FeNi_3$@Ni) in both sides, consistently with the trend observed in section IV.1.1. Then, the potential gain trends are different in the HER than in the OER side. In HER, higher potential gains are obtained at lower loading, while it is much less marked for $FeNi_3$ in OER, and similar ΔE are visible for $FeNi_3$@Ni at the two loadings in OER. These various trends suggest that the magnetic activation mechanism is different in the HER than in the OER side. Especially, for OER, the fact that the potential gains are nearly independent on the loading and saturates could indicate that the AMF influences more the mass-transport (the kinetics being at its maximum). In HER, charge-transfer activation seems prominent as higher overpotential leads to higher potential gain. The less significant magnetic activation at higher loading (in HER and in OER for $FeNi_3$ only) might be explained that at higher loading, more agglomerates are present (or are bigger) which reduce the magnetic heating due to hysteresis losses (as seen in subsection I.3.1.4). However, this effect is not visible for $FeNi_3$@Ni, perhaps because this effect is less significant at lower SAR ($FeNi_3$@Ni exhibits a SAR twice lower than $FeNi_3$ SAR). Nevertheless, as it is not sure if hysteresis losses are at stake, such reasoning is delicate.

Then, CP measurements at higher current density (30 mA.cm^{-2}) were conducted, to test whether the potential gain trend is current density dependent.

IV.1.5 CP measurements at ± 30 mA.cm^{-2}

Figure IV.16 presents the CP measurements at ± 30 mA.cm^{-2} on $FeNi_3$@Ni, $FeNi_3$@Mo and IrO_2 loaded at 1000 µg.cm^{-2}, and Pt/C loaded at 100 µg.cm^{-2}. $FeNi_3$@Ni was chosen as this catalyst was very active in both HER and OER side. $FeNi_3$@Mo was chosen

because its composition is close to $FeNi_3$@Ni, but its magnetic properties are weaker, which influences the heating capacity. Then, benchmark catalysts were chosen as comparison.

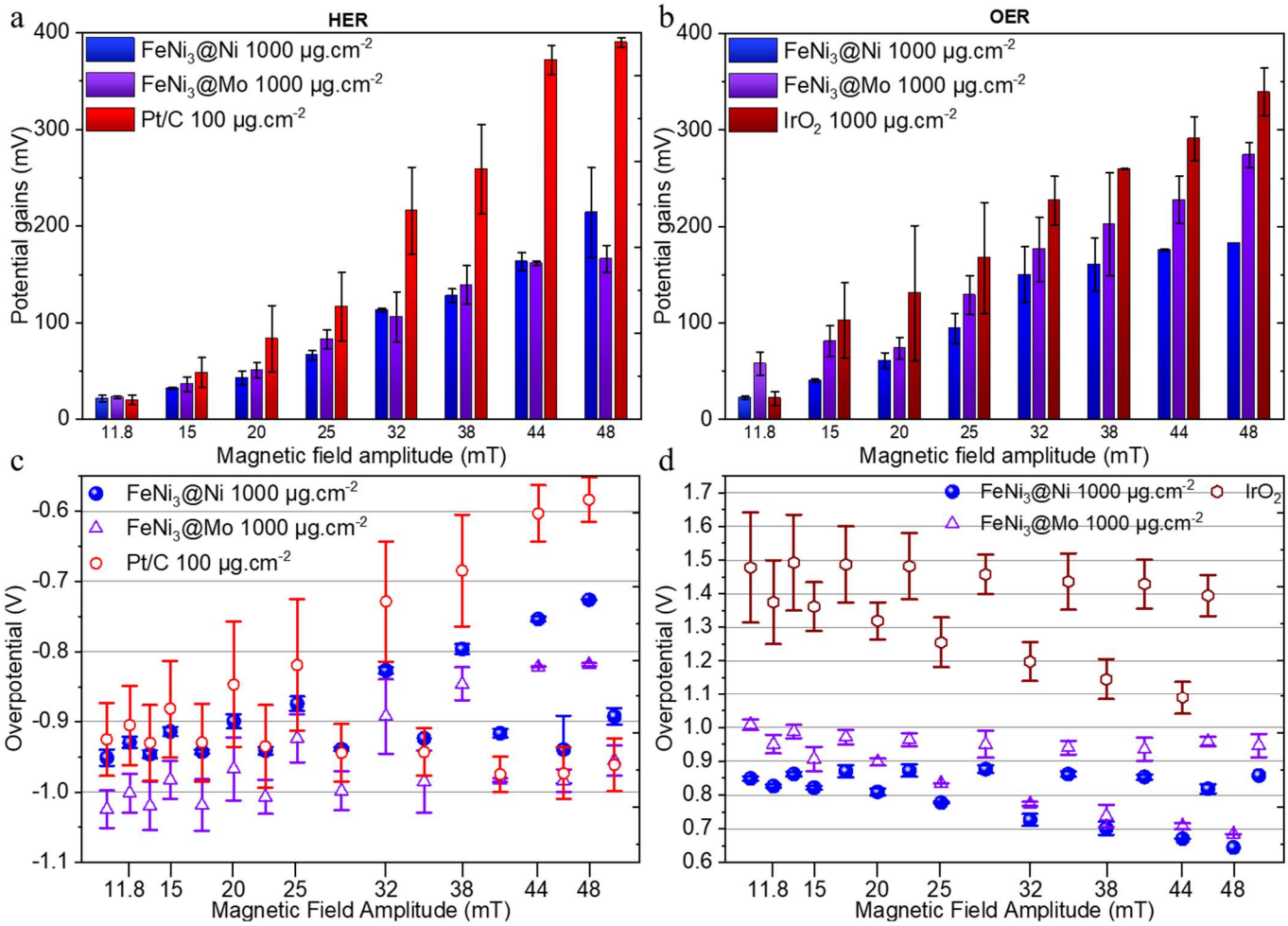

Figure IV.16: CP measurements at ± 30 mA.cm^{-2} on $FeNi_3$@Ni, $FeNi_3$@Mo, IrO_2 loaded at 1000 µg.cm^{-2} and Pt/C loaded at 100 µg.cm^{-2}: potential gains in (a) the HER and (b) the OER side at AMF ranging in [11.8; 48] mT, corresponding overpotentials in (c) the HER and (d) OER side. Only the labels corresponding to the AMF amplitudes are displayed, the points between these labels correspond to the overpotentials without AMF, *i.e.* before or after AMF application.

Curiously, the potential gains exhibited by Pt/C are much higher than the other materials. This could be partly explained by the fact that Pt/C gets purified from adsorbed impurities thanks to the temperature elevation and the gas evolution (bubbling), more intense at 30 mA.cm^{-2} than at 10 mA.cm^{-2}. Indeed, this catalyst is known to be easily poisoned by contaminants, and to be purified by pyrolysis [209]. However, from 38 mT, the overpotential of this catalyst without AMF decreases, so that the previous explanation is not true from this AMF amplitude. This huge activation seems to be mainly due to mass-transport enhancement. Indeed,

Pt/C is a reference catalyst in HER, its kinetics regarding this reaction is fast and it shall not be the limiting factor. Besides, the AMF is more likely to enhance mass-transport in the HER side. Indeed, as H_2 bubbles have a diameter generally twice lower than O_2 bubbles in this medium [110,111,112], they should be more easily disrupted by the AMF, and thus leave the WE sooner, reducing the bubble coverage issue (kind of Maxwell/Marangoni effect which will be developed in section IV.3). Moreover, twice more H_2 bubbles are generated than O_2, so that the mass-transport enhancement should be more visible in HER. Thus, Pt/C activity seems improved because of mass-transport enhancement, although a change in HER mechanism could occur (change of the rate determining step), due to the higher temperature generated by eddy currents. Similar potential gains were obtained for $FeNi_3$-based materials in HER. Thus, the hysteresis losses seem overwhelmed by eddy current heating at higher current. This is strange, as the ΔE of $FeNi_3$@Mo at 10 mA.cm^{-2} were inferior to $FeNi_3$@Ni in HER, consistently with the lower magnetic properties. The reason accounting for this is unknown. In OER, $FeNi_3$@Mo displays higher ΔE than $FeNi_3$@Ni, in contradiction with the SAR and magnetic properties, again. The trend regarding the potential gains and the overpotential is in contradiction with the previous hypothesis in the HER side (higher η lead to higher ΔE), but verified in the OER side, while one must have in mind that at potential superior to 2-2.2 V_{RHE} (*i.e.* overpotential above 0.73-0.93 V), the carbon support is likely non-negligibly corroded. Thus, an oxidation current due to the carbon oxidation is collected, and this effect is probably enhanced by the magnetic field, so that the potential gains in the OER side has two contributions: enhancement of the OER, and enhancement of the carbon felt corrosion. Furthermore, the potential gains reached almost 390 mV (Pt/C) in the HER side, and 340 mV (IrO_2) at 48 mT, being superior to the potential gains at 10 mA.cm^{-2} (134 and 242 mV for these catalysts at 48 mT respectively). For FeNi-based catalyst, the potential gains at 30 mA.cm^{-2} are 30-50 mV above those at 10 mA.cm^{-2} (214 compared to 179 mV for $FeNi_3$@Ni and 166 compared to 111 mV for $FeNi_3$@Mo) in the HER

side, while in the OER side, a potential gain superior of more than 100 mV is observed between those at 30 and 10 mA.cm^{-2} (184 compared to 94 mV for $FeNi_3$@Ni and 274 compared to 85 mV for $FeNi_3$@Mo). Thus, the mechanism of magnetic activation for HER and OER are very different, although one cannot exclude one or the other mechanism. Again, it is possible that a change in the rate determining step occurs at such current density. A Tafel study could give hint regarding this point (see IV.2.2). Nevertheless, it seems consistent that at higher current density, and so higher gas production rate, the magnetic activation increased too, especially on the mass-transport kinetics. Besides, it is also rational to think that the influence of the AMF could change the Gibbs free energy $\Delta_r G$ (= $\mu°_{X/Y}(T)$ + $RT\ln(a_i)$, $\mu°$ being the standard chemical potential of the X/Y redox couple and a_i their chemical activity), in function of the AMF amplitude (*i.e.* the temperature), but also their standard chemical potential. Thus, the evolution of $\Delta_r G$ of the different materials may differ, which could account partially for the different trends between the catalysts [268,269].

In summary, the application of an AMF impacts positively the WS reaction, by rising the temperature of the catalyst. The heating is non-negligibly due to eddy currents generated inside the carbon felt. It is the main heating source for catalysts whose SAR is below 50 W.g^{-1} (PGM catalysts and $FeNi_3$@Mo), and possibly for the others also. This result was unexpected, as the cell was purposely designed to limit at maximum eddy current generation. Thus, thinking about the practicity of a magnetically-enhanced WS system, exploiting eddy currents instead of optimizing the SAR of the NPs seems an easier/complementary route. This approach was tried, where new cells have been designed to optimize eddy current generation, and preliminary results will be given in Supplementary Figure 19. Coming back to the influence of the AMF on the WS process, the exact action of the magnetic field is not fully understood. It surely influences the kinetics of the reaction, but does the thermodynamic equilibrium of the system shift? Besides, as a non-negligible heating is generated, a temperature gradient appears and a

Soret effect can influence mass-transport [270]. Moreover, the AMF can also influence the surface tension, the surface coverage or the void fraction of the adsorbed bubbles, according to a Maxwell stress or Marangoni effect induced by a temperature/concentration gradient [271] or a magnetic field [110,111]. The latter stems from a temperature gradient or a concentration gradient. In this case, due to an imbalance between an isolated bubble where a higher supersaturation level exists (lower surface tension in the vicinity) and a population of bubble where the opposite applies, a surface tension gradient is formed and forces the population of bubble to coalesce with the isolated bubble [271]. The Maxwell stress is triggered by the application of a MF, and corresponds to an interaction between the MF and the dipole moment of a charged specie (gas bubbles or hydroxide anions in this work). In function of the MF direction, the dipole moment can be stretched or shrank, which modifies its surface tension [272,273]. Such phenomena have already been observed for static magnetic fields, where the surface tension of paramagnetic species increased [274] or decreased [275] of a few percent, under a homogeneous magnetic field up to 10 T, or for the paramagnetic radical nitrobenzene NB•, where the charge-transfer and double layer capacitance was modified by 50% under 500 mT [272]. While these effects had been observed under SMF, and that the AMF amplitude range herein is much lower, the samples could undergo a magnetic field gradient, by creating a surface tension gradient around the bubble (the surface tension varying from one side to the other side of the bubble) due to the continuously changing AMF direction, which could disrupt the bubble attachment and thus have an impact on its departure. In addition, other effects, Lorentz, Kelvin, spin polarization, presented in chapter I (section I.4), can also influence the system. The thermodynamic and kinetics changes are evaluated in section IV.2 below, while the influence of other possibly interfering phenomena is addressed in section IV.3.

IV.2 Thermodynamics and kinetics evolution

IV.2.1 Thermodynamics/kinetics change at T > 25°C under a magnetic field

Subsection IV.1.3 showed that $FeNi_3$ catalyst heats up to ~ 85°C, inducing a temperature gradient between the surface of the electrode and the diffuse layer. This temperature increase is not negligible, and it raises the following questions: (1) does the temperature gradient have an impact on the mass-transport (bubbles)? How does the void fraction profile look like? (2) How do the thermodynamics and the kinetics change exactly at such temperature and (3) under a magnetic field? Is the Nernst law, depicting the potential of an electrode in a given medium still valid in these conditions, and especially under a magnetic field which can induce MHD effects? (4) Besides, do the temperature gradient or the AMF spark other temperature-related effect(s) (Marangoni, Maxwell stress: surface tension gradient around the bubble)?

(1) The effect of a temperature gradient on the void fraction profile has been simulated by Durand Brunel Zozime Tsiatsipy during a three-months internship at the LEPMI, under Jonathan Deseure's supervision.

In order to take into account the temperature gradient, the thermophoretic velocity v_T of the bubbles (stemming from the Soret effect) was considered and compared to the Stokes velocity v_S of the bubbles. Their expressions are as follow [276]:

Thermophoretic velocity
$$v_T = k\upsilon \frac{\nabla T}{T} \quad \text{IV.1}$$

Stokes velocity
$$v_S = \frac{\Delta\rho \, d_{bubble} \, g}{18\upsilon} \quad \text{IV.2}$$

With k an attenuation factor depending on the geometry of the system and the environment, and also accounting for the shielding due to surrounding bubbles (dimensionless), $k \in [0; 1]$, υ the cinematic velocity of the fluid ($m^2.s^{-1}$), ∇T the temperature gradient inside the

electrolyte, T the electrolyte temperature, $\Delta\rho = \rho_{bubble} - \rho_{fluid}$ the density difference between the gas density ρ_{bubble} and the electrolyte density ρ_{fluid} (both in $g.cm^{-3}$), d_{bubble} the bubble diameter (~ 150 nm for H_2 and 300 nm for O_2 [110,111,112]) and g the gravitational constant ($m.s^{-2}$).

Simulating the temperature gradient due to a heating of the carbon felt of ~ 80°C at maximum gives the following void fraction (*i.e.* the bubble number at the electrode surface) and velocity profile, Figure IV.17. at the vicinity of the electrode surface, symbolised by the red vertical line on the y axis.

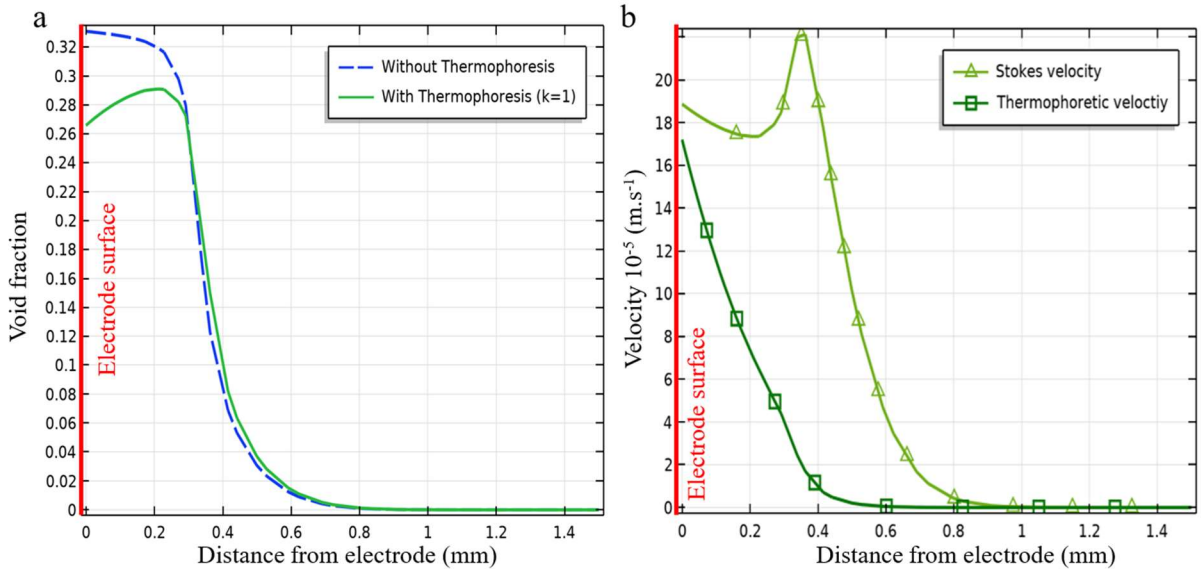

Figure IV.17: (a) Void fraction profile without taking the Soret effect, or with it, *i.e.* when considering the influence of the temperature gradient induced by the AMF exposure (b) Stokes and thermophoretic velocity profiles at the surface of the electrode, which is symbolised by the red vertical line on y axis in (a) and (b).

The simulation indicates that the void fraction at the electrode/electrolyte interface is reduced when a temperature gradient inducing a Soret effect is applied, *i.e.* when the AMF is switched on. The bubbles' coverage is reduced by 20%, supporting the mass-transport enhancement under AMF. This behaviour is confirmed by the velocity profile, showing that the thermophoretic and Stokes forces are of same order of magnitude close to the electrode surface. The peak in the Stokes velocity profile is shifted compared to the peak in void fraction, due to the hindering of the other bubbles. In this simulation, the velocities are "superficial velocity", that is, they are averaged by the ratio of the bubble volume by the electrolyte mixture.

(2) To study the thermodynamic and kinetics of the water electrolysis reaction at high temperature, our study is based on a paper from 1976 by Miles *et al* [39]. Several other papers surveyed this influence, but at higher pressure (8-25 bar [37,38]), not mimicking the present working conditions, where the total pressure should not be much higher than 1-2 bars. Miles *et al.* studied the electrode kinetics on Ni surfaces in HER and OER at 5 temperatures: 25, 80, 150, 208 and 264°C in 50 wt.% KOH. They indicate that the reversible potential U_{rev} goes from 1.229 V in STP to 1.027 V at 264°C, while the thermoneutral potential U_{tn} barely varies from 1.48 V in STP to 1.49 V at 1000°C. Thus, the thermodynamics of WS is unfavoured at higher temperature. However, the kinetics of the reactions is enhanced (Figure IV.18).

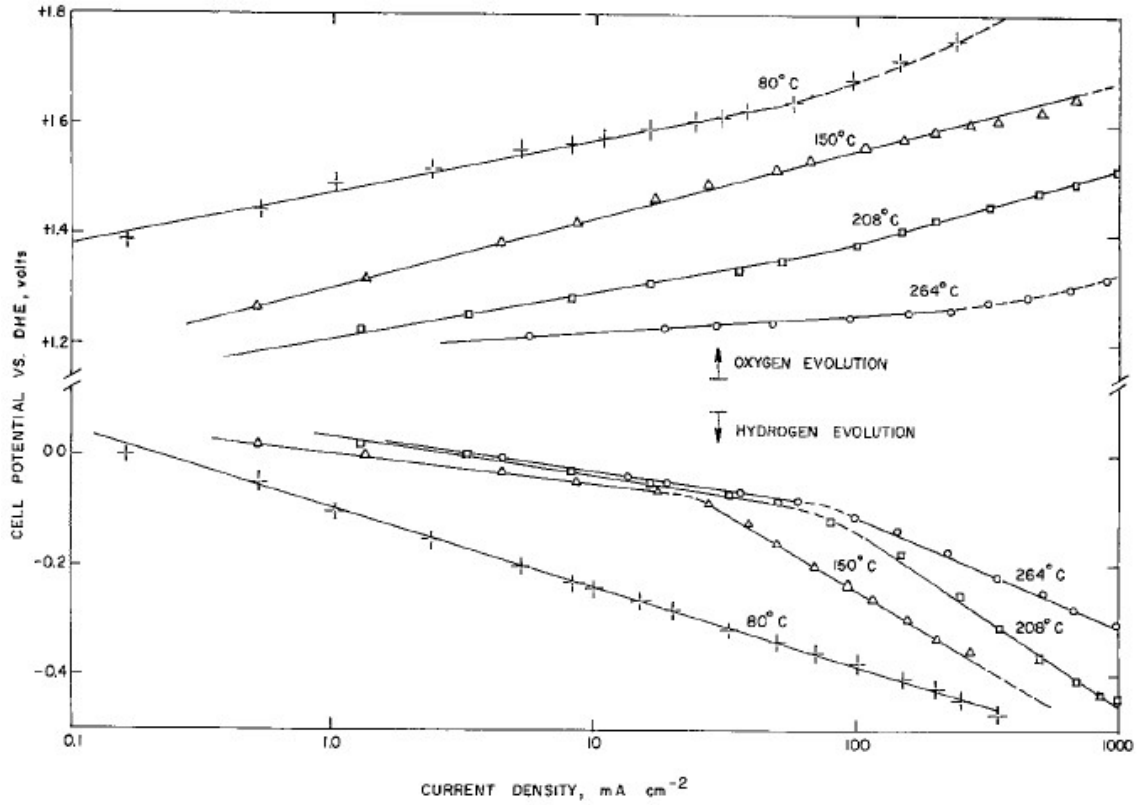

Figure IV.18: Potential *vs*. current density (log scale) for HER and OER on polished Ni electrodes in 50 wt.% KOH at $T \in \{80; 150; 208; 264\}$°C. Both Ni electrodes had a geometrical area of 0.20 cm^2. Reprinted from [39] with permission from the Electrochemical Society.

The effect of temperature is more significant on OER than on HER kinetics. It can be seen on the graph that the cell potential exhibits a slope discontinuity. The author calculated the Tafel slope, the charge-transfer coefficient and the exchange current density in low and high

overpotential regions, and found that the electrochemical desorption step is the rate determining step in the HER side (corresponding to the equations II.4 and II.5), while it is the electron-transfer step in the OER side (equation II.6). The Ni oxides undergoes a magnetic transition from antiferromagnetic to paramagnetic at its Néel temperature, T_N = 250°C, where a change in O_2 chemisorption occurs, suggesting that the recombination step becomes the rate determining step above T_N. Thus, increasing the temperature does reduce the cell voltage, and it induces mechanism changes. A Tafel investigation is presented below in subsection IV.2.2. No magnetic transition should be observed in the PMMA cell as the Néel temperature is not reached.

(3) Although the MHD equation was studied when considering a magnetic field contribution inducing an enhanced mass-transport, as discussed in section I.4.1, only one paper (as found by the author) deals with a change of the equilibrium constant under a magnetic field [277]. It considers the variation of magnetic susceptibility of the electrolyte containing paramagnetic or diamagnetic ions, which can create gradient concentrations of these species (Kelvin effect). The effect on the equilibrium constant is of the order of 10^{-5}, indicating a very small or rather negligible influence. Considering the kinetics under a MF, no paper relates an adapted Nernst law under this condition. Devos *et al.* questioned the effect of a 1 T static magnetic field on the electrochemical kinetics of different systems (Fe^{3+}/Fe^{2+}, Zn^{2+}/Zn electrodeposition, Cu electrodissolution) by conducting EIS measurements and found no change in the charge-transfer coefficient [278], while an enhanced electron-transfer is found in papers dealing with a spin polarization effect [147,153,158,161], or Lorentz [86] and Kelvin [135] effects. As no consensus is found in the literature regarding a potential charge-transfer kinetics effect due to the application of a magnetic field, experiments under constant magnetic field were conducted to evaluate if these phenomena intervene in the PMMA cell system. The results are presented in subsection IV.3.2.

(4) A temperature gradient (Marangoni effect) or a Maxwell stress influencing the surface tension and enhancing mass-transport are surveyed in subsection IV.3.3.

IV.2.2 Tafel investigation

As emphasized in part II.2.1.2, this method could be a powerful tool, as intrinsic kinetics parameters such as the charge-transfer coefficient, the exchange current density j_0 and the Tafel slope, which gives insight onto the rate determining step could be extracted. However, the required conditions are not often realized. Indeed, the portion of the curve fitted should be at least 50 mV away from the corrosion (or equilibrium) potential E_{corr} (being the potential of the sample dipped into the electrolyte, thus at an overpotential around 0 V, see Figure IV.19 below) and the fitting should be done on a decade of current. Besides, the mass-transport limitation has to be completely negligible and Ohmic-drop corrected. These requirements are seldomly verified, especially in the case of gas evolution, when bubbles block new reactants adsorption, impede mass-transport and may alter the Ohmic drop in the electrolyte. Accordingly, “strange” (mass-transport/Ohmic drop altered) results could appear, as exhibited by the Tafel values found, presented in Figure IV.19 and developed below, where 3000 $\mu g.cm^{-2}$ loaded $FeNi_3$ cyclic voltammetry curves are presented.

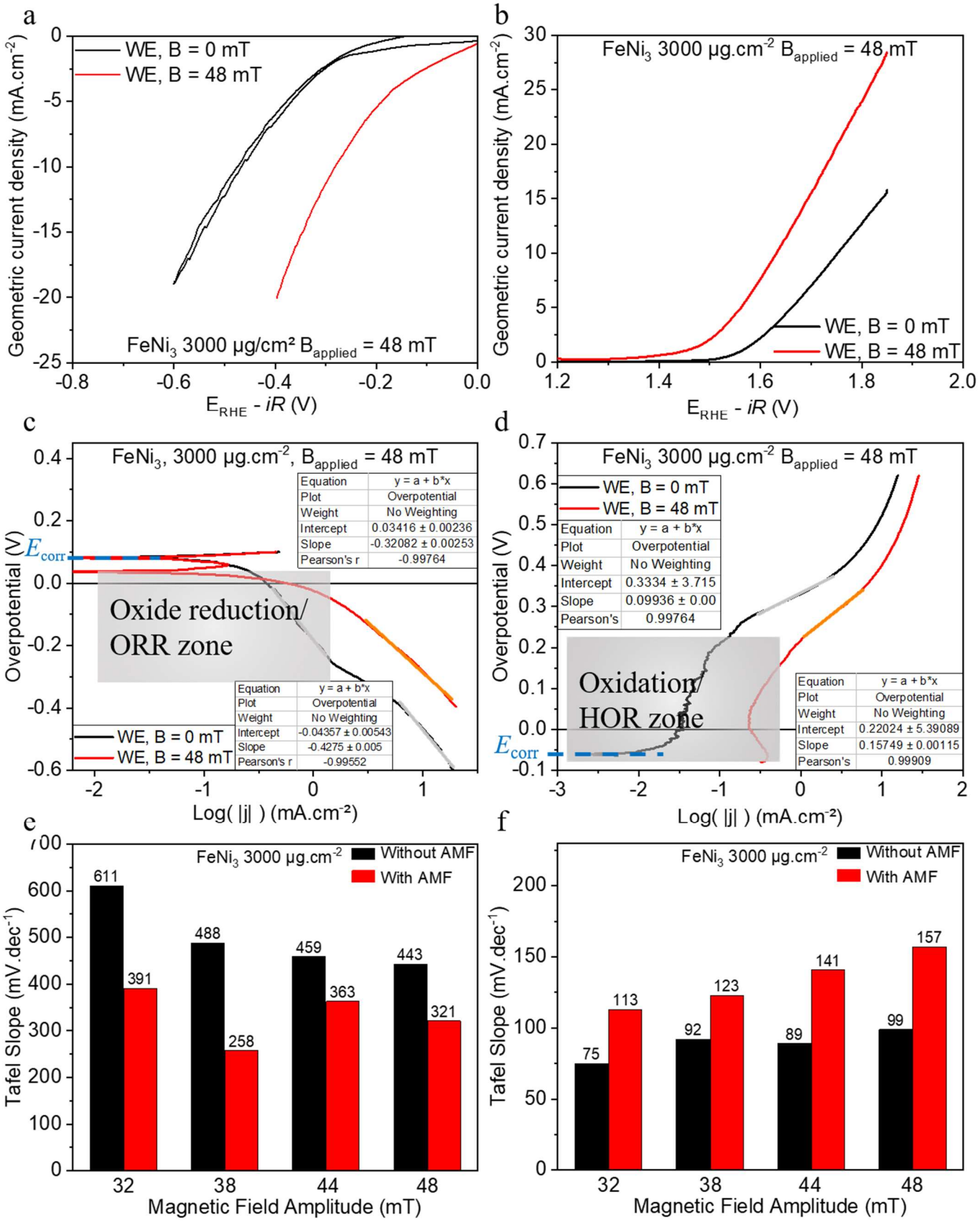

Figure IV.19: Geometric current density (considering a deposit area of 1 cm^2, as measured over many samples) *vs.* compensated potential at 48 mT for $FeNi_3$ loaded at 3000 $\mu g.cm^{-2}$, recorded at a scan rate of 10 $mV.s^{-1}$, at (a) the HER and (b) the OER side. Corresponding Tafel representation for (c) HER and (d) OER with the linear fitting (grey curve without AMF, orange curve under AMF). Tafel slope values measured for the curves under magnetic field amplitude in the [32; 48] mT range, tested for (e) HER and (f) OER.

The displayed set of curves present a better activity than those showed in subsection IV.1.1 as the current collector was a rake-shape gold wire, diminishing the Ohmic losses, although these are partly compensated. On the graphs (a) and (b), it is clear that the application of the AMF enhances the overall kinetics of the reaction: the onset potential diminishes a lot under AMF. Plotting the overpotential versus the logarithm of the current density (considering a deposit area of 1 cm^2, as measured over many samples) – the so-called Tafel representation (c-d), a linear fitting could be done on two curve portions. The first one is at low overpotential, $\eta \in [0;0.25]$ V, and corresponds to the capacitive current linked to the reduction of the oxides and the oxygen reduction reaction (ORR) in the HER side, and to the oxidation of the material and the hydrogen reduction reaction (HOR) in the OER side; and thus does not correspond to the gas evolution. The second portion at $\eta \in [0.3; 0.4]$ V is of interest. It is visible that the linear fitting does not span over one decade of current, but barely on half a decade. It indicates that the conditions are not ideal to use the Tafel method, mass-transport (and Ohmic-drop?) limitations being not negligible. By diminishing the scan rate (being 10 $mV.s^{-1}$) to 1 $mV.s^{-1}$ or less, one could have limited the capacitive influence (obvious in the low overpotential region), but the experiment time would have been too long to be realized (especially under AMF), and this would not have decreased the effect of mass-transport. The absolute values of the "Tafel" slopes obtained at magnetic field amplitudes ranging from 32 to 48 mT and without AMF are summarized in a bar chart for HER (e) and OER (f) (similar trend is observed at lower AMF amplitude). On the HER side, high values superior to 200 $mV.dec^{-1}$ are obtained. This is much higher than classic Tafel slope values for this reaction (Miles *et al.* obtained values below 80 $mV.dec^{-1}$); they are biased by significant mass-transport (at least) effect and can thus not be used to extract and interpret charge-transfer kinetics parameters. In the OER side, lower values are obtained, more consistent with the literature, even if they are a bit higher (Miles *et al.* presented values below 80 $mV.dec^{-1}$). The first striking observation is the higher Tafel slope

under AMF than without, with values increasing when rising AMF amplitude. Having a closer look on the graph (d), the fitting of the curve under AMF could not be made on the same current range than the curve without AMF. Thus, the magnetic field seems to improves that much the kinetics that the curve is shifted negative (in potential), and the higher Tafel values are due to the much higher bubble release rate, sparking immediate mass-transport hindrance. Unexpectedly, the Tafel slope values without AMF increase in the course of the experiment. This could be due to the degradation of the sample, and by the bubbles which are increasingly trapped into the carbon felt, again due to the higher bubble production under the magnetic field. Thus, the charge-transfer kinetics parameters cannot be reliably extracted and interpreted. Nevertheless, these observations support the high enhancement of the kinetics under AMF, being superior to the mass-transport improvement, in accordance with the discussions in the section IV.1. Furthermore, no abrupt change in the Tafel slope was visible in HER, indicating that no change in the rate determining step is obvious in these experimental conditions (for OER, it could exist).

IV.2.3 Open circuit voltage study

In order to see if the double layer dynamics (that may affect the thermodynamics of the O_2/HO^- and H_2O/H_2 couples) changed under the AMF, Open Circuit Potential (OCP) measurements were carried out. They consisted of applying ±10 mA (CP) during 30 s at the WE, then cut the current and the electrolyte flux, and let the WE potential come back to its potential when no current passes through it, the so-called OCP. Applying a current enables to produce the oxidant O_2 of the O_2/HO^- couple, or the reductor H_2 of the H_2O/H_2 couple. Indeed, the OCP is defined by the Nernst law when both species are present (*cf.* equations I.4 and I.5). This has been done under several magnetic field amplitudes, for $FeNi_3$(@Ni) catalysts. Figure

IV.20 displays the OCP measurements of $FeNi_3$@Ni loaded at 3000 µg.cm^{-2}, at B ∈ {0; 32; 44} mT. $FeNi_3$ curves were similar, and no other catalyst was tested.

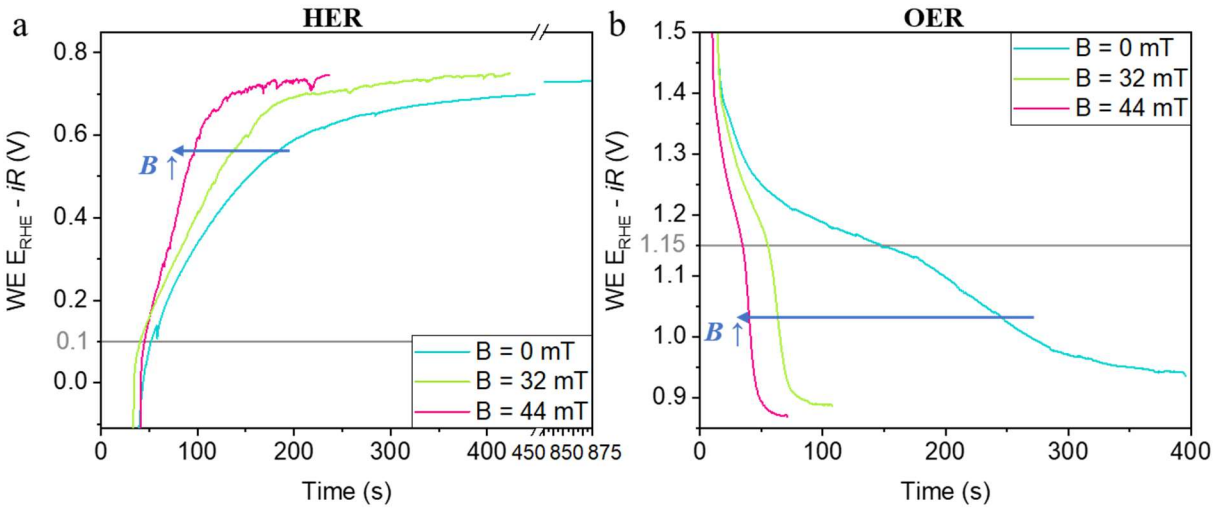

Figure IV.20: OCP measurements on $FeNi_3$@Ni loaded at 3000 µg.cm^{-2} in (a) the HER side and (b) the OER side for different magnetic field amplitudes.

The OCP (being usually 0.85 V_{RHE} without AMF in this medium) does not change under AMF. Besides, the inflexion point is at the same potential, whatever the AMF amplitude, on both sides (indicated by a grey line). This inflexion point results from an equilibrium of the concentration of OH^- ions at the electrode||electrolyte interface, between OH^- from the solution, and OH^- which desorbed from the catalyst surface. This equilibrium comes from the balance between the electron chemical potential of the catalyst and the electrolyte which become equal when the current is switched off (like at an interface between a semiconductor and a metal). It sparks a potential gradient where the ions in the double layer reorganize to reach the electroneutrality. The electron chemical potential is directly proportional to the Gibbs free energy. The fact that the inflexion point does not change even under AMF indicates that the AMF does not change the Gibbs free energy. However, the time necessary for the potential to go back to the open circuit differs in function of the AMF amplitude. It decreases when the magnetic field increases, in both half-reaction sides. A hypothesis is that the temperature elevation facilitates the oxide reduction/formation in the OER/HER side (better kinetics), which

could reduce the time to reach stable OCP. Nevertheless, it is thought that this enhanced kinetics is not sufficient to explain the time diminution. Therefore, the AMF must also improve mass-transport, in support of the previous hypotheses.

Furthermore, *iR* drop determination was also measured under AMF, to see if the electromagnetic noise does not modify the Ohmic losses, which could lead to an inaccurate compensation. No difference between the Ohmic drop without or under AMF was measured.

IV.3 Evaluation of possible contributing effects to the system

In a first instance, orders of magnitude were calculated to evaluate the possible influence of the considered effects. Then, experiments were carried out to confirm the calculation.

IV.3.1 Order of magnitude calculations: preliminary study

Several forces were taken into account: forces existing in an electrochemical cell [88], magnetic forces, and four dimensionless numbers used in MHD: the Hartmann and three Reynold numbers. The former characterizes conductive fluid movements in a magnetic field whereas the latter are a ratio between the convection and diffusion terms in a fluid being magnetic or not, or a bubble plume. The forces and their order of magnitudes are given in Table IV.2 while the parameters and their estimated values are given in Table IV.3. The reader can refer to Supplementary Figure 14 for the calculation details of the Lorentz force on bubbles. The Maxwell stress is barely discussed in the literature, and not related force has been found. The effect is link to a tensor, which depend on the permittivity, the permeability and the electric and magnetic fields. Its calculus was not conducted as no comparable data currently exist.

Table IV.2: Typical forces acting in aqueous electrolytes, magnetic forces, Hartmann and several Reynold numbers, besides with thermophoretic and Stokes velocities. Red colour indicates a force acting on species, black force on fluids, and blue force on bubbles.

	Physical parameters	Expression	Typical value
Body forces ($N.m^{-3}$)	Driving force for diffusion	$RT\,\nabla c$	10^{8}
	Driving force for electromigration	$n\mathcal{F}c\nabla V$	10^{10}
	Lorentz force on ions	$\boldsymbol{j} \times \boldsymbol{B}$	10^{1} | 10^{3}
	Concentration Marangoni effect on ions	$\frac{3}{d_{bubble}} \frac{\partial \gamma}{\partial p} \nabla p$	10^{8}
	Driving force for natural convection	$\Delta\rho_{fluid}\,\mathbf{g}$	10^{3}-10^{4}
	Viscous drag	$\zeta \nabla^2 v$	10^{-1}
	Lorentz force on bubbles	$\boldsymbol{j} \times \boldsymbol{B}$	$3\ 10^{2}$ | $5\ 10^{3}$
	Kelvin force on O_2	$-\frac{1}{\mu_0}\chi_m c B\,\nabla)$	10^{3}-10^{7}
	Paramagnetic force on O_2	$-\frac{1}{2\mu_0}\chi_m B^2 \nabla c$	10^{4}
	Concentration Marangoni effect on bubbles	$\frac{3}{d_{bubble}} \frac{\partial \gamma}{\partial c} \nabla c$	10^{8}
	Thermal Marangoni effect	$\frac{3}{d_{bubble}} \frac{\partial \gamma}{\partial T} \nabla T$	10^{5}
Dimensionless numbers	Hartman number H_a	$B\delta\sqrt{\frac{\sigma}{\eta}}$	10^{-2} | 10^{-3}
	Magnetic Reynold Number Re_{mag}	$\mu_0 \sigma \upsilon L_{c1}$	10^{-9}
	Channel Reynold number $Re_{channel}$	$\frac{L_{c2} v}{\upsilon}$	10^{1}
	Bubble Reynold Number Re_{bubble}	$\frac{d_{bubble} v}{\upsilon}$	10^{0}
Velocities ($m.s^{-1}$)	Thermophoretic velocity	$k\upsilon \frac{\nabla T}{T}$	10^{-4} for k=1
	Stokes velocity[3]	$\frac{\Delta\rho d_{bubble}{}^2 g}{18\zeta}$	10^{-3} with $\Delta\rho = 10^{2}$ $kg.m^{-3}$ as it is in a mixture phase

[3] The indicated formula does not take into account the hindering sparked by the surrounding bubbles. It gives however the velocity reached by one single bubble. Thus, the value found in the simulation in subsection IV.2.1 is lower of one order of magnitude.

Table IV.3: Parameters and their estimated values sorted by alphabetic order.

Parameters	Expression	Considered value
Magnetic field	B	50 10^{-3} T | 1 T
Magnetic field gradient	∇B	10^{3} | 10^{7} T.m^{-1}
Ionic concentration	c	10^{3} mol.m^{-3}
Ionic concentration gradient	∇c	10^{5} mol.m^{-3}
Variation of surface tension with c or P	$\frac{\partial \gamma}{\partial c}$ or $\frac{\partial \gamma}{\partial P}$	0.05 N.m^{2} or 0.05 m [271]
Variation of surface tension with T	$\frac{\partial \gamma}{\partial T}$	10^{-4} N.m^{-1}.K^{-1} [271]
Distance between the electrodes, used to calculate ∇V	d	10^{-2} m
H_2 or O_2 bubble diameter (in KOH 1 mol.L^{-1})	d_{bubble}	2 10^{-4} m
Temperature difference	ΔT	80 K
Distance over the temperature gradient	Δz	2 10^{-3} m
Diffusion layer, used to calculate Hartmann number	δ	10^{-4} m
Dynamic viscosity	ζ	10^{-3} Pa.s [279]
Gravitational constant	g	9.81 m.s^{-2}
Current density	j	10^{3} A.m^{-2}
Characteristic length (felt diameter)	L_{c1}	1.6 10^{-2} m
Characteristic length (For Re $_{channel}$)	L_{c2} =4*section*perimeter	1.3 10^{-2} m
The mole number of exchanged ions	n	2
Kinematic viscosity of KOH 1 mol.L^{-1}	υ	5 10^{-7} m^{2}.s^{-1}
Pressure gradient	∇P	10^{5} N.m^{-3}
Fluid density	ρ_{fluid}	10^{3} kg.m^{-3}
Density difference between gas and fluid	$\Delta\rho$	10^{2}-10^{3} kg.m^{-3}
Electrolyte conductivity	σ	21.53 S.m^{-1} [280]
Temperature	T	298 K
Temperature gradient	$\nabla T = \frac{\Delta T}{\Delta z}$	10^{5} K.m^{-1}
Fluid velocity	v	10^{-2} m.s^{-1}
Voltage	V	1 V
Voltage gradient	∇V	10^{2} V.m^{-1}
Molar magnetic susceptibility of O_2	χ_m	3.449 10^{-12} m^{3}.mol^{-1}

It can be concluded that the driving force by diffusion and electromigration overwhelms by far the Lorentz force on ions, but the Marangoni concentration effect can have an influence. While the Lorentz force on bubbles is small, the concentration Marangoni and Kelvin forces can have an influence on them (at a very local scale for Kelvin [281]). The Hartmann estimation indicates that there is no MHD effect on the electrolyte, supported by the magnetic Reynolds number which indicates that no MHD convection should drive the electrolyte, the system remaining in a laminar regime. Besides, the channel Reynold number proves that the electrolyte flux applied remains in a laminar regime as well, and the bubble Reynold number states that the bubble plume are also in a laminar regime. Therefore, no huge influence of magnetic forces is expected. Especially, a remnant Kelvin effect due to remaining magnetic gradients at a very local scale after MF exposure is ruled out, as the remnant magnetic field of the catalysts is nearly null (see Table III.7). Nevertheless, spin polarization effect can arise, as observed by Garcès-Pineda *et al.* [156] and Ren *et al.* [157]. Moreover, a change in surface tension could arise, facilitating bubble departure and thus improving mass-transport. In order to confirm these calculations, experiments with permanent magnets were realized (static magnetic field - SMF).

IV.3.2 Experimental evaluation of F_L, F_K and the spin polarization

Experiments under a SMF were conducted on $FeNi_3$ at 3000 µg.cm^{-2}, as this catalyst was more magnetic (larger M_S and M_R) compared to the others. A perpendicular magnetic field of 200 mT, corresponding to a magnetization equals to 91% of M_S, and a parallel magnetic field of 80 mT corresponding to a magnetization of 75% M_S were applied using commercial NdFeB magnets. A magnitude close to the saturation magnetization was important as the spin polarization effect appear when ferromagnetic materials are magnetized. While the applied MF is not above the M_S value of the material, it is larger than the one applied in the PMMA cell under AMF, so that it is sufficient to check if other magnetic forces are at stakes in this system.

Figure IV.21 presents representative CP at ± 10 mA.cm^{-2} and CV_F tests. Three samples were tested for reproducibility. The noise is due to the electrolyte flux rate and bubbles departure.

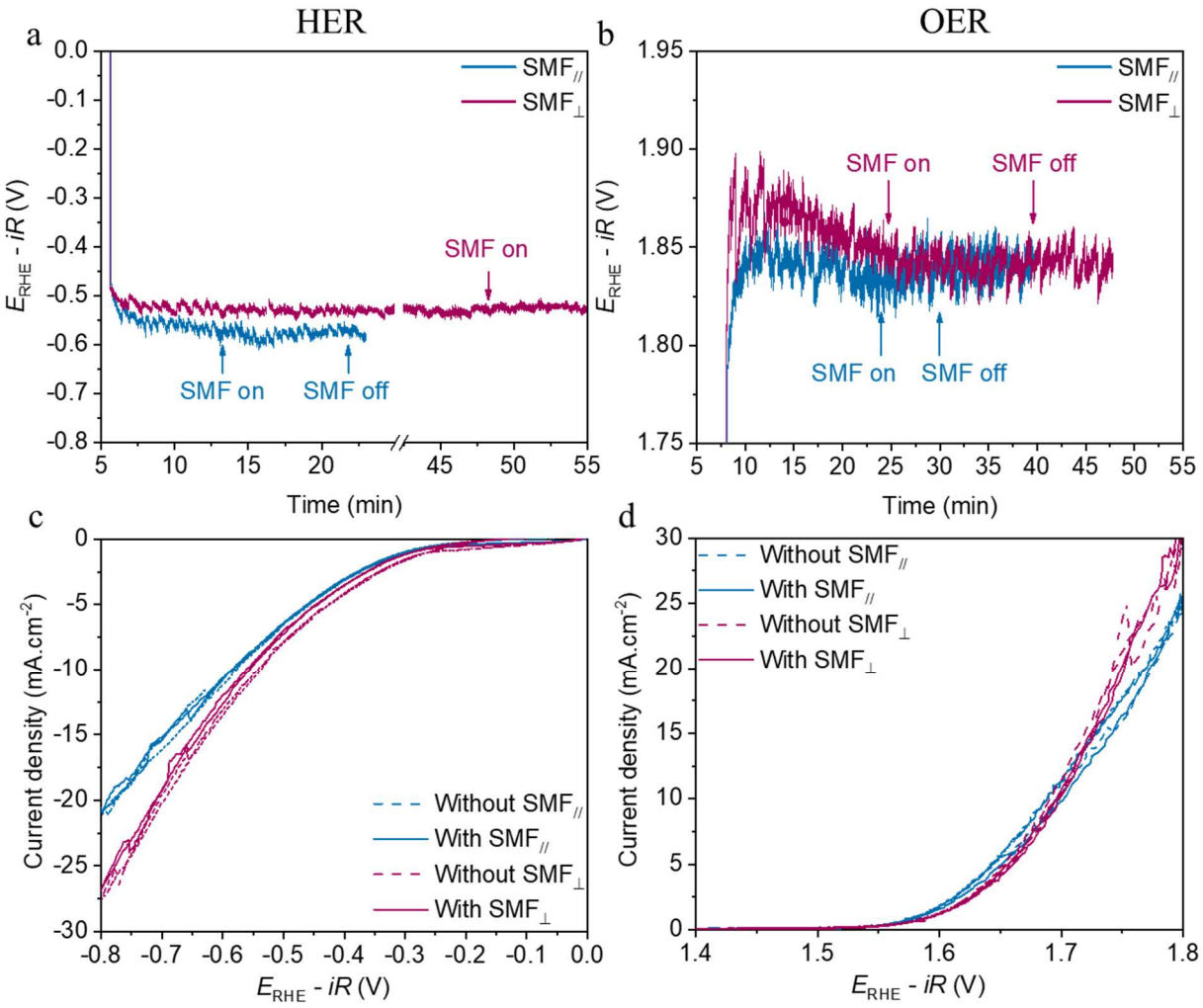

Figure IV.21: (a-b) CP at ± 10 mA.cm^{-2} and (c-d) CV_F measurements of $FeNi_3$ at 3000 µg.cm^{-2} under a parallel (SMF//) or perpendicular (SMF⊥) magnetic field, for HER on the left, and OER on the right. "Switch on" and "Switch off" indicates that the permanent magnet is approached to the PMMA cell or removed from it, respectively.

The application of the MF, whether parallel (SMF//) or perpendicular (SMF⊥) to the electrode surface, has no influence on the potential during CP measurements (or it is smaller than the noise), neither on the current density during CV_F measurements. Especially, no spin effect was observed, while Garcès-Pineda *et al.* and Ren *et al.* found a striking change, with materials presenting similar saturation magnetizations. In order to go deeper into a possible spin polarization effect, further OER measurements were conducted in a beaker - similar to Garcès-Pineda setup - which allowed to approach closer the permanent magnets and increase

accordingly the MF amplitude. A classical {carbon felt+NPs deposit} and a Ni slab served as samples. HER measurements were conducted and no influence of the SMF could be detected, consistently with the fact this effect should not arise since this half-reaction does respect the spin conservation rule. No effect was found for OER CV_F measurements on the carbon felt, and a fuzzy, non-reproducible effect was observed during an OER chronoamperometry measurement. The bulk Ni slab - much more magnetic (more magnetic mass) - was not influenced by the SMF during CV_F and CP tests either. The variation of the potential for this latter was in the range of bubble departure noise. This is in contradiction with Garcès-Pineda results, where a positive effect was found for both configurations, being much more significant for a parallel SMF. The measurements of the Ni slab are given in .

In any case, no magnetic force influence was observed in the PMMA cell.

IV.3.3 Marangoni and Maxwell stress: surface tension measurements

In order to evaluate if the magnetic field could have an influence on the surface tension of the electrolyte and on the bubbles, which may weaken their attachment at the electrode surface, measurements of surface tension of water were realized in Chambéry, by Durand Brunel Zozime Tsiatsipy and Jonathan Deseure. The pendant drop technique was employed, where the drop is hanging from a capillary, and the surface tension is deduced from a mathematical model which considers that the drop shape is dictated by the interplay of the forces acting on the drop (surface tension and gravity) [275]. The following Figure IV.22 was drawn, were the surface tension of water at 20°C was measured in the absence of a magnet (a), when the exterior edge of a ring magnet was at 200 µm of the drop (b), and when the drop was at 200 µm of the centre of the ring magnet (c).

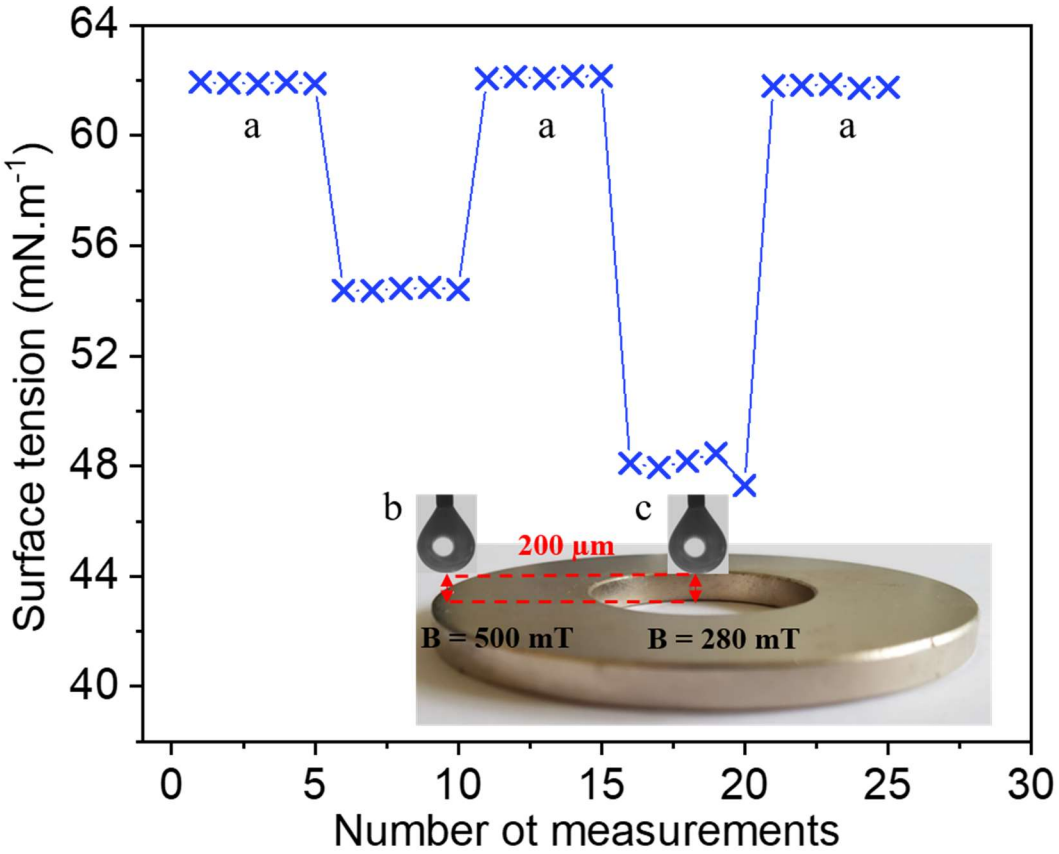

Figure IV.22: Surface tension measurements of a water drop at 20°C, (a) without a magnet, (b) with the drop at the edge of a ring magnet, and (c) at the centre of the ring magnet. The magnet was approached to 200 µm to the drop.

Clearly, the presence of a magnetic field does have an impact on the water surface tension, reducing it by 12% (b) or 23% (c). The values in (b) and (c) are not comparable regarding the MF amplitude, because the magnetic field lines are very different: they are very straight in the vertical direction in (c), and diverging toward the exterior in (b). These results are preliminary, and further measurements need to be conducted, especially on KOH 1 mol.L^{-1} and on bubbles, in order to confirm these results and assess that there exists a change in the surface tension of the electrolyte and bubble under a magnetic field (*i.e.* an additional contribution affects the shape drop close to the magnet surface). Especially, it is most likely the air flow around the bubble which may be influenced by the magnetic field, leading to a change in the surface tension, than a direct effect of the MF on the bubble surface tension. Nevertheless, this change is likely to modify the way the bubbles detach from the electrode in presence/absence of magnetic field, thereby influencing the limitations from mass-transport in gas-evolution regime for HER and OER.

IV.4 Structure evolution and degradation of the samples

The harsh conditions of water electrolysis degrade the catalyst (see III.2.1.2). Adding an AMF which increases the local temperature could enhance this degradation and cause aggregation (see I.3.1.4). Besides, the temperature can induce structure and morphology changes. In order to scrutinize these possible evolutions, different experiments were conducted on the $FeNi_3$@Ni sample, as it displays among the best catalysts' properties compared to other materials. An ILSEM survey allowed to observe the agglomerate distribution onto the carbon felt and to check if AMF led to aggregation. Then, an XRD investigation at several temperatures associated with ETEM observations under different temperatures and H_2/O_2 atmospheres enabled to inspect the crystallographic change of the $FeNi_3$@Ni catalyst.

IV.4.1 ILSEM study

Several ILSEM studies were conducted. The first one (not shown) was conducted on $FeNi_3$@Ni at 1000 $\mu g.cm^{-2}$, and allowed to validate the process to find back the same zone after a test: a hole was drilled through the deposit on the carbon felt thanks to a needle. Then, two edges of different sizes were cut around the felt (Figure IV.23). This allowed to keep the same felt position and trace back the observed zones.

Figure IV.23: $FeNi_3$@Ni sample used for the ILSEM study. The little hole in the centre and the two cut edges of different sizes allowed to identify different positions in the carbon felt.

The second study dealt with the evolution of the same catalyst and loading while doing CV_F experiment with 6 cycles, in the HER and OER side (different samples were employed for HER and OER). The micrographs are given in Supplementary Figure 16. Is presented here the third study, from which similar conclusions can be drawn. It was conducted on the same catalyst, but at a loading of 3000 $\mu g.cm^{-2}$, which undergone a CP treatment under AMF, with an identical protocol of the measurements in subsection IV.1.2. Unfortunately, such a longer and harsher treatment rendered difficult the identification of the same zones, while it has been possible for the CV_F test. Very close zones were found for HER and OER.

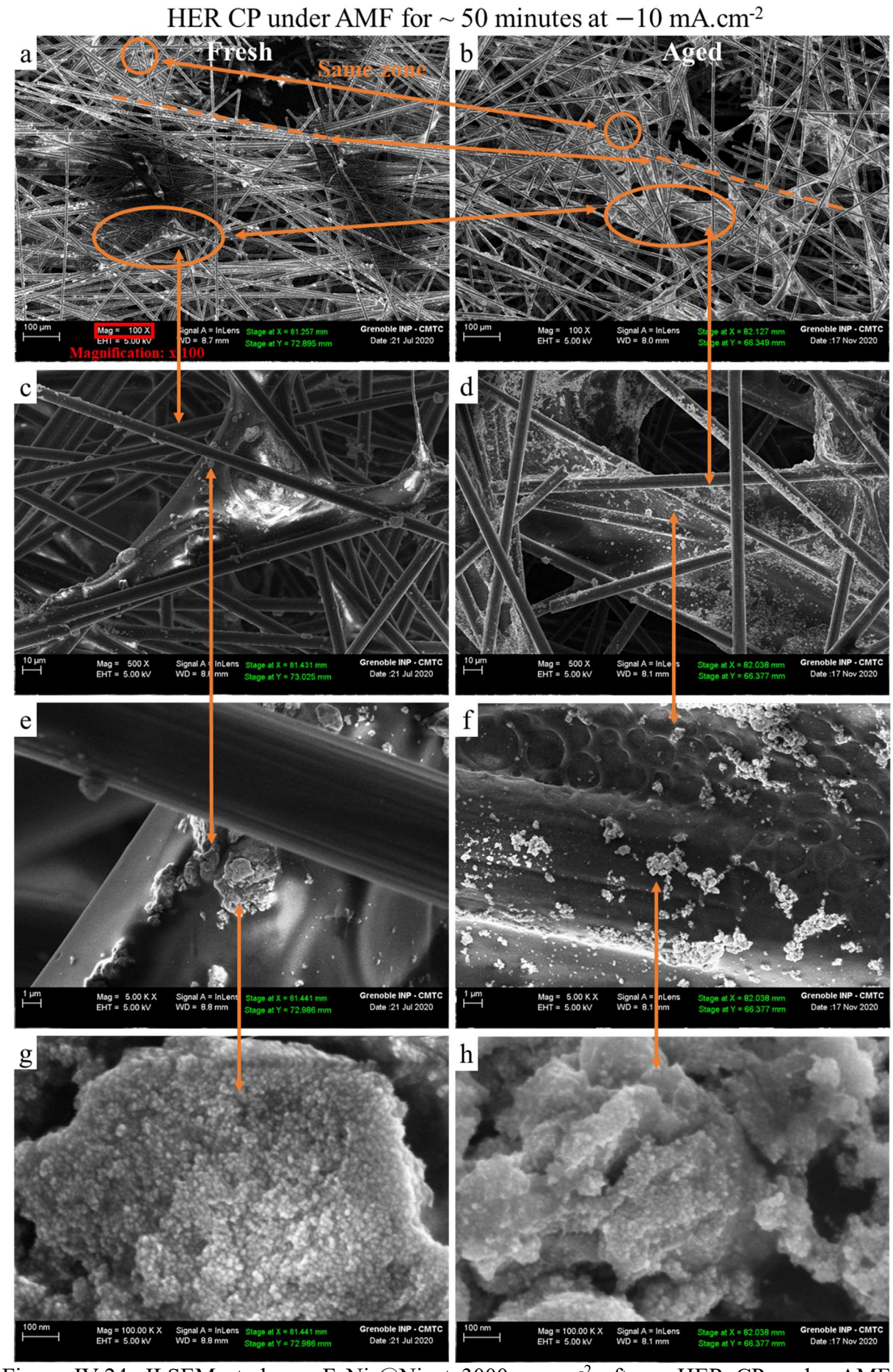

Figure IV.24: ILSEM study on $FeNi_3$@Ni at 3000 µg.cm^{-2} after a HER CP under AMF treatment. Micrographs (a-c-e-g) were taken before the experiment, while the micrographs (b-d-f-j) were taken after it. The exact zone was not successfully found back after the treatment.

Before the test, it is visible that the agglomerates are located either on the carbon fibre, or on a sort of glue. They present random shapes and are unevenly distributed. Grains are visible at the highest magnification x100 k (Figure IV.24 (g-h)). The glue creates a lot of charge effects; its surface seems smooth, thick and "not dried". It is likely the Nafion® constitutive of the ink, as X-EDS analyses in Figure IV.27 (a) indicate the presence of carbon, oxygen and fluor.

After the test, the carbon fibres moved, so that the same agglomerate were not found back, but the same zone was observed. This displacement can be caused by the electrolyte flux, the bubble departure, or by manipulation. The Nafion® seems to have spread onto the carbon felt (Figure IV.24 (a-b)), less charge effects are visible, but it solidified and got thinner at a same location. Besides, scale forms appeared (Figure IV.24 (f)) which could correspond to a KOH deposit (Supplementary Figure 16 (x)), or, a reticulation/crystallization of the Nafion®, which possibly underwent a glass transition (expected to occur around 100°C [282] – temperature that could be reached at a local scale), or cavitation effect due to bubble departure. These forms are not present in all Nafion® parts, which is consistent with the glass transition hypothesis, as probably the temperature of the felt was not homogeneous, especially due to bubble coverage. Looking closely to Figure IV.24 (h), a gangue exists among the grains. It comes from the electrolyte deposition, as confirmed by X-EDS analyses (Supplementary Figure 16 (s-t and aa)), although caution was taken to limit the deposition by dipping the felts several times into deionised water to remove KOH. No diameter measurement was realized, as it was thought not relevant owing to the dispersity of the agglomerate shape. Considering the three observed zones, it seems that no significant aggregation was triggered. The contour of the observed agglomerate seems better defined after test, possibly indicating that the local heating led to material crystallisation.

Unfortunately, no X-EDS analysis on the sample after the experiment was realized, as time was wasted trying to find back the same zones. The X-EDS analysis of the sample before test is presented in Figure IV.25. It confirms the nature of the sample: $FeNi_3$@Ni.

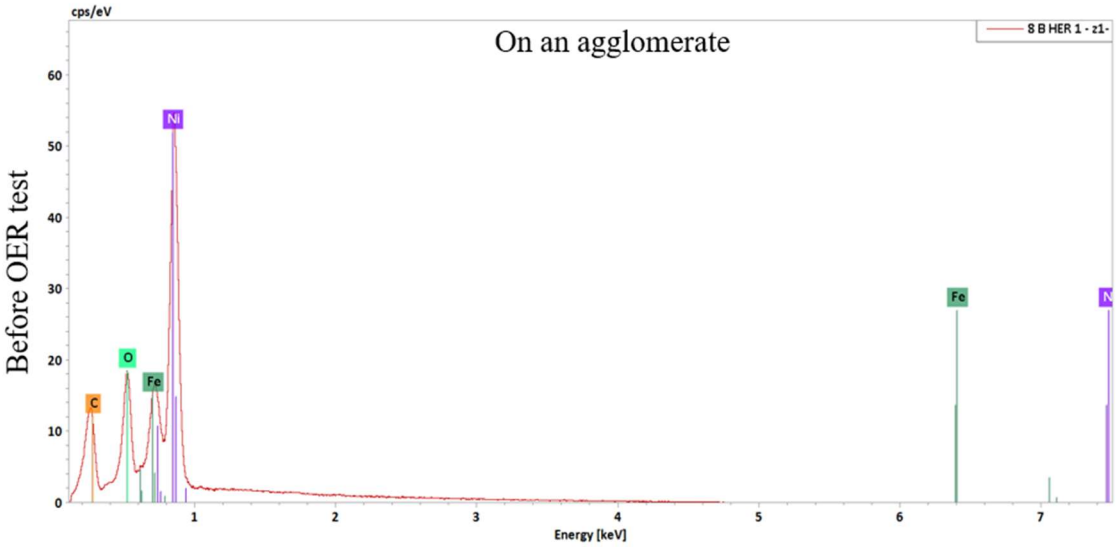

Figure IV.25: X-EDS analysis of the $FeNi_3$@Ni sample before HER test.

The micrographs before and after OER experiment are displayed in Figure IV.26. Similar conclusions can be drawn. The Nafion® seems to have moved and shrank (c-d), dragging the agglomerates with it. Taking into account the three observed zones, it seems that the Nafion® movement induces the agglomerate displacement, and that AMF exposure did not lead to significant aggregation. As the Nafion® shrinks, the agglomerates on it get closer, which could limit the number of active sites and also reduce heating.

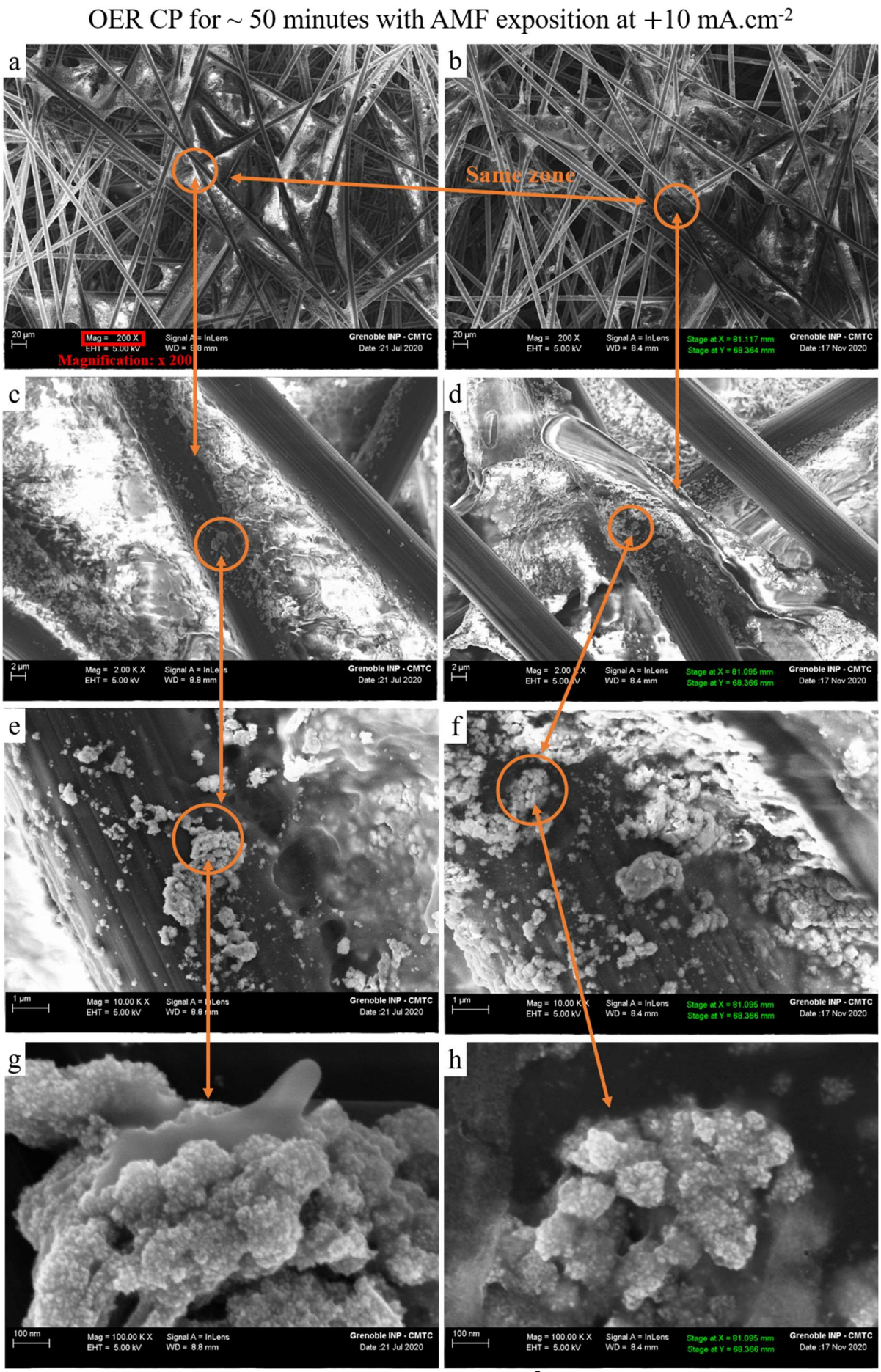

Figure IV.26: ILSEM study on $FeNi_3$@Ni at 3000 µg.cm^{-2} after a CP under AMF treatment in the OER side. Micrograph (a-c-e-g) were taken before the test, while the micrographs (b-d-f-h) were taken after it. The exact agglomerate was not successfully found back after the treatment, but the same zone is observed.

The X-EDS analyses of the glue and of an agglomerate before and after OER experiment are given in Figure IV.27. The first graph lets indicate that the glue is the Nafion®, as a lot of carbon, and peaks of fluor and oxygen are visible (confirmed by other X-EDS graphs of other zones). Contaminants such as Na and N are present, and probably come from the cell or the electrolyte tank which were not completely cleaned, or from manipulation. Figure IV.27 (b-c) indicates that there is no major contamination on the agglomerates.

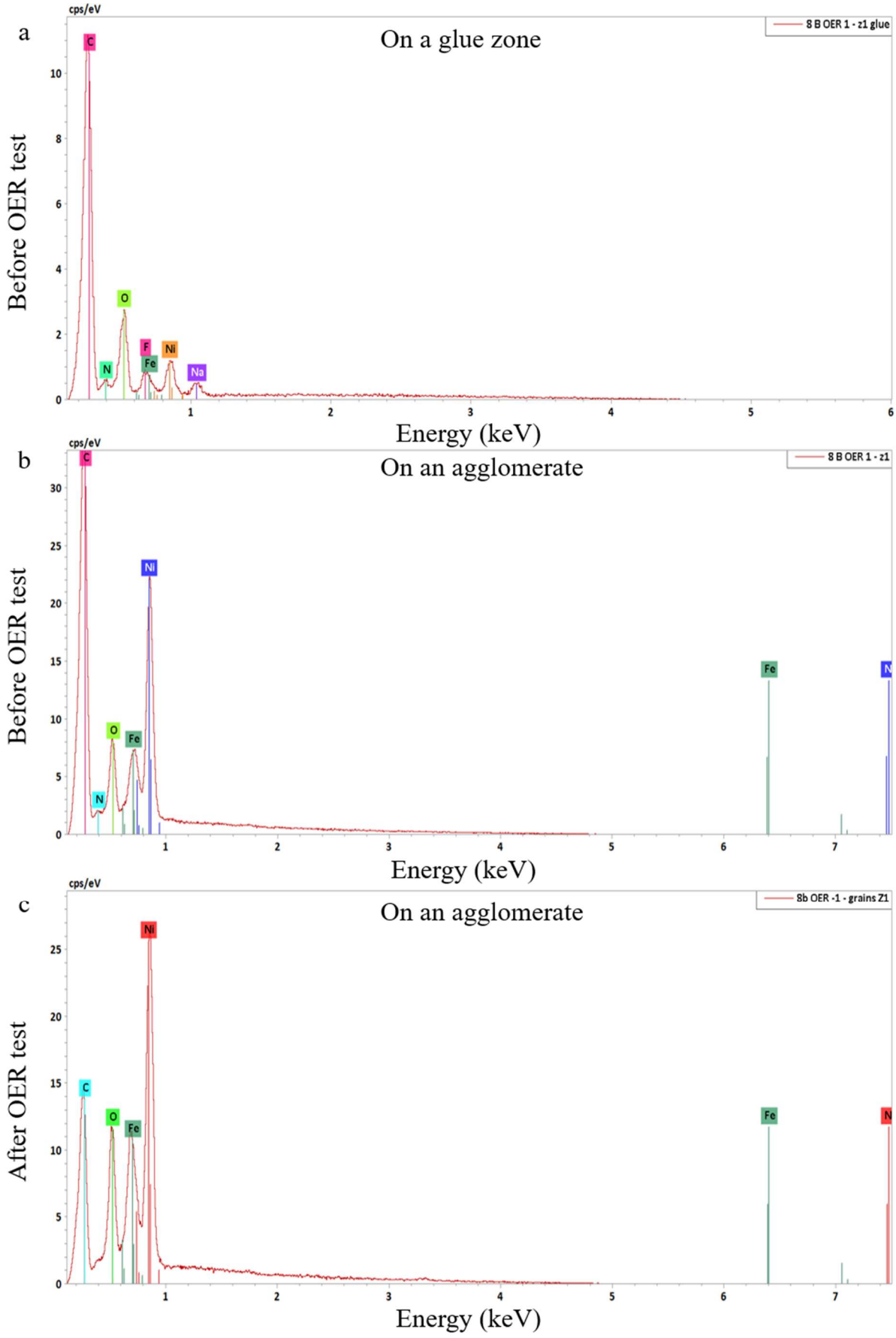

Figure IV.27: X-EDS analysis of the $FeNi_3$@Ni sample on (a) a glue zone, and on an agglomerate (b) before and (c) after OER CP under AMF.

To summarize, the ILSEM study indicates that the agglomerates are not evenly distributed on the carbon felt support, so that not all the surface is used for electrocatalysis. The Nafion® is not homogeneously distributed onto the carbon felt either. Besides, it moves and seems to undergo a glass transition, which tends to dry/shrink the Nafion® veils. This observation is consistent with ILTEM micrographs. Thus, the ink formulation is not optimized (as it was for the glassy-carbon support III.2.1.2). Especially, the use of Nafion® is surely not adapted, as it is a highly acidic ionomer which could degrade the catalyst. An alternative would have been to ion-exchange the Nafion® within the ink with potassium hydroxide (K^+ instead of H^+), similarly to what has been done with sodium hydroxide [283]. A commercial anionic binder such as Aemion+™ from Ionomr, a durable anion exchange membrane sustaining high temperatures, could also be considered. In addition, as Nafion® moves, agglomerates on it move accordingly, which is likely to cut the electric connection, could reduce the availability of the active sites and reduce their heating capacities, as the distance between the agglomerate is a significant factor influencing the SAR (I.3.1.4). Nevertheless, AMF exposure does not seem to trigger aggregation. After a test, the electrolyte deposits onto the carbon fibres, between them and on the agglomerates (even if this could be limited by DI water rinsing). KOH crystallites grow, which could move/detach the agglomerates. This indicates that although the $FeNi_3$(@Ni) performances in the PMMA cell are quite good, its activity could be further improved.

Moreover, an ILSEM investigation on the gold wire, after a CP measurement mimicking the CP test under AMF both in the HER and OER side, indicated that after HER a cathodic corrosion could have appeared [284,285], has been conducted (Supplementary Figure 17).

After having scrutinized the shape of $FeNi_3$@Ni, its potential structure change was probed by *in situ* XRD investigation at several temperatures under air, and ETEM observations.

IV.4.2 XRD investigation at different temperatures

XRD patterns were measured at eight temperatures: {25, 100, 200, 300, 400, 500, 600, back to 50}°C, with a temperature ramp of 12.5°C.min^{-1}. Unfortunately, not enough $FeNi_3$@Ni powder was put inside the Al_2O_3 corundum cell support (because of a lack of material), so that the XRD peaks of this latter are visible. The maximum temperature was chosen in function of the $FeNi_3$ Curie temperature (which is around 600°C [286,287]). Indeed, the temperature reached by the magnetic NPs during catalysis experiments is unknown, but Curie temperature is an upper limit, above which particles turn from ferromagnetic to paramagnetic, and thus do not heat by hysteresis losses anymore. The last temperature was 50°C instead of 25°C, as it takes a detrimentally-long time to cool down the sample from 50 to 25°C; nevertheless, these temperatures are close enough to consider that the material is back to room temperature. In order to fit accurately the phases, thermal expansion parameters of pure Ni [288,289,290,291] and FeNi alloys [292,293,294,295,296,297] (especially the $FeNi_3$ phase) were considered. Unfortunately, no data for $FeNi_3$ oxides were found, but some on NiO were examined [298,299].

Figure IV.28 presents the diffractograms of $FeNi_3$@Ni at different temperatures. In brackets are indicated the diffracting planes.

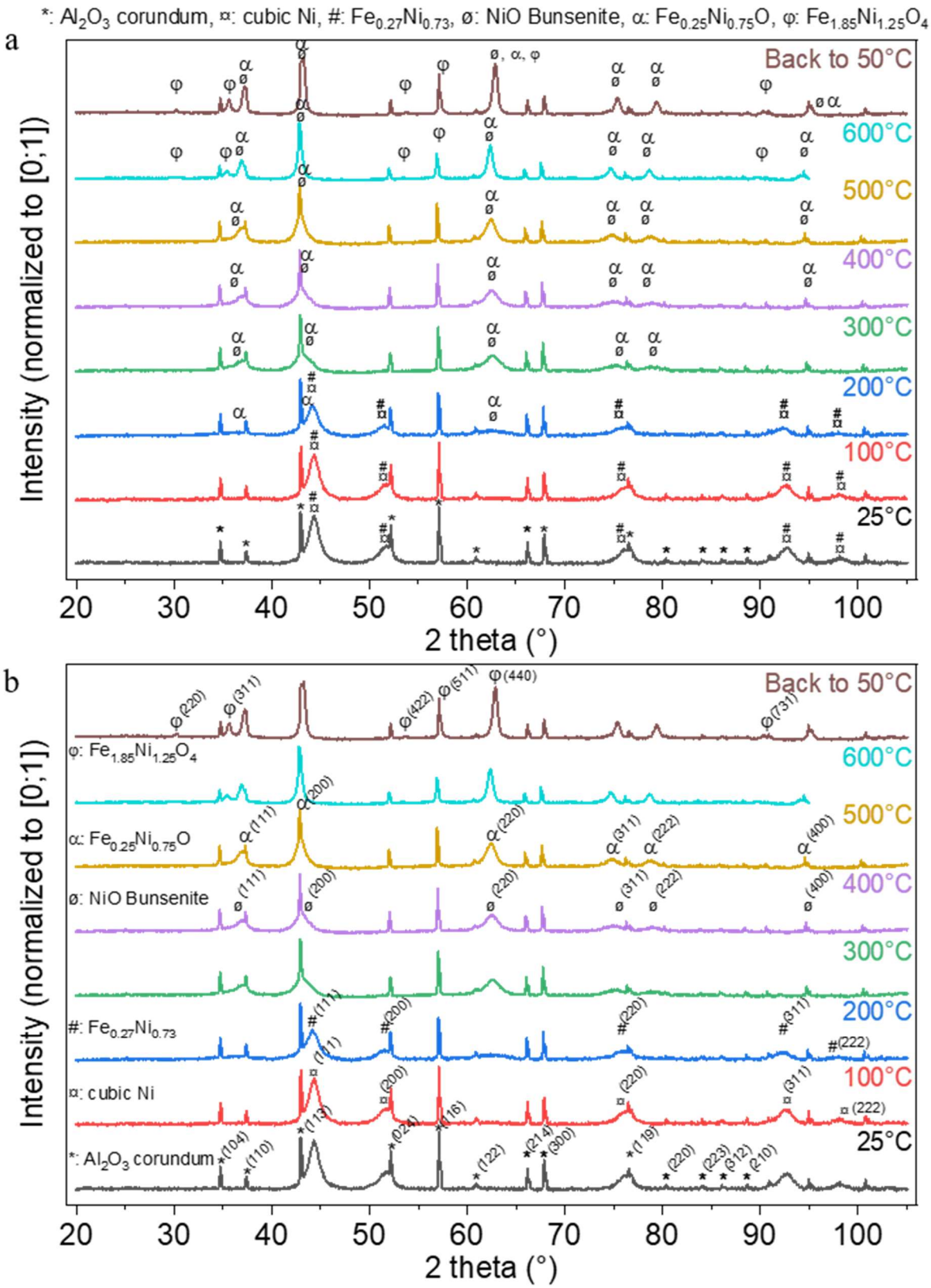

Figure IV.28: XRD patterns of $FeNi_3$@Ni at different temperatures. The intensities were normalized to unity. On (a), at each temperature, the present crystallographic phases are displayed. On (b), only one phase is displayed at each temperature (even if they could be present at several temperatures), but with its diffracting planes in brackets, to avoid burdening the graph: *e.g.* at 200°C, the (111) plane of $Fe_{0.27}Ni_{0.73}$ phase diffracts at 44°, but this peak is also present at 25 and 100°C.

At room temperature (RT), $Fe_{0.27}Ni_{0.73}$ and cubic Ni phases exist, consistently with the nature of the material. From 25 to 200°C, these phases disappear (peaks at 44°, 52°, 76°, 93° and 98°). From 200°C and up, NiO and $Fe_{0.25}Ni_{0.75}O$ phases emerge, overlap and keep growing up to the end of the measurement (the peaks increase in intensity and get thinner, indicating a higher crystallinity). From 600°C, the $Fe_{1.85}Ni_{1.25}O$ phase develops and keeps growing after coming back to room temperature. So, the material gets oxidized, and oxidized phases crystallise and grow. It seems that the $FeNi_3$@Ni get separated in some places, giving growth of NiO phases, while certain zones contains more Fe, as in the $Fe_{1.85}Ni_{1.25}O_4$ phase from 600°C. Another phase was possible, $Fe_{0.97}O$, which could explain where the Fe goes while NiO grow, but its fit was less relevant, so it is not presented on the diffractograms. This is probably due to a Kirkendall effect, where Fe, having a diffusion coefficient superior to Ni, diffuses toward the outskirt [300,301,302]. The Rietveld method could have been used to calculate the size of the crystallites. However, as several phases overlap on the diffractograms and that the peaks are broad except from 600°C, the calculation would not have been reliable.

Thus, this survey shows that at room temperature, cubic Ni and $Fe_{0.27}Ni_{0.73}$ phases are present up to 200°C. So, no crystallographic change should operate in the $FeNi_3$@Ni sample under AMF (neither in $FeNi_3$). Indeed, according to Figure IV.13, the temperature of the deposit goes up to ~ 70°C for these catalysts. Nevertheless, this measurement corresponds to the temperature of the surface of the carbon felt. The temperature at the nanometre scale is unknown. An ETEM study was conducted to confirm these results.

IV.4.3 ETEM observations

We had the chance to use the ETEM FEI Titan G2 had the IRCE in collaboration with Mimoun Aouine and Christophe Geantet. The purpose was to observe the possible structural/chemical changes of $FeNi_3$@Ni catalyst under a reductor (H_2) and an oxidant (O_2) atmosphere at different temperatures, and compare the results with the *in situ* XRD investigation. The partial pressure of the gas could be set up to 20 mbar, but it was maintained at 1 mbar, otherwise the micrographs got blurred. Special chips were used, allowing to heat the sample with a very high temperature ramp. The same temperatures values as the XRD investigation were applied. Unfortunately, difficulties were faced while putting the sample under the electron beam: the remaining ligands from the NPs syntheses were evolving, dragging the particles and preventing to have a stable initial state. Even a harsh reductor or oxidant treatment during several hours at high temperature was not sufficient to remove them. So, the $FeNi_3$@Ni powder was dipped into KOH 1 $mol.L^{-1}$ during 30 minutes, which allowed to degrade sufficiently the ligands to obtain a reference initial state. The following protocol was chosen: after having selected one agglomerate to be observed during the whole operation, the powder was first submitted to H_2 during 15 minutes at RT and micrographs were acquired at the end of this period. Afterward, O_2 was introduced during the same time and micrographs were taken afterwards. Then, the temperature was increased to 100°C, and the same atmosphere conditions were applied. So on and so forth up to 500°C. Unfortunately, the agglomerate was lost at 400°C because the chip membrane tore and detached. The closest agglomerate was pictured instead. A temperature of 600°C could have been interesting to compare with the XRD results. X-EDS analyses (and micrographs under vacuum at RT) were realized on different agglomerates at the beginning of the survey, and then at the end only. Indeed, such technique is time-consuming and harms the particles and the membrane (beam damages for long-exposure

times). Figure IV.29 presents the micrograph of the selected agglomerate, throughout the protocol.

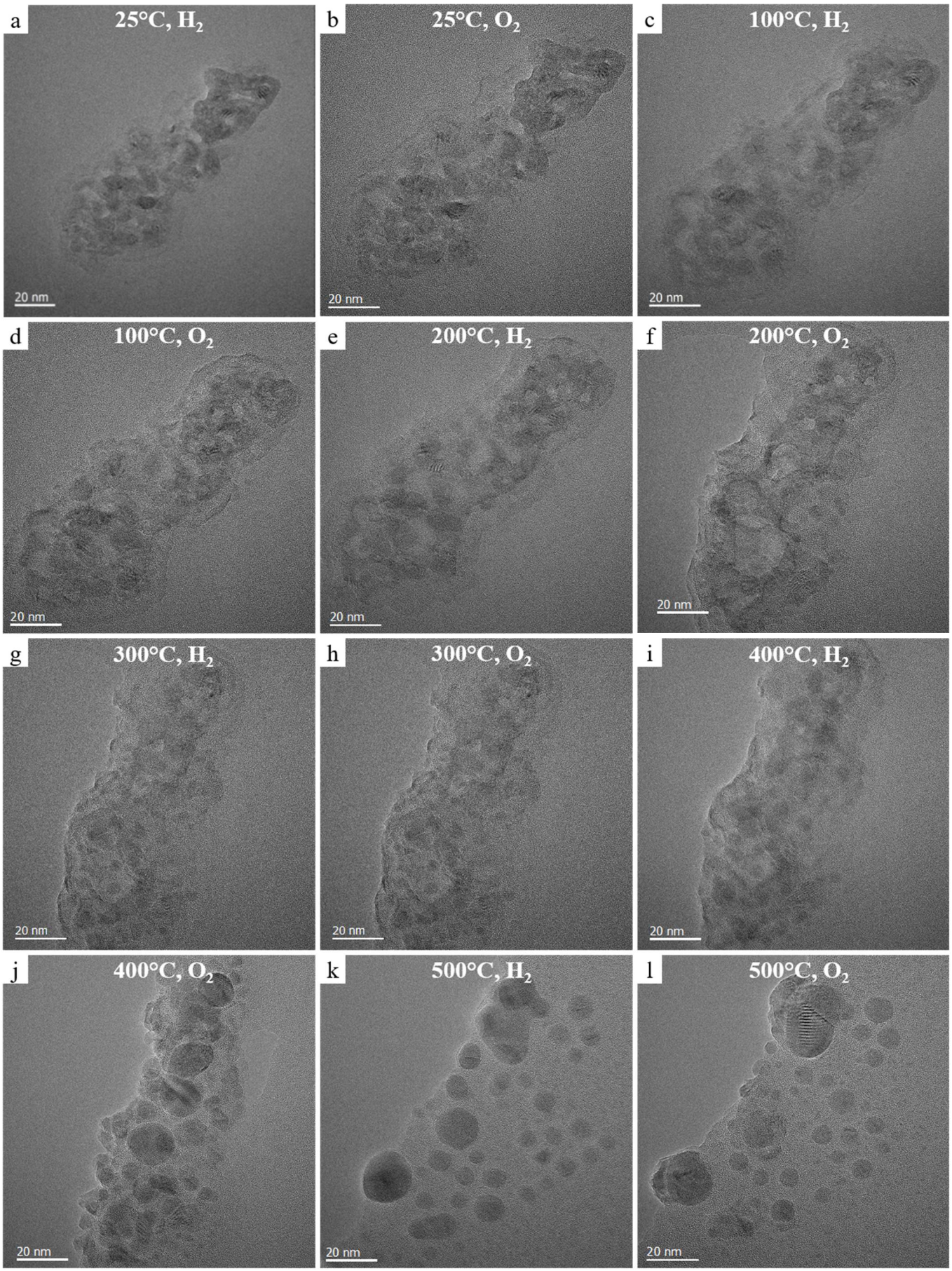

Figure IV.29: ETEM micrographs under H_2 and O_2 at different temperatures. The left part of the membrane was lost from (f) 200°C O_2, and the agglomerate fell down after (j) 400°C, O_2. (k) and (l) corresponds to the closest agglomerate.

With a naked eye, it is visible that the particles are polycrystalline and evolve a lot under the different atmospheres (especially (c-d), (e-f) and (i-j)). Besides, they grow in size when increasing temperature (j-l), as illustrates Figure IV.30, where selected particle counting is shown (when significant changes appear). A close look indicates that they get reduced under H_2 (size diminishes), and oxidized under O_2 (more crystal planes are visible and particle contour are more perceptible as the size increases due to the oxide layer). From 400°C O_2, the particles tend to separate or at least are more distinguishable (j).

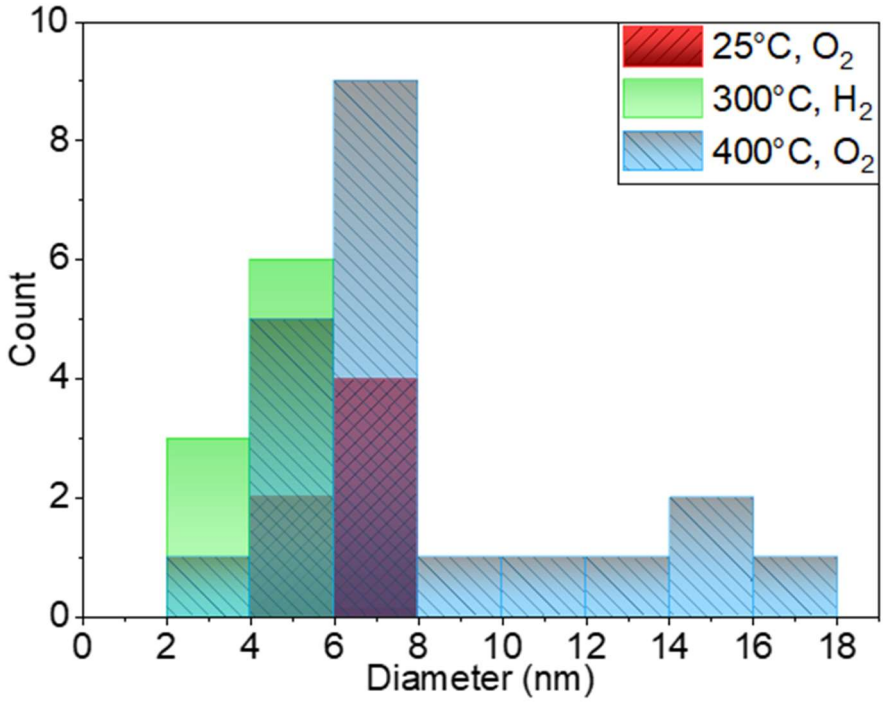

Figure IV.30: Selected particle diameter measurements of the same $FeNi_3$@Ni agglomerate.

Fast Fourier transform were conducted on several crystallized parts. The phase identification was realized by considering different crystallographic phases: cubic Ni, $FeNi_3$, $Fe_{0.27}Ni_{0.73}$, $Fe_{0.25}Ni_{0.75}O$, NiO (Fm-3m) and $NiFe_2O_4$ (Fd-3m). Since a huge number of phases was possible, a first selection was conducted by considering the phases which fitted the best for the XRD survey, or the closest one - in function of their availability in the database. The second selection consisted of comparing the experimental diameter and angle to the theoretical ones of the selected phases, and choosing accordingly the best fitting phase. These latter are summarized in Table IV.4. All the suitable phases are presented.

Table IV.4: Fitted phase by fast Fourier transform on several steps.

Steps	(a) RT, H_2	(d) 100°C, O_2	(g) 300°C, H_2	(h) 300°C, O_2	(k) 500°C, H_2	(l) 500°C, O_2
Phases fit	$NiFe_2O_4$ $Fe_{0.25}Ni_{0.75}O$ NiO $FeNi_3$ Ni	NiO $Fe_{0.25}Ni_{0.75}O$ $NiFe_2O_4$	NiO $Fe_{0.25}Ni_{0.75}O$ $NiFe_2O_4$	NiO $Fe_{0.25}Ni_{0.75}O$ $NiFe_2O_4$ (3 zones) Ni	Ni $FeNi_3$ $Fe_{0.27}Ni_{0.73}$	NiO $NiFe_2O_4$ $Fe_{0.25}Ni_{0.75}O$

Table IV.4 shows that the catalyst is initially oxidized and that phases such as $Fe_{0.27}Ni_{0.73}$ and $Fe_{0.25}Ni_{0.75}O$ are present at low temperature, consistently with the previous studies in the RDE setup and the XRD survey. It also indicates that a temperature of 500°C under H_2 is necessary to reduce the material (or a longer time exposure). A difference with the XRD is noticed: a phase rich in Fe is found early, from room temperature. In any case, it is important to note that the XRD method is a volumic technique, thus it gives insight on the average phase in the sample volume, while the ETEM is a very local technique. Accordingly, discrepancies can appear, as only one zone was scrutinized during the ETEM survey.

X-EDS analyses give complementary insights regarding the atomic amount of the elements in certain parts of the agglomerate (Figure IV.31).

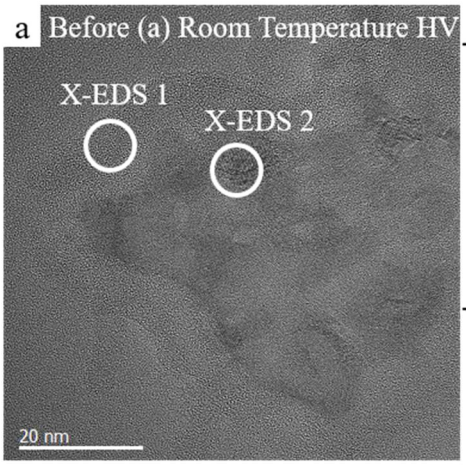

Spectrum 1	at.%
Fe	4.5
Ni	12
O	82
K	1.4

Spectrum 2	at.%
Fe	6.8
Ni	19
O	58
K	16

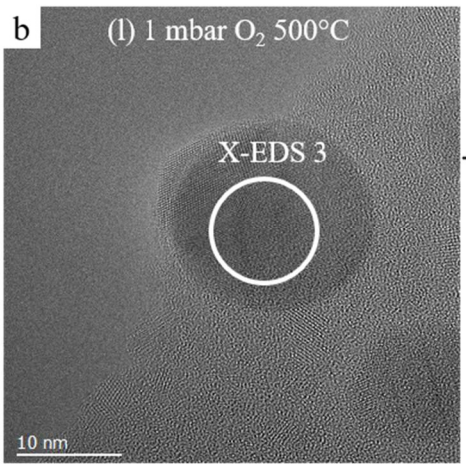

Spectrum 3	at.%
Fe	5.2
Ni	92
O	0
K	3.2

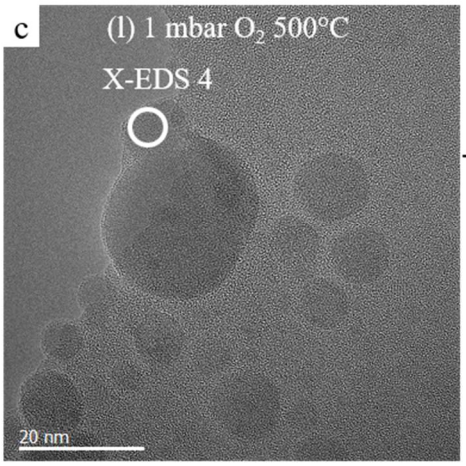

Spectrum 4	at.%
Fe	28
Ni	68.90
O	0.00
K	3.2

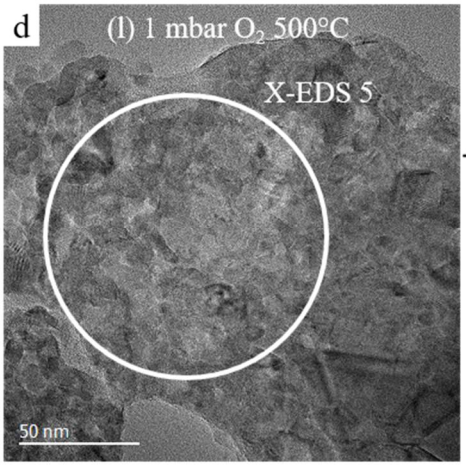

Spectrum 5	at.%
Fe	11
Ni	34
O	52
K	2.5

Figure IV.31: X-EDS analyses at different steps: analysis of the studied agglomerate at room temperature under high vacuum (HV) (a) analysis in the centre of a huge particle in another agglomerate at the beginning of the experiment (b) analysis on the outskirt of the same particle at 500°C and 1 mbar O_2 (c) analysis on a large different agglomerate at 500°C and 1 mbar O_2 (d).

The analysis in (a) confirms the ratio 1:3 of FeNi, being a lot oxidized (an oxide layer is visible). Spectrum 3 shows that Ni particles sintered and hence grow in size. One deduces from spectrum 4 that the Fe goes in the outskirt of the sintered Ni particle, due to the Kirkendall effect, in accordance with the XRD survey. Spectrum 5 focuses on a large different agglomerate taking it in its totality, and indicates a ratio 1:3 of FeNi, oxidized, as at the beginning of the investigation, and in the same proportion (Fe and Ni content are higher because the area probed is bigger). A small amount of K is found in all X-EDS analyses. This is due to the KOH bath used to remove the ligands.

A deeper investigation on the previous samples - that were not stabilized by KOH - indicates that the sintering occurs under H_2 atmosphere, as the Kirkendall effect, while under O_2, this process reverses and a 1:3 ratio of FeNi is found again (Supplementary Figure 18). Obviously, the temperature plays a role, facilitating the processes, but the non-negligible presence of ligand calls for caution in the interpretations.

In a nutshell, the ETEM investigation corroborates the XRD study on some points: a Kirkendall effect, an Fe enrichment in some zones (especially outskirt of sintered Ni particles), and an oxidation of the Ni and $FeNi_3$ phases are also concluded. Nevertheless, a phase rich in Fe is found early, in contradiction with the XRD results. Obviously, misinterpretation and mistakes in the phase determination could have occurred. Moreover, a longer time exposure to gas, or using two samples, one submitted to H_2 and the second to O_2, would have been interesting to really distinguish the effect of the atmosphere. Besides, it would have been preferable to remove completely the KOH by rinsing the powder with DI water, to be sure that the agglomerates were fully in contact with the atmosphere. This has not been done due to a lack of facility and time. Finally, the working conditions are not those under AMF, so that the results could vary. Whatever these biases, these *in situ* experiments were of great added value to unveil the behavior of these complex materials as a function of temperature and atmosphere.

To conclude this chapter, classical electrochemistry tests have been realized under different AMF amplitudes. The AMF positively impacts the activity of the catalysts - being magnetic or not - by reducing the overpotential at a given current density thanks to a temperature increase of the sample. The activation is not always correlated to the SAR of the material, since a non-negligible heating source is the eddy currents generated inside the carbon felt support, as deduced from temperature elevation measurements on final samples. It seems that heating improves mass-transport, facilitating bubbles' departure and enhancing ionic transport. The charge-transfer kinetics is also significantly improved as indicated by Tafel results. Experiments under parallel or perpendicular static magnetic field showed that no other magnetic or thermodynamic effects (Marangoni, Maxwell stress) significantly influence the performances of the (magnetic) catalysts under a MF in this setup. The *post mortem* investigation of the electrodes indicates first that the ink is not homogeneously-distributed over the carbon felt support (the performance can be improved) and that AMF does not trigger aggregation (ILSEM). The composition of the $FeNi_3$-based materials could change, even at reasonable temperature (100°C), leading to Ni-enriched zones forming huge particles, and Fe-rich zones around (XRD, ETEM) which could impact the electrochemical activity. Thus, these conclusions suggest that an alternative/complementary way to optimize the AMF activation (and reduce the electric consumption) could be to use eddy currents as the heating source instead of hysteresis losses. Indeed, high eddy currents can be generated at lower frequencies and magnetic field amplitudes. This conclusion has also been drawn very recently for catalytic reactions (CO_2 methanation) at the LPCNO [303].

Chapter V: General conclusion & prospects

The work in this PhD, driven by the Hy-WalHy project, was dedicated to the finding of better magnetic and catalytic materials for alkaline water splitting under alternating magnetic field, and to the understanding of the effect of the AMF on the water electrolysis reaction. To answer these two points, the problematic was divided into three parts: (i) the first experimental chapter (Chapter III) examined the activity and durability of new (supposed magnetic) materials toward WS, in two different cells, the first one allowing an "ideal" working environment, the second being the cell adapted to the coil for measurements under AMF, where the working conditions are very different; (ii) the second one (Chapter IV) focused on the WS activity of the same materials under AMF, where several electrochemical tests were conducted, besides with *post mortem* analyses, leading to different analyses on the magnetic activation. Also, a bibliographic review (iii) on the effects of a magnetic field in electrochemical processes (discussed in Chapter I and evaluated in Chapter IV), besides with other forces, permitted to take into account and evaluate the various phenomena likely to intervene under AMF exposure.

Firstly, the different NPs, FeNi-based ($FeNi_3$, $FeNi_3$@Ni, $FeNi_3$@Mo), Ni-based (Ni_{HI} and Ni_{OGM}) and reference benchmark PGM materials (Pt/C and IrO_2) were tested in the rotating disk electrode setup. It permitted to evaluate the intrinsic activity of the materials, and several of them proved to be better catalysts than the previously used FeC-Ni NPs, which was a major objective of this work. A loading study on the most active materials (Ni_{HI} in HER and $FeNi_3$ in OER) indicated the influence of the loading in this setup. It revealed that too high loading is detrimental to the activity in the studied setup, as resistive effect within thick layers inducing potential gradients and preventing all active sites to operate homogeneously occurs, besides with larger active site masking due to bubbles. A durability survey composed of accelerated stress tests (AST) and Identical Location TEM (ILTEM) on the most active catalysts ($FeNi_3$(@Ni) and Ni_{HI}) toward HER and OER indicated that the materials suffered from Fe dissolution and layer detachment (the ink formulation being not optimized). Then, the activity

of the same catalysts was characterized in the cell designed to experiments under AMF (called PMMA cell). The activity evaluation was also conducted on this setup as the working conditions are very different from the RDE setup: the mass-transport is not controlled by the rotation of the working electrode, but an electrolyte flow is applied to cool down the heating produced by the magnetic field and improve mass-transport by bubble removing. Besides, the working electrode support is a carbon felt, with a larger surface area than the glassy-carbon disk used in RDE, and a porous structure. Accordingly, the performances of the NPs changed. Nevertheless $FeNi_3$(@Ni) remained among the best catalysts. A loading study in these conditions indicated that the use of a carbon felt supresses the detrimental effect of thick active layer, as more geometric surface is available within the volume of the felt, that exhibit open (and large) pore structure between the carbon fibres. Also, magnetic characterizations permitted to evaluate the intrinsic magnetic features of the catalysts, as well as their heating capacity under AMF, in colloidal suspension at 100 kHz. It showed that $FeNi_3$(@Ni) materials heat at lower magnetic field amplitude than the previous FeC-Ni (which was interesting as less energy would be consumed to produce a high AMF) although their SAR are inferior to FeC-Ni's one (but remained high: > 350 $W.g^{-1}$). Ni-based materials exhibit a low SAR below 100 $W.g^{-1}$, benchmark catalysts do not heat, as expected. Neither does $FeNi_3$@Mo heat, while it was expected to, nevertheless, this latter served as a witness to evaluate the AMF effect.

Then, the influence of the AMF on the water splitting reactions is evaluated in the PMMA cell. Firstly, CV_F tests on $FeNi_3$(@Ni) at three different loadings (100, 1000 and 3000 $\mu g.cm^{-2}$) were conducted. Several observations are deduced: (i) whatever the loading, the AMF reduces the onset potential; (ii) this reduction is an increasing function of the AMF amplitude, in both HER and OER side; (iii) the magnetic activation is more significant at lower loading, while saturation was visible at higher loading. CP tests at ± 10 $mA.cm^{-2}$ on all materials show that all of them are positively-impacted by the magnetic field, that is, the overpotential of any

catalyst decreases (in absolute value), in both HER & OER side. Curiously, even the null SAR materials are positively impacted. Thus, it was deduced that the eddy currents are a non-negligible heating source, which was unexpected as all caution had been taken to minimize them. Further heating measurements confirmed their presence, especially in the electrode support: the carbon felt. Then, discussions were carried out in order to distinguish the magnetic activation influence on the mass-transport kinetics and the electron-transfer kinetics. It seemed, according to the trends in potential gains (higher overpotential in absence of AMF leads to higher potential gain under AMF), that the charge-transfer is more enhanced by the AMF than the mass-transport. However, CP measurements at different loadings (1000 and 3000 $\mu g.cm^{-2}$) on $FeNi_3$(@Ni) indicate clearly that the AMF influence on HER follows a different trend than in OER. In HER, the higher the loading, the lower the potential gain, whereas the overpotential is much inferior at higher loading. This is probably because at higher loading, bigger agglomerates are present, which could reduce the heating (I.3.1.4), not speaking from complex mass-transport effects in thick active layers. This trend suggests that the AMF influences mainly the mass-transport in HER, while no influence of the loading is visible in OER. Finally, measurements at higher current density (30 $mA.cm^{-2}$) were conducted. They support the prominent mass-transport enhancement in HER, as well as the more significant charge-transfer kinetics improvement in OER (as higher overpotentials without AMF lead to higher potential gain under AMF), although both types of activation occur. Tafel analyses confirm the high charge-transfer enhancement and no rate determining step change seemed to appear, whereas open circuit potential (OCP) measurements rules out the possible influence of the AMF on the Gibbs free energy.

Afterwards, the magnetic phenomena which were observed to intervene in electrochemical processes submitted to static MF are evaluated, besides with other effects: solutal Marangoni or Maxwell stress, and thermophoretic effect (*i.e.* Soret), scarcely mentioned

in the literature. According to order of magnitude calculations, only these two latter effects, besides with the Kelvin force, may intervene in a significant manner. Experiments under SMF show that no influence is visible in the PMMA setup. Nevertheless, simulation and tension surface measurements suggest that an effect exists (and needs to be confirmed), but was not sufficient to be noticed in the PMMA setup.

Finally, *post mortem* analyses were conducted. An ILSEM survey indicates that no aggregation occurs, but the Nafion®, serving as binder in the ink composition, undergoes severe changes under AMF: it spreads, gets thinner, and drags the agglomerates with it. Moreover, these latter are not homogeneously distributed onto the carbon felt, a result of the insufficient optimization of the ink formulation (which was not the primary objective of this work). Then, the influence of the temperature and of a reductive (H_2) or oxidant (O_2) atmosphere on $FeNi_3$@Ni catalyst were scrutinized. While the environmental conditions between the two studies (XRD in temperature and Environmental TEM) were not identical, the measurements showed that the temperature triggers phase changes, especially from 200°C, and that the atmosphere induces composition change: a Kirkendall effect is visible under H_2 at high temperature, while the ratio 1:3 of Fe/Ni is found back after O_2 exposure. These changes are likely to alter the activity of this catalyst toward water splitting, and agree with the trends of durability noted in electrochemical experiments.

To conclude, this work was dedicated to the understanding of the action of an alternating magnetic field at radio frequency and of maximum amplitude 48 mT, on the water splitting reaction in an alkaline media (KOH, 1 $mol.L^{-1}$). Non-PGM materials, especially FeNi or Ni-based materials, compared to benchmark PGM catalyst, namely Pt/C in HER and IrO_2 in OER were employed. While the application of an AMF has a very positive impact on any material,

reducing the overpotential in both HER and OER side, the key point to address is if such a system could be optimized to be cost-effective.

Regarding the optimization, several axes are open. Firstly, the formulation of the ink needs to be reworked. Indeed, the Nafion® serving as binder is not dedicated to alkaline media, and does not lead to a homogeneous particle distribution on the carbon felt support, even if the inks seemed homogeneous after sonication. Furthermore, the Nafion® was severely damaged by the AMF exposure. So, a temperature and alkaline-resistant binder has to be found, which should also improve the poor durability of the active layers of the catalytic materials. The support needs also to be improved. Indeed, it corrodes in the OER side, especially during AMF application. Even if very active materials are employed, so that the potential at the anode is lower than the corroding potential of carbon, it is likely to be degraded in these harsh conditions. Especially, durability tests under AMF needs to be conducted, to assess the stability of the electrodes on a long-term use.

Another axis of research could be the optimization of the catalyst morphology and structure, to benefit from the magnetic forces which could intervene to facilitate mass-transport, namely Kelvin, Soret, solutal Marangoni, and Maxwell stress effects. These latter should be confirmed by further measurements. Especially, knowing the exact temperature reached by the particles under AMF at a nanometre scale would be relevant to determine the real Kelvin force magnitude, and develop further the temperature gradient influence simulations. At this respect, measurement of the material lattice parameter elongation at different temperatures (*i.e.* different AMF amplitudes) at the European Synchrotron Radiation Facility (ESRF) would allow to reach these data. Similar work has been conducted by Stéphane Faure and LPCNO colleagues in 2020 [304]. Unfortunately, we had no possibility to plan experiment at the ESRF because of the Covid crisis and the deep maintenance (shutdown) of ESRF in 2020.

Eventually, the cornerstone of the cost-effective bet is the optimization of the cell and coil designs, and the choice of the heating mechanism. Two options exist. What has been initiated in this thesis is the use hysteresis losses, with the idea to heat exactly at the reaction active site, in order to provide just the necessary energy to enhance the WS reaction without heating the rest of the cell, which is a waste of energy and triggers component degradation. The coil used to this goal was obviously oversized, so that it needs to be adapted to decrease its energy consumption. Moreover, synthesis of materials which heat at even lower AMF would be useful. Besides, the research toward a support which do not heat due to eddy current is necessary, although this task is difficult. Indeed, on one hand, one would like a support which do not heat, being thus an insulator, and in another hand, a conductive material is required to permit electrons to flow through the electrical circuit. One idea would be to use a very thin support, like a felt but made with thinner fibres. Indeed, if the depth of the material in the direction of propagation of the magnetic wave is very small compared to its skin depth, the wave is not absorbed by the material, so that this latter does not heat. In this work, the skin depth was 137 µm in the gold wire (while its diameter was 200 µm), and 4.1 cm in the carbon felt (while its thickness was 41 10^{-2} cm). So, more than two orders of magnitude between the skin depth and the material thickness are necessary to limit the eddy current generation. Using a thin conducting wire (few micrometres) covered with FeNi nanorods could be interesting, even though the internal electrical resistance could become an issue.

The other option is to use eddy currents as second or first heating source. Indeed, their minimization is a complex task, while one could benefit from them. On this matter, preliminary measurements have been carried out to evaluate the eddy current effect on WS when maximizing them. They are presented in Supplementary Figure 19.

Moreover, the efficiency of the system has to be calculated. To this goal, this latter could be separated into two parts: the efficiency of the coil, and the efficiency of the electrochemical cell, enhanced by the magnetic activation. The first one evaluates the magnetic restitution of the coil (η_{mag}). Then, the electrochemical cell efficiency enhanced by the AMF activation could be calculated with Eq. V.1:

$$\eta_{\mathrm{H2,yield}}(25°\mathrm{C}, \mathrm{X\ mT}) = \frac{\mathrm{HHV}\ (\mathrm{H_2}, T)}{U_{\mathrm{cell}} i + P_{\mathrm{r}}} \qquad \text{V.1}$$

With HHV the High Heating Value of dihydrogen ($W.mol^{-1}$), *i.e.* the available thermal energy produced by a complete combustion of 1 mol of H_2, U_{cell} the cell tension (non Ohmic-drop corrected), reduced by the potential gains, taking the best catalyst activity for HER and OER, i the current and P_r the heat supported to the electrodes under AMF. An attempt of these efficiency is given in Supplementary Figure 20. Moreover, an idea to decrease the energy consumption would be to modulate the AMF (alternating on/off for short periods) to heat while consuming less energy.

Besides, experiments in a two-electrode cell (in a closer configuration to industrial cells), where both CE and WE are subjected to the AMF, have to be conducted.

Thus, still a long way to go before producing green hydrogen this way!

To conclude with my personal opinion, finding and improving current renewable energy sources is an emergency, but the technological solutions will not be enough and implemented on time to solve efficiently the issues at stake. Thus, I believe that the best way to solve the current ecological crisis is, in first instance, by an energy sobriety (implying limiting consumer good possessions). This requirement and principle of life will change our habits, but this does not mean to make us unhappy, and could allow a better share of the planet resources.

Annexes

Supplementary Figure 1: Averaged critical diameters taken from [305], anisotropy constants taken from [306] and magnetic moments in Bohr magnetons μ_B (μ_B = 9.274 10^{-24} A.m^2) taken from [307].

Elements	Critical diameter (nm)	Anisotropy constant (J.m^{-3})	Magnetic Moment of the ions (in Bohr magnetons μ_B)
Fe	19 ± 8	4.8 × 10^4	5.2 (Fe^{2+}), 5.9 (Fe^{3+})
Co	69 ± 1	-0.5 × 10^4	5.0 (Co^{2+})
Ni	43.5 ± 12	4.5 × 10^5	3.2 (Ni^{2+})

Supplementary Figure 2; Table of the magnetic field amplitude, power, current and voltage of the 300 kHz coil, Fives Celes.

RF Power (%)	Magnetic field (mT)	Power (kW)	Current (A)	Voltage (V)
10	23.9	1.5	10.3	164
20	32.1	2.8	14.1	220
30	38.4	4.2	17.1	264
40	43.6	5.5	19.7	299
50	48.5	6.8	22	332
60	52.5	8.2	24.2	360
70	56.5	9.5	26.1	387
80	60.2	10.8	28	413
90	63.6	12.2	29.8	436
100	65.3	12.9	30.8	448

Supplementary Figure 3: Table of the magnetic field amplitude, power, current and voltage of the 100 kHz coil, air-cooled (ID Partner®).

RF Power (%)	Magnetic field (mT)	Power (W)	Current (A)
10	5.1	70	5.0
20	10	70	8.6
30	14	70	12.2
40	18	130	16.1
50	22	190	19.5
60	25	265	23
70	29	338	26
80	33	450	30
90	37	561	33.5
100	42	722	38

Below 40% of RF power, the magnetic field and current were not given, values indicated are extrapolated values. The corresponding power accounts for the consumption of the air flow, being 70 W at maximum (at 100% B). These 70 W are added to all power values, so that these latter are overestimated at RF power below 100%.

Supplementary Figure 4: Temperature heating (ΔT) under AMF at different magnetic field values. Most of the measurements were realized by Christiane Niether.

Materials	**Sample // to B**			**Sample ⊥ to B**
	24 mT	48 mT	60 mT	24 mT
Nickel fibre felt				Burned
Nickel grid				Burned
Nickel foam				260
Platinum grid	3	74		40
Platinum plate				157
Glod sheet				157
Carbon fibre felt + 100 nm Au capping	0	1.5	10.5	56
Carbon fibre felt + 50 nm Au capping	0	2.2	11	13
Carbon fibre felt + 100 nm Ag capping	0	2.4	12	17
Carbon fibre felt + 50 nm Ag capping	0	2.3	11.3	17
Glassy carbon cylinder	burned			

Supplementary Figure 5: Mass and calorific capacity of the calorimetry SAR measurement setup.

Materials	**Cp ($J.kg^{-1}.K^{-1}$)**	**m (kg)**
Mesitylene	1750	$4.3\ 10^{-4}$
Water	4186	$1.8\ 10^{-3}$
Glass	720	$2\ 10^{-3}$
Iron	449	Depends on the samples
Ni	444	Depends on the samples

Supplementary Figure 6: Correction factors used to calculate the final SAR values.

Time	**Correction factor**
10	1.013
20	1.025
30	1.038
40	1.051
60	1.077
80	1.103
100	1.13
120	1.157
150	1.199
180	1.242

Supplementary Figure 7:

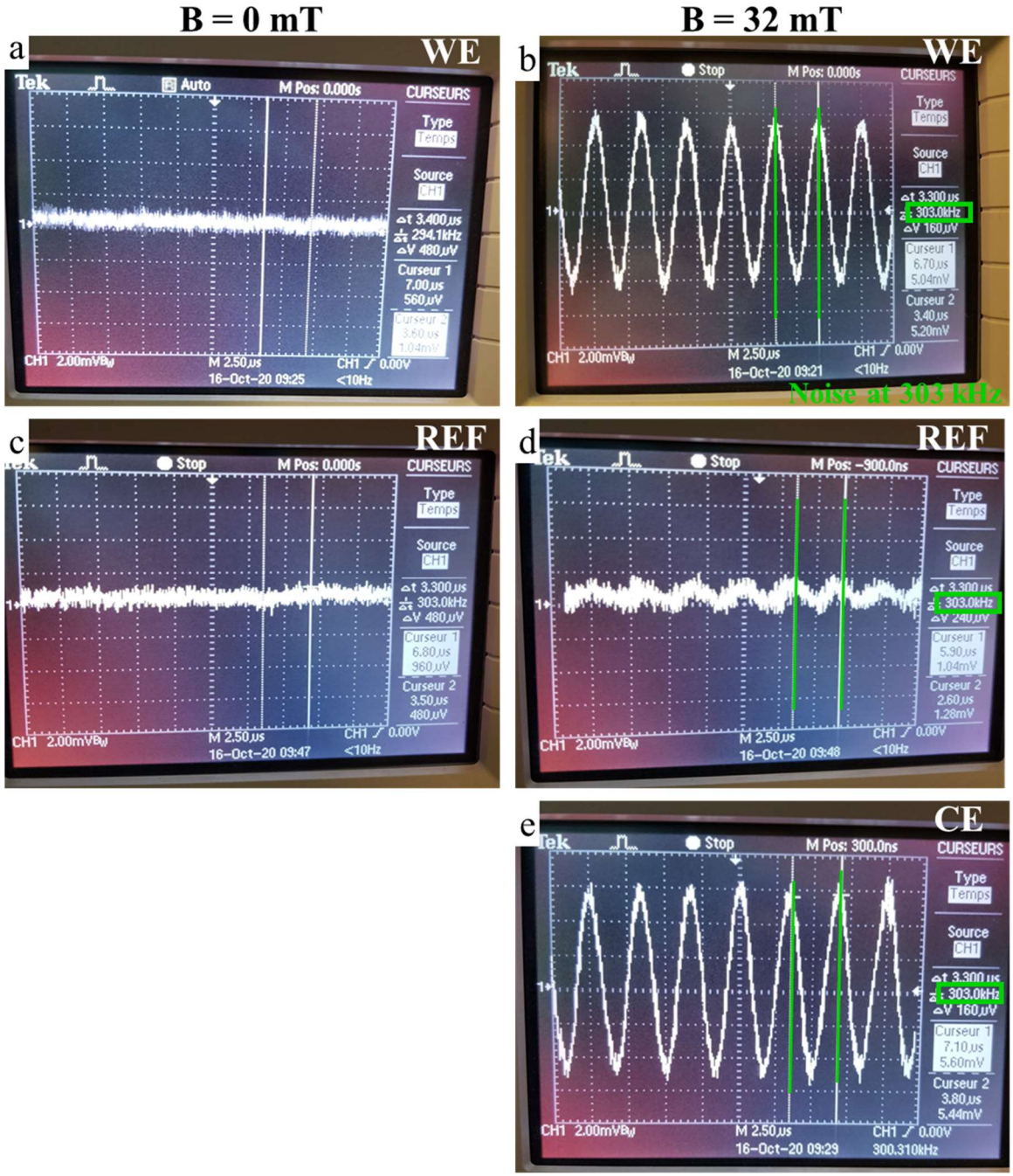

Oscilloscope pictures of the electromagnetic noise on the WE (a-b), REF (c-d) and CE (e), without (left) or with (right) the alternating magnetic field at 32 mT. Unfortunately, the picture of the noise at the CE at B = 0 mT was not recorded, but was similar to (a). The pictures indicate a strong electromagnetic noise at 300 kHz on the WE and CE, due to the coil. The REF is less affected as it is remoted at 20 cm from the coil.

Supplementary Figure 8:

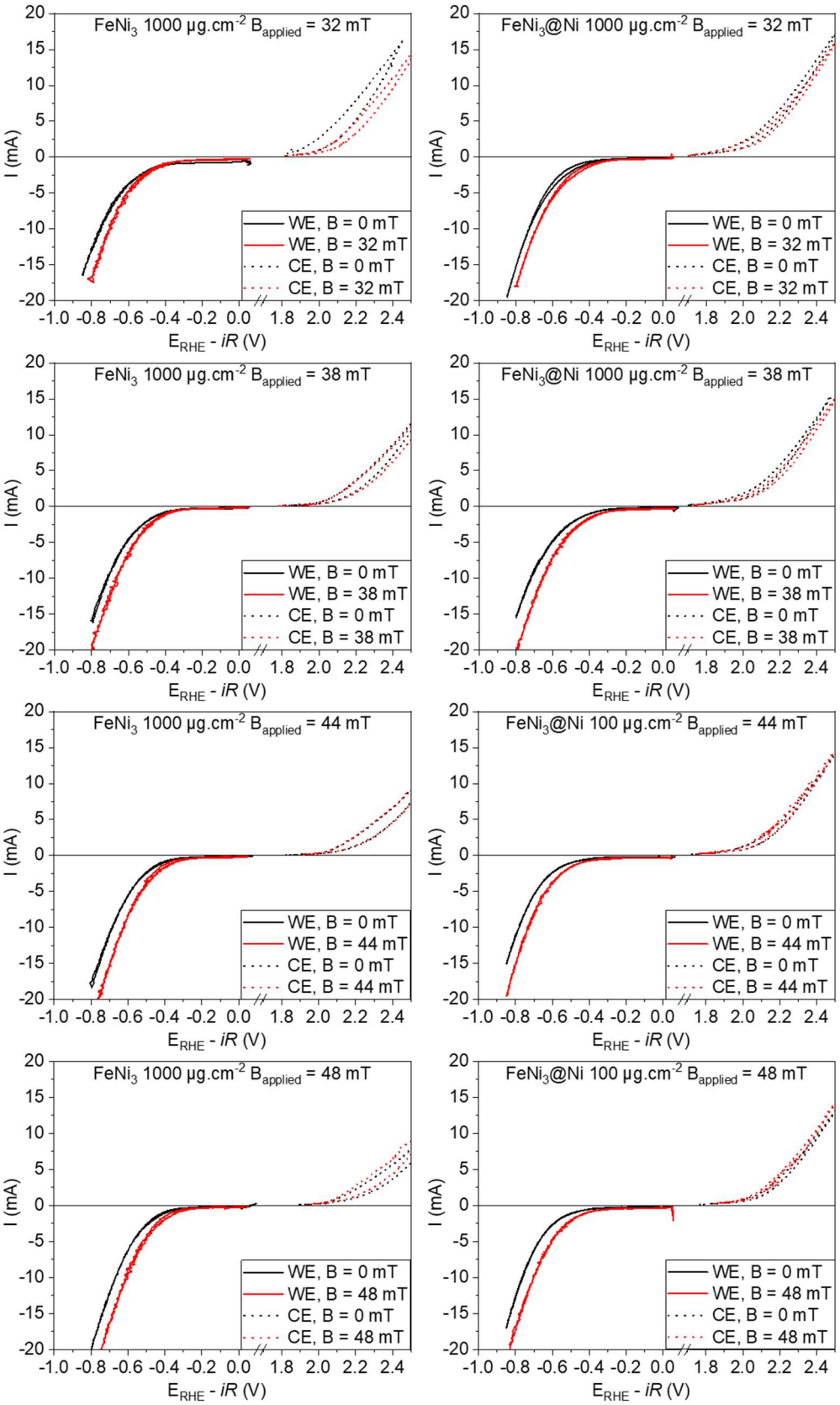

CV_F of $FeNi_3$ (left) and $FeNi_3$@Ni (right) loaded at 1000 µg.cm^{-2} without AMF (black curve) and under AMF (red curve), for the WE polarized in HER (solid lines) and CE in OER (dashed lines). The AMF amplitude increases from top to bottom.

Supplementary Figure 9:

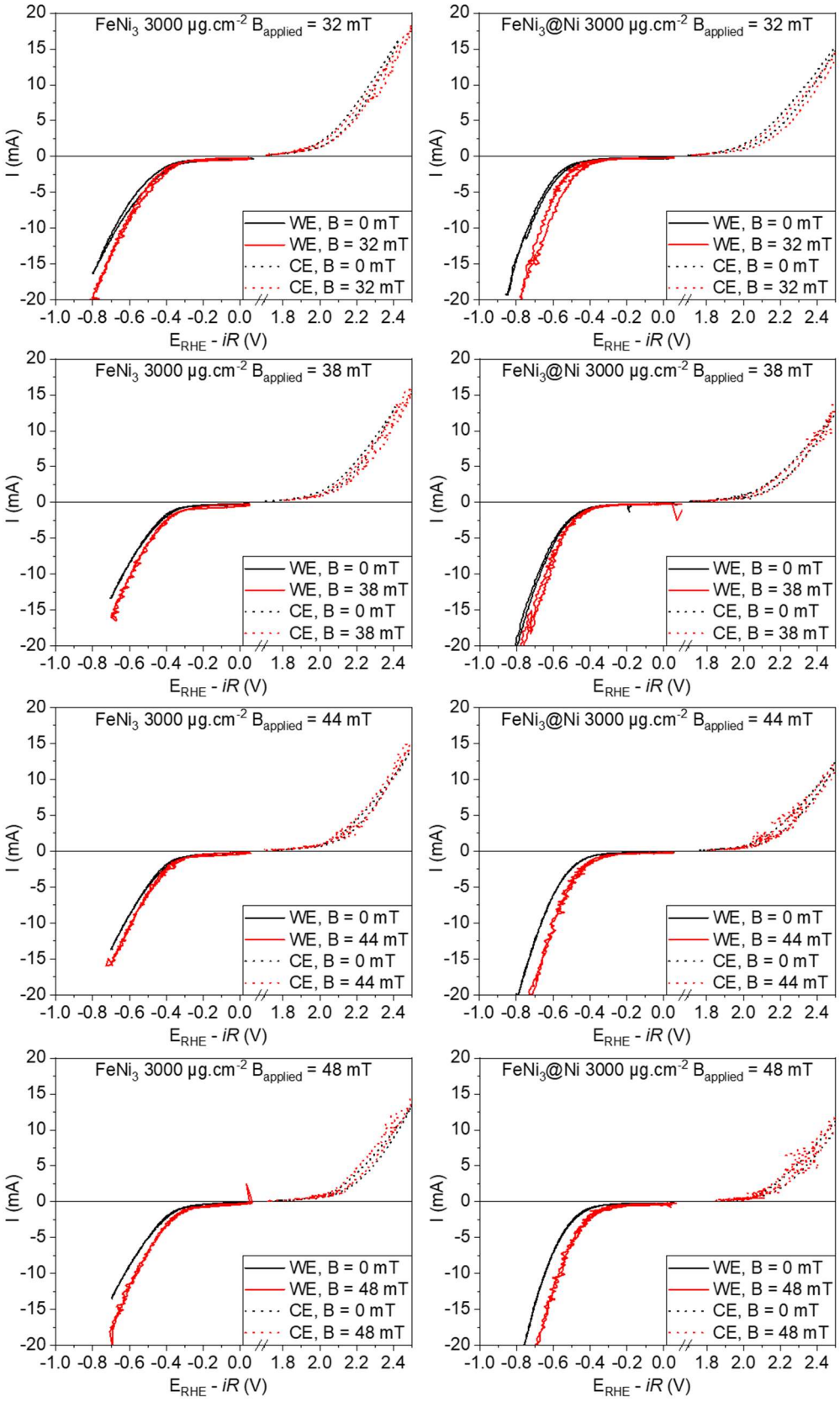

CV_F of $FeNi_3$ (left) and $FeNi_3$@Ni (right) loaded at 3000 µg.cm^{-2} without AMF (black curve) and under AMF (red curve), for the WE polarized in HER (solid lines) and CE in OER (dashed lines). The AMF amplitude increases from top to bottom.

Supplementary Figure 10:

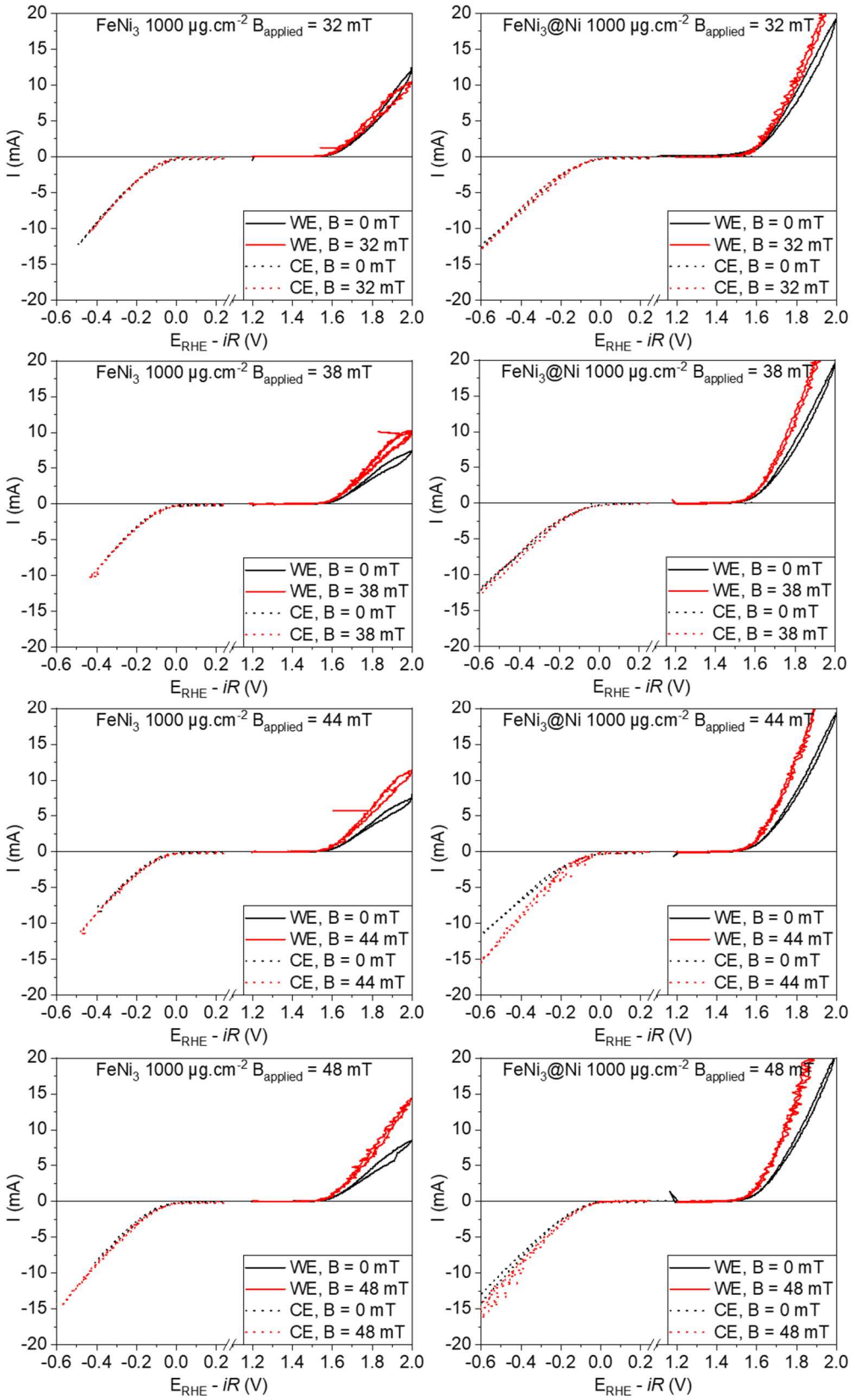

CV_F of $FeNi_3$ (left) and $FeNi_3$@Ni (right) loaded at 1000 µg.cm^{-2} without AMF (black curve) and under AMF (red curve), for the WE polarized in OER (solid lines) and CE in HER (dashed lines). The AMF amplitude increases from top to bottom.

Supplementary Figure 11:

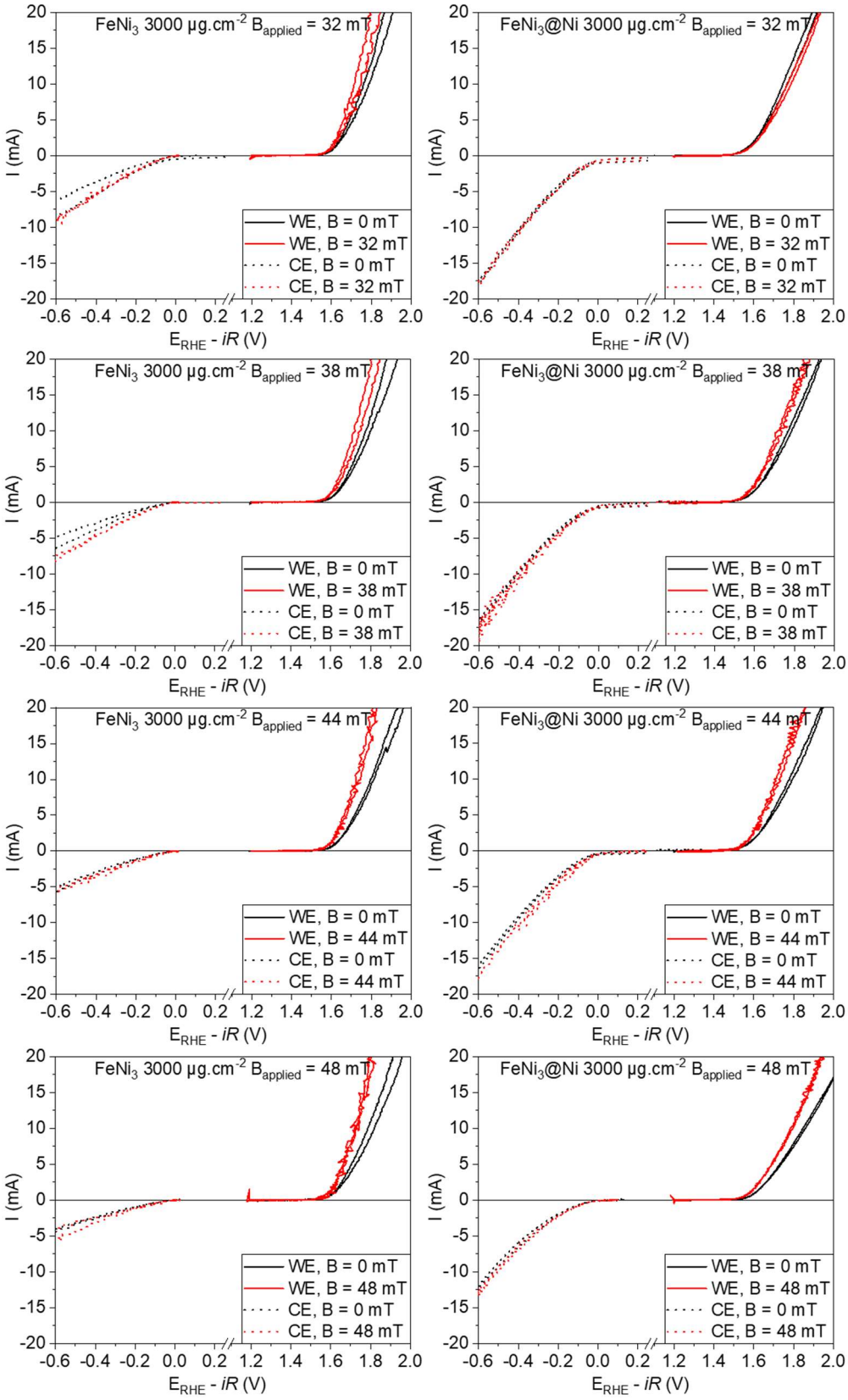

CV_F of $FeNi_3$ (left) and $FeNi_3$@Ni (right) loaded at 3000 µg.cm^{-2} without AMF (black curve) and under AMF (red curve), for the WE polarized in OER (solid lines) and CE in HER (dashed lines). The AMF amplitude increases from top to bottom.

Supplementary Figure 12:

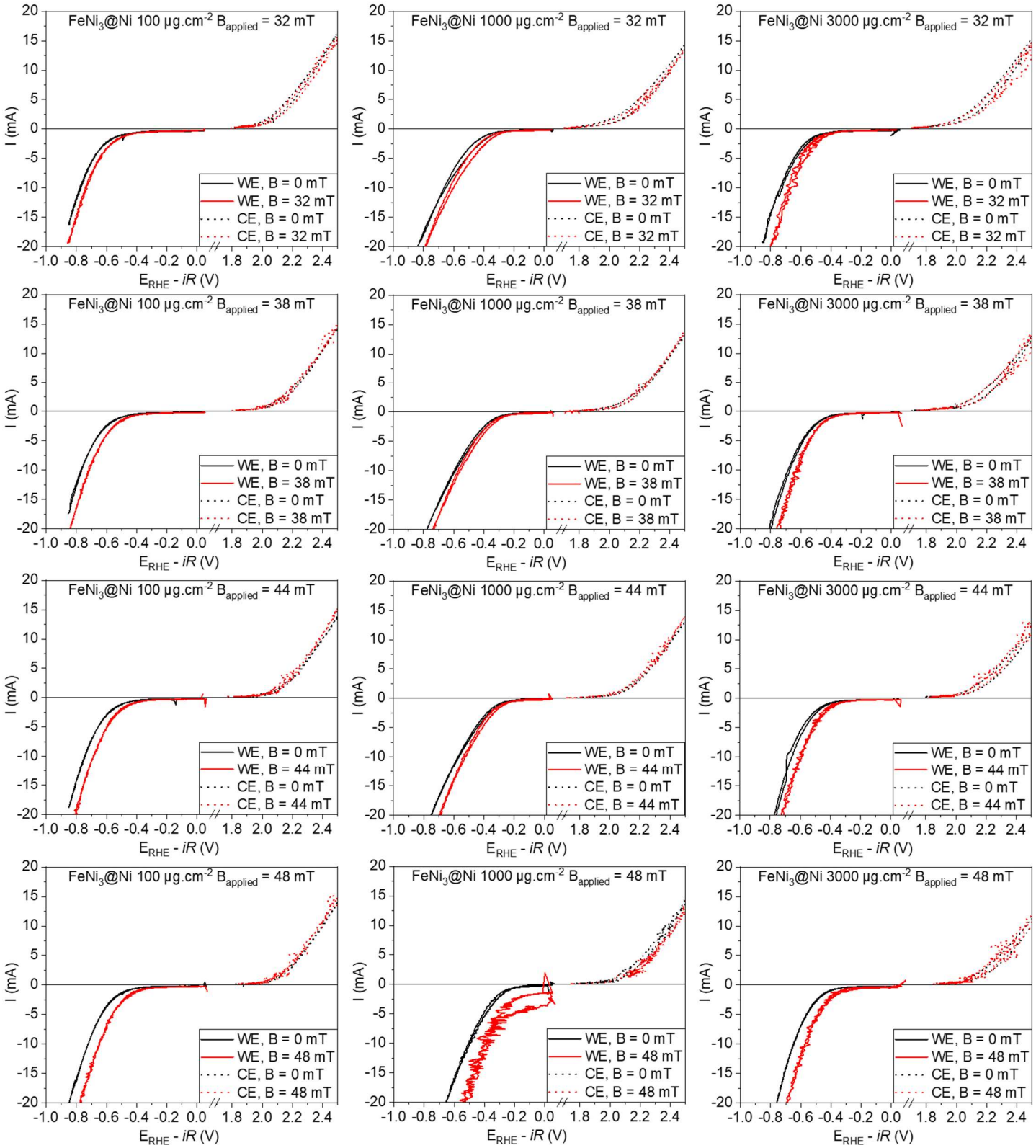

CV_F of $FeNi_3$@Ni loaded at 100 (left), 1000 (middle) and 3000 µg.cm^{-2} (right), without AMF (black curve) and under AMF (red curve), for the WE in HER (solid lines) and CE in OER (dashed lines). The AMF amplitude increases from top to bottom.

Supplementary Figure 13:

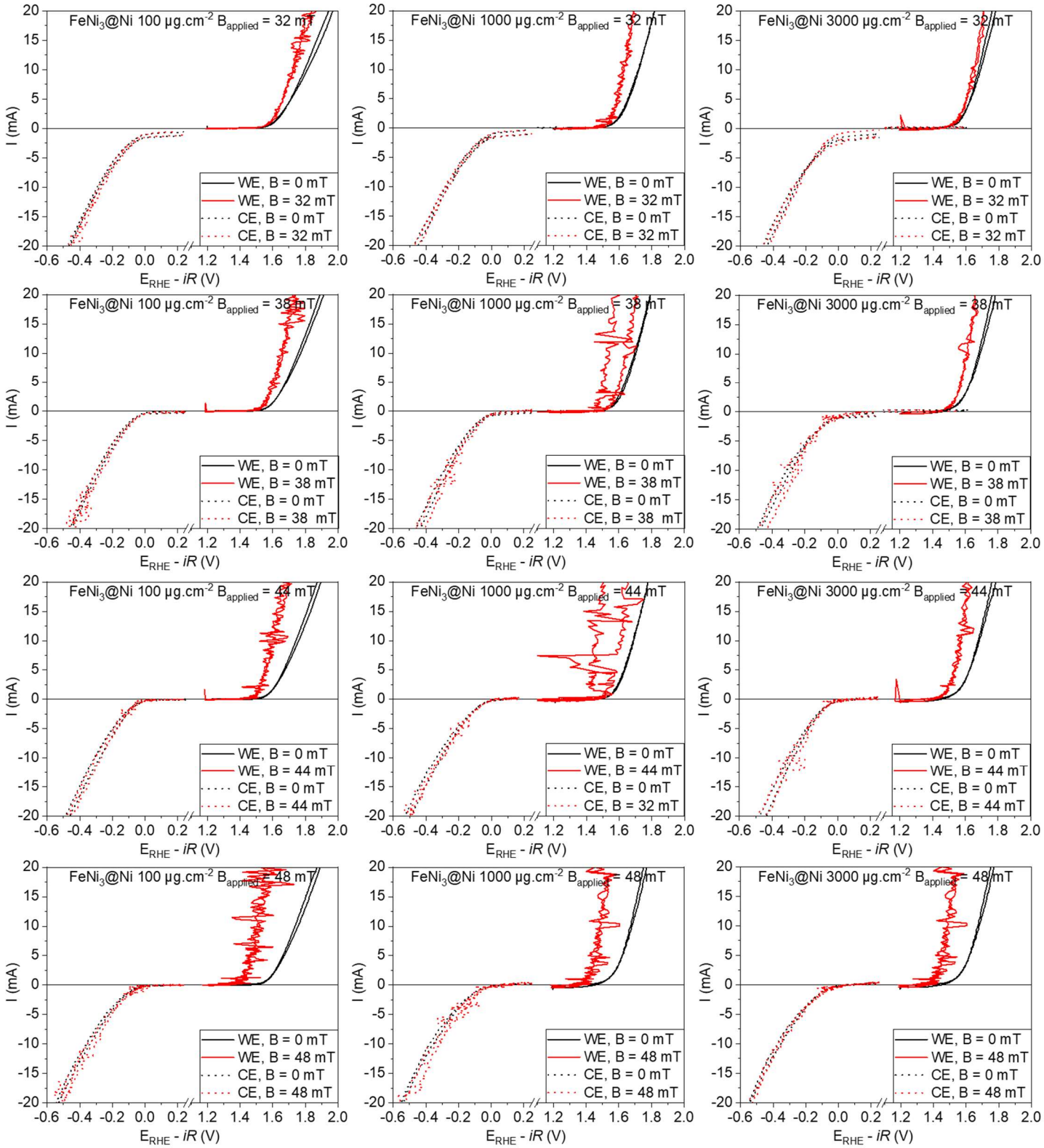

CV_F of $FeNi_3$@Ni loaded at 100 (left), 1000 (middle) and 3000 µg.cm^{-2} (right), without AMF (black curve) and under AMF (red curve), for the WE (solid lines) in OER and CE in HER (dashed lines). The AMF amplitude increases from top to bottom.

Supplementary Figure 14:

Lorentz force on the bubbles: Monzon *et al.* reported in [109] an estimation of the surface charge density q_S of O_2 and H_2 bubbles, being approximately ~ 0.1 C.m^{-2}. While this value appears to be large, it was used to estimate the current generated by the bubble current due to convection in the electrolyte. The time of convection was taken as *ca.* 10^0 second, and the number of H_2 bubbles was calculated according to the following formula:

Faraday's law	$n(H_2) = \frac{1}{2}\frac{it}{\mathcal{F}}$
Ideal gas law	$P(H_2)\ V(H_2) = n(H_2)RT$
Hence by mixing previous equations	$P(H_2)\ Q_V = \frac{1}{2}\frac{i}{\mathcal{F}}RT$
Lorentz force on the bubbles	$\|\| j \times B \|\| = Q_V q_S B$

With $P(H_2)$ and $V(H_2)$ the partial pressure and volume of H_2 inside the cell respectively, $Q_V = V(H_2)/t$ the gas flux rate, and t the time during which the current i is applied. This latter was (over)estimated at 10^3 A.m^{-2}, $P(H_2)$ was majorized at 1 bar, T was taken at 298 K. The number of bubbles per second N ($=Q_V/V(H_2)$) was calculated to be 5 10^4 bubbles.s^{-1} carrying thus a current density of: 5 10^3 A.m^{-2}. The Lorentz force exerts on the bubbles a force of 5 10^3 N.m^{-3} for 1 T, or 3 10^2 N.m^{-3} for 50 mT.

Supplementary Figure 15:

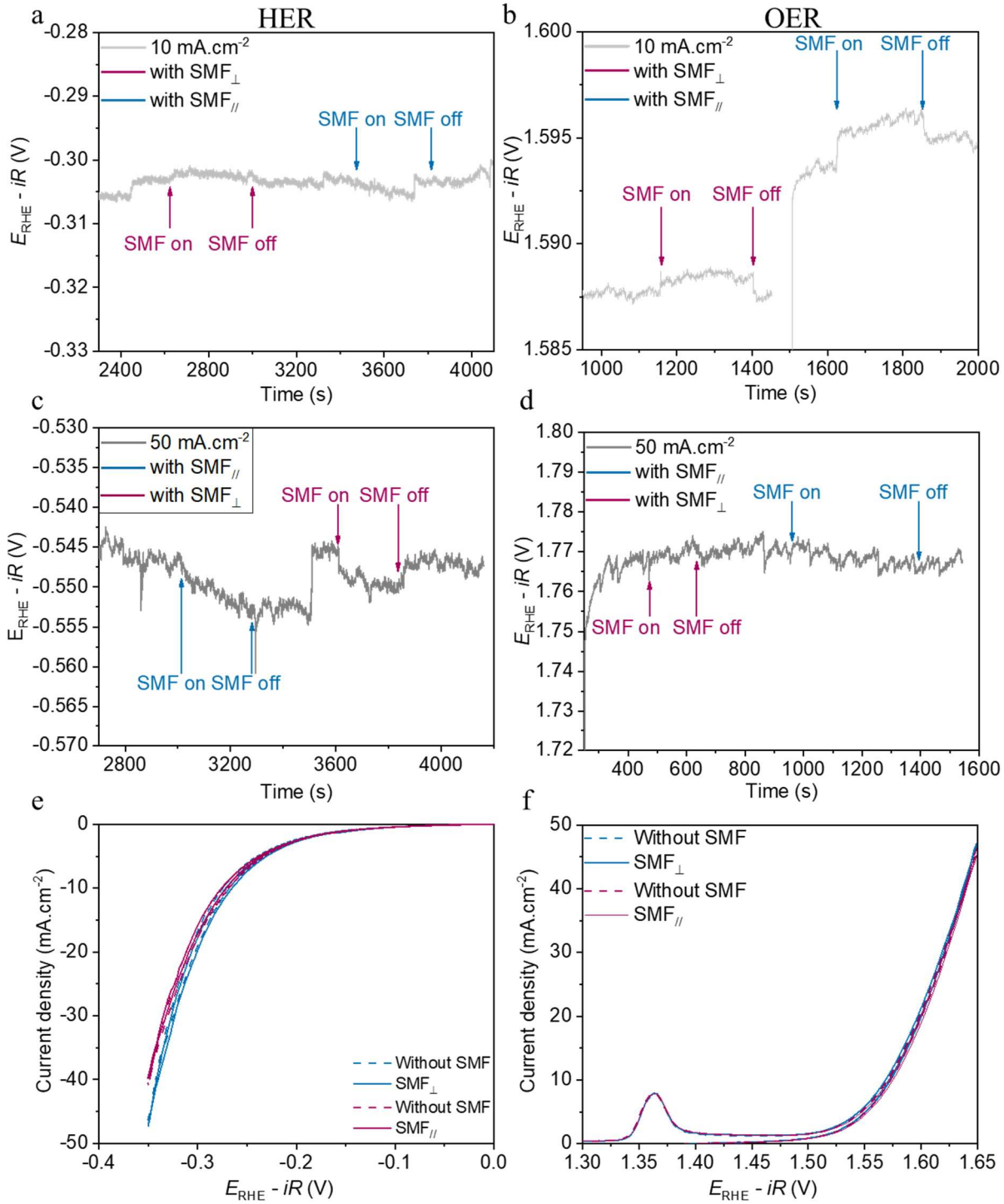

CP at (a-b) ±10 mA.cm^{-2} and at (c-d) ±50 mA.cm^{-2}. CV_F measurements (e-f) of a Ni slab under a parallel ($SMF_{//}$) or perpendicular ($SMF_{\perp}$) magnetic field, for HER on the left, and OER on the right. "Switch on" and "Switch off" indicates that the permanent magnet is approached to the PMMA cell or removed from it, respectively.

The tiny changes visible when the SMF is on or off during CP measurements is due to the manipulation of the magnet, which got attracted to the Ni slab, and thus hit the beaker which triggered bubble departure, hence sometimes a lower overpotential. No difference in the CV_F cycles is visible, between the curve "without AMF" or under "$SMF_{//}$" or "$SMF_{\perp}$".

Supplementary Figure 16:

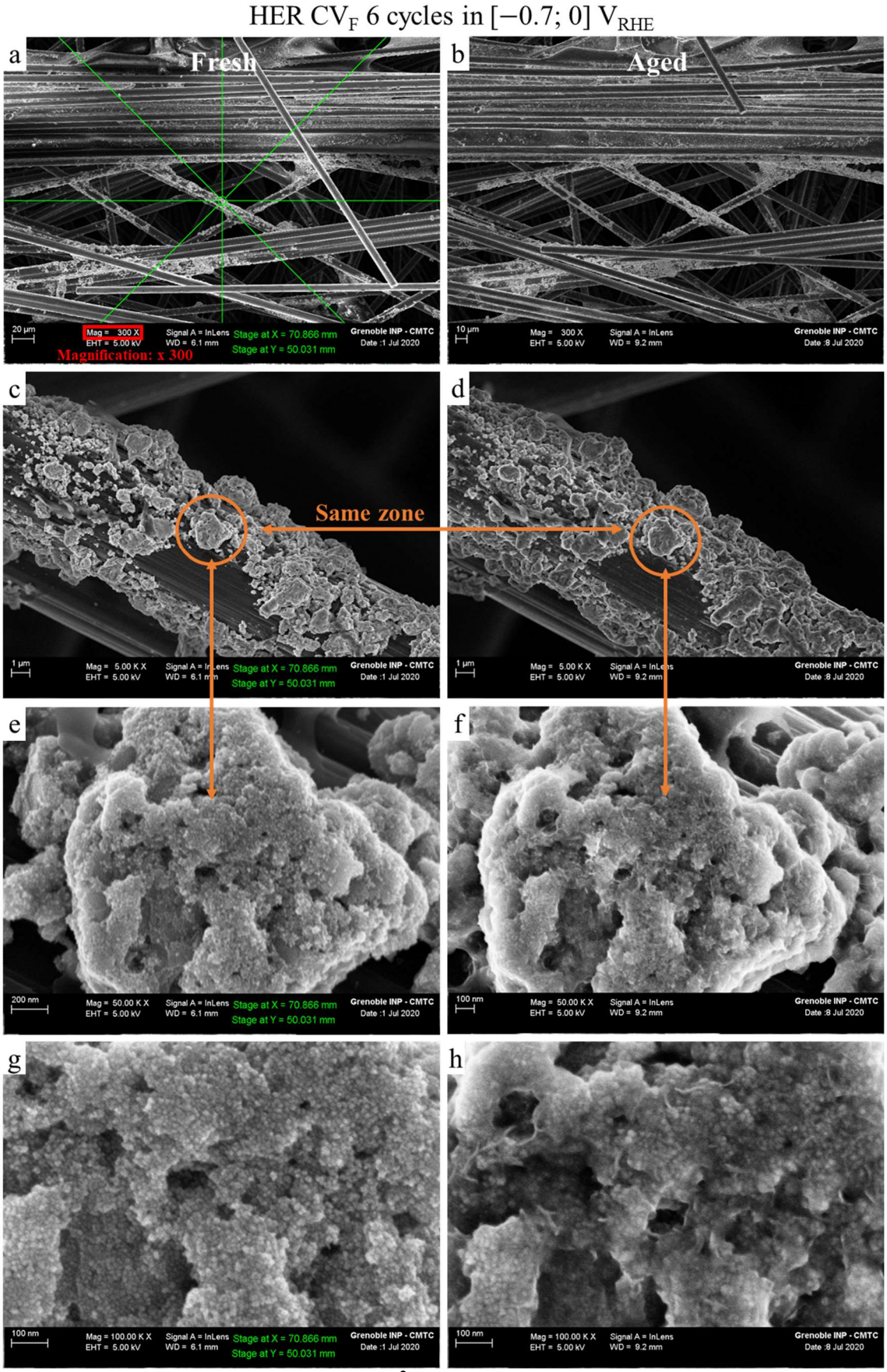

ILSEM study on $FeNi_3$@Ni at 1000 µg.cm^{-2} after CV_F test of 6 cycles, with a similar protocol given in II.2.1.2. Micrographs (a-c-e-g) were taken before and (b-d-f-h) taken after HER test.

The description of these micrographs is similar to the one in IV.4.1, but is quickly repeated here for convenience. Before HER test, the agglomerates are visible on the carbon fibre. They present random shapes and are not homogeneously distributed (c-d). The grains are visible at high magnification (e-h). A kind of a veil/glue is visible at the top of the micrographs (a) and (b). After HER test, a sort of a gangue appeared at the surface of the agglomerates. By transparency the grains are visible through it, but their faces and shapes are less perceptible. At the highest magnification (h), thin white lines are visible, these correspond to Ni oxide needles, as observed by Taylor *et al.* [308]. The agglomerates did not move and their shapes is quite the same. The glue has not moved either. The carbon fibres moved a bit, as one can see at x300 magnification for the foreground fibre, which moved a bit upward (a-b).

Similar observations are made from the micrographs after OER CV_F test (below). Especially, the glue has spread (i-j) and the deposited gangue after test is significant (o-p). Ni oxide needles were also visible in the different observed zones, although they are hidden by the KOH deposition in (p).

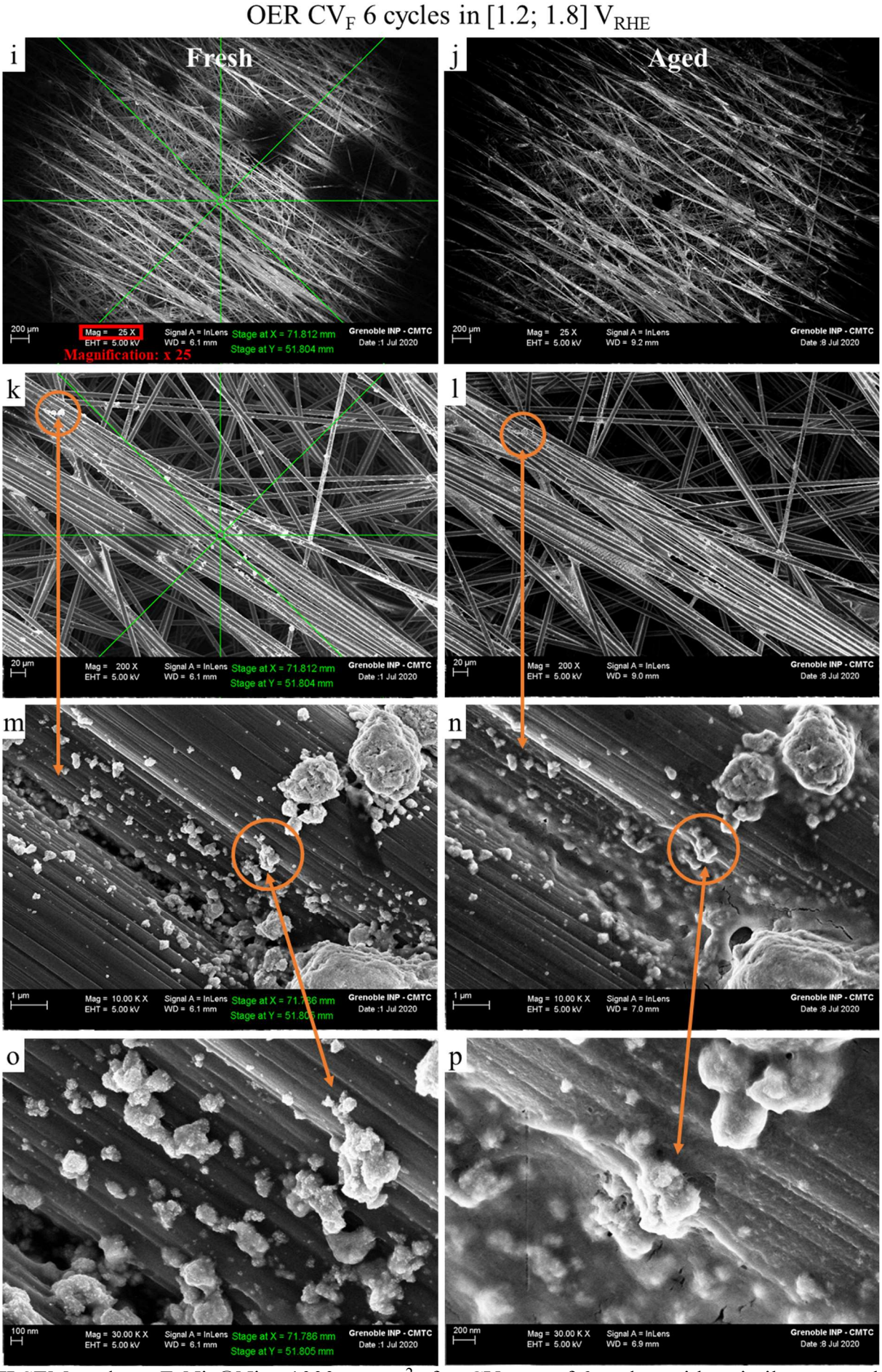

ILSEM study on $FeNi_3$@Ni at 1000 µg.cm^{-2} after CV_F test of 6 cycles, with a similar protocol given in II.2.1.2. Micrographs (i-k-m-o) were taken before and (j-l-n-p) taken after OER test.

The X-EDS analysis before test (q) confirms the nature of the catalyst: oxidized $FeNi_3$@Ni, deposited on the carbon felt (r). The glue exhibits a carbon and an oxygen peak. Its nature is Nafion® (Figure IV.27 (a)). A peak of potassium is present after tests which was not present before tests (s and t). Therefore, the gangue visible after test stems from the electrolyte deposition onto the carbon felt. As the test was short, agglomerates did not dissolve into the electrolyte. Of course, the surface is oxidized, as testifies the oxygen peak before (q) and after test (s-t).

Micrographs of the virgin sample which dipped into the electrolyte during 1 hour indicates that the KOH deposited on and between the carbon felt (u-v). A closer loop on a veil between two carbon fibres exhibit kind of bubble/scale forms (x), as observed after a HER CP under AMF treatment in the other side (Figure IV.26 (f)). A zoom on a carbon fibre presents KOH crystallites (z), as confirmed by X-EDS analysis (aa).

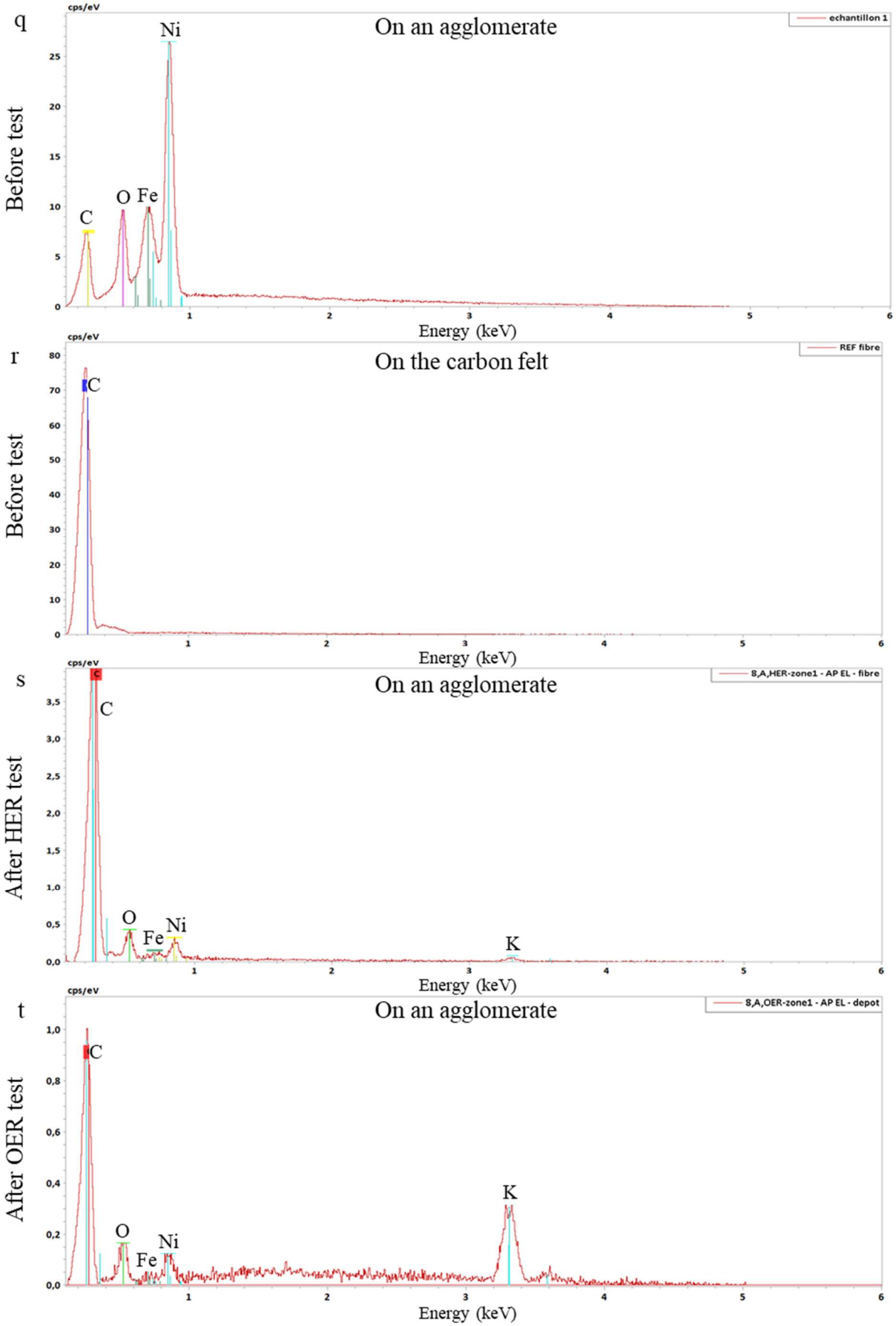

X-EDS analyses of the agglomerate (q) before and after (s) HER and (t) OER test, and ® an analysis of the carbon felt.

OER CP under AMF for ~ 50 minutes at +10 mA.cm^{-2}

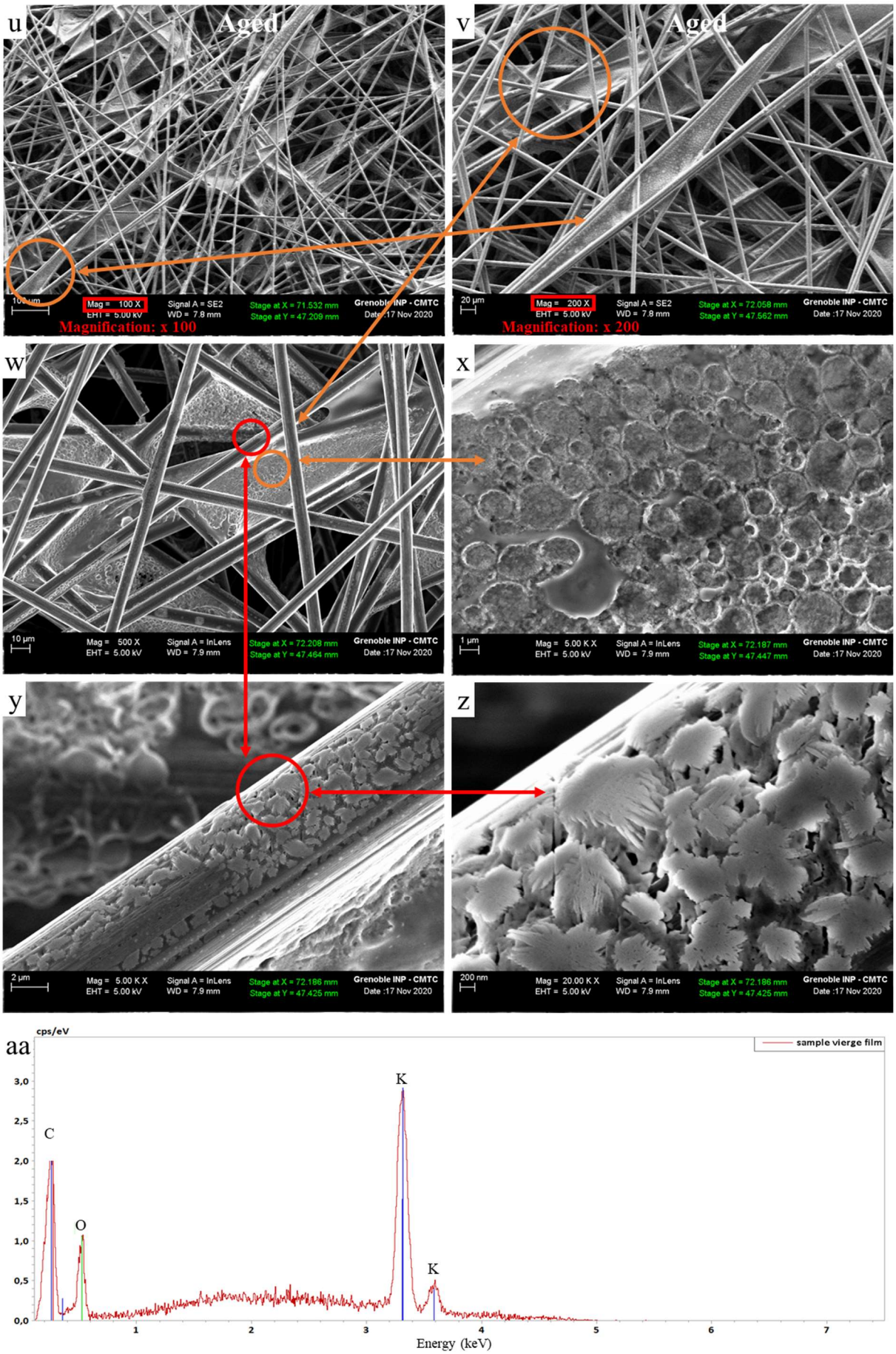

Micrographs of a virgin sample (carbon felt without deposit) which dipped into KOH 1 mol.L^{-1} during 1 hour (u-v-w-x-r-z); X-EDS analysis of the (r) micrograph is displayed (aa).

Supplementary Figure 17:

The surface of the gold wire on (a), before any treatment, is clean. Lines due to the moulding are visible. Small scratches from manipulation are also present. After HER treatment without a catalytic material, the surface changed: kind of island, possibly due to a dissolution and redeposition of gold appear, but not on all the wire surface. This reminds of the cathodic corrosion observed by Koper *et al.* [284,285]. However, when a carbon felt with catalytic NPs are present on the gold wire, almost no change in morphology is visible (c-d), indicating that the gold wire is not the reaction place, contrary to (b). After an OER treatment (f), oxidation bites are visible all over the gold surface. Finally, after several CP treatments (HER and OER) under AMF but with catalytic sample on it, the gold surface is damaged a lot. Many dark stains are present (which were also visible in the other gold wire after treatment, but in smaller number), and corresponds to deposit of potassium oxides, as proved the X-EDS analysis (j). Besides, having a closer look on the surface (h), furrows are visible, with discontinued grain boundaries. Thus, the gold material has been attacked by the electrolyte and by manipulation. The overpotentials under AMF of the gold wire are above those of the catalyst (Figure IV.14), so that it should not have been the place of reaction (even under AMF), and its contribution to the Faradaic current should be negligible.

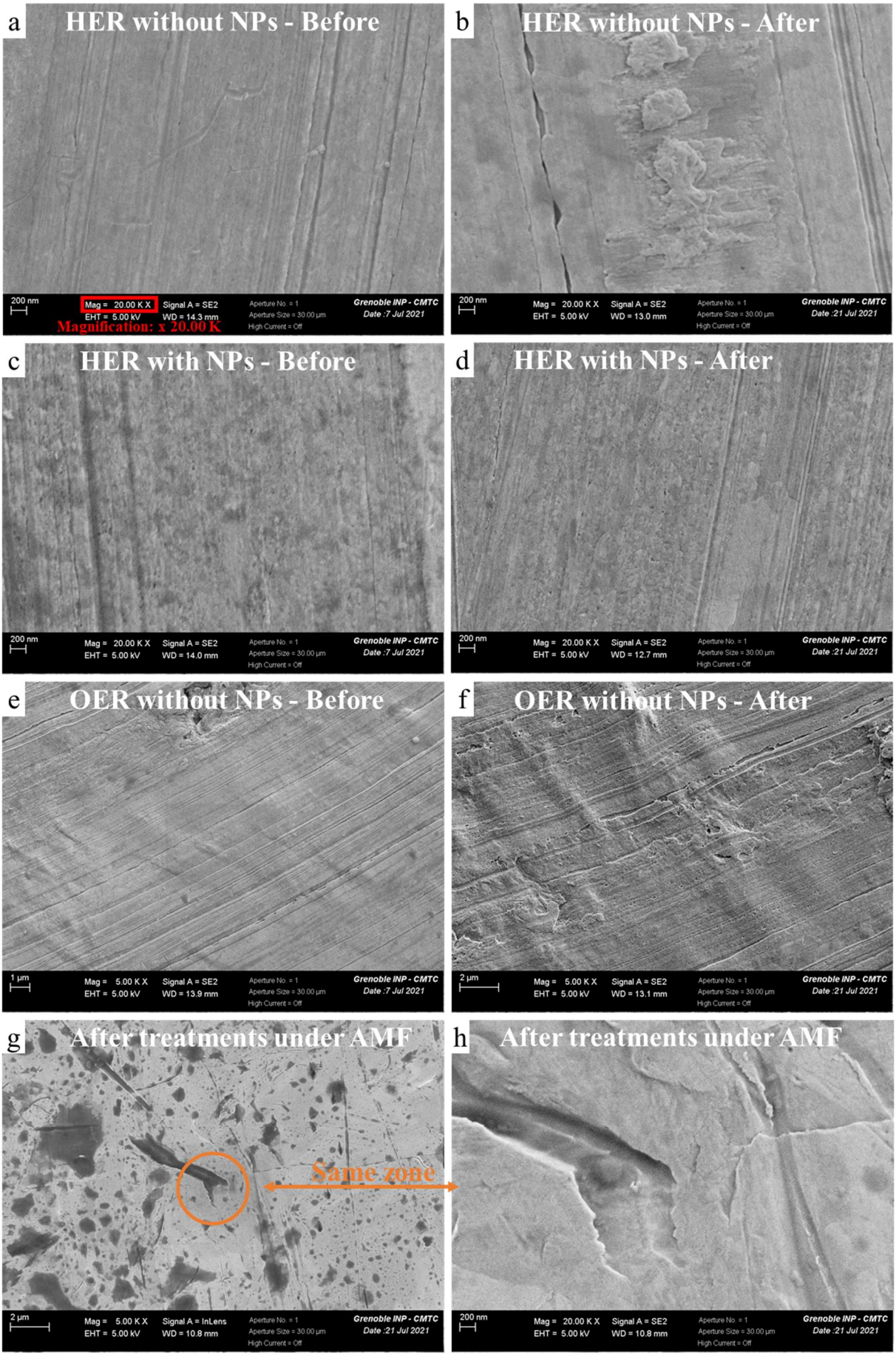

ILSEM micrographs of a rake shape gold wire (a) before and (b) after a CP HER treatment of 50' without carbon felt nor NPs, (c) before and (d) after a CP HER treatment of 50' but with a carbon felt with $FeNi_3$ NPs deposited on it, (e) before and (f) after a CP OER treatment of 50' without carbon felt nor catalytic NPs, (g) before and (h) after several CP HER and OER treatment under AMF - contrary to previous micrographs, (h) being a magnified picture of (g).

i

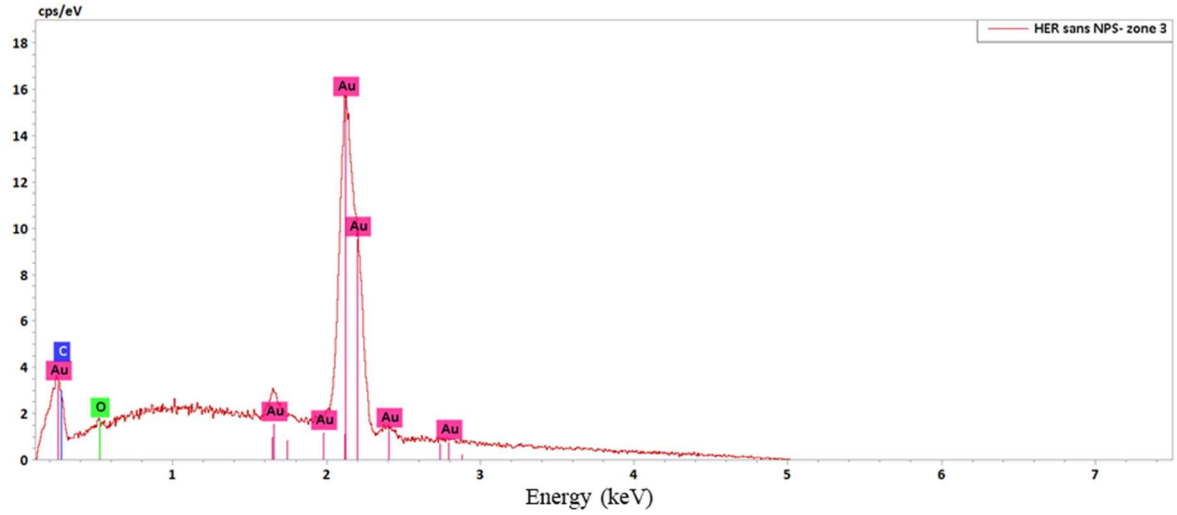

j

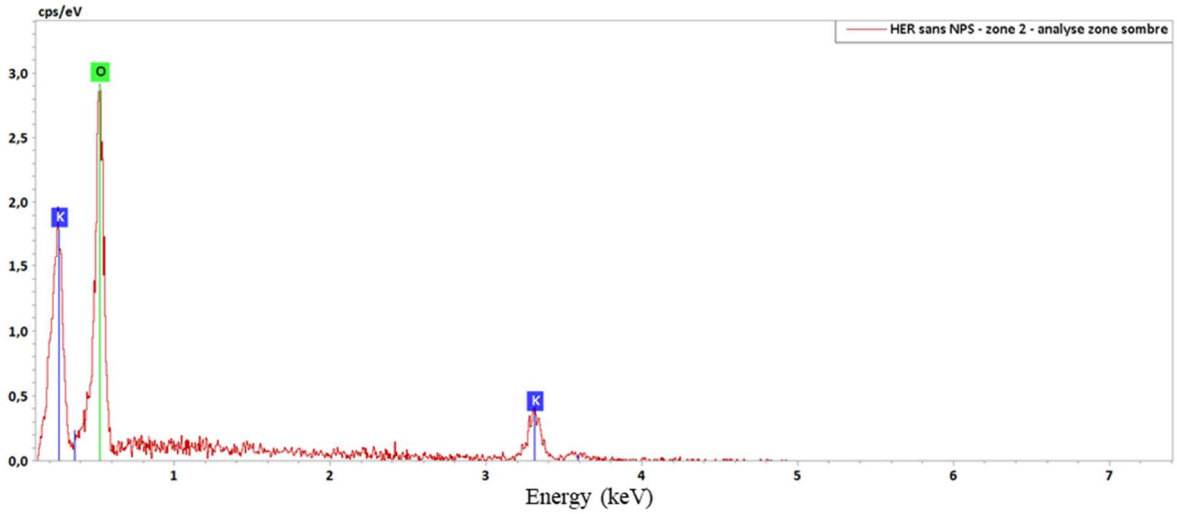

X-EDS (i) before treatment and (j) on a dark stain after HER treatment.

Supplementary Figure 18:

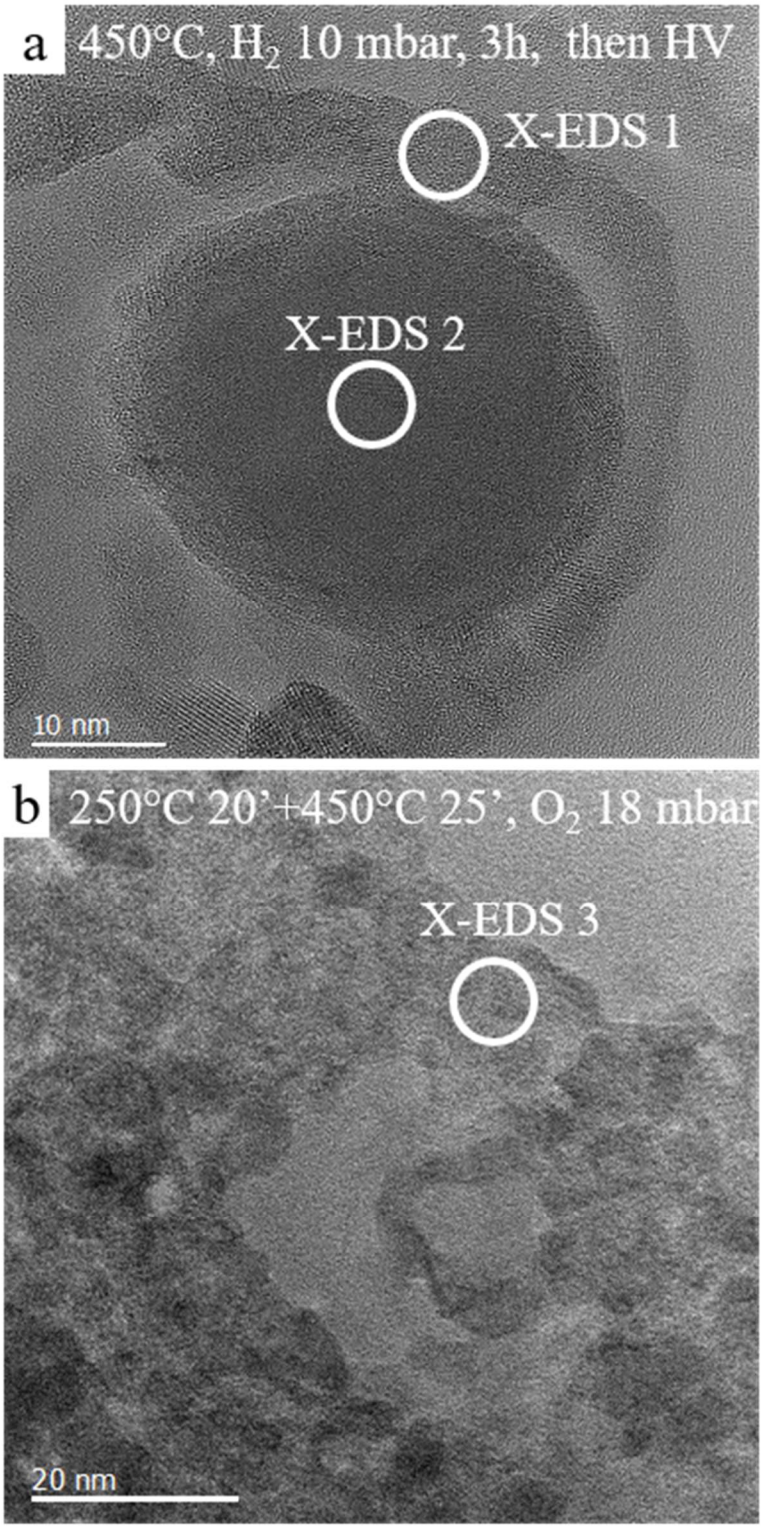

Spectrum 1	at.%
Fe	46
Ni	29
O	25
K	1.4

Spectrum 2	at.%
Fe	2.7
Ni	93
O	0
K	3.8

Spectrum 3	at.%
Fe	6.9
Ni	19
O	70
K	3.8

X-EDS analyses of a $FeNi_3$@Ni powder not subjected to KOH. It first underwent a reductor treatment at 450°C under H_2 at 10 mbar for 3h (a), then an oxidant treatment under O_2 at 250°C during 20', and then 450°C for 25' (b). The pictures are shot in high vaccum (HV).

Supplementary Figure 19:

A cell where the WE is placed perpendicularly to the AMF, in a position which maximizes eddy current generation was designed (Figure II.12Figure II.13). The cylindrical cell has a smaller external diameter to enter into a 100 kHz air-cooled coil, which electric consumption is lower (Supplementary Figure 3). Ni foams (Sorapec®) of two thicknesses 1.0 and 1.6 mm and a Ni felt (Nitech®) of 0.6 mm thickness were employed as WE. All having a diameter of ~ 6 mm. Heating measurements similar to those presented in IV.1.3 were conducted:

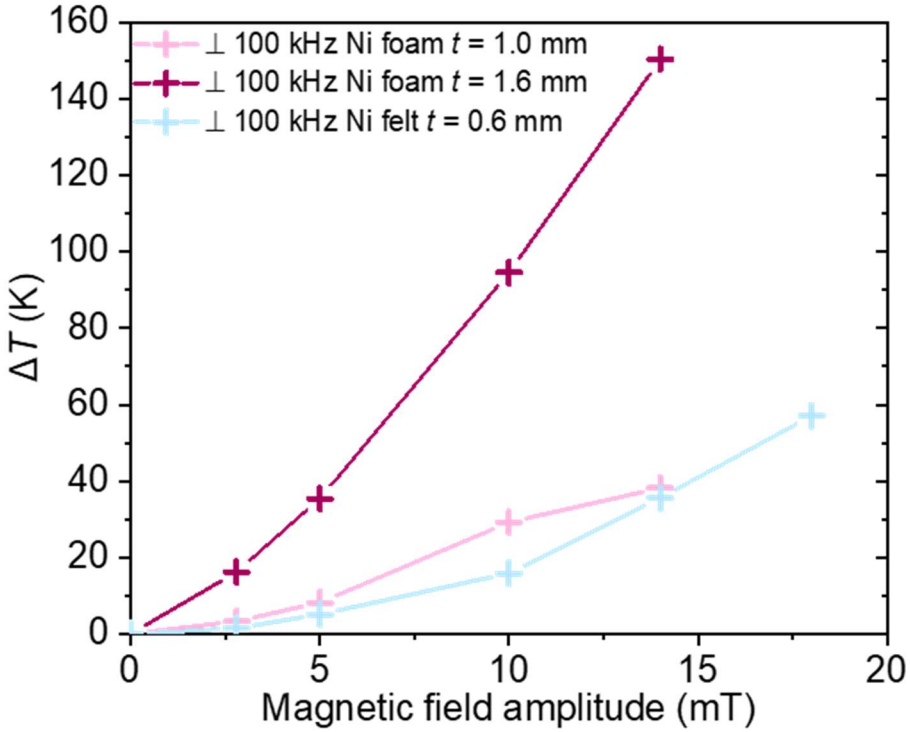

Temperature elevations Δ*T* as measured by a pyrometer targeting the centre of the samples. The perpendicular ⊥ symbols indicate the position of the sample toward the magnetic field. The frequency of the coil and the thickness of the samples used are also indicated.

The Ni foam of 1.6 mm thickness reached a very high temperature. The thickness is a key parameter as indicates the low Δ*T* of the 1.0 mm Ni foam. This explains the lower Δ*T* (Ni felt) while its dense fibre network presents more potential circuit loops where eddy current can be generated.

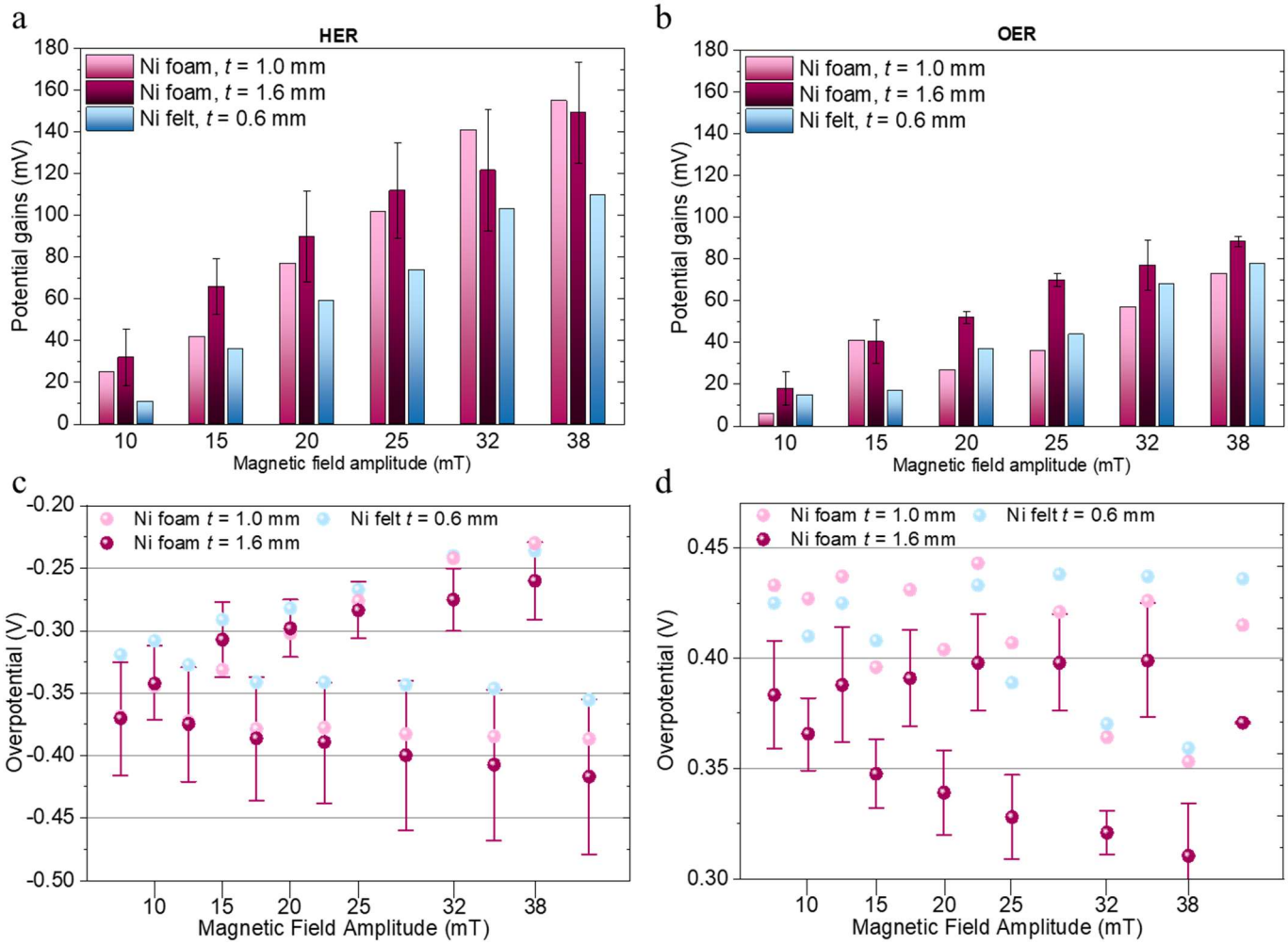

CPs tests were also conducted in the 100 kHz coil.

CP measurements at ±10 mA (supposed ~ 10 mA.cm^{-2}) on two Ni foams of thicknesses t = 1.0 and 1.6 mm respectively, and a Ni felt of thickness 0.6 mm under a 100 kHz AMF: potential gains in the HER (a) and OER (b) side, at AMF ranging from [10; 38] mT, corresponding overpotentials in the HER (c) and OER (d) side. Only the labels corresponding to the AMF amplitudes are displayed, the points between these labels correspond to the overpotentials without AMF, *i.e.* before or after AMF application.

The Ni samples present very good WS activity in both HER and OER side. In HER, the weaker materials lead to higher potential gains, corresponding to a kinetics enhancement, as discussed in subsection IV.1.2. Besides, the overpotentials without AMF continuously increase for all catalysts. This is probably due to the reduction of the Ni, becoming metallic, which is not a good active state. In OER, it is the exact reverse: the more active catalyst, the lower the potential gains. Thus, the mass-transport it perhaps more enhanced in OER for these catalysts in this setup. Especially, the overpotential without AMF increases up to 25 mT were

it becomes stable. An explanation attempt would be that the foams/felt become saturated of bubbles (maximal bubble coverage), the AMF application helping to remove them.

Supplementary Figure 20:

The efficiency of the system can be separated into two parts: the efficiency of the coil, and the efficiency of the electrochemical cell, enhanced by the magnetic activation.

The first one evaluates the magnetic restitution of the coil (η_{mag}). It has been done by measuring the heating of the electrolyte at the outlet of the cell (where the flow rate is well defined) after 5 minutes, with an optic fibre probe (Neoptix®) at different magnetic field amplitudes in the two cells used. By assuming that the thermic losses are only conductive (indeed, no radiation and very little diffusion exist), one can use Eq. II.13 ($P = q_m\, c_p\, \Delta T$) to estimate the power of the WE heating, and hence the heating triggered by the AMF (c_p of water was used, and a flow rate of 83 mL.min^{-1} was applied). Then, the ratio of this restituted power P_r by the electricity consumed by the coil indicates the efficiency of the magnetic system:

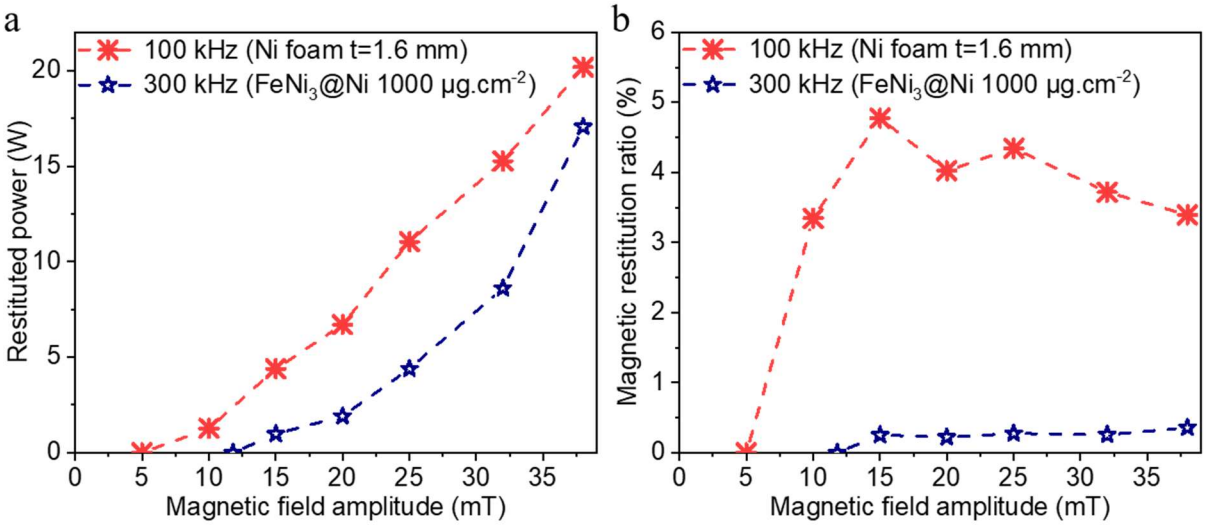

(a) Temperature elevation and (b) magnetic restitution ratio of the setup used in the 100 kHz coil with a Ni foam of thickness t = 1.6 mm and the 300 kHz coil with a $FeNi_3$@Ni sample loaded at 1000 µg.cm^{-2}.

Obviously, the restituted power is superior with the 100 kHz setup than the 300 kHz, even if the frequency of the former setup is three times lower (indeed, the efficiency reached by cooking inductor are very high: 90-98% [52][296]). The magnetic restitution ratio is low, as expected since the coils are not optimized to the electrochemical cell. However, it has to be noted that eddy currents are also generated inside the electrolyte. Indeed, a small order of magnitude calculation indicates that a power of 0.78 W is generated for the 100 kHz setup (and negligible for the 300 kHz setup - Supplementary Figure 21). So, the temperature elevation at a given AMF amplitude is overestimated.

Then, a calculation of the efficiency of the electrochemical cell η_{cell} was estimated, using Eq. V.1. In order to determine the amount of hydrogen produced, a gas chromatographer was used. Unfortunately, the recipe to measure hydrogen and the collecting of hydrogen was not optimized, so that the values obtained were inconsistent. Instead, the Faraday law was employed to compute the number of H_2 mole produced:

Faraday law

$$n = \frac{it}{z\mathcal{F}}$$

With n the number of H_2 mole produced, *t* the time during which the current *i* is applied and *z* the valence of H_2 (being 2).

The Faraday law assumes that no side reaction occurs. This is certainly the case as the atmosphere is saturated in Ar. Besides, chronoamperometry tests (setting a potential and recording the current) in the HER side were conducted, so that the CE potential (carbon torray paper) remained under 1.8 V_{RHE}. The carbon did not corrode in the case of $FeNi_3$@Ni. Thus, only the water splitting reaction happened in the 300 kHz coil. For the Ni foam, the CE potential increased up to 6.1 V_{RHE}, as the application of the AMF enhanced a lot the current. So, the

carbon corroded and the recorded current has an oxidation contribution from the carbon. Nevertheless, an efficiency was calculated:

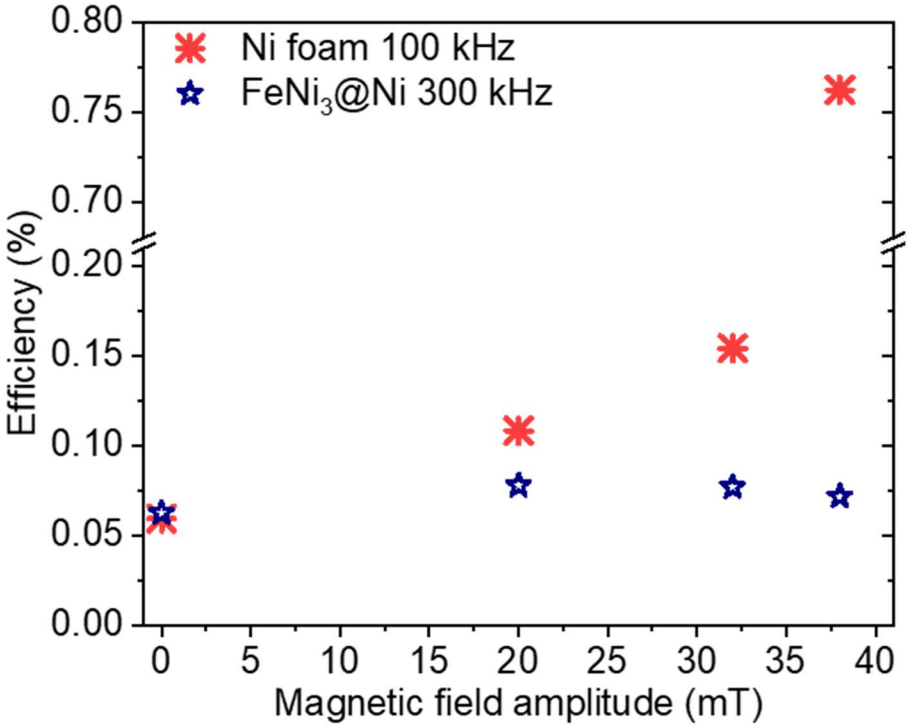

Efficiency estimation of the 100 kHz and the 300 kHz electrochemical setup under AMF.

The efficiency is low, as expected. Nevertheless, it increases under the magnetic field, testifying its added value while the cell and coils are not optimized. Besides, for the calculus, the potential of the CE was the one of the carbon torray paper. The power of the peristaltic pump has also been taken into account (24 W) while this latter was not optimized either. Indeed, no CE potential of a catalyst under AMF was recorded at the different current densities increased under AMF. Thus, the efficiency could be much further improved.

Supplementary Figure 21:

The estimation of the power of the eddy current in the electrolyte was realized as follow. The local Ohm's law indicates that:

Ohm's law $$j = \sigma\, e_{\mathrm{mag}}$$

σ is the conductivity of the electrolyte, being equals to 27.27 $S.m^{-1}$ for KOH at 1 $mol.L^{-1}$, e_{mag} is the electromotive force induced by the magnetic field. Its expression is:

$$e_{\text{mag}} = -\frac{d\Phi}{dt} = -\Phi f$$

With f the frequency of the AMF, Φ the magnetic flux calculated as follow:

$$\Phi = \oiint B.dS = B\ Cell\ section$$

$$\Phi = B_{\max} \frac{Cell\ section}{Coil\ section} Cell\ section$$

Indeed, only the flux through the section of the cell is taken into account. The *Cell section* is 1.8 cm^2 and the Coil section is 7.1 cm^2. Hence the magnetic flux: $\Phi = 1.7\ 10^{-6}$ V.s (at 38 mT). This leads to an electromotive force of: $e_{mag} = 170$ mV, hence a current of 4.6 A, and a heating power of 0.78 W. Thus, the electrolyte is heated by eddy currents, although a part of this power is removed by the electrolyte flux. The calculus for the 300 kHz coil leads to a heating of 0.022 W, being negligible.

List of Figures

References

1. Coyle EF. Improved muscular efficiency displayed as Tour de France champion matures. *J Appl Physiol*. 2005;98(6):2191-2196. doi:10.1152/japplphysiol.00216.2005

2. Carrey J. *Sans Pétrole et sans Charbon - Tome 1*. Vol 53. (IS Edition, ed.).; 2020. https://sans-petrole-et-sans-charbon.fr/sans-charbon-et-sans-petrole-le-livre/sans-charbon-et-sans-petrole-le-livre-tome-1/

3. Morris SC, Novak KM, Hamilton LD. Health effects of coal in the National Energy Plan - United States Department of Energy. Published online 1979. doi:10.2172/5759183

4. Steenland K. Lung Cancer and Diesel Exhaust : A Review. *Am J Ind Med*. 1986;10:177-189. doi:10.1002/ajim.4700100208

5. Ministère de la transition écologique et solidaire - Comissariat général au développement durable. Chiffres clés des énergies renouvelables - Édition 2019. Published online 2019. https://www.statistiques.developpement-durable.gouv.fr/sites/default/files/2019-05/datalab-53-chiffres-cles-des-energies-renouvelables-edition-2019-mai2019.pdf

6. International Energy Agency. World energy Balances: Overview. Published online 2019. https://iea.blob.core.windows.net/assets/8bd626f1-a403-4b14-964f-f8d0f61e0677/World_Energy_Balances_2019_Overview.pdf

7. United Nations Department of Economic and Social Affairs. *World Population Prospects 2019 Highlights*.; 2019. https://population.un.org/wpp/Publications/Files/WPP2019_Highlights.pdf

8. Watson RT, Albritton DL, Barker T, et al. IPCC - Climate Change 2001: Synthesis

Report (Summary for Policymakers). In: ; 2003:34. https://www.grida.no/publications/267

9. IPCC. IPCC Special Report Emissions Scenarios. *Int Panel Clim Chang*. Published online 2000:1-161. http://ebooks.cambridge.org/ref/id/CBO9781107415416A011

10. Dziba L, Erpul G, Fazel A, Fischer M, Hernández AM. Summary for policymakers of the global assessment report on biodiversity and ecosystem services of the Intergovernmental Science-Policy Platform on Biodiversity and Ecosystem Services - ADVANCE UNEDITED VERSION – assessment Key messages. *Adv Unedited*. Published online 2019. https://www.un.org/sustainabledevelopment/blog/2019/05/nature-decline-unprecedented-report/

11. Welsby D, Price J, Pye S, Ekins P. Unextractable fossil fuels in a 1.5 °C world. *Nature*. 2021;597(7875):230-234. doi:10.1038/s41586-021-03821-8

12. Sawyer JS. Man-made carbon Dioxide and the " Greenhouse " Effect. *Nature*. 1972;239:23-26. https://doi-org.gaelnomade-2.grenet.fr/10.1038/239023a0

13. Held IM, Soden BJ. Water Vapor Feedback and Global Warming. *Annu Rev Energy Environ*. 2000;25:441-482. https://doi-org.gaelnomade-2.grenet.fr/10.1146/annurev.energy.25.1.441

14. Chen L, Li T, Yu Y, Behera SK. A possible explanation for the divergent projection of ENSO amplitude change under global warming. *Clim Dyn*. 2017;49(11-12):3799-3811. doi:10.1007/s00382-017-3544-x

15. Masson-Delmotte V, Zhai P, Pörtner H-O, et al. *IPCC, 2018: Global Warming of 1.5°C.*

An IPCC Special Report on the Impacts of Global Warming of 1.5°C above Pre-Industrial Levels and Related Global Greenhouse Gas Emission Pathways, in the Context of Strengthening the Global Response to the Threat of Cli.; 2019. https://www.ipcc.ch/site/assets/uploads/sites/2/2019/06/SR15_Full_Report_High_Res.pdf

16. Nations Unies. *Accord de Paris.*; 2015:1-28. https://unfccc.int/sites/default/files/french_paris_agreement.pdf

17. Fishman T, Graedel TE. Impact of the establishment of US offshore wind power on neodymium flows. *Nat Sustain*. 2015;2:332-338. doi:10.1038/s41893-019-0252-z

18. Chakarvarty U. Renewable Energy Materials Supply Implications - International Association for Energy Economics. Published online 2018:37-39. https://www.google.com/url?sa=t%257B%255C&%257Drct=j%257B%255C&%257Dq=%257B%255C&%257Desrc=s%257B%255C&%257Dsource=web%257B%255C&%257Dcd=15%257B%255C&%257Dcad=rja%257B%255C&%257Duact=8%257B%255C&%257Dved=2ahUKEwiwwZK5vo3pAhUJtRoKHQ5bCcIQFjAOegQIBRAB%257B%255C&%257Durl=https%257B%255C%2525%257D3A%257B%255C%2525%257D2F%257B%255C%25

19. Vesborg PCK, Jaramillo TF. Addressing the terawatt challenge: scalability in the supply of chemical elements for renewable energy. *RSC Adv*. 2012;2(21):7933. doi:10.1039/c2ra20839c

20. Croci L. Gestion de l ’ énergie dans un système multi-sources photovoltaïque et éolien avec stockage hybride batteries / supercondensateurs. Published online 2013. https://tel.archives-ouvertes.fr/tel-00943296

21. Li M, Lu J, Chen Z, Amine K. 30 Years of Lithium-Ion Batteries. *Adv Mater*. 2018;1800561:1-24. doi:10.1002/adma.201800561

22. Ferry J, Cs T, Cedex T. *Etude Portant Sur l'hydrogène et La Méthanation Comme Procédé de Valorisation de l'électricité Excédentaire, Synthèse.*; 2014. https://www.actu-environnement.com/media/pdf/news-25572-power-to-gas-ademe-grtgaz.pdf

23. Boucly P, Percebois J, Defaye S, et al. Transition énergétique : l'hydrogène, vecteur des possibles. *La Rev l'Energie*. 2019;644:43-56. https://www.larevuedelenergie.com/transition-energetique-lhydrogene-vecteur-des-possibles/

24. Green DDW, Southard DMZ. *Perry's Chemical Engineers' Handbook, 9th Edition*. 9th editio. McGraw-Hill Education; 2019. https://www.accessengineeringlibrary.com/content/book/9780071834087

25. Safari F, Dincer I. A review and comparative evaluation of thermochemical water splitting cycles for hydrogen production. *Energy Convers Manag*. 2020;205(December 2019):112-182. doi:10.1016/j.enconman.2019.112182

26. Holladay JD, Hu J, King DL, Wang Y. An overview of hydrogen production technologies. *Cat Today*. 2009;139:244-260. doi:10.1016/j.cattod.2008.08.039

27. Hanley ES, Deane JP, Gallachóir BPÓ. The role of hydrogen in low carbon energy futures – A review of existing perspectives. *Renew Sustain Energy Rev*. 2018;82(November 2017):3027-3045. doi:10.1016/j.rser.2017.10.034

28. Beeker E. Y a-t-il une place pour l'hydrogène dans la transition énergétique ? Published

online 2014. https://www.strategie.gouv.fr/sites/strategie.gouv.fr/files/atoms/files/201-08-06na-fs-hydrogene-hd.pdf

29. Züttel A. Materials for hydrogen storage. *Materialtoday*. 2003;6(9):24-33. doi:10.1016/S1369-7021(03)00922-2

30. Murray LJ, Dinca M, Long JR. Metal – organic frameworks issue Hydrogen storage in metal – organic frameworks w. *Chem Soc Rev*. 2009;38(5):1294-1314. doi:10.1039/b802256a

31. Press Service. Zero Emission Valley (ZEV), le plan régional pour le déploiement de l'hydrogène, remporte l'appel à projet européen Blending call 2017. Published online 2017:2017-2019. https://www.auvergnerhonealpes.fr/cms%7B%5C_%7DviewFile.php?idtf=1909%7B%5C&%7Dpath=CP-ZEv-20-12-2017.pdf

32. Boucly P. L'hydrogène en France, le mouvement, le moment. Published online 2019. https://www.google.com/url?sa=t%7B%5C&%7Drct=j%7B%5C&%7Dq=%7B%5C&%7Desrc=s%7B%5C&%7Dsource=web%7B%5C&%7Dcd=2%7B%5C&%7Dved=2ahUKEwi48uHH7JzpAhWPHhQKHYgBA-sQFjABegQIAxAB%7B%5C&%7Durl=https%7B%5C%25%7D3A%7B%5C%25%7D2F%7B%5C%25%7D2Fwww.afhypac.org%7B%5C%25%7D

33. Schalenbach M, Zeradjanin AR, Kasian O, Cherevko S, Mayrhofer KJJ. A perspective on low-temperature water electrolysis - Challenges in alkaline and acidic technology. *Int J Electrochem Sci*. 2018;13(2):1173-1226. doi:10.20964/2018.02.26

34. Zeng K, Zhang D. Recent progress in alkaline water electrolysis for hydrogen production and applications. *Prog Energy Combust Sci*. 2010;36(3):307-326.

doi:10.1016/j.pecs.2009.11.002

35. Carmo M, Fritz DL, Mergel J, Stolten D. A comprehensive review on PEM water electrolysis. *Int J Hydrog Energy*. 2013;38(12):4901-4934. doi:10.1016/j.ijhydene.2013.01.151

36. Carmo M, Fritz DL, Mergel J, Stolten D. A comprehensive review on PEM water electrolysis. *Int J Hydrog Energy*. 2013;38(12):4901-4934. doi:10.1016/j.ijhydene.2013.01.151

37. Divisek J, Mergel J, Schmitz H. Improvements of Water ELectrolysis in Alkaline Media at Intermediate Temperatures. *Int J Hydrog Energy*. 1982;7(9):695-701. doi:10.1016/0360-3199(82)90017-9

38. LeRoy RL. The Thermodynamics of Aqueous Water Electrolysis. *J Electrochem Soc*. 1980;127(9):1954. doi:10.1149/1.2130044

39. Miles MH. Effect of Temperature on Electrode Kinetic Parameters for Hydrogen and Oxygen Evolution Reactions on Nickel Electrodes in Alkaline Solutions. *J Electrochem Soc*. 1976;123(3):332. doi:10.1149/1.2132820

40. Ogawa T, Takeuchi M, Kajikawa Y. Analysis of Trends and Emerging Technologies in Water Electrolysis Research Based on a Computational Method: A Comparison with Fuel Cell Research. *Sustainability*. 2018;10(2):478. doi:10.3390/su10020478

41. Pourbaix M. Atlas d'Equilibres Electrochimiques, Gauthier-Villars, Paris. Published online 1963. doi:10.1002/maco.19630140821

42. Schalenbach M, Zeradjanin AR, Kasian O, Cherevko S. A Perspective on Low-Temperature Water Electrolysis – Challenges in Alkaline and Acidic Technology. *Int J*

Electrochem Sci. 2018;13:1173-1226. doi:10.20964/2018.02.26

43. Baysinger G, Berger LI, Goldberg RN, et al. *CRC Handbook of Chemistry and Physics*. (Taylor & Francis Group L, ed.).; 2014. https://edisciplinas.usp.br/pluginfile.php/4557662/mod_resource/content/1/CRC Handbook of Chemistry and Physics 95th Edition.pdf

44. Chi J, Yu H. Water electrolysis based on renewable energy for hydrogen production. *Chinese J Catal*. 2018;39(3):390-394. doi:10.1016/S1872-2067(17)62949-8

45. Buttler A, Splietho H. Current status of water electrolysis for energy storage , grid balancing and sector coupling via power-to-gas and power-to-liquids : A review. 2018;82(February 2017):2440-2454. doi:10.1016/j.rser.2017.09.003

46. Manabe A, Kashiwase M, Hashimoto T, et al. Basic study of alkaline water electrolysis. *Electrochim Acta*. 2013;100:249-256. doi:10.1016/j.electacta.2012.12.105

47. Marini S, Salvi P, Nelli P, et al. Advanced alkaline water electrolysis. *Electrochim Acta*. 2012;82:384-391. doi:10.1016/j.electacta.2012.05.011

48. Wang L, Chen M, Küngas R, et al. Power-to-fuels via solid-oxide electrolyzer : Operating window and techno-economics. *Renew Sustain Energy Rev*. 2019;110(January):174-187. doi:10.1016/j.rser.2019.04.071

49. O'Brien JE, Stoots CM, Herring JS, et al. Performance of Planar High-Temperature Electrolysis Stacks for Hydrogen Production from Nuclear Energy. *Nucl Technol*. 2017;158:118-131. doi:10.13182/NT07-A3830

50. Bertotti G. *Hysteresis in Magnetism*. (9780080534374 eBook I, ed.). Elsevier; 1998.

51. Lucia O, Maussion P, Dede EJ, Burdio JM. Induction heating technology and its applications: Past developments, current technology, and future challenges. *IEEE Trans Ind Electron*. 2014;61(5):2509-2520. doi:10.1109/TIE.2013.2281162

52. Sweeney M, Dols J, Fortenbery B, Sharp F. Induction Cooking Technology Design and Assessment. *2014 ACEEE Summer Study Energy Effic Build*. Published online 2014:370-379. https://aceee.org/files/proceedings/2014/data/papers/9-702.pdf

53. Holmquest HJ. Application of High Frequency Phenomena in Medicine. *Q Bull Northwest Univ Med Sch*. 1941;19:41-47.

54. Selwood PW. Magnetism and Catalysis. *Chem Rev*. 1946;38:41-82. doi:10.1021/cr60119a002

55. Mortensen PM, Engbæk JS, Vendelbo SB, Hansen MF, Østberg M. Direct Hysteresis Heating of Catalytically Active Ni-Co Nanoparticles as Steam Reforming Catalyst. *Ind Eng Chem Res*. 2017;56(47):14006-14013. doi:10.1021/acs.iecr.7b02331

56. Chatterjee S, Degirmenci V, Rebrov E V. Design and operation of a radio-frequency heated micro-trickle bed reactor for consecutive catalytic reactions. *Chem Eng J*. 2015;281:884-891. doi:10.1016/j.cej.2015.06.096

57. Varsano F, Bellusci M, La Barbera A, Petrecca M, Albino M, Sangregorio C. Dry reforming of methane powered by magnetic induction. *Int J Hydrogen Energy*. 2019;44(38):21037-21044. doi:10.1016/j.ijhydene.2019.02.055

58. Bordet A, Lacroix L, Fazzini P, Carrey J, Soulantica K, Chaudret B. Magnetically Induced Continuous CO2 Hydrogenation Using Composite Iron Carbide Nanoparticles of Exceptionally High Heating Power. *Angew Chem Int Ed*. 2016;55:15894-15898.

doi:10.1002/anie.201609477

59. Hallali N, Clerc P, Fourmy D, et al. Influence on cell death of high frequency motion of magnetic nanoparticles during magnetic hyperthermia experiments. *Appl Phys Lett*. 2016;109:32402. doi:10.1063/1.4958989

60. Niether C, Faure S, Bordet A, et al. Improved water electrolysis using magnetic heating of FeC–Ni core–shell nanoparticles. *Nat Energy*. 2018;3:476-483. doi:10.1038/s41560-018-0132-1

61. Mille N. Utilisation de nanoparticules pour la catalyse activée par des champs magnétiques haute fréquence : étude des aspects physiques. *Thesis*. Published online 2019. http://www.theses.fr/2019ISAT0029

62. Stephen Blundell. *Magnetism in Condensed Matter*. Oxford University Press Inc.; 2001. http://linux0.unsl.edu.ar/~froma/libros/BlunforDirac0198505914.pdf

63. Kittel C. *Introduction to Solid State Physics - 8th Edition*. 8th ed. (John Wiley & Sons I, ed.).; 2005.

64. De Blois RW. Ferromagnetic Domains in Thin Single-Crystal Nickel Platelets. *J Appl Phys*. 1965;36(5):1647-1658. doi:10.1063/1.1703103

65. De Masi D. Nanoparticules bimétalliques combinant propriétés catalytiques et physiques pour la valorisation du CO2 et de la biomasse. Published online 2019. http://www.theses.fr/2019ISAT0024/document

66. Bordet A. Thèse: Une nouvelle génération de nano-catalyseurs à base de carbure de fer pour le stockage chimique de l'énergie. *Inst Natl des Sci Appliquées Toulouse*. Published online 2016:1-271.

http://www.tandfonline.com.prox.lib.ncsu.edu/doi/abs/10.1080/089356901101242009

67. Stoner EC, Wohlfarth EP. A Mechanism pf Magnetic Hysteresis in Heterogeneous Alloys. *Philos Trans R Soc London Ser A, Math Phys Sci*. 1948;240(May):599-642. doi:10.1098/rsta.1948.0007

68. Meffre A, Mehdaoui B, Connord V, et al. Complex nano-objects displaying both magnetic and catalytic properties: A proof of concept for magnetically induced heterogeneous catalysis. *Nano Lett*. 2015;15(5):3241-3248. doi:10.1021/acs.nanolett.5b00446

69. Deatsch AE, Evans BA. Heating efficiency in magnetic nanoparticle hyperthermia. *J Magn Magn Mater*. 2014;354:163-172. doi:10.1016/j.jmmm.2013.11.006

70. Mohammed L, Gomaa HG, Ragab D, Zhu J. Magnetic nanoparticles for environmental and biomedical applications: A review. *Particuology*. 2016;30(August):1-14. doi:10.1016/j.partic.2016.06.001

71. Carrey J, Mehdaoui B, Respaud M. Simple models for dynamic hysteresis loop calculations of magnetic single-domain nanoparticles: Application to magnetic hyperthermia optimization. *J Appl Phys*. 2011;109(8):83921. doi:10.1063/1.3551582

72. Hergt R, Dutz S, Röder M. Effects of size distribution on hysteresis losses of magnetic nanoparticles for hyperthermia. *J Phys Condens Matter*. 2008;20(38). doi:10.1088/0953-8984/20/38/385214

73. De la Presa P, Luengo Y, Multigner M, et al. Study of Heating Efficiency as a Function of Concentration, Size, and Applied Field in $γ$-Fe 2 O 3 Nanoparticles. *J Phys Chem C*. 2012;116:25602-25610. doi:10.1021/jp310771p

74. Mehdaoui B, Meffre A, Carrey J, et al. Optimal size of nanoparticles for magnetic hyperthermia: A combined theoretical and experimental study. *Adv Funct Mater*. 2011;21(23):4573-4581. doi:10.1002/adfm.201101243

75. Asensio JM, Marbaix J, Mille N, et al. To heat or not to heat: A study of the performances of iron carbide nanoparticles in magnetic heating. *Nanoscale*. 2019;11(12):5402-5411. doi:10.1039/c8nr10235j

76. Guibert C, Dupuis V, Peyre V, Fresnais J. Hyperthermia of Magnetic Nanoparticles: Experimental Study of the Role of Aggregation. *J Phys Chem C*. 2015;119(50):28148-28154. doi:10.1021/acs.jpcc.5b07796

77. Yadel C, Michel A, Casale S, Fresnais J. Hyperthermia efficiency of magnetic nanoparticles in dense aggregates of cerium oxide/iron oxide nanoparticles. *Appl Sci*. 2018;8(8). doi:10.3390/app8081241

78. Andreu I, Natividad E, Solozábal L, Roubeau O. Nano-objects for addressing the control of nanoparticle arrangement and performance in magnetic hyperthermia. *ACS Nano*. 2015;9(2):1408-1419. doi:10.1021/nn505781f

79. Serantes D, Simeonidis K, Angelakeris M, et al. Multiplying magnetic hyperthermia response by nanoparticle assembling. *J Phys Chem C*. 2014;118(11):5927-5934. doi:10.1021/jp410717m

80. Saville SL, Qi B, Baker J, et al. The formation of linear aggregates in magnetic hyperthermia: Implications on specific absorption rate and magnetic anisotropy. *J Colloid Interface Sci*. 2014;424:141-151. doi:10.1016/j.jcis.2014.03.007

81. Mehdaoui B, Tan RP, Carrey J, Lachaize S, Chaudret B. Increase of magnetic

hyperthermia efficiency due to dipolar interactions in low anisotropy magnetic nanoparticles: theoretical and experimental results. *Phys Rev B*. 2013;87(17):1-21. doi:10.1103/PhysRevB.87.174419

82. Fahidy TZ. Hydroynamic Models in Magnetoelectrolysis. *Electrochim Acta*. 1973;18(8):607-614. doi:10.1016/0013-4686(73)85026-1

83. Aogaki R, Fueki K, Mukaibo T. Application of Magnetohydrodynamic Effect to the Analysis of Electrochemical Reactions 1. MHD Flow of an Electrolyte Solution in an Electrode－Cell with a short Rectangular Channel. *Denki Kagaku oyobi Kogyo Butsuri Kagaku*. Published online 1975:504-508. doi:10.5796/kogyobutsurikagaku.43.504

84. Gatard V, Deseure J, Chatenet M. Use of magnetic fields in electrochemistry: A selected review. *Curr Opin Electrochem*. 2020;23:96-105. doi:10.1016/j.coelec.2020.04.012

85. Kołodziejczyko K, Miękoś E, Zieliński M, Jaksender M, Szczukocki D, Czarny K. Influence of constant magnetic field on electrodeposition of metals , alloys , conductive polymers , and organic reactions. *J Solid State Electrochem*. 2018;22:1629-1647. doi:10.1007/s10008-017-3875-x

86. Monzon LMA, Coey JMD. Magnetic fields in electrochemistry: The Lorentz force. A mini-review. *Electrochem commun*. 2014;42:38-41. doi:10.1016/j.elecom.2014.02.006

87. Monzon LMA, Rode K, Venkatesan M, Coey JMD. Electrosynthesis of Iron, Cobalt, and Zinc Microcrystals and Magnetic Enhancement of the Oxygen Reduction Reaction. *Chem Mater*. 2012;24(20):3878-3885. doi:10.1021/cm301766s

88. Hinds G, Coey JMD, Lyons MEG. Influence of magnetic forces on electrochemical mass transport. *Electrochem Commun*. 2001;3:215-218. doi:10.1016/S1388-2481(01)00136-

89. Fahidy TZ. Augmentation of natural convective mass transfer via magnetoelectrolysis. *Chem Eng J*. 1974;7(1):21-27. doi:10.1016/0300-9467(74)80022-5

90. Leventis N, Chen M, Gao X, Canalas M, Zhang P. Electrochemistry with stationary disk and ring-disk millielectrodes in magnetic fields. *J Phys Chem B*. 1998;102(18):3512-3522. doi:10.1021/jp980498f

91. Leventis N, Gao X. Steady-state voltammetry with stationary disk millielectrodes in magnetic fields: Nonlinear dependence of the mass-transfer limited current on the electron balance of the faradaic process. *J Phys Chem B*. 1999;103(28):5832-5840. doi:10.1021/jp9903920

92. Katz E, Lioubashevski O, Willner I. Magnetic field effects on bioelectrocatalytic reactions of surface-confined enzyme systems: Enhanced performance of biofuel cells. *J Am Chem Soc*. 2005;127(11):3979-3988. doi:10.1021/ja044157t

93. Uhlemann M, Krause A, Chopart JP, Gebert A. Electrochemical Deposition of Co under the Influence of High Magnetic Fields. *J Electrochem Soc*. 2005;152(12):C817. doi:10.1149/1.2073167

94. Cierpka C, Weier T, Gerbeth G, Uhlemann M, Eckert K. Copper deposition and dissolution in seemingly parallel electric and magnetic fields: Lorentz force distributions and flow configurations. *J Solid State Electrochem*. 2007;11(6):687-701. doi:10.1007/s10008-006-0215-y

95. Lee J, Ragsdale SR, Gao X, White HS. Magnetic field control of the potential distribution and current at microdisk electrodes. *J Electroanal Chem*. 1997;422(1-2):169-177.

doi:10.1016/S0022-0728(96)04878-4

96. Mogi I, Morimoto R, Aogaki R, Takahashi K. Effects of Vertical Magnetohydrodynamic Flows on Chiral Surface Formation in Magnetoelectrolysis. *Magnetochemistry*. 2018;4(3):40. doi:10.3390/magnetochemistry4030040

97. Mogi I, Morimoto R, Aogaki R. Surface chirality effects induced by magnetic fields. *Curr Opin Electrochem*. 2018;7:1-6. doi:10.1016/j.coelec.2017.09.029

98. Wang A, Deng Q, Deng L, Guan X, Luo J. Eliminating Tip Dendrite Growth by Lorentz Force for Stable Lithium Metal Anodes. *Adv Funct Mater*. 2019;29(25):1-7. doi:10.1002/adfm.201902630

99. Nishikawa K, Saito T, Matsushima H, Ueda M. Holographic interferometric microscopy for measuring Cu2+ concentration profile during Cu electrodeposition in a magnetic field. *Electrochim Acta*. 2019;297:1104-1108. doi:10.1016/j.electacta.2018.12.025

100. Koza JA, Karnbach F, Uhlemann M, et al. Electrocrystallisation of CoFe alloys under the influence of external homogeneous magnetic fields — Properties of deposited thin films. *Electrochem Acta*. 2010;55:819-831. doi:10.1016/j.electacta.2009.08.069

101. Chiba A, Kitamura K, Ogawa T. Magnetic Field Effects On The Electrodeposition Of Nickel From a High pH Watt's Bath. *Surf Coatings Technol*. 1986;27(1):83-88. doi:10.1016/0257-8972(86)90047-2

102. Franczak A, Levesque A, Bohr F, Douglade J, Chopart J. Structural and morphological modifications of the Co-thin films caused by magnetic field and pH variation. *Appl Surf Sci*. 2012;258(22):8683-8688. doi:10.1016/j.apsusc.2012.05.074

103. Zou P, Li J, Zhang Y, Liang C, Yang C, Jin H. Nano Energy Magnetic- field-induced

rapid synthesis of defect-enriched Ni-Co nanowire membrane as highly efficient hydrogen evolution electrocatalyst. *Nano Energy*. 2018;51(June):349-357. doi:10.1016/j.nanoen.2018.06.080

104. Yang L, Chen C, Yuan J, Gao L, Shang Z, Liu Z. Effect of applied magnetic field on the electroplating and magnetic properties of amorphous FeNiPGd thin film. *J Magn Magn Mater*. 2020;495(September 2019):165872. doi:10.1016/j.jmmm.2019.165872

105. Rhen FMF, Fernandez D, Hinds G, Coey JMD. Influence of a Magnetic Field on the Electrochemical Rest Potential. *J Electrochem Soc*. 2006;153(1):J1. doi:10.1149/1.2135207

106. Kiciński W, Sęk JP, Matysiak-brynda E, et al. Environmental Enhancement of PGM-free oxygen reduction electrocatalyst performance for conventional and enzymatic fuel cells : The influence of an external magnetic field. *Appl Catal B*. 2019;258(July):117955. doi:10.1016/j.apcatb.2019.117955

107. Lu Z, Huang D, Yang W, Congleton J. Effects of an applied magnetic field on the dissolution and passivation of iron in sulphuric acid. *Corros Sci*. 2003;45(10):2233-2249. doi:10.1016/S0010-938X(03)00045-3

108. Romero J, Prima-garcia H, Varela M, et al. Giant Enhancement in the Supercapacitance of NiFe – Graphene Nanocomposites Induced by a Magnetic Field. *Adv Mater*. 2019;31(28):1-8. doi:10.1002/adma.201900189

109. Monzon LMA, Nair V, Reilly B, Coey JMD. Magnetically-Induced Flow during Electropolishing. *J Electrochem Soc*. 2018;165(13):6-11. doi:10.1149/2.0581813jes

110. Matsushima H, Iida T, Fukunaka Y. Observation of bubble layer formed on hydrogen

and oxygen gas-evolving electrode in a magnetic field. *J Solid State Electrochem*. 2012;16(2):617-623. doi:10.1007/s10008-011-1392-x

111. Matsushima H, Iida T, Fukunaka Y. Gas bubble evolution on transparent electrode during water electrolysis in a magnetic field. *Electrochim Acta*. 2013;100:261-264. doi:10.1016/j.electacta.2012.05.082

112. Liu H, Zhong D, Han J, Pan L. Hydrogen bubble evolution from magnetized nickel wire electrode. *Int J Hydrog Energy*. 2019;44(60):31724-31730. doi:10.1016/j.ijhydene.2019.10.063

113. Weerasiri LD, Das S. Characteristics of sliding bubble in aqueous electrolyte: In presence of an external magnetic field. *Colloids Surfaces A Physicochem Eng Asp*. 2018;538(2017):404-416. doi:10.1016/j.colsurfa.2017.11.026

114. Koza JA, Mühlenhoff S, Uhlemann M, Eckert K, Gebert A, Schultz L. Desorption of hydrogen from an electrode surface under influence of an external magnetic field - In-situ microscopic observations. *Electrochem commun*. 2009;11(2):425-429. doi:10.1016/j.elecom.2008.12.010

115. Wang M, Wang Z, Gong X, Guo Z. The intensification technologies to water electrolysis for hydrogen production - A review. *Renew Sustain Energy Rev*. 2014;29:573-588. doi:10.1016/j.rser.2013.08.090

116. Koza JA, Mühlenhoff S, Zabiński P, et al. Hydrogen evolution under the influence of a magnetic field. *Electrochim Acta*. 2011;56(6):2665-2675. doi:10.1016/j.electacta.2010.12.031

117. Liu H, Pan L, Qin Q, Li P. Experimental and numerical investigation of gas – liquid flow

in water electrolysis under magnetic field. *J Electroanal Chem*. 2019;832(November 2018):293-302. doi:10.1016/j.jelechem.2018.11.020

118. Koza JA, Uhlemann M, Gebert A, Schultz L. Desorption of hydrogen from the electrode surface under influence of an external magnetic field. *Electrochem commun*. 2008;10(9):1330-1333. doi:10.1016/j.elecom.2008.07.003

119. Scott K. Process intensification: An electrochemical perspective. *Renew Sustain Energy Rev*. 2018;81(May 2017):1406-1426. doi:10.1016/j.rser.2017.05.189

120. Li Y, Zhang L, Peng J, Zhang W, Peng K. Magnetic field enhancing electrocatalysis of Co3O4/NF for oxygen evolution reaction. *J Power Sources*. 2019;433(March):226704. doi:10.1016/j.jpowsour.2019.226704

121. Iida T, Matsushima H, Fukunaka Y. Water Electrolysis under a Magnetic Field. *J Electrochem Soc*. 2007;154(8):E112. doi:10.1149/1.2742807

122. Matsushima H, Kiuchi D, Fukunaka Y. Measurement of dissolved hydrogen supersaturation during water electrolysis in a magnetic field. *Electrochem Acta*. 2009;54:5858-5862. doi:10.1016/j.electacta.2009.05.044

123. Cho MS, Yun YY, Nam JD, Son Y, Lee Y. Effect of magnetic field on electrochemical polymerization of EDOT. *Synth Met*. 2008;158:1043-1046. doi:10.1016/j.synthmet.2008.07.006

124. Karpowicz R, Lewkowski J, Morawska M. The aza-Pudovik reaction accelerated in external constant magnetic field. *Chem Pap Short Commun*. 2016;70(11):1529-1532. doi:10.1515/chempap-2016-0087

125. Leventis N, Gao X. Magnetohydrodynamic electrochemistry in the field of Nd-Fe-B

magnets. Theory, experiment, and application in self-powered flow delivery systems. *Anal Chem*. 2001;73(16):3981-3992. doi:10.1021/ac010172u

126. Coey JMD, Hinds G. Magnetoelectrolysis - the effect of magnetic fields in electrochemistry. In: *Pamir*. ; 2002:1-7. https://www.researchgate.net/publication/273755851_Magnetoelectrolysis_-_the_effect_of_magnetic_fields_in_electrochemistry

127. WM Haynes. Magnetic Susceptibility of the Elements and Inorganic Compounds. *Handb Chem Phys*. Published online 1998:130-135.

128. Dunne P, Coey JMD. Magnetic Structuring of Electrodeposits. *Phys Rev Lett*. 2012;109(22):229402. doi:10.1103/PhysRevLett.109.229402

129. Tschulik K, Koza JA, Uhlemann M, Gebert A, Schultz L. Effects of well-defined magnetic field gradients on the electrodeposition of copper and bismuth. *Electrochem commun*. 2009;11(11):2241-2244. doi:10.1016/j.elecom.2009.09.041

130. Gorobets OY, Gorobets VY, Derecha DO, Brukva OM. Nickel electrodeposition under influence of constant homogeneous and high-gradient magnetic field. *J Phys Chem C*. 2008;112(9):3373-3375. doi:10.1021/jp0762572

131. Tschulik K, Cierpka C, Mutschke G, Gebert A, Schultz L, Uhlemann M. Clarifying the mechanism of reverse structuring during electrodeposition in magnetic gradient fields. *Anal Chem*. 2012;84(5):2328-2334. doi:10.1021/ac2029612

132. Sueptitz R, Tschulik K, Uhlemann M, Schultz L, Gebert A. Magnetic field effects on the active dissolution of iron. *Electrochim Acta*. 2011;56(17):5866-5871. doi:10.1016/j.electacta.2011.04.126

133. Ohma A, Shinohara K, Iiyama A, Yoshida T, Daimaru A. *Membrane and Catalyst Performance Targets for Automotive Fuel Cells by FCCJ Membrane, Catalyst, MEA WG*. Vol 41.; 2011. doi:10.1149/1.3635611

134. Wang LB, Wakayama NI, Okada T. Numerical simulation of a new water management for PEM fuel cell using magnet particles deposited in the cathode side catalyst layer. *Electrochem commun*. 2002;4:584-588. doi:10.1016/S1388-2481(02)00383-1

135. Shi J, Xu H, Zhao H, Lu L, Wu X. Preparation of Nd2Fe14B/C magnetic powder and its application in proton exchange membrane fuel cells. *J Power Sources*. 2014;252:189-199. doi:10.1016/j.jpowsour.2013.11.106

136. Chaure NB, Rhen FMF, Hilton J, Coey JMD. Design and application of a magnetic field gradient electrode. *Electrochem commun*. 2007;9(1):155-158. doi:10.1016/j.elecom.2006.08.059

137. Cai J, Wang L, Wu P. Oxygen enrichment from air by using the interception effect of gradient magnetic field on oxygen molecules. *Phys Lett A*. 2007;362:105-108. doi:10.1016/j.physleta.2006.10.004

138. Wakayama NI. Behavior of gas flow under gradient magnetic fields. *J Appl Phys*. 1991;69:2734-2736. doi:10.1063/1.348629

139. Fontanesi C. Spin-dependent electrochemistry : A novel paradigm. *Curr Opin Electrochem*. 2019;7:36-41. doi:10.1016/j.coelec.2017.09.028

140. Naaman R, Waldeck DH. Chiral-Induced Spin Selectivity Effect. *J Phys Chem Lett*. 2012;3:2178-2187. doi:10.1021/jz300793y

141. Naaman R, Waldeck DH. Spintronics and Chirality: Spin Selectivity in Electron

Transport Through Chiral Molecules. *Annu Rev Phys Chem*. 2015;66:263-281. doi:10.1146/annurev-physchem-040214-121554

142. Naaman R, Paltiel Y, Waldeck DH. Chiral molecules and the electron spin. *Nat Rev Chem*. 2019;3:250-260. doi:10.1038/s41570-019-0087-1

143. Chrétien S, Metiu H. O2 evolution on a clean partially reduced rutile TiO2(110) surface and on the same surface precovered with Au1 and Au2 : The importance of spin conservation. *J Chem Phys*. 2008;129:74705. doi:10.1063/1.2956506

144. Wayne RP. Singlet Molecular Oxygen. In: *Advances in Photochemistry*. John Wiley & Sons, Ltd; 1969:311-371. doi:10.1002/9780470133378.ch4

145. Herzberg G. *Spectra of Diatomic Molecules*. Vol 1. van Nostrand; 1950. https://toaz.info/doc-viewer

146. Behler J, Delley B, Lorenz S, Reuter K, Scheffler M. Dissociation of O2 at A1(111): The role of spin selection rules. *Phys Rev Lett*. 2005;94(3):1-4. doi:10.1103/PhysRevLett.94.036104

147. Nazmutdinov RR, Santos E, Schmickler W. Spin effects in oxygen electrocatalysis: A discussion. *Electrochem commun*. 2013;33:14-17. doi:10.1016/j.elecom.2013.04.001

148. Torun E, Fang CM, Wijs GA De, Groot RA De. Role of Magnetism in Catalysis: RuO2(110) Surface. *J Phys Chem C*. 2013;2(110):6353-6357. doi:10.1021/jp4020367

149. Engel T, Reid P. *Physical Chemistry*. PEARSON Benjamin Cummings; 2006.

150. Ray K, Ananthavel SP, Waldeck DH, Naaman R. Asymmetric Scattering of Polarized Electrons by Organized Organic Films of Chiral Molecules. *Science (80-)*.

1999;283:814-817. doi:10.1126/science.283.5403.814

151. Gracia J, Biz C, Fianchini M. The trend of chemisorption of hydrogen and oxygen atoms on pure transition metals : Magnetism justifies unexpected behaviour of Mn and Cr. *Mater Today Commun*. 2020;23(December 2019):100894. doi:10.1016/j.mtcomm.2020.100894

152. Bhattacharjee S, Lee S. Controlling Oxygen-Based Electrochemical Reactions through Spin Orientation. *J Phys Chem C*. 2018;122:894-901. doi:10.1021/acs.jpcc.7b10147

153. Gracia J, Sharpe R, Munarriz J. Principles determining the activity of magnetic oxides for electron transfer reactions. *J Catal*. 2018;361:331-338. doi:10.1016/j.jcat.2018.03.012

154. Gracia J, Sl M, Polavieja G. Itinerant Spins and Bond Lengths in Oxide Electrocatalysts for Oxygen Evolution and Reduction Reactions. *J Phys Chem C*. 2019;123:9967-9972. doi:10.1021/acs.jpcc.9b01635

155. Forslund RP, Hardin WG, Rong X, et al. Exceptional Electrocatalytic Oxygen Evolution Via Tunable Ruddlesden-Popper Oxides. *Nat Commun*. 2018;9:3150. doi:10.1038/s41467-018-05600-y

156. Garcés-pineda FA, Blasco-ahicart M, Nieto-castro D, López N, Galán-mascarós JR. Direct magnetic enhancement of electrocatalytic water oxidation in alkaline media. *Nat Energy*. 2019;4(June):519-525. doi:10.1038/s41560-019-0404-4

157. Ren X, Wu T, Sun Y, et al. Spin-polarized oxygen evolution reaction under magnetic field. *Nat Commun*. 2021;12(1). doi:10.1038/s41467-021-22865-y

158. Kurahashi M, Yamauchi Y. Spin correlation in O2 chemisorption on Ni(111). *Phys Rev*

Lett. 2015;114(1):1-4. doi:10.1103/PhysRevLett.114.016101

159. Gracia J, Munarriz J, Polo V, et al. Analysis of the Magnetic Entropy in Oxygen Reduction Reactions Catalysed by Manganite Perovskites. *ChemCatChem*. 2017;9(17):3358-3363. doi:10.1002/cctc.201700302

160. Jiao Y, Sharpe R, Lim T, Niemantsverdriet JWH, Gracia J. Photosystem II Acts as a Spin-Controlled Electron Gate during Oxygen Formation and Evolution. *J Am Chem Soc*. 2017;139:16604-16608. doi:10.1021/jacs.7b07634

161. Gracia J. Spin dependent interactions catalyse the oxygen electrochemistry. *PhysChemChemPhys*. Published online 2017:20451-20456. doi:10.1039/c7cp04289b

162. Pan H, Wang M, Shen Y, Hu B. Large Magneto-Current Effect in the Electrochemical Detection of Oxalate in Aqueous Solution. *J Phys Chem C*. 2018;122:19880-19885. doi:10.1021/acs.jpcc.8b04193

163. Mtangi W, Tassinari F, Vankayala K, et al. Control of Electrons' Spin Eliminates Hydrogen Peroxide Formation during Water Splitting. *J Am Chem Soc*. 2017;139(7):2794-2798. doi:10.1021/jacs.6b12971

164. Bullard G, Tassinari F, Ko C, et al. Low-Resistance Molecular Wires Propagate Spin-Polarized Currents. *J Am Chem Soc*. 2019;141:14707-14711. doi:10.1021/jacs.9b06142

165. Mishra S, Pirbadian S, Mondal AK, El-naggar MY. Spin-Dependent Electron Transport through Bacterial Cell Surface Multiheme Electron Conduits. *J Am Chem Soc*. 2019;141:19198-19202. doi:10.1021/jacs.9b09262

166. Kumar A, Capua E, Fontanesi C, Carmieli R, Naaman R. Injection of Spin-Polarized Electrons into a AlGaN/GaN Device from an Electrochemical Cell: Evidence for an

Extremely Long Spin Lifetime. *ACS Nano*. 2018;12:3892-3897. doi:10.1021/acsnano.8b01347

167. Tassinari F, Banerjee-ghosh K, Parenti F, Kiran V, Mucci A, Naaman R. Enhanced Hydrogen Production with Chiral Conductive Polymer-Based Electrodes. *J Phys Chem C*. 2017;121:15777-15783. doi:10.1021/acs.jpcc.7b04194

168. Bin G, Peng Z, Yongping JIN, Shukang C. Effects of alternating magnetic field on the corrosion rate and corrosion products of copper. *Rare Met*. 2008;27(3):324-328. doi:10.1016/S1001-0521(08)60138-2

169. Chehade G, Dincer I. A novel method for a new electromagnetic-induced ammonia synthesizer. *Int J Energy Res*. 2020;44(November 2019):7183-7197. doi:10.1002/er.5355

170. Zheng H, Chen H, Wang Y, Gao P, Liu X, Rebrov E V. Fabrication of Magnetic Superstructure NiFe2O4@MOF-74 and Its Derivative for Electrocatalytic Hydrogen Evolution with AC Magnetic Field. *ACS Appl Mater Interfaces*. 2020;12:45987-45996. doi:10.1021/acsami.0c11816

171. Bordet A, Lacroix LM, Soulantica K, Chaudret B. A New Approach to the Mechanism of Fischer-Tropsch Syntheses Arising from Gas Phase NMR and Mass Spectrometry. *ChemCatChem*. 2016;8(9):1727-1731. doi:10.1002/cctc.201600245

172. Masi D De, Asensio JM, Fazzini P, Lacroix L, Chaudret B. Engineering Iron – Nickel Nanoparticles for Magnetically Induced CO2 Methanation in Continuous Flow. *Angew Chem Int Ed*. 2020;59:1-6. doi:10.1002/anie.201913865

173. Trotochaud L, Young SL, Ranney JK, Boettcher SW. Nickel-Iron oxyhydroxide oxygen-

evolution electrocatalysts: The role of intentional and incidental iron incorporation. *J Am Chem Soc*. 2014;136(18):6744-6753. doi:10.1021/ja502379c

174. Davodi F, Mühlhausen E, Tavakkoli M, et al. Catalyst Support Effect on the Activity and Durability of Magnetic Nanoparticles: Toward Design of Advanced Electrocatalyst for Full Water Splitting. *ACS Appl Mater Interfaces*. 2018;10(37):31300-31311. doi:10.1021/acsami.8b08830

175. Ahn HS, Bard AJ. Surface Interrogation Scanning Electrochemical Microscopy of Ni1−xFexOOH (0 < x < 0.27) Oxygen Evolving Catalyst: Kinetics of the "fast" Iron Sites. *J Am Chem Soc*. 2016;138(1):313-318. doi:10.1021/jacs.5b10977

176. Görlin M, Ferreira J, Arau D, et al. Tracking Catalyst Redox States and Reaction Dynamics in Ni−Fe Oxyhydroxide Oxygen Evolution Reaction Electrocatalysts: The Role of Catalyst Support and Electrolyte pH. *J Am Chem Soc*. 2017;139:2070-2082. doi:10.1021/jacs.6b12250

177. Trzešniewski BJ, Diaz-Morales O, Vermaas DA, et al. In Situ Observation of Active Oxygen Species in Fe-Containing Ni-Based Oxygen Evolution Catalysts: The Effect of pH on Electrochemical Activity. *J Am Chem Soc*. 2015;137(48):15112-15121. doi:10.1021/jacs.5b06814

178. Li N, Bediako DK, Hadt RG, et al. Influence of iron doping on tetravalent nickel content in catalytic oxygen evolving films. *Proc Natl Acad Sci U S A*. 2017;114(7):1486-1491. doi:10.1073/pnas.1620787114

179. Bates MK, Jia Q, Doan H, Liang W, Mukerjee S. Charge-Transfer Effects in Ni−Fe and Ni−Fe−Co Mixed-Metal Oxides for the Alkaline Oxygen Evolution Reaction. *Catal*. 2016;6:155-161. doi:10.1021/acscatal.5b01481

180. Friebel D, Louie MW, Bajdich M, et al. Identification of highly active Fe sites in (Ni,Fe)OOH for electrocatalytic water splitting. *J Am Chem Soc*. 2015;137(3):1305-1313. doi:10.1021/ja511559d

181. O'Grady WE, Pandya KI, Swider KE, Corrigan DA. In Situ X-Ray Absorption Near-Edge Structure Evidence for Quadrivalent Nickel in Nickel Battery Electrodes. *J Electrochem Soc*. 1996;143(5):1613-1617. doi:10.1149/1.1836687

182. Chung DY, Lopes PP, Farinazzo Bergamo Dias Martins P, et al. Dynamic stability of active sites in hydr(oxy)oxides for the oxygen evolution reaction. *Nat Energy*. 2020;5(3):222-230. doi:10.1038/s41560-020-0576-y

183. Sun Y, Sun S, Yang H, Xi S, Gracia J, Xu ZJ. Spin-Related Electron Transfer and Orbital Interactions in Oxygen Electrocatalysis. *Adv Mater*. 2020;32(39):1-8. doi:10.1002/adma.202003297

184. Görlin M, Chernev P, Ferreira J, et al. Oxygen Evolution Reaction Dynamics , Faradaic Charge Efficiency , and the Active Metal Redox States of Ni−Fe Oxide Water Splitting Electrocatalysts. *J Am Chem Soc*. 2016;138:5603-5614. doi:10.1021/jacs.6b00332

185. Görlin M, Chernev P, Paciok P, et al. Formation of unexpectedly active Ni–Fe oxygen evolution electrocatalysts by physically mixing Ni and Fe oxyhydroxydes. *Chem Commun*. 2019;55:818-821. doi:10.1039/c8cc06410e

186. Landon J, Demeter E, Inoğlu N, et al. Spectroscopic characterization of mixed Fe-Ni oxide electrocatalysts for the oxygen evolution reaction in alkaline electrolytes. *ACS Catal*. 2012;2(8):1793-1801. doi:10.1021/cs3002644

187. Stevens MB, Trang CDM, Enman LJ, Deng J, Boettcher SW. Reactive Fe-Sites in Ni/Fe

(Oxy)hydroxide Are Responsible for Exceptional Oxygen Electrocatalysis Activity. Published online 2017:8-11. doi:10.1021/jacs.7b07117

188. Liang C, Zou P, Nairan A, et al. Exceptional performance of hierarchical Ni-Fe oxyhydroxide@NiFe alloy nanowire array electrocatalysts for large current density water splitting. *Energy Environ Sci*. 2020;13(1):86-95. doi:10.1039/c9ee02388g

189. Qiu Y, Xin L, Li W. Electrocatalytic Oxygen Evolution over Supported Small Amorphous Ni−Fe Nanoparticles in Alkaline Electrolyte. *ACS Pub*. 2014;30:7893. doi:10.1021/la501246e

190. Suryanto BHR, Wang Y, Hocking RK, Adamson W, Zhao C. Overall electrochemical splitting of water at the heterogeneous interface of nickel and iron oxide. *Nat Commun*. 2019;10(1):1-10. doi:10.1038/s41467-019-13415-8

191. Li D, Liu H, Feng L. A Review on Advanced FeNi-Based Catalysts for Water Splitting Reaction. *Energy and Fuels*. 2020;34(11):13491-13522. doi:10.1021/acs.energyfuels.0c03084

192. Balamurugan J, Nguyen TT, Kim DH, Kim NH, Lee JH. 3D nickel molybdenum oxyselenide (Ni1-xMoxOSe) nanoarchitectures as advanced multifunctional catalyst for Zn-air batteries and water splitting. *Appl Catal B Environ*. 2021;286(January):119909. doi:10.1016/j.apcatb.2021.119909

193. Premnath K, Arunachalam P, Amer MS, Madhavan J, Al-Mayouf AM. Hydrothermally synthesized nickel molybdenum selenide composites as cost-effective and efficient trifunctional electrocatalysts for water splitting reactions. *Int J Hydrogen Energy*. 2019;44(41):22796-22805. doi:10.1016/j.ijhydene.2019.07.034

194. Jia J, Zhai M, Lv J, Zhao B, Du H, Zhu J. Nickel Molybdenum Nitride Nanorods Grown on Ni Foam as Efficient and Stable Bifunctional Electrocatalysts for Overall Water Splitting. *ACS Appl Mater Interfaces*. 2018;10(36):30400-30408. doi:10.1021/acsami.8b09854

195. Kong F, Sun L, Huo L, Zhao H. In-situ electrochemical self-tuning of amorphous nickel molybdenum phosphate to crystal Ni-rich compound for enhanced overall water splitting. *J Power Sources*. 2019;430:218-227. doi:10.1016/j.jpowsour.2019.05.037

196. Wu Y, He H. Electrodeposited nickel–iron–carbon–molybdenum film as efficient bifunctional electrocatalyst for overall water splitting in alkaline solution. *Int J Hydrogen Energy*. 2019;44(3):1336-1344. doi:10.1016/j.ijhydene.2018.11.168

197. Schalenbach M, Kasian O, Mayrhofer KJJ. An alkaline water electrolyzer with nickel electrodes enables efficient high current density operation. *Int J Hydrog Energy*. Published online 2018:1-7. doi:10.1016/j.ijhydene.2018.04.219

198. Braesch G. Electrocatalyseurs pour la Réaction d'Oxydation des Borohydrures : des surfaces modèles aux électrodes non-nobles de piles à combustible. Published online 2020. http://www.theses.fr/2020GRALI059/document

199. KOCH, Theodore A, MEHDIZADEH M, ASHMEAD, James W, BLACKWELL, Benny E, KIRBY, Gregory S, SENGUPTA, Sourav K. Inductively Heated Catalytic Reactor. Published online 1999. https://patentscope.wipo.int/search/en/detail.jsf?docId=WO1999001212

200. Ovenston A, Walls JR. Generation of heat in a single catalyst pellet placed in an electromagnetic field for endothermic reforming of hydrocarbons. *J Chem Soc Faraday Trans 1 Phys Chem Condens Phases*. 1983;79(5):1073-1084.

doi:10.1039/F19837901073

201. Rashid MM, Mesfer MK Al, Naseem H, Danish M. Hydrogen Production by Water Electrolysis: A Review of Alkaline Water Electrolysis, PEM Water Electrolysis and High Temperature Water Electrolysis. *Int J Eng Adv Technol*. 2015;4(3):2249-8958.

202. Schalenbach M, Tjarks G, Carmo M, Lueke W, Mueller M, Stolten D. Acidic or Alkaline? Towards a New Perspective on the Efficiency of Water Electrolysis. *J Electrochem Soc*. 2016;163(11):F3197-F3208. doi:10.1149/2.0271611jes

203. Gatard V, Masi D De, Chattot R, et al. FeNi3 and Ni-Based Nanoparticles as Electrocatalysts for Magnetically Enhanced Alkaline Water Electrolysis. *Electrocatalysis*. 2020;11(5):567-577. doi:10.1007/s12678-020-00616-9

204. Chattot R, Bacq O Le, Beermann V, et al. Surface distortion as a unifying concept and descriptor in oxygen reduction reaction electrocatalysis. *Nat Mater*. 2018;17:827-833. doi:10.1038/s41563-018-0133-2

205. Cognard G, Ozouf G, Beauger C, et al. Benefits and limitations of Pt nanoparticles supported on highly porous antimony-doped tin dioxide aerogel as alternative cathode material for proton-exchange membrane fuel cells. *Appl Catal B Environ*. 2017;201:381-390. doi:10.1016/j.apcatb.2016.08.010

206. Cherevko S, Zeradjanin AR, Keeley GP, Mayrhofer KJJ. A Comparative Study on Gold and Platinum Dissolution in Acidic and Alkaline Media. *J Electrochem Soc*. 2014;161(12):H822--H830. doi:10.1149/2.0881412jes

207. Zadick A, Dubau L, Sergent N. Huge Instability of Pt/C Catalysts in Alkaline Medium. *ACS Cat*. 2015;5:4819-4824. doi:10.1021/acscatal.5b01037

208. Herrmann CC, Perrault GG, Pilla AA. Dual Reference Electrode for Electrochemical Pulse Studies. *Anal Chem*. 1968;40(7):1173-1174. doi:10.1021/ac60263a011

209. Clavilier J, Faure R, Guinet G, Durand R. Preparation of monocrystalline Pt microelectrodes and electrochemical study of the plane surfaces cut in the direction of the {111} and {110} planes. *J Electroanal Chem Interfacial Electrochem*. 1980;107(1):205-209. doi:10.1016/S0022-0728(79)80022-4

210. Mayrhofer KJJ, Crampton AS, Wiberg GKH, Arenz M. Analysis of the Impact of Individual Glass Constituents on Electrocatalysis on Pt Electrodes in Alkaline Solution. *J Electrochem Soc*. 2008;155(6):P78. doi:10.1149/1.2904882

211. Garsany Y, Baturina OA, Swider-Lyons KE, Kocha SS. Experimental methods for quantifying the activity of platinum electrocatalysts for the oxygen reduction reaction. *Anal Chem*. 2010;82(15):6321-6328. doi:10.1021/ac100306c

212. Chlistunoff J, Sansiñena JM. On the use of Nafion® in electrochemical studies of carbon supported oxygen reduction catalysts in aqueous media. *J Electroanal Chem*. 2016;780:134-146. doi:10.1016/j.jelechem.2016.09.014

213. Alia SM, Anderson GC. Iridium Oxygen Evolution Activity and Durability Baselines in Rotating Disk Electrode Half-Cells. *J Electrochem Soc*. 2019;166(4):F282-F294. doi:10.1149/2.0731904jes

214. Curnick OJ, Pollet BG, Mendes PM. Nafion®-stabilised Pt/C electrocatalysts with efficient catalyst layer ionomer distribution for proton exchange membrane fuel cells. *RSC Adv*. 2012;2(22):8368-8374. doi:10.1039/c2ra21071a

215. Sasikumar G, Ihm JW, Ryu H. Dependence of optimum Nafion content in catalyst layer

on platinum loading. *J Power Sources*. 2004;132(1):11-17. doi:10.1016/j.jpowsour.2003.12.060

216. Xu W, Scott K. The effects of ionomer content on PEM water electrolyser membrane electrode assembly performance. *Int J Hydrogen Energy*. 2010;35(21):12029-12037. doi:10.1016/j.ijhydene.2010.08.055

217. Sapountzi FM, Divane SC, Papaioannou EI, Souentie S, Vayenas CG. The role of Nafion content in sputtered IrO2 based anodes for low temperature PEM water electrolysis. *J Electroanal Chem*. 2011;662(1):116-122. doi:10.1016/j.jelechem.2011.04.005

218. Garsany Y, Singer IL, Swider-lyons KE. Impact of film drying procedures on RDE characterization of Pt/VC electrocatalysts. *J Electroanal Chem*. 2011;662(2):396-406. doi:10.1016/j.jelechem.2011.09.016

219. Wendt H, Garsany Y, Ge J, St-Pierre J, Rocheleau R, Swider-Lyons KE. Standardizing Thin-Film Rotating Disk Electrode Measurements of the Oxygen Reduction Activity of Pt/C. *ECS Trans*. 2013;58(1):3-14. doi:10.1149/05801.0003ecst

220. Garsany Y, Ge J, St-pierre J, Rocheleau R. Analytical Procedure for Accurate Comparison of Rotating Disk Electrode Results for the Oxygen Reduction Activity of Pt/C. *J Electrochem Soc*. 2014;161(5):628-640. doi:10.1149/2.036405jes

221. Pollet BG, Goh JTE. The importance of ultrasonic parameters in the preparation of fuel cell catalyst inks. *Electrochim Acta*. 2014;128:292-303. doi:10.1016/j.electacta.2013.09.160

222. Pollet BG. Let's Not Ignore the Ultrasonic Effects on the Preparation of Fuel Cell Materials. *Electrocatalysis*. 2014;5:330-343. doi:10.1007/s12678-014-0211-4

223. Bolt GH. Analysis of the validity of the Gouy-Chapman theory of the electric double layer. *J Colloid Sci*. 1955;10(2):206-218. doi:10.1016/0095-8522(55)90027-1

224. Alsabet M, Grdeń M, Jerkiewicz G. Electrochemical Growth of Surface Oxides on Nickel. Part 3: Formation of β-NiOOH in Relation to the Polarization Potential, Polarization Time, and Temperature. *Electrocatalysis*. 2015;6(1):60-71. doi:10.1007/s12678-014-0214-1

225. Trasatti S, Petrii OA. Real surface area measurements in electrochemistry. *J Electroanal Chem*. 1992;327(1-2):353-376. issn: 1572-6657

226. Cuesta A, Couto A, Rincon A, Pérez MC, Lopez-Cudero A, Gutiérrez C. Potential dependence of the saturation CO coverage of Pt electrodes: The origin of the pre-peak in CO-stripping voltammograms. Part 3: Pt (poly). *J Electroanal Chem*. 2006;586(2):184-195. doi:https://doi.org/10.1016/j.jelechem.2005.10.006

227. Beden B, Floner D, Leger JM, Lamy C. A voltammetric study of the formation on hydroxides and oxyhydroxides on nickel single crystal electrodes in contact with an alkaline solution. *Surf Sci*. 1985;162(1-3):822-829. doi:10.1016/0039-6028(85)90985-9

228. Machado SAS, Avaca LA. The hydrogen evolution reaction on nickel surfaces stabilized by H-absorption. *Electrochim Acta*. 1994;39(10):1385-1391. doi:10.1016/0013-4686(94)E0003-I

229. Oshchepkov AG, Braesch G, Bonnefont A, Savinova ER, Chatenet M. Recent Advances in the Understanding of Nickel-Based Catalysts for the Oxidation of Hydrogen-Containing Fuels in Alkaline Media. *ACS Catal*. 2020;10(13):7043-7068. doi:10.1021/acscatal.0c00101

230. Grdeń M, Alsabet M, Jerkiewicz G. Surface science and electrochemical analysis of nickel foams. *ACS Appl Mater Interfaces*. 2012;4(6):3012-3021. doi:10.1021/am300380m

231. Mccrory CCL, Jung S, Peters JC, Jaramillo TF. Benchmarking Heterogeneous Electrocatalysts for the Oxygen Evolution Reaction. *J Am Chem Soc*. 2013;135:16977-16987. doi:10.1021/ja407115p

232. Watzele S, Hauenstein P, Liang Y, et al. Determination of Electroactive Surface Area of Ni-, Co-, Fe-, and Ir-Based Oxide Electrocatalysts. *ACS Catal*. 2019;9(10):9222-9230. doi:10.1021/acscatal.9b02006

233. Hall DS, Bock C, MacDougall BR. An Oxalate Method for Measuring the Surface Area of Nickel Electrodes. *J Electrochem Soc*. 2014;161(12):H787-H795. doi:10.1149/2.0711412jes

234. Ho JCK, Piron DL. Active surface area in oxide electrodes by overpotential deposited oxygen species for the oxygen evolution reaction. *J Appl Electrochem*. 1996;26(5):515-521. doi:10.1007/BF01021975

235. Lyons MEG, Brandon MP. The oxygen evolution reaction on passive oxide covered transition metal electrodes in alkaline solution part ii - cobalt. *Int J Electrochem Sci*. 2008;3(12):1425-1462.

236. Gasteiger HA, Kocha SS, Sompalli B, Wagner FT. Activity benchmarks and requirements for Pt, Pt-alloy, and non-Pt oxygen reduction catalysts for PEMFCs. *Appl Catal B Environ*. 2005;56(1-2 SPEC. ISS.):9-35. doi:10.1016/j.apcatb.2004.06.021

237. El-sayed HA, Weiß A, Olbrich LF, Putro GP, Gasteiger HA. OER Catalyst Stability

Investigation Using RDE Technique: A Stability Measure or an Artifact ? *J Electrochem Soc*. 2019;166(8):458-464. doi:10.1149/2.0301908jes

238. Matsumoto Y, Sato E. Electrocatalytic properties of transition metal oxides for oxygen evolution reaction. *Mater Chem Phys*. 1986;14(5):397-426. doi:10.1016/0254-0584(86)90045-3

239. Lefrou C, Fabry P, Poignet J-C. *Electrochimie (Concepts Fondamentaux Illustrés): Concepts Fondamentaux Illustrés*. EDP sciences; 2013. https://books.google.fr/books?hl=fr&lr=&id=UcQ2AAAAQBAJ&oi=fnd&pg=PR5&dq=electrochimie+concepts+fondamentaux+illustrés&ots=Phh0Ac-WFp&sig=9qjZc2TsKwKVVgr1fFAKPEcQDxI#v=onepage&q=electrochimie concepts fondamentaux illustrés&f=false

240. Oshchepkov AG, Bonnefont A, Parmon VN, Savinova ER. On the effect of temperature and surface oxidation on the kinetics of hydrogen electrode reactions on nickel in alkaline media. *Electrochim Acta*. 2018;269:111-118. doi:10.1016/j.electacta.2018.02.106

241. Fang Y, Liu Z. Tafel Kinetics of Electrocatalytic Reactions: From Experiment to First-Principles. *ACS Catal*. 2014;4:4364-4376. doi:10.1021/cs501312v

242. Spöri C, Kwan JTH, Bonakdarpour A, Wilkinson DP, Strasser P. The Stability Challenges of Oxygen Evolving Catalysts: Towards a Common Fundamental Understanding and Mitigation of Catalyst Degradation. *Angew Chemie - Int Ed*. 2017;56(22):5994-6021. doi:10.1002/anie.201608601

243. Durst J, Simon C, Hasché F, Gasteiger HA. Hydrogen Oxidation and Evolution Reaction Kinetics on Carbon Supported Pt, Ir, Rh, and Pd Electrocatalysts in Acidic Media. *J*

Electrochem Soc. 2015;162(1):F190-F203. doi:10.1149/2.0981501jes

244. Sievers GW, Jensen AW, Brüser V, Arenz M, Escudero-Escribano M. Sputtered Platinum Thin-films for Oxygen Reduction in Gas Diffusion Electrodes: A Model System for Studies under Realistic Reaction Conditions. *Surfaces*. 2019;2(2):336-348. doi:10.3390/surfaces2020025

245. Inaba M, Jensen AW, Sievers GW, Escudero-Escribano M, Zana A, Arenz M. Benchmarking high surface area electrocatalysts in a gas diffusion electrode: Measurement of oxygen reduction activities under realistic conditions. *Energy Environ Sci*. 2018;11(4):988-994. doi:10.1039/c8ee00019k

246. Lin X, Zalitis CM, Sharman J, Kucernak A. Electrocatalyst Performance at the Gas/Electrolyte Interface under High-Mass-Transport Conditions: Optimization of the "floating Electrode" Method. *ACS Appl Mater Interfaces*. 2020;12(42):47467-47481. doi:10.1021/acsami.0c12718

247. Chaudret B, Carrey J, Faure S, et al. *Rapport Confidentiel Final Science & Tec, LEPMI, LPCNO, LEAF Preuve de Concept de l'intensification de l'électrolyse de l'eau Par Hyperthermie En Milieu Alcalin*.; 2016.

248. RUSTE J. Microscopie électronique à balayage Images, applications et développements. *Tech l'ingénieur Tech d'analyse par Imag*. 2013;base docum(ref. article : p866). https://www.techniques-ingenieur.fr/base-documentaire/mesures-analyses-th1/techniques-d-analyse-par-imagerie-42387210/microscopie-electronique-a-balayage-p866/

249. Sarigiannidou E, Pignard S. *Techniques de Caractérisation à Sonde Électronique (Cours Interne PHELMA)*.; 2017.

250. KARLÍK M, JOUFFREY B. Étude des métaux par microscopie électronique en transmission (MET) Formation des images. *Tech l'ingénieur Essais métallographiques des métaux alliages*. 2008;base docum(ref. article : m4135). https://www.techniques-ingenieur.fr/base-documentaire/materiaux-th11/essais-metallographiques-des-metaux-et-alliages-42343210/etude-des-metaux-par-microscopie-electronique-en-transmission-met-m4135/

251. Schlögl K, Mayrhofer KJJ, Hanzlik M, Arenz M. Identical-location TEM investigations of Pt/C electrocatalyst degradation at elevated temperatures. *J Electroanal Chem*. 2011;662(2):355-360. doi:10.1016/j.jelechem.2011.09.003

252. Claudel F. Vers le développement d'électrocatalyseurs de dégagement d'oxygène actifs et stables. Published online 2019. http://www.theses.fr/2019GREAI052/document

253. MERMET J-M. Systèmes dispersifs en spectrométrie atomique. *Tech l'ingénieur Fondam l'optique*. 2002;base docum(ref. article : p2660). https://www.techniques-ingenieur.fr/base-documentaire/electronique-photonique-th13/fondamentaux-de-l-optique-42448210/systemes-dispersifs-en-spectrometrie-atomique-p2660/

254. Wildeboer RR, Southern P, Pankhurst QA. On the reliable measurement of specific absorption rates and intrinsic loss parameters in magnetic hyperthermia materials. *J Phys D Appl Phys*. 2014;47(49). doi:10.1088/0022-3727/47/49/495003

255. Jiles DC. Modelling the effects of eddy current losses on frequency dependent hysteresis in electrically conducting media. *IEEE Trans Magn*. 1994;30(6):4326-4328. doi:10.1109/20.334076

256. Connord V, Mehdaoui B, Tan RP, et al. An air-cooled Litz wire coil for measuring the high frequency hysteresis loops of magnetic samples — A useful setup for magnetic

hyperthermia applications An air-cooled Litz wire coil for measuring the high frequency hysteresis loops of magnetic samples —. 2014;093904. doi:10.1063/1.4895656

257. Cognard G. Electrocatalyseurs à base d'oxydes métalliques poreux pour pile à combustible à membrane échangeuse de protons. Published online 2017. http://www.theses.fr/2017GREAI007

258. Claudel F. Degradation Mechanisms of Oxygen Evolution Reaction Electrocatalysts: A Combined Identical-Location Transmission Electron Microscopy and X-ray Photoelectron Spectroscopy Study. *ACS Catal*. 2019;9:4688-4698. doi:10.1021/acscatal.9b00280

259. Cherevko S, Geiger S, Kasian O, et al. Oxygen and hydrogen evolution reactions on Ru, RuO2, Ir, and IrO2 thin film electrodes in acidic and alkaline electrolytes: A comparative study on activity and stability. *Catal Today*. 2016;262:170-180. doi:10.1016/j.cattod.2015.08.014

260. Schalenbach M, Kasian O, Ledenecker M, et al. The Electrochemical Dissolution of Noble Metals in Alkaline Media. *Electrocatalysis*. 2018;9:153-161. doi:10.1007/s12678-017-0438-y

261. Kasian O, Geiger S, Schalenbach M, et al. Using Instability of a Non-stoichiometric Mixed Oxide Oxygen Evolution Catalyst As a Tool to Improve Its Electrocatalytic Performance. *Electrocatalysis*. 2018;9:139-145. doi:10.1007/s12678-017-0394-6

262. Ferreira EB, Jerkiewicz G. On the Electrochemical Reduction of β-Ni (OH) 2 to Metallic Nickel. *Electrocatalysis*. 2021;12(2):199-209. doi:10.1007/s12678-021-00643-0v

263. Oshchepkov AG, Bonnefont A, Saveleva VA. Exploring the Influence of the Nickel

Oxide Species on the Kinetics of Hydrogen Electrode Reactions in Alkaline Media. *Top Catal*. 2016;59(15):1319-1331. doi:10.1007/s11244-016-0657-0

264. Moureaux F. Etude des réactions mettant en jeu l'oxygène dans un système électrochimique lithium-air aqueux rechargeable électriquement. Published online 2011. http://www.theses.fr/2011GRENI061/document

265. Pozio A, De Francesco M, Cemmi A, Cardellini F, Giorgi L. Comparison of high surface Pt/C catalysts by cyclic voltammetry. *J Power Sources*. 2002;105(1):13-19. doi:10.1016/S0378-7753(01)00921-1

266. Wang J, Chen Y, Zhang Y, et al. 3D boron doped carbon nanorods/carbon-microfiber hybrid composites: Synthesis and applications in a highly stable proton exchange membrane fuel cell. *J Mater Chem*. 2011;21(45):18195-18198. doi:10.1039/c1jm13796d

267. Lafforgue C. Activity and degradation mechanisms of anodic electrocatalysts for the direct borohydride fuel cell. Published online 2019. https://hal.archives-ouvertes.fr/tel-02441645v1

268. Boettcher SW, Oener SZ, Lonergan MC, et al. Potentially Confusing: Potentials in Electrochemistry. *ACS Energy Lett*. 2021;6(1):261-266. doi:10.1021/acsenergylett.0c02443

269. Bockris JOM, Khan SUM. Comment on "Fermi levels in electrolytes and the absolute scale of redox potentials." *Appl Phys Lett*. 1984;45(8):913. doi:10.1063/1.95412

270. Light BS, Zepeda-Rosales M, Li Y, Safinya CR. Forced Crowding of Colloids by Thermophoresis and Convection in a Custom Liquid Clusius-Dickel Microdevice.

Langmuir. 2021;37(2):675-682. doi:10.1021/acs.langmuir.0c02721

271. Lubetkin S. The motion of electrolytic gas bubbles near electrodes. *Electrochim Acta*. 2002;48(4):357-375. doi:10.1016/S0013-4686(02)00682-5

272. Dunne P, Coey JMD. Influence of a Magnetic Field on the Electrochemical Double Layer. *J Phys Chem C*. 2019;123(39):24181-24192. doi:10.1021/acs.jpcc.9b07534

273. Zhang Y, Liang C, Wu J, et al. Recent advances in magnetic field-enhanced electrocatalysis. *ACS Appl Energy Mater*. 2020;3(11):10303-10316. doi:10.1021/acsaem.0c02104

274. Fujimura Y, Iino M. Magnetic field increases the surface tension of water. *J Phys Conf Ser*. 2009;156. doi:10.1088/1742-6596/156/1/012028

275. Hayakawa M, Vialetto J, Anyfantakis M, et al. Effect of moderate magnetic fields on the surface tension of aqueous liquids: A reliable assessment. *RSC Adv*. 2019;9(18):10030-10033. doi:10.1039/c9ra00849g

276. McNab GS, Meisen A. Thermophoresis in liquids. *J Colloid Interface Sci*. 1973;44(2):339-346. doi:10.1016/0021-9797(73)90225-7

277. Fahidy TZ. The Effect of Magnetic Fields on Electrochemical Processes BT - Modern Aspects of Electrochemistry. In: Conway BE, Bockris JO, White RE, eds. Springer US; 2002:333-354. doi:10.1007/0-306-46916-2_5

278. Devos O, Aaboubi O, Chopart J, et al. Is There a Magnetic Field Effect on Electrochemical Kinetics? *J Phys Chem A*. 2000;104(1):1544-1548. doi:10.1021/jp993696v

279. Hitchcock B, McIlhenny JS. Viscosity and Density of Pure Alkaline Solutions and Their Mixtures. *Ind Eng Chem*. 1935;27(4):461-466. doi:10.1021/ie50304a027

280. Gilliam RJ, Graydon JW, Kirk DW, Thorpe SJ. A review of specific conductivities of potassium hydroxide solutions for various concentrations and temperatures. *Int J Hydrogen Energy*. 2007;32:359-364. doi:10.1016/j.ijhydene.2006.10.062

281. Monzon LMA, Coey JMD. Magnetic fields in electrochemistry: The Kelvin force: a mini-review. *Electrochem Commun*. 2014;42:42-45. doi:10.1016/j.elecom.2014.02.005

282. Alberti G, Narducci R, Di Vona ML, Giancola S. Annealing of nafion 1100 in the presence of an annealing agent: A powerful method for increasing ionomer working temperature in PEMFCs. *Fuel Cells*. 2013;13(1):42-47. doi:https://doi.org/10.1002/fuce.201200126

283. Suntivich J, Gasteiger HA, Yabuuchi N, Shao-Horn Y. Electrocatalytic Measurement Methodology of Oxide Catalysts Using a Thin-Film Rotating Disk Electrode. *J Electrochem Soc*. 2010;157(8):B1263. doi:10.1149/1.3456630

284. Rodriguez P, Tichelaar FD, Koper MTM, Yanson AI. Cathodic corrosion as a facile and effective method to prepare clean metal alloy nanoparticles. *J Am Chem Soc*. 2011;133(44):17626-17629. doi:10.1021/ja208264e

285. Yanson AI, Rodriguez P, Garcia-Araez N, Mom R V., Tichelaar FD, Koper MTM. Cathodic corrosion: A quick, clean, and versatile method for the synthesis of metallic nanoparticles. *Angew Chemie - Int Ed*. 2011;50(28):6346-6350. doi:10.1002/anie.201100471

286. Swartzendruber LJ, Itkin VP, Alcock CB. The Fe-Ni (Iron-Nickel) System. *J Phase*

Equilibria. 1991;12(3):288-312. https://link-springer-com.gaelnomade-2.grenet.fr/content/pdf/10.1007/BF02649918.pdf

287. Yanai T, Tanaka R, Ueno R, et al. Magnetic properties of Fe-Ni-system films prepared by electroless deposition. *AIP Adv*. 2020;10(1). doi:10.1063/1.5130446

288. Kollie TG. Measurement of the thermal-expansion coefficient of Nickel from 300 to 1000 K and determination of the power-law constants near the Curie temperature. *Phys Rev B*. 1977;16:4872-4882. doi:10.1103/PhysRevB.16.4872

289. Hidnert P. Thermal Expansion of Some Nickel Alloys. *J Res Natl Bur Stand (1934)*. 1957;58(2):89-92. https://books.google.fr/books?hl=fr&lr=&id=o_ca19qBas8C&oi=fnd&pg=PA89&dq=Thermal+Expansion+of+Some+Nickel+Alloys&ots=wQlp-_FoNh&sig=v_a-lpV1xDOeMwHNSu1gYAA48ZI#v=onepage&q=Thermal Expansion of Some Nickel Alloys&f=false

290. Yousuf M, Sahu PC, H K J, Rajagopalan R, Govinda Rajan K. Metal Physics Related content Effect of magnetic transition on the lattice expansion of nickel Effect of magnetic transition on the lattice expansion of nickel. *J Phys F Met Phys*. 1986;16:373-380. doi:10.1088/0305-4608/16/3/015

291. Nix FC, Macnair D. The Thermal Expansion of Pure Metals: Copper, Gold, Aluminum, Nickel, and Iron. *Phys Rev*. 1941;10(1926). doi:10.1103/PhysRev.60.597

292. Owen EA, Yates EL. An X-ray investigation of pure iron-nickel alloys. Part 1: thermal expansion of alloys rich in nickel. *Proceeding Phys Soc*. 1937;49:17-28. doi:10.1088/0959-5309/49/1/305

293. Owen EA, Yates EL. An X-ray investigation of pure iron-nickel alloys. Part 2: Thermal expansion of some further alloys. *Proc Phys Soc*. 1937;49(2):178-188. doi:10.1088/0959-5309/49/2/309

294. Owen EA, Yates EL. An X-ray investigation of pure iron-nickel alloys. Part 3: The thermal expansion of alloys rich in Fe. *Proc Phys Soc*. 1937;49(3):307-314. doi:10.1088/0959-5309/49/3/312

295. Owen EA, Yates EL, Sully AH. An X-ray investigation of pure iron-nickel alloys. Part 4: The variation of lattice-parameter with composition. *Proc Phys Soc*. 1937;49(3):315-322. doi:10.1088/0959-5309/49/3/314

296. Owen EA, Yates EL. An X-ray investigation of pure iron-nickel alloys. Part 5: the variation of thermal expansion with composition. *Proc Phys Soc*. 1937;49:323-325. doi:10.1088/0959-5309/49/3/314

297. Mckeehan LW. The Crystal Structure of Iron-Nickel Alloys. *Phys Rev*. 1923;21(4):402-407. doi:https://doi-org.gaelnomade-2.grenet.fr/10.1103/PhysRev.21.402

298. Peck MA, Langell MA. Comparison of Nanoscaled and Bulk NiO Structural and Environmental Characteristics by XRD, XAFS, and XPS. *Chem Mater*. 2012;24:4483-4490. doi:dx.doi.org/10.1021/cm300739y

299. Nadeem K, Ullah A, Mushtaq M, Kamran M, Hussain SS, Mumtaz M. Effect of air annealing on structural and magnetic properties of Ni/NiO nanoparticles. *J Magn Magn Mater*. 2016;417:6-10. doi:10.1016/j.jmmm.2016.05.064

300. Smigelskas AD, Kirkendall E. Zinc diffusion in Alpha Brass. *Trans AIME*. 1947;171:130-142.

301. Liu Z, Yu H, Dong B, Yu X, Feng L. Electrochemical oxygen evolution reaction efficiently boosted by thermal-driving core-shell structure formation in nanostructured FeNi/S, N-doped carbon hybrid catalyst. *Nanoscale*. 2018;10(35):16911-16918. doi:10.1039/c8nr05587d

302. Ugaste Ü, Kodentsov AA, Van Loo FJJ. Interdiffusion and Kirkendall-effect in the Fe-Ni-Cu system. *Solid State Phenom*. 2000;72(January 2000):117-122. doi:10.4028/www.scientific.net/ssp.72.117

303. Faure S, Kale SS, Mille N, et al. Improving energy efficiency of magnetic CO2 methanation by modifying coil design, heating agents, and by using eddy currents as the complementary heating source. *J Appl Phys*. 2021;129(4). doi:10.1063/5.0035655

304. Faure S, Mille N, Kale SS, et al. Internal Temperature Measurements by X-Ray Diffraction on Magnetic Nanoparticles Heated by a High-Frequency Magnetic Field. *J Phys Chem C*. 2020;124(40):22259-22265. doi:10.1021/acs.jpcc.0c03350

305. Gubin SP, Koksharov YA, Khomutov GB, Yurkov GY. Magnetic nanoparticles: Preparation, structure and properties. *Usp Khim*. 2005;74(6):539-574. doi:10.1070/rc2005v074n06abeh000897

306. Cullity BD, Graham CD. *Introduction to Magnetic Materials*. Vol 111. (Wiley, ed.). IEEE Press; 2009. doi:10.1021/cr2001349

307. Pauling L. *General Chemistry*. A Series o. Freeman, W. H.; 1970.

308. Taylor AK, Andreu I, Gates BD. Regular Dimpled Nickel Surfaces for Improved Efficiency of the Oxygen Evolution Reaction. *ACS Appl Energy Mater*. 2018;1(4):1771-1782. doi:10.1021/acsaem.8b00338

309. Serrano J, Acero J, Lope I, Carretero C, Burdio JM. A flexible cooking zone composed of partially overlapped inductors. *IEEE Trans Ind Electron*. 2018;65(10):7762-7771. doi:10.1109/TIE.2018.2801815

Résumé de la thèse en français

Résumé de l'introduction : L'introduction s'ouvre sur le contexte actuel de crise écologique mondiale [8,9] et propose l'utilisation du dihydrogène comme source d'énergie renouvelable - une solution parmi d'autres [27]. L'accent est mis sur les méthodes actuelles de production d'hydrogène, et des voies « vertes » sont illustrées : les électrolyseurs en milieu acide et basique [35]. Quelques notions thermodynamiques et cinétiques sur l'électrolyse de l'eau sont également abordées [34,39]. Puis, une méthode pour réduire l'énergie nécessaire à la réalisation de l'électrolyse de l'eau est proposée : l'utilisation d'un champ magnétique alternatif permettant de chauffer des nanoparticules à une échelle très locale grâce au phénomène de pertes par hystérésis [60]. Ce principe ainsi que quelques-unes de ses applications sont introduites [58,59,60].

Résumé du chapitre I : Dans la suite de ce chapitre bibliographique sont présentés différents effets provoqués par l'application d'un champ magnétique (le plus souvent statique) sur des systèmes électrochimiques [84,86,281]. D'abord, la force de Lorentz, bien connue, qui augmente les courants limites des réactions étudiées (effet magnétohydrodynamique) et induit différents profils dans les électrodépôts, selon l'orientation du champ magnétique, parallèle ou perpendiculaire à la surface de l'électrode de travail. Ensuite, l'effet Kelvin est présenté. Il agit sur les espèces chimiques présentant une forte susceptibilité magnétique : les espèces paramagnétiques sont attirées vers les régions de fort gradient de champ tandis que les espèces diamagnétiques sont repoussées vers les régions de faible gradient de champ. L'effet de polarisation de spin est ensuite introduit. Il survient avec des matériaux ferromagnétiques ou chiraux, et permettrait d'améliorer le transfert d'électrons lors de processus électrochimiques. Enfin, l'utilisation d'un champ magnétique alternatif (AMF) en électrochimie dans la littérature

est rapportée. Un large éventail d'effets est présenté, ne concernant pas tous ce travail. Néanmoins, cela fournit un aperçu relativement exhaustif des effets observés dans la littérature.

Résumé du chapitre II : Le chapitre II développe le choix des matériaux utilisés ainsi que leurs synthèses [171,172,173], et détaille toutes les techniques utilisées pour les caractérisations électrochimiques, physicochimiques, et magnétiques. Notamment, des notions électrochimiques telles que l'interface de double couche au niveau d'une électrode, la nature des courants capacitif ou Faradique selon les phénomènes qui surviennent aux interfaces, les étapes élémentaires reconnues pour les réactions HER et OER et l'analyse de type Tafel sont abordées.

Résumé du chapitre III : L'activité intrinsèque des matériaux par rapport aux réactions HER et OER est étudiée dans un montage en électrode à disque tournant (RDE). Des catalyseurs plus actifs que celui utilisé au début de ce projet (FeC-Ni) ont été obtenus. L'influence du chargement du matériau dans l'encre est évaluée, et montre une limite du système RDE (couche catalytique épaisse préjudiciable à l'activité) [203]. Des mesures de durabilité montrent que les matériaux les plus actifs [$FeNi_3$(@Ni) et Ni_{HI}] sont dégradés, notamment par détachement de la couche active et dissolution de Fe. Ensuite, les performances des matériaux sont évaluées dans la cellule conçue pour les mesures sous AMF. Ces dernières changent par rapport aux mesures en RDE car les conditions de travail sont différentes (flux d'électrolyte, support d'électrode différent). Toutefois, les catalyseurs $FeNi_3$(@Ni) restent parmi les matériaux les plus actifs. Une nouvelle étude du chargement indique que plus l'encre est chargée, meilleure est l'activité (plus de sites actifs). Enfin, des caractérisations magnétiques montrent que les NPs $FeNi_3$(@Ni) chauffent (SAR élevé), les catalyseurs à base de Ni beaucoup moins, et les autres ne chauffent pas (Pt/C, IrO_2 et $FeNi_3$@Mo).

Résumé du Chapitre IV : Ce chapitre présente des tests de cycles voltampérométriques (CV_F) et chronopotentiométriques (CP) sous AMF. Le champ améliore les performances de tous les catalyseurs, en diminuant le potentiel de départ (CV_F) et en diminuant la surtension (CP), que ce soit en HER ou en OER, et quel que soit le chargement de l'encre. Etonnamment, même les matériaux qui présentaient un SAR faible ou nul sont améliorés. Il est ainsi déduit que les courants de Foucault jouent un rôle non négligeable, bien que tout a été mis en œuvre pour les minimiser. Des mesures de chauffe confirment leur présence. Ensuite, des discussions sont menées pour comprendre comment l'AMF améliore les performances. Il semble que le transport de matière soit particulièrement facilité côté HER, et que la cinétique de transfert d'électrons soit améliorée côté OER, les deux effets étant toujours présents. Puis, les phénomènes pouvant survenir sous champ magnétique statique (SMF) et abordés au Chapitre I section I.4 sont évalués, ainsi que les effets Soret, Marangoni et Maxwell (gradient de température, variation de tension de surface). Seuls ces trois derniers effets, ainsi que la force de Kelvin, pourraient intervenir dans le système. Enfin, des analyses *post mortem* sont présentées. Une étude en localisation identique avec un microscope électronique à balayage (ILSEM) montre qu'aucune agrégation survient, et que les agglomérats sont mal répartis sur le feutre. Des mesures XRD et ETEM en température (jusqu'à 600°C) et sous atmosphères réductrice (H_2) et oxydante (O_2) sur $FeNi_3$@Ni montrent que les phases cristallographiques de ce matériau évoluent, ce qui peut modifier sa réactivité par rapport à l'électrolyse de l'eau.

Cette thèse s'inscrit dans le projet Hy-WalHy (ANR-1-CE05-0017), dont le but est d'améliorer l'électrolyse de l'eau en milieu alcalin par une approche innovante : l'utilisation d'un champ magnétique alternatif pour chauffer localement et catalyser ainsi la réaction. Ce projet a eu pour objectif de trouver des matériaux meilleurs catalyseurs et agents chauffants que ceux précédemment utilisés, et de comprendre les mécanismes d'amélioration de l'électrolyse de l'eau sous champ magnétique alternatif (AMF). Pour cela, le travail a été divisé en trois

points : (i) une première partie expérimentale (chapitre III) a permis de tester l'activité et la stabilité de nouveaux matériaux dans deux cellules électrochimiques différentes : la première présentant des conditions « idéales », la seconde correspondant à la cellule utilisée pour réaliser les tests sous AMF, dans laquelle les conditions sont très différentes. De plus, des mesures ont permis de caractériser les propriétés magnétiques de ces matériaux ; (ii) un second chapitre expérimental (chapitre IV) a permis d'évaluer l'influence de l'application d'un champ magnétique de 300 kHz ayant des amplitudes de 10 à 48 mT sur l'électrolyse de l'eau. Différentes analyses ont permis de comprendre les mécanismes d'activation de cette réaction sous AMF. En parallèle, des analyses *post mortem* ont été réalisés, amenant à d'autres conclusions sur l'influence de l'AMF ; (iii) une étude bibliographique approfondie sur les effets d'un champ magnétique sur des processus électrochimiques (présenté au chapitre I et évalué au chapitre IV) a permis de connaître ces derniers et de les évaluer dans le système étudié, afin de savoir si l'activation observée n'était pas également due à d'autres phénomènes.

Tout d'abord, différentes nanoparticules de FeNi ($FeNi_3$, $FeNi_3$@Ni, $FeNi_3$@Mo - @ pour dopage), de Ni (Ni_{HI}, Ni_{OGM}) et des catalyseurs de références (Pt/C, IrO_2) ont été testées en électrode à disque tournant (RDE). Cette étude a permis d'évaluer l'activité intrinsèque de ces matériaux par rapport à l'électrolyse de l'eau, et certains catalyseurs ont présenté une meilleure activité que celui précédemment utilisé, les FeC-Ni (cœur-coquille), ce qui était un des objectifs majeurs de la thèse. L'influence du chargement a été évaluée sur les matériaux les plus actifs (Ni_{HI} côté HER et $FeNi_3$ côté OER). Des chargements trop importants sont préjudiciables à l'activité électrochimique, car une couche catalytique trop épaisse entraîne des effets résistifs et des gradients de potentiels, empêchant les sites actifs d'être tous au même potentiel, et augmentant le problème de masquage des sites actifs par les bulles. Une étude de durabilité composée de tests de vieillissement accéléré (AST) et d'imagerie en localisation identique avec un microscope électronique en transmission (ILTEM) sur les catalyseurs les plus

actifs [$FeNi_3$(@Ni)] et Ni_{HI} côté HER et OER a montré un détachement de la couche catalytique et une dissolution du Fe (la formulation de l'encre n'étant pas optimisée). Ensuite, l'activité de ces mêmes matériaux a été testée dans la cellule conçue pour les tests sous AMF (cellule en PMMA). En effet, les performances des catalyseurs pouvaient varier à cause des conditions de travail très différentes : le transport de matière n'étant pas contrôlé par la rotation de l'électrode de travail mais par un flux d'électrolyte, qui permet également de refroidir la chauffe créée par l'application de l'AMF et de dégager les bulles de la surface de l'électrode de travail. De plus, le support de l'électrode de travail utilisé était un feutre de carbone, présentant une structure poreuse et une surface développée très supérieure au support de la RDE (disque de carbone vitreux). En conséquence, l'activité des catalyseurs s'est bien révélée différente de celle en RDE. Néanmoins, les catalyseurs $FeNi_3$(@Ni) restent les matériaux les plus actifs. L'influence du chargement dans ces conditions a montré que l'utilisation du feutre de carbone évite l'effet préjudiciable d'une couche catalytique épaisse, grâce à sa structure poreuse et sa grande surface développée. Puis, des caractérisations magnétiques ont permis d'évaluer les propriétés magnétiques des nouveaux matériaux, et notamment de leur puissance de chauffe (SAR), caractérisée à 100 kHz sur des suspensions colloïdales des catalyseurs. Les $FeNi_3$(@Ni) chauffent à plus bas champ que les FeC-Ni (ce qui était intéressant car moins d'énergie électrique est nécessaire pour produire un champ magnétique plus faible) bien que leur puissance de chauffe soit inférieure (mais reste élevée : > 350 $W.g^{-1}$). Les matériaux à base de Ni présentent une SAR faible (< 100 $W.g^{-1}$) et les catalyseurs de référence ainsi que les $FeNi_3$@Mo ne chauffent pas. Ce dernier résultat était inattendu, mais ce matériau a servi de catalyseur témoin pour évaluer l'influence de l'AMF.

Ensuite, l'influence du champ magnétique alternatif sur la réaction d'électrolyse de l'eau a été évaluée dans la cellule en PMMA. D'abord, des CV_F sur $FeNi_3$(@Ni) à différents chargements (100, 1000 et 3000 $\mu g.cm^{-2}$) ont été réalisés. Plusieurs observations ont été faites :

(i) quel que soit le chargement, l'application de l'AMF réduit le potentiel de départ ; (ii) cette réduction est une fonction croissante de l'amplitude de l'AMF ; (iii) l'activation magnétique est plus importante à faible chargement, tandis qu'une saturation d'activation est visible à fort chargement. Des CP à ± 10 $mA.cm^{-2}$ sur tous les matériaux montrent qu'ils sont tous activés sous AMF, c'est-à-dire que la surtension est réduite (en valeur absolue) sous AMF, du côté HER comme OER. Etonnement, les matériaux à SAR nul sont aussi activés. Il a alors été déduit que les courants de Foucault sont à l'origine de cette activation, ce qui était inattendu car le montage a été conçu pour limiter leur apparition. Des mesures complémentaires de chauffe de l'échantillon « final » (feutre de carbone avec ou sans dépôt catalytique) confirment leur présence, notamment dans le feutre seul. Puis, des discussions sont menées pour essayer de distinguer l'effet de l'AMF sur la cinétique par transport de matière et la cinétique par transfert de charge. Selon la tendance des gains en potentiel (*i.e.* valeur absolue de la différence entre la surtension sans champ magnétique et celle sous AMF) : plus la surtension sans champ est grande, plus le gain en potentiel sous AMF est grand, il semble que la cinétique par transfert de charge soit davantage améliorée que celle par transport de matière.

Toutefois, des mesures CP à différents chargements (1000 et 3000 $\mu g.cm^{-2}$) sur $FeNi_3$(@Ni) indiquent que l'AMF influence différemment l'HER que l'OER. Côté HER, plus le chargement est grand, plus le gain en potentiel est faible, mais la surtension est plus faible. Ceci est probablement dû au fait qu'à fort chargement, des agglomérats plus grands sont présents, ce qui peut influencer/réduire la chauffe, et risque d'aggraver le problème de masquage par les bulles. Cette tendance indique que c'est davantage le transport de matière qui est amélioré côté HER, alors qu'aucune influence du chargement n'est visible côté OER. Enfin, des CP à plus fortes densités de courant (± 30 $mA.cm^{-2}$) confirment l'activation du transport de matière côté HER et l'activation du transfert de charge côté OER, bien que les deux effets surviennent. Des analyses de Tafel corroborent l'activation du transfert de charge, et indiquent

qu'il n'y a pas, à priori, de changement d'étape limitante. Des mesures de tension en circuit ouvert montrent que l'AMF ne modifie l'énergie libre de Gibbs de la réaction.

Dans un second temps, les phénomènes survenant lors de l'application d'un champ magnétique statique sur des systèmes électrochimiques (étude bibliographique approfondie) ont été évalués, ainsi que d'autres effets : l'effet Marangoni, Maxwell et thermophorétique (*i.e.*Soret), peu discutés dans la littérature. Selon des calculs d'ordre de grandeur, seuls les effets Kelvin, Marangoni et Soret pourraient intervenir de manière significative dans le système étudié. Des expériences avec des champs statiques indiquent qu'aucune influence est notable dans la cellule en PMMA. Toutefois, une simulation et des mesures de tensions de surface suggèrent qu'un effet d'un gradient de température influence le dégagement des bulles, et que le champ magnétique pourrait modifier la tension de surface des ions et/ou des bulles (mais reste à confirmer).

Enfin, des analyses *post mortem* ont été menées. Une étude en localisation identique avec un microscope électronique à balayage (ILSEM) montre que l'application de l'AMF ne provoque pas d'agglomération, mais que le Nafion®, constituant le liant de l'encre, subit une transition vitreuse ce qui change significativement sa morphologie : le Nafion s'étend, devient plus fin, et entraîne les agglomérats situés dessus. De plus, les images indiquent que ces derniers ne sont pas répartis de manière homogène sur le feutre de carbone, une conséquence du manque d'optimisation de la formulation de l'encre (qui n'était pas l'objectif premier des travaux). Ensuite, l'influence de la température et d'une atmosphère réductrice (H_2) et oxydante (O_2) sur $FeNi_3$@Ni a été évaluée. Des mesures de DRX en température et de TEM environnemental indiquent que ce matériau subit des changements cristallographiques, notamment à partir de 200°C, et que l'atmosphère induit un effet Kirkendall sous H_2 à haute température (séparation

des phases de Ni et de Fe), réversible sous O_2. Ces modifications peuvent entraîner une altération de l'activité électrochimique, ce qui corrobore l'étude de durabilité.

Pour conclure, ce travail a été dédié à la compréhension de l'action d'un champ magnétique alternatif radiofréquence de 300 kHz et d'amplitude maximale 48 mT sur la réaction d'électrolyse de l'eau en milieu alcalin (KOH, 1 $mol.L^{-1}$). Des matériaux non nobles, à base de FeNi et de Ni, comparés à des matériaux nobles de référence, Pt/C côté HER et IrO_2 côté OER, ont été utilisés. Bien que l'application de l'AMF ait une influence positive significative en réduisant les surtensions des deux côtés de la réaction, la clef de voûte de la suite du projet est de savoir si cette approche peut être rentable en terme énergétique.

Par rapport à l'optimisation de cette méthode, plusieurs axes de développement peuvent être adressés. D'abord, la formulation de l'encre doit être retravaillée. En effet, le Nafion® servant de liant n'est pas compatible avec une utilisation en milieu alcalin avec une chauffe locale. Ainsi, un liant résistant à un milieu alcalin, à la température, permettant une meilleure homogénéisation de l'encre et une plus grande durabilité doit être trouvé. Ensuite, le support doit être également amélioré. En effet, le feutre de carbone se corrode côté OER, notamment sous AMF. Même si des matériaux très catalytiques sont utilisés, présentant des surtensions très inférieures au potentiel de corrosion du carbone, ce dernier peut être dégradé par les conditions agressives de ce milieu alcalin. Egalement, des mesures de durabilité sous AMF doivent être conduites pour conclure sur la stabilité des matériaux non nobles sous AMF sur le long terme.

Un autre axe de recherche peut être l'optimisation de la structure et de la morphologie des catalyseurs, notamment dans le but de tirer profit des forces magnétiques qui pourraient entrer en jeu et faciliter le transport de matière (Lorentz, Kelvin, Soret, Marangoni et Maxwell). La présence des effets Soret et Maxwell doit d'ailleurs être confirmée par des mesures

expérimentales. De plus, connaître la température atteinte par les nanoparticules sous AMF serait un réel atout pour déterminer précisément l'amplitude de la force de Kelvin, et affiner le modèle de Soret en connaissant les gradients de température en jeu. Dans cette optique, des mesures d'élongation du paramètre de maille à différentes températures et sous AMF au sein de l'European Synchrotron Radiation Facility (ESRF) permettraient de remonter à cette information. Des mesures similaires ont été réalisées par Stéphane Faure et des collègues du LPCNO [304]. Malheureusement, nous n'avons pas eu la possibilité de planifier une campagne d'expérience au sein de l'ESRF à cause du Covid19 et des travaux de maintenance qui s'y sont déroulés en 2020.

Enfin, la pierre angulaire du pari de rentabilité de cette approche concerne l'optimisation de la géométrie de la cellule et des bobines, et par conséquent le choix du mécanisme de chauffe. Deux options sont possibles. Ce qui a été initié dans cette thèse est l'utilisation des pertes hystérésis dans le but de chauffer exactement au niveau du site actif, donc de fournir de l'énergie pour activer uniquement la réaction d'électrolyse de l'eau sans chauffer le reste de la cellule, ce qui conduit à des pertes énergétiques et augmente la dégradation des composants de la cellule. La bobine utilisée dans cette étude était évidemment surdimensionnée, et nécessite donc d'être adaptée à la géométrie de la cellule pour fournir un champ magnétique alternatif juste là où il est nécessaire : au niveau des électrodes. De plus, synthétiser des matériaux qui chauffent à encore plus bas champ serait pertinent, et trouver un support qui ne chauffe pas par courant de Foucault est nécessaire, bien que cette tâche soit délicate. En effet, on recherche d'un côté un support qui ne chauffe pas, donc qui soit isolant, et de l'autre côté, on recherche un matériau conducteur permettant aux électrons de circuler dans le circuit électrique. Une solution pourrait être d'utiliser un support très fin, tel un fil support présentant une grande surface développée et un diamètre très fin (plutôt qu'un réseau de fibres – feutre – propre à créer des boucles électriques). Dans ce cas, si l'épaisseur du matériau dans la direction de propagation de l'onde

du champ magnétique est très inférieure comparée à l'épaisseur de peau, l'onde n'est pas absorbée, et le matériau ne chauffe pas. Dans les conditions expérimentales de ce travail, l'épaisseur de peau était de 137 µm pour le fil d'or, alors que son diamètre était de 200 µm, or celui-ci chauffait très peu.

L'autre possibilité est d'utiliser les courants de Foucault comme source principale de chaleur. En effet, leur minimisation est une tâche complexe, alors que l'on pourrait tirer profit de leur présence. En ce sens, des expériences préliminaires ont été réalisées pour mesurer l'effet de la chauffe par courant de Foucault sur l'électrolyse de l'eau. Les résultats sont probants.

Enfin, il est primordial de calculer ou au moins d'estimer l'efficacité du système. Cette dernière peut être séparée en deux : d'un côté l'efficacité de la bobine, et de l'autre l'efficacité de la cellule électrochimique, activée par l'utilisation de l'AMF. La première évalue la restitution magnétique de la bobine sous forme de chaleur (η_{mag}), la seconde peut se calculer selon la formule suivante, Equation 1:

$$\eta_{\mathrm{H2,yield}}(25°\mathrm{C}, \mathrm{X\ mT}) = \frac{\mathrm{HHV\ (H_2}, T)}{U_{\mathrm{cell}}\mathrm{I} + P_{\mathrm{r}}} \qquad 1$$

Avec HHV le High Heating Value de l'hydrogène ($W.mol^{-1}$), c'est-à-dire la quantité d'énergie thermique libérée par la combustion complète d'une mole de H_2, U_{cell} la tension de la cellule (non corrigée de la chute ohmique) réduite des gains en potentiel, en prenant les meilleures performances des catalyseurs côté HER et OER, i le courant et P_r la chaleur fournie aux électrodes par le champ magnétique. Un premier calcul a été réalisé, et indique une efficacité très faible, ce qui n'est pas étonnant au vu du surdimensionnement de la bobine.

Par ailleurs, une solution pour réduire la consommation énergétique de la bobine est d'utiliser un champ pulsé (alterner des périodes sans et avec champ à haute fréquence).

Des mesures dans un montage expérimental deux électrodes, se rapprochant de la configuration des cellules industrielles, dans lesquelles l'électrode de travail ainsi que la contre électrode sont soumises à l'AMF, doivent être également réalisées.

Ainsi, de nombreuses recherches sont nécessaires pour produire de l'hydrogène via cette méthode !

Pour conclure avec mon avis personnel, trouver et améliorer les sources d'énergie renouvelables actuelles est urgent, mais les solutions technologiques ne seront jamais suffisantes et mises en place à temps pour résoudre la crise écologique actuelle. Ainsi, je crois que le meilleur moyen de répondre à l'urgence climatique est, en premier lieu, d'adopter une sobriété énergétique (impliquant une limitation forte de la société consumériste). Cette exigence et ce principe de vie changera nos habitudes actuelles, mais cela ne signifie pas un avenir moins heureux, et permettrait notamment une meilleure répartition et distribution des ressources de notre planète.

Abstract

This PhD aimed at studying the influence of a radio frequency alternating magnetic field (AMF) on the water splitting reaction in alkaline media (KOH, 1 mol/L). The objective of this approach was to heat the catalyst at a very local scale to enhance water electrolysis, without heating the electrolyte and the other cell component, especially to limit their degradation and provide the energy exactly where it is needed: on the catalyst active sites. The heat stems from (a priori) hysteresis losses of ferromagnetic nanoparticles submitted to an AMF. In such respect, the work consisted in a first place of finding non-PGM materials (especially FeNi and Ni-based) which are fast water splitting catalysts, as well as magnetically sensitive materials. Thus, several electrochemical tests (cyclic voltammetry, durability tests, Identical Location TEM) were conducted, as well as magnetic characterization (VSM, SAR), without an AMF application in first instance, then with it. The magnetic field proved to influence both the charge-transfer kinetics and the mass-transport kinetics (cyclic voltammetry, chronopotentiometry, Tafel, open-circuit voltage analysis), and that the heating came also from eddy current generation in the electrode support (non-graphitized carbon felt). No influence on the thermodynamics was concluded. In parallel, a bibliographic survey permitted to account for the various effects which can occur in an electrochemical system submitted to a magnetic field. Thus, Lorentz, Kelvin, spin polarization, as well as Soret, Marangoni and Maxwell stress effects were evaluated in the system. No influence of a Lorentz or spin polarization effects was observed, but the others are likely to intervene. Then, post mortem analyses (ILSEM, XRD, ETEM) allowed to study the influence of the temperature and of a reductive/oxidant atmosphere on the best catalyst (FeNi3@Ni). Finally, preliminary experiments were conducted to take benefit from the eddy current as main heating source. The efficiency of the system is also discussed.

Keywords: Hydrogen, Electrochemistry, Magnetism, Process Engineering, Materials

Résumé

Cette thèse a porté sur l'influence d'un champ magnétique alternatif radio fréquence (AMF) sur l'électrolyse de l'eau en milieu alcalin (KOH 1 mol/L). L'objectif de cette approche était de chauffer le catalyseur à une échelle très locale pour améliorer la réaction d'électrolyse, sans chauffer l'électrolyte ni les autres composants de la cellule. Ainsi, l'énergie est apportée exactement là où elle est nécessaire : au niveau des sites actifs du catalyseur, sans chauffer le reste de la cellule, ce qui limite notamment la dégradation des composants et les pertes thermiques dans le reste de la cellule. La chaleur provient (à priori) de pertes hystérésis de matériaux ferromagnétiques soumis à un champ magnétique alternatif. Le travail de cette thèse a donc consisté dans un premier temps à trouver des catalyseurs non-nobles (notamment à base de Ni et/ou Fe), à la fois actifs pour les réactions d'électrolyse de l'eau, et sensibles à l'application d'un AMF. Des tests électrochimiques (voltammétrie cyclique, durabilité, MET à localisation identique) ont été menés, ainsi que des caractérisations magnétiques (VSM, SAR), d'abord sans champ magnétique, puis sous l'influence d'un AMF. Les résultats indiquent que le champ magnétique améliore à la fois le transfert d'électron ainsi que le transport de matière (voltammétrie cyclique, chronopotentiométrie, analyse de Tafel, mesure de potentiel d'abandon). De plus, il s'est avéré que le chauffage provient également de la génération de courant de Foucault à travers le support de l'électrode (feutre de carbone non graphitisé). Aucune influence sur la thermodynamique n'a été relevée. En parallèle, une étude bibliographique sur les effets survenant lors de l'application d'un champ magnétique sur un système électrochimique a permis d'évaluer ces effets dans le système étudié. Ainsi, les effets de Lorenz, de polarisation de spin, de Kelvin, mais aussi de Soret, Marangoni et Maxwell ont été évalués. Ces quatre derniers semblent intervenir dans le système, ce qui n'est pas le cas de Lorentz et de la polarisation du spin des électrons. Ensuite, des analyses post mortem ont été menées (MEB à localisation identique, DRX, MET Environnemental) pour étudier l'influence de la température et d'une atmosphère réductrice/oxydante sur le meilleur catalyseur ($FeNi_3$@Ni). Enfin, des études préliminaires portant sur l'utilisation des courants de Foucault comme source première de chaleur ont été réalisées. L'efficacité du système est également discutée.

Mots-clefs : Hydrogène, Electrochimie, Magnétisme, Génie des procédés, Science des Matériaux